THE UNIVERSITY OF QUEENSLAND

AUSTRALIA

Characterisation of the liberation kernel

Snezana Bajic

Bachelor of Science, Bachelor of Engineering

A thesis submitted for the degree of Doctor of Philosophy at

The University of Queensland in 2014

Sustainable Minerals Institute

Abstract

Liberation is a fundamental process of mineral processing for almost all ores. A long-standing and challenging problem is the estimation of the liberation kernel in comminution. In this context the kernel means the mathematical transformation which relates the feed sizing and liberation distribution presented to a breakage or comminution device to the size or liberation distribution of the progeny.

Previously it was difficult to adequately quantify the liberation status of the feed particles without size reduction in order to prepare adequate samples for various two dimensional analysis methods. This destructive preparation process would not only change the size of the parent particle, but also lead to destruction of texture and liberation information. The texture information of a feed material is defined as the internal arrangement of mineral grains, their size and spatial distribution. Earlier work has been almost entirely restricted to binary composites which may be non-destructively classified by particle density and/or magnetic susceptibility or electrical conductivity. (Wiegel 1976b, 2006; Wiegel and Li 1967)

Micro-cone Beam Tomography (Micro CBT) was used for sorting feed particles into different composition classes and into different texture classes before breakage. While this technology still does not provide as wide a range of mineral differentiation or resolution as might be desired it is a significant advance over earlier approaches. The grains are observed in three dimensions by analysing Micro CBT cross sectional images using eCognition image analysis software.

The image analysis method developed in this Thesis enables the user to adequately characterise texture and liberation of the parent particle and progeny particles in three dimensions. A range of methods for quality assurance have also been established. The validation of mineral classification was performed using the Mineral Liberation Analyser (FEI, 2014). This technology provides excellent mineral recognition at high resolution.

The method developed here measures intact particle texture and allows for measurement of the texture and liberation of the progeny particles with no destruction of the particles. The sample preparation process for Micro CBT does not involve any physical damage to the particles. The full composition of the parent and its progeny particles can be measured in three dimensions using this method.

A random breakage model prediction has been presented where the measured liberation of progeny created by breaking the parent particle was compared with the liberation simulated by cutting the Micro CBT reconstructed two dimensional images of the parent particle into different size cubes.

The measured degree of liberation of the progeny particles confirms that below a certain particle size, liberation becomes selective as previously observed by Wiegel (2006). The random simulation of breakage helped reveal liberation by size reduction. The selective breakage identified in this research plays a major role especially in the range where the particle to grain size ratio is 1. There was a tendency for the gangue to break into the coarser liberated particles, unlike the valuable phase which has a tendency to break into finer, liberated particles. The need for a detachment factor (Hsih and Wen 1994) to be incorporated into random liberation models was confirmed. In many cases, the predicted grind size required to liberate gangue sufficiently may be the most useful outcome of the measurement.

Although available techniques, such as MLA, provide excellent mineral recognition at high resolutions, the two dimensional mineral data obtained needs to be adjusted to estimate three-dimensional characteristics. This process is called stereological adjustment and the degree of adjustment depends on ore texture. The new technology can be used for testing the methods of stereological adjustments.

Improved measurement of liberation leads to an improved understanding and the possibility of optimisation of the process of liberation. This Thesis brings the new testing technology which can be used to characterise the liberation kernel, that is to predict the

liberation distribution which would occur at any reasonable degree of liberation, for a known ore type and a known energy.

Declaration by author

This Thesis is composed of my original work, and contains no material previously published or written by another person except where due reference has been made in the text. I have clearly stated the contribution by others to jointly-authored works that I have included in my Thesis.

I have clearly stated the contribution of others to my Thesis as a whole, including statistical assistance, survey design, data analysis, significant technical procedures, professional editorial advice, and any other original research work used or reported in my Thesis. The content of my Thesis is the result of work I have carried out since the commencement of my research higher degree candidature and does not include a substantial part of work that has been submitted to qualify for the award of any other degree or diploma in any university or other tertiary institution. I have clearly stated which parts of my Thesis, if any, have been submitted to qualify for another award.

I acknowledge that an electronic copy of my Thesis must be lodged with the University Library and, subject to the General Award Rules of The University of Queensland, immediately made available for research and study in accordance with the *Copyright Act 1968*.

I acknowledge that copyright of all material contained in my Thesis resides with the copyright holder(s) of that material. Where appropriate I have obtained copyright permission from the copyright holder to reproduce material in this Thesis.

Publications during candidature

Introduction to X-Ray microtomography, ICAM Sep 2008, workshop presentation

The use of Cone Beam Tomography for identifying and quantifying minerals, 2008, JKMRC SMI RHD Conference paper (Chapter 3 and appendix 9.12 data)

Quantitative analyses of minerals in multiphase particles using X-Ray microtomography procedures, 2010, JKMRC SMI RHD Conference paper, The University of Queensland (Chapter 5)

Characterisation of liberation kernel, public presentation at JKMRC, confirmation of candidature June 2011 (Chapters 2 to 5)

Publications included in this Thesis

No publications included

Contributions by others to the Thesis

I received advice and support from the supervisors of this PhD research work:

- Dr Rob Morrison supported the research work from its beginning. His help in concept and the design of the Thesis, as well as in data interpretation and writing was priceless.

- Dr Cathy Evans joined the project in its last two years. She supported it in every aspect and gave very important advice in drafting of the Thesis, data interpretation and writing.

I received research assistance from:

- Dr Tim Napier-Munn for some statistical analysis of the data. He also made a significant contribution during the Thesis reviews, where he expressed his opinion on the data and pointed in important research design directions.

I received advice and support from:

- Dr Luke Keeney on micro tomography imaging.

- Dr Richard Hartner on image analysis and image registration.

- Dr Steve Larbi-Bram on RBT data.

- Ion Gurnett in 2009 published Ore Characterisation of Dense Medium Separated Particles by Cone Beam Tomography and MLA Analysis as his Undergraduate Thesis at The University of Queensland. Ion was supervised by Dr Rob Morrison and me. His research data helped in defining some measurement and analysis parameters for this research. The images were from Murat Cakici, 2009, 'Characterisation of Samples of Ore Particles using X-Ray Microtomography', Master of Philosophy Thesis, The University of Queensland.

Statement of parts of the Thesis submitted to qualify for the award of another degree

None

Acknowledgements

> "*Scio me nihil scire.*" *"I know that I know nothing."* Socrates

This life-changing PhD journey would not have been possible without the support and guidance that I have received from many people. Everything I achieved I own to, and share with the people below.

This PhD started with the encouraging conversations with Dr Aleksandar Janković in 2005. My deep appreciation goes to him and his family for their priceless help in the early days of my settlement.

I will forever be thankful to my mentor Dr Robert Morrison. You are the supervisor everybody could wish to have, a blessing from the God. It is your encouragement that was giving me the strength to continue. Without your guidance and constant feedback this PhD would not have been achievable.

Many thanks to Dr Catherine Evans for her support, patience and guidance. Your help and understanding were precious. Rob and Cathy are my dream supervisory team, I could not have asked for better role models. I am very proud of my JKMRC team and I truly hope I will continue to share the research values, dreams and wisdom that you have given to me.

Special thanks and gratitude goes to Julius Kruttschnitt Mineral Research Centre (JKMRC), a place which would always bring special nice memories in my hearth. I am also very grateful to all those at JKMRC, especially Jill, Karen, Leith, Sherrin, Neva, Mike, Ton and Ray, who were always so helpful and provided me with their assistance every time. Thanks to the Pilot Plant and MLA laboratory staff for their help during my experimental work. Many thanks to Dr Tim Napier-Munn for his valuable inputs and ideas. Without the use of Dr Matt Brennan's "powerful" computer the work would not be possible. Thanks to my student colleagues Richard, Luke and many others at JKMRC. I would also like to thank Dr Steve Morrell and Dr Toni Kojović for their support and many encouraging conversations.

Hvala vam najdraži moji na strpljenju i ohrabrenju na ovom teškom putu ka uspehu. Moja dečice, vama je ovo sve posvećeno, jer vi ste porasli u maminim mukama. Hvala mom suprugu Milovanu za neizmernu ljubav i snagu tokom svih godina zajedničkog života. Bez tvoje ljubavi i podrške ja ne bih ni krenula na ovaj težak i daleki put. Mojim dragim roditeljima Vukici i Svetislavu Perić na svoj pomoći i odricanjima koje su imali zbog mene. Miloj majčici I tati posebno hvala. Mom bratu Draganu zahvaljujem na podršci i što me je uputio na rudarske staze davne 1999. godine. Dragi moji, vi ste svi više verovali u mene nego ja u sebe. Vi ste sa mnom proživeli svaki minut ove pustolovine. Vama za ljubav, hvala.

A special heartfelt thanks to my dearest family, my kids, my husband, Mum, Dad, brother and all friends. To my kids, Jelisaveta and Vukasin, we went through mum's pain together so mum dedicated this achievement to you. Dedicated to my lovely husband Milovan, I would never be able to get through this if it wasn't your unlimited love and strength to guide me. Without your love and support, I would never decide to "travel" so far. Dedicated to my parents, Vukica and Svetislav Perić, for all your help and support. Special thanks to my dearest beautiful mum. I would never decide to follow mining path if it wasn't my brother Dragan who encouraged me in 1999. My dearest family, you believed in me more than myself. You were with me on every step of this journey. For your love, thanks.

"Alea iacta est." & *"Eppur si muove."*

"The die has been cast." & " And yet it moves." Julius Caesar and Galileo Galilei

Снежана Бајић (Snežana Bajić, dev. Perić)

Keywords

Liberation; liberation model; liberation kernel; image analysis; automated SEM-based mineralogy system; micro tomography; random model.

Australian and New Zealand Standard Research Classifications (ANZSRC)

ANZSRC code: 091404, Mineral Processing/Beneficiation, 100%

Fields of Research (FoR) Classification

FoR code: 0914 Resources Engineering and Extractive Metallurgy, 100%

Table of Contents

15

17

List of figures

21

24

25

26

27

List of tables

1 Introduction

Liberation is a fundamental process of mineral processing. A long standing and challenging problem is the estimation of the liberation kernel in comminution. In this context the kernel means the mathematical transformation which relates the feed sizing and liberation distribution presented to a breakage or comminution device to the size and liberation distribution of the progeny. Even with many simplifying assumptions, a mathematical solution to the general problem remains elusive - in part because of the difficulty of testing potential solutions.

Perhaps the dominant reason for the intractability of this problem is how to adequately quantify the liberation status of the feed particles without destroying them by the measurement process. Previous work has therefore been almost entirely restricted to binary composites which may be non-destructively classified by particle density and/or magnetic susceptibility or electrical conductivity. While many ingenious approaches have been devised, none of these can consider the mineral "texture" of the feed material – that is, the internal arrangement of minerals within feed grains as well as the concentrations of minerals present.

Improved measurement of liberation should lead to an improved understanding and the possibility of optimisation of the process of liberation. It should also lead to the improvement of the process of comminution, where the size at which mineral of interest would be sufficiently liberated can be predicted. Existing models can then be confirmed and/or adopted to suit the "real" world observations.

"The basic problem in liberation analysis is the following. Given a representative sample of an ore, is it possible to make appropriate measurements to characterise the mineralogical texture of the unbroken ore in a quantitative way so that the composition spectrum of the particles can be predicted as a function of the particle size in the comminution products when the ore is milled? This is a difficult problem to solve because

the geometry of both the mineralogical textures and the particles formed by comminution is highly irregular. "(King 1987)

Because of the problem of measurement of the feed texture, researchers have used stereology to derive probability equations and estimate the distribution based on areal or intercept measurements of the progeny particles.   The major inverse stereological problems as Keith (2000) stated, are volume correction problem and composition correction problem. In the first one researchers are estimating a statistical distribution of particle volumes (King 1982; Miles 1985). The second is estimating liberation using area or intercept measurements. Other problems are estimation of statistical distributions of surface area, binary surface composition, multiphase volumetric composition and multiphase surface composition (Keith 2000).

These Thesis provides a proof of concept for an experimental strategy to address that two important problems.

The title of the Thesis is "Characterisation of the Liberation Kernel" which indicates that this Thesis applies new testing technology to solve the problems of non-destructively measuring valuable phase in the parent material. The kernel or conditional probability density is relating the distribution of progeny composition produced by parent particles. So far both of this parameters have to be estimated as apparent composition (based on areal or intercept measurements) and "likely" parent composition. Equation 1 shows that apparent particle distribution p (s) (breakage function) which is based on area or intercept measurement depends on true particle three-dimensional volume distribution f(c) and conditional probability density in particle space or the kernel.

Equation 1 (Keith 2000):

$$p(s) = \int_P k\left(\frac{s}{c}\right) f(c)\, dc$$

To be able to characterise kernel breakage function and true volumetric particle properties are needed. Kernel (K) explanation is given in detail in section 2.7.1.

If breakage and distribution functions are given as vectors, then K has to be a square matrix with solutions for different breakage events per liberation per size class. The parameters for locked values or gangue are simple as once liberated stays liberated. Hence, locked particles produce more complicated solutions and none of the technology that are available can provide the exact solution.

Many of the researchers simplified the assumptions to solve the problem and satisfy with "likely" solution.

The Thesis hypothesis is that the method proposed here should enable the non-destructive measurement of true volumetric composition and liberation of parent particles and its progeny particles in three dimensions. Thus two unknowns in the kernel equation can be measured and the kernel true characterisation is enabled. By knowing feed particle true composition using the method presented here, the kernel can be characterised.

The method developed enables adequate quantification of three dimensional liberation status and mineral grain size distribution of feed particles and progeny after the breakage event.

This enables comparison of the results of the measured liberation of progeny created by breaking the parent particle and the liberation simulated by cutting the parent particle Micro CBT reconstructed two dimensional images into different size cubes. This would help simulate Gaudin's Rubik's cube arrangement concept.

The method enables the simulation of random breakage model and thus provide a base line for comparison of breakage modes. The proposed methodology can then be used to predict the progeny liberation and thus characterise the liberation kernel for a known ore type and a known energy.

Several complementary measurement and experimental techniques have been developed and optimised within the scope of this project.

The original contributions made by this work are:

- Optimisation of Micro CBT three dimensional mineral identification technique. The parameters that influence the image quality are optimised to suit the analysis and image reconstruction process. Although some of the techniques presented can be used for three phase mineral identification, assuming that certain key mineral properties are satisfied (such as sufficient difference in mineral attenuation coefficients discussed further in 2.6.4.3.1), the liberation kernel measured here has been based on a binary phase mineral matrix: within a high density phase (magnetite) and low density phase (quartz). These particles measured were mounted in Styrofoam for two major reasons:

   a) Enabling particle stability during X-ray image acquisition;

   b) Filtering low energy X-rays which cause problems in detecting X-rays and in image reconstruction process.

- Characterisation of the liberation kernel in three dimensions using:

   a) A method for non-destructive measurement of mineral composition, grain size and liberation identification of both parent and progeny particles.

   b) A number of quality assurance and control measures, such as radiograph X-ray count rate comparison for radiographs generated during the acquisition stage at different measurement times and rotation angles. The second method proposed here is optimised direct calibration of identified mineral phases using automated mineral liberation analyser.

   c) Contribution of a new platform for understanding the liberation process enabling extension of two dimensional mineral liberation analyser compositional data.

d) A method for comparing simulated random breakage model using measured three dimensional parent mineral data and liberation breakage model calculated by measuring three dimensional mineral progeny mineral data.

e) Measured progeny mineral liberation maps in three dimensions.

f) A method for identification of a breakage mode for binary magnetite (high density phase) and quartz (low density phase) ore. This method can be used for predicting the grind size at which the gangue phase becomes sufficiently liberated and therefore can be rejected in earlier stages of mineral processing.

Testing of published models by introducing the third dimension of the mineral grain inside the matrix is enabled, leading to a new model of liberation. The Wiegel model of liberation was also tested and confirmed.

The new measurement technique can be used for testing stereological correction procedures.

Demonstration of the new methodology enabled detailed characterisation of the liberation, texture and behaviour of parent particles through the size reduction. The mineral "texture" of the feed material was considered in terms of the internal arrangement of minerals within feed grains particles as well as the concentrations of minerals present. All measurements before breakage were conducted without destroying the particle by the measurement process. This approach offers the prospect of an improved understanding and characterisation of the liberation process.

Micro-cone Beam Tomography (Micro CBT) was used for sorting feed particles into different composition classes and into different texture classes before breakage. This technology still does not provide as wide a range of mineral differentiation or resolution as might be desired but it is a significant advance over earlier approaches.

The image analysis methods developed in this Thesis enable the user to adequately characterise texture and liberation of the parent particle and progeny particles in three dimensions

In the ore tested here the first group of minerals consists of gangue minerals (which includes quartz, K-feldspar etc). The second mineral group consists of chalcopyrite, pyrite and magnetite minerals. The last group is made of a single mineral, barite, although this mineral may be substituted with galena, mercury, platinum or some other high density minerals if needed. When making this change, a relatively simple change in the code for analysis is required.

Kernel characterisation has been based on binary (magnetite-gangue) composites. However, it is possible to extend the method to multicomponent particles using more advanced technology and automated computerised analysis but this is beyond the scope of this work.

A range of methods for quality assurance have also been established. The tomographic data can be validated using chemical assay or other mineral identification techniques. Reproducible results can be achieved by using the SkyScan1172 microtomography instrument and analysing images using eCognition8 software (discussed in Chapter 3). The optimised calibration technique presented also offers an opportunity to investigate mineral grains in multiphase particles in three dimensions.

The second area of new technology used here is particle breakage at much better controlled levels of input energy than has previously been possible. Good correlations already exist for most comminution devices between input energy and particle breakage. The JK Rotary Breakage Tester - JK RBT (Shi et al. 2009) used here incorporates the effect of particle size and input energy. Particles are broken using single point contact, where the total energy used for breaking is imparted by the rotor and kinetic energy of the particle. The specific energy used for breaking particles is defined as kinetic energy per particle mass (section 2.7.2.2) Hence, the outcomes of this project should find ready

application within mathematical models of comminution. However, development of those models is beyond the scope of this Thesis.

Gaudin (1939) presented a mineral liberation model for binary mineral system using an idealised Rubik cube arrangement concept. Gaudin assumed that cubic shape mineral phases were aligned adjacent to each other in such a way that the eight corners of the cube were touching the corners of the other cubes. The binary system in this model was broken in size reduction mode with parallel fracture planes. (Wiegel and Li 1967) developed the model based on Gaudin's concept with the difference of random location of mineral grain species and randomised fracture planes.

Wiegel's experimental work showed the tendency for the magnetite to grind at more rapid rates than the gangue phase. This observation led to the introduction of a directional coefficient which described the proportion of material that started in a specific size or composition location and proceeded in progeny size or composition class as a result of a size reduction process. (Wiegel 1976b)

One of the limitations of the model is that the assumption that progeny liberation depends only on the particle size and composition and not on the history of the particle (original size or already the result of a breakage event). Using this model it is not possible to calculate directly the proportion of the volume in a specific composition range that moves to each composition range in the next finer size class. (Wiegel 2006)

The overall aim of this work was to develop a method for measuring liberation in three dimensions and apply it to identify the mechanism of breakage of particles that consists of mineral phases with different hardness parameters, introducing mineral composition and mineral grain size distribution considerations by measuring both parent and progeny. This process establishes the relationship between progeny size distribution and liberation to parent grain size distribution and liberation, and thus presents a way to characterise the liberation kernel.

The following chapters demonstrate the technique for better measurement and understanding of the liberation distribution at reasonable degree of liberation. This Thesis presents a methodology for characterising the liberation kernel for a known ore type and well defined breakage energies. Hence it provides proof of concept for experimental measurement of the liberation kernel.

2 Literature review

2.1 Introduction

A long standing and challenging problem in mineral processing is the estimation of the liberation kernel in comminution, as outlined in chapter 1. A more general approach to estimating the liberation kernel requires a way of measuring a spatial arrangement of the grains of interest within the gangue. This arrangement is called the texture of the ore.

Common mineral identification techniques are automated two-dimensional techniques which use destructive sample preparation methods. Thus it is not possible to consider the mineral "texture" of the feed material. The definition of texture here is the internal arrangement of minerals within feed grains as well as concentration of minerals present.

Researchers have been dealing with limitations of available measurement techniques for decades. Some used mechanical techniques to separate liberated gangue phase from mid-range and liberated value magnetic phase (Wiegel 1975, 1976a, 1976b, 1976c, 1979, 1999a, 1999b, 2002, 2006, 2010) in order to validate proposed liberation models. Others used two dimensional image analyses techniques (Barbery 1991; Schneider et al. 1991).

2.2 Mineral identification

This chapter focuses on the general information about minerals and methods used for their identification. A useful but incomplete mineral definition is:

"A naturally occurring, homogeneous, solid substance which is generally of inorganic origin, it usually has a well-defined crystalline structure and the chemical composition that lies between well-defined limits " (Jones 1987, p5). However, the International

Mineralogical Association in 1995 (Nickel 1995) adopted a new definition of a mineral as an element or chemical compound that is normally crystalline and that has been formed as a result of geological processes. The modern classifications include an organic class - in both the Dana (Gaines et al. 1997) and the Strunz (Strunz) classification schemes.

An ore is a mineral deposit from which it is possible to produce a metal by using technological methods that already exist or can reasonably be developed based on existing methods (Jones 1987).

Manual mineral identification techniques use a particular combination of characteristics are considered (lustre, hardness, colour and physical description). They are rarely used nowadays in the mining industry. The properties of minerals have been combined taking into account their terrestrial distribution that is governed by geological processes (Carmichael 1989). The Mineralogical Society of America features an on-line mineral identification key by Alan Plante, Donald Peck, & David Von Bargen (Plante et al. 2003).

Nowadays more automated mineral identification is in common use. The challenge in these systems is to set the measurement templates based on the mineralogy knowledge of the person who is building them. If the person is not competent, the identification may be misleading and identify a completely different mineral. The advantage of automation is much reduced time to data, and the acquisition of more complicated computed mineral properties such as sectional mineral liberation and association.

The physical properties of the minerals are of great importance to liberation, especially if the adjacent gangue/valuable mineral species are considered. These include crystal structure, habit, hardness, fracture, specific gravity and magnetism. Properties of economic minerals are provided in appendix 9.1 and terminology used is provided in appendix 9.2.

A number of mineral analysis technologies are used to measure the basic composition of ore. The techniques that are presented in this document are Automated Scanning Electron Microscope (SEM) Based Microscopes - MLA and Micro CBT.

The MLA system is used for identification of the minerals as well as for measuring mineral grain size, associations, locking and liberation characteristics within a polished section of a sample. This technology is in common use. A description of this technology is in section 2.6.3.

Micro cone beam tomography uses a point source of X-rays directed at an array of detectors. The object to be measured is placed between the X-ray source and the detectors. The object is rotated in small increments to generate a series of images. These images can be reconstructed in two or three dimensions.

When considering images acquired with Micro CBT, visualisation of the internal structure is possible due to the variations in density and atomic composition of the mineral grains inside the rocks. It is the contrast between the X-ray attenuation of the phases inside the rocks that brings the variation in the grey scale of the mineral grains. The effective atomic weight Z is the major factor controlling the attenuation of the minerals scanned with X-ray energies below 100kV. The linear attenuation coefficients are calculated from X-ray CT images and these are directly proportional to the mineral density and mass attenuation coefficients of different X-ray energies. The later one was obtained from XCOM Photon cross section database provided by the National Institute of standards and Technology (NIST 2011). More details of this technology are given in section 2.6.4.

2.3   Texture

The texture of a rock is commonly defined as the arrangement of mineral grains, their size and shape, the degree of uniformity of the grains, the interaction and relationship between neighbouring grains as well as the orientation of grains within a rock. The texture of the rock influences its liberation characteristics and therefore has direct impact on equipment and process selection in mineral processing.

There are three main types of rocks (Blatt and T. 1996; Roberts et al. 1974):

- **Igneous**, formed through the cooling and solidification of magma, having crystallised from a molten material;

- **Sedimentary**, formed by deposition of the material or mineral accumulation at the Earth's crust;

- **Metamorphic** (change in form), formed by adjusting mineralogical or textural properties of solid rocks under the influence of temperature or pressure, changes in physical and chemical environment.

Igneous and metamorphic rocks make up 90–95% of the top 16 km of the Earth's crust by volume (Prothero and Schwab 2004).

In geological and other rock based studies there are the common textural features of interest. **Coarse grained texture** is when there are visible crystals or grains (for example granite). **Fine grained texture** is when there are small grains which are invisible to the unaided eye (for example shale texture). **Homogenous rock texture** is if the grains appear of the same size in all direction, such as in basalt. **Porphyritic texture** is when large visible crystals are based in a fine grained matrix (granite porphyry texture). There is s**chistose layers** texture of flattened minerals (mica schist) and **foliated texture in** a metamorphic rock texture of parallel mineral banding (gneiss). (Blatt and T. 1996)

In this Thesis texture is considered as the internal arrangement of grains, their size and distribution as well as the concentration of minerals present.

2.4   Liberation

Economic minerals in ores were created an anomalous concentration of valuable materials or elements. In general this initial concentration is too low to make the ore directly usable for the production of a finished product through metallurgical or chemical processing. However, a hundred years ago many concentration plants sent their ore directly to the

smelters because of relatively high concentrations of valuables in the ore (for copper ore over 3% Cu in feed material). The silver lead ore at Finney's Hill (site of the JKMRC) now the University of Queensland Experimental Mine was direct shipping grade.

Minerals are normally present in small amounts in the crust of the Earths except in mineral deposits where accumulation of a certain mineral leads to higher concentrations. It is not only quantity that counts, but economic importance, i.e whether the mineral in the deposit can be exploited efficiently. We are faced with the problem that there are only few mineral deposits in the world that have a high percentage of valuable minerals. Most of the deposits currently being exploited have ore with a percentage of valuables that was previously considered to be a low grade deposit. Since the demand for metals on the world market is increasing constantly and recycling is not covering the demand, we are in the situation where treatment of low grade ores is essential. For this reason, it is very important to optimise the liberation process as much as possible and collect the valuable minerals in concentrate. If we grind just enough to obtain liberation adequate for separation, we will also save an enormous amount of the energy used for grinding of the ore.

The valuable minerals present in the ore must be concentrated by separation from their gangue, usually by physical processes of separation, making use of differences in the properties of minerals (Evans 2002). In the initial in-situ ore, these minerals are present as grains, which, in order to reveal their differences in properties, must be first transformed into particles consisting of only one mineral. This state is defined as "liberation" of mineral in particles (Barbery 1991). However, this definition suffers from a number of limitations; in particular, a particle that is predominantly liberated may have a very minor impurity thus causing it to be treated as composite (Evans 2002). "**A grain**" is considered to be a mineral in its original state in the ore matrix before breakage and the term particle relates to already broken rock.

Although it rarely happens, some minerals are liberated by natural processes. Some examples are beach sands and other alluvial deposits.

2.4.1 Effect of Comminution on Liberation

The purpose of the comminution stage of the mineral concentration process is to break the ore in order to liberate the valuable components so that they can be separated from the valueless parts and concentrated in a saleable product. Technical and economic significance of comminution is considerable. The particles must not be overground because valuable fine particles could be lost during the concentration processes. Overgrinding also leads to increased cost of the process by applying excessive energy during a breakage process. Comminution is a costly process, which also consumes a significant amount of the world's energy. (DOE 2001)

During comminution, there is, however, a natural tendency towards liberation and particles that are smaller than the mineral grains that occur in the ore can appear as a single mineral. This happens when a progeny particle is formed entirely within a mineral grain. Obviously this will occur more frequently the smaller the particle size and it is impossible when the particle is substantially larger than the mineral grains in the ore (King 2001).

As the mineralogical texture of the ore is typically complex and heterogeneous, the processes of comminution, crushing and grinding produce a vast network of fractures throughout each particle. These fractures ultimately determine the distribution of particle sizes that are produced in the comminution equipment. The relationship between the network of fractures and the underlying mineralogical texture determines how the mineral phases are distributed among the particles in the population after fracture (King 2001).

"The choice of size to which the comminution step must reduce the host rock to ensure an economic level of liberation is one of the most critical design criteria for a mineral processing plant. If the size to which the rock is reduced is insufficient, then a relatively large proportion of the valuable constituents will not be extracted, leading to the loss of potential revenue. If the size chosen is too small, an oversized and overcostly plant with unnecessarily high-energy costs will result" (Napier-Munn et al. 1999). For a low grade

ore, the liberation size for the primary separation will usually be the liberation size of the gangue.
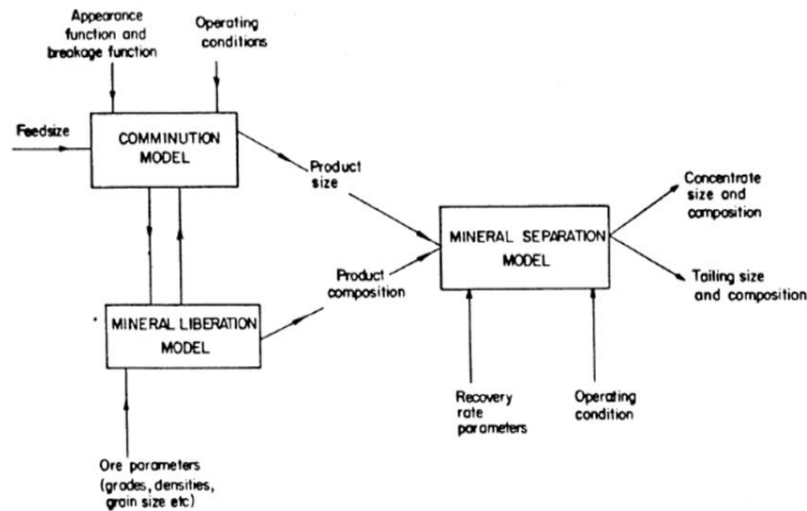
Figure 1: How breakage, liberation and separation models interact (From Evans 2002, after Wiegel 1976b)

It is standard practice to regrind low grade concentrate to generate further liberation (RTB Bor Copper Mine, Telfer Gold Mine, Century Mine and others).

A study on the influence of regrind on saving and optimising the energy in comminution and smelting has been published in Evans et al 2011. An MLA system was used to measure the liberation and mineral association in two dimensional space. Stereological correction procedures have not been applied to data. The two dimensional approach was final here. There was a limited amount of sample available which restricted separation of Cu-Ni bulk concentrate into Cu and Ni concentrates. However, plant performance figures were used to approximate the separation. Simplifying liberation 2D MLA spectrum in graphical presentation is achieved in Wightman and Evans (2014).

Wightman and Evans (2014) presented the MLA liberation spectrum for three ores in a form that can be used to better understand a processing context. If the size of the particles was determined using equivalent circle diameter calculation within MLA, the results would give reasonable estimate only if the grain shape is discrete and euhedral (Figure 2 d and e). The more complex texture (Figure 2a and c) and when the grains are not segmented

47

properly (Figure 2b) the equivalent circle diameter would provide results with reduced confidence. The graphical output shown in Figure 4 helped in these cases to identify the size at which pyrite grains begin to liberate. This information can be used to optimise the grain size liberation in comminution. However, care should be taken as this was based on a single cross sectional data of the presented particles given in 2D and stereological information has not been applied. The application of the method developed in this Thesis with the above mentioned 2D method can make a valuable contribution to energy reduction in comminution.
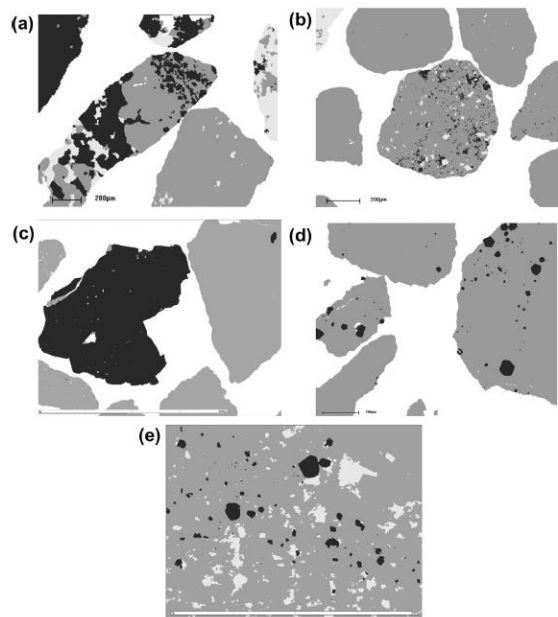
Figure 2: Classified particle maps from MLA measurement on different ore, pyrite (dark grey), other sulphides (light grey) and gangue minerals (mid grey), (fromWightman and Evans 2014)
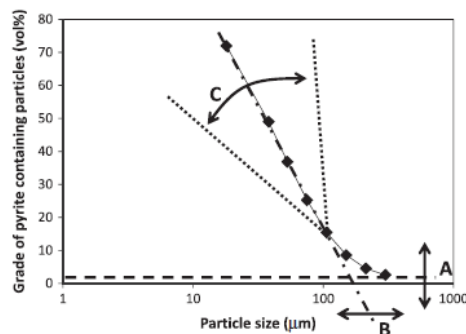
Figure 3: Representation of the liberation spectrum derived from MLA measurement (after Wightman and Evans 2014)
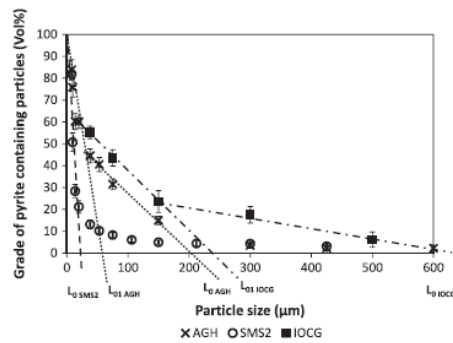
Figure 4: Liberation spectrum of pyrite in AGH, SMS2 and IOCG (from Wightman and Evans 2014)

2.4.1.1 Types of Breakage

As the mode of breakage of the particle is an important aspect of comminution, it can be considered in terms of liberation. The following types have been reviewed by Evans (2002).

Non-preferential breakage means that breakage is independent of particle composition. For example, in a binary particle, if the properties of the one mineral phase are different from the second mineral phase present, it does not mean that the breakage crack would prefer to develop only through one mineral phase. Although it is not mandatory, when particles break non-preferentially for a given similarly-sized set of parent particles, the average composition of corresponding progeny particles does not vary with size (see also Random breakage below).

Preferential breakage means the breakage depends on the composition of the particles. Preferential breakage can be exhibited by either particles breaking more easily because of interfacial breakage, or because breakage is occurring more through one mineral than another because of selective breakage (Fandrich 1997). **Selective** breakage is a breakage mechanism favouring breakage of one mineral over another.(King and Schneider 1998a)

When the position of cracks is random, breakage is considered to be **random**. Random breakage is independent of both the particle composition and the particle shape. In this

case, attrition is not considered to be random breakage. In this case attrition refers to particle disintegration caused by more frequent grain to grain contact. As for non-preferential breakage the average composition of progeny particle resulting from similarly-sized parent particles does not vary with size; however in this case this relationship is mandatory. (Gaudin 1939)

In this Thesis, attention has been paid to random breakage because almost all liberation models assume random breakage.

Since the method presented here can deal with different mineral properties and their arrangement in the particle matrix, the importance and key concept of the mode of breakage is detailed in section 2.5.3.

2.4.1.2 The interpretation of liberation

For automated SEM data it is usual to determine the amounts and sizes of apparently liberated and unliberated grains by image analysis. Point counting for optical microscope image has also been used with some success Petruk (2000).

This manual method is carried out by superimposing a suitably sized grind on the image of the particle (or a group of particles) and identifying the mineral and particle within each square of the grid.

Figure 5 is taken from Petruk (2000) and shows the grade of each particle (e.g. percentage of mineral of interest in the particle). The degree of liberation of minerals is usually determined by analysis of the polished sections and obtaining the particle grades and the distribution of the mineral of interest among the particles (for example percentage of mineral in each particle section).
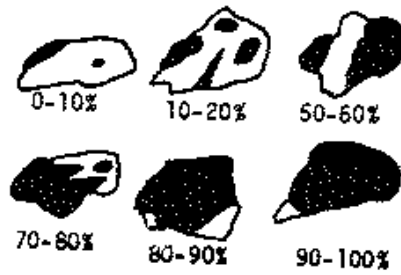
Figure 5: Particle grades (percentage mineral of interest in particle) (from Petruk 2000)

The apparently liberated mineral is the particle section that contains 100% of the mineral. Here "apparently" refers to the fact that the orientation of the particle may be such that only the mineral of interest is visible in the revealed particle section. If mineral liberation is measured for different sizes of particle sections, classified by either sieving or image analysing, the data can be combined into one table as shown on Table 1. (Petruk 2000).

Table 1: Example of proportion by area of mineral distributed among different grades of particles.(Petruk 2000)

Particle grades (%)	0.1-10	10-20	20-30	30-40	40-50	50-60	60-70	70-80	80-90	90-99.9	100 (free)
% mineral in grade range	6.5	3.5	1.5	1	1	1	2.5	6.5	11.5	23.5	41.5

Figure 6, which is also taken from King and Schneider (1998b) shows the distribution of mineral of interest among sectional particle grades. It is commonly reported as a cumulative liberation yield curve. The curve begins with the amount of the mineral that is apparently liberated, and the quantities of mineral in 90-99.9%, 80-90%, particle categories are added sequentially.
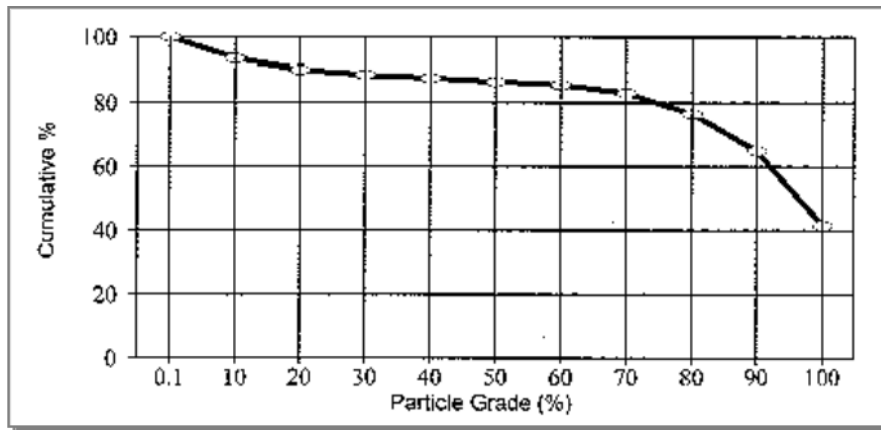
Figure 6: Liberation data plotted as cumulative liberation yield for mineral in particles of different grades. (Table 1 plot)(King and Schneider 1998b)

2.4.2 Stereology

Stereology is a branch of mathematics which uses mathematical procedures, such as derivation of geometric probability equations, for estimating three dimensional characteristics of the particle based on available one dimensional (line) or two dimensional (area) data.

Nowadays the normal practise using an automated SEM is to measure a single particle section per particle. In order to achieve statistically significant results, a large number of particles have to be tested. With the use of stereology, the two dimensional information is transformed into approximate three dimensional data. Approximately because two dimensional measurements do not fully define three dimensional space.

Figure 7 illustrates the basic problem when the liberation measurement is based on two dimensional data. The particle is composite yet a section through the particle may appear liberated (having only one mineral) for either mineral or correctly designated as composite. This means that, in general, the proportion of liberated particle sections that appear in two-dimensional analysis is larger than in the three dimensional particles themselves. Hence, liberation is over-represented, as liberated particles will never produce a section indicating composite particles whilst composite particles can produce a 'liberated' section.(Barbery 1991; Gaudin 1939; King 1994b; Meloy 1984; Wiegel 1976b)
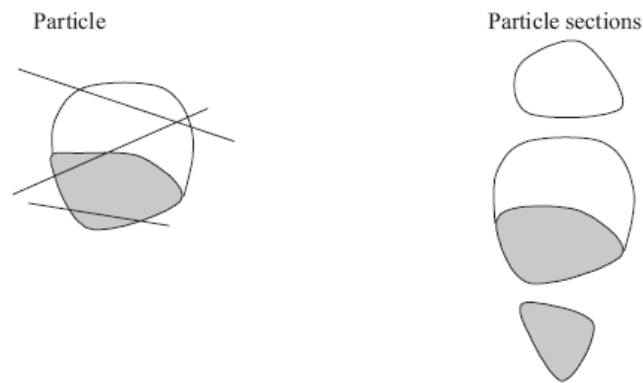
Figure 7: A composite particle, when sectioned can appear either as: liberated (valuable mineral or gangue) or composite (from Gay and Morrison 2006)

If the particle texture is complex, the estimation of volumetric liberation curve from linear and liberation curves from area measurement is also complex. For this reason, stereological adjustment has been a long-standing challenge for the mineralogists and mineral processors. Particle specific gravity has typically been used to physically separate binary liberation classes but fails absolutely if more than two minerals are involved.(Gay and Morrison 2006)

The complexity of estimation of volumetric mineral liberation based on sections and the difficulty of mathematical description and analysis of liberation leads to increased interest in developing three dimensional measuring techniques.

Correction methods (to estimate volumetric to sectional data) have been proposed by Gaudin (1939), Wiegel (1976b), Meloy (Meloy 1984), Barbery (1991), Latti (Latti and Adair 2001) and King (1994c; 1998b) but these methods are applicable to particular arrangements of minerals. The work of Gay (1995) and Keith (1997) provides an approach which is more complex but more general as it takes more of the mineral texture into account. Some of the adjustments will be discussed further later. (Section 2.5)
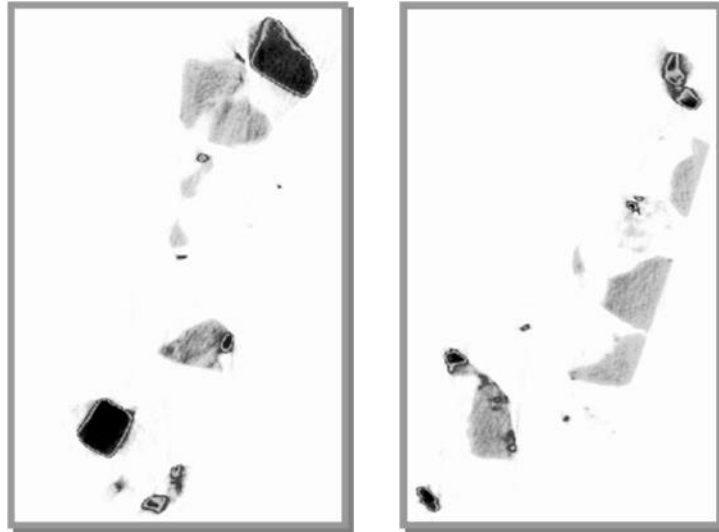
Figure 8: Two CBT sectional bit maps of the same sample showing two large grains of galena (left hand section) and the polished surface for SEM measurement in the right hand section.(Gay and Morrison 2006)

As a particle is sectioned, some of the texture information is destroyed. This means that it is not possible to precisely determine all of the original three-dimensional information from the available two-dimensional information (Cruz-Orive 1976).

An example of this loss of information during transformation is Meloy's model of liberation. Meloy investigated the original interfacial area between two mineral phases in binary and locked particles. A review of his model is given in section 2.5. The liberation measurements presented in this Thesis avoid these transformations and loss of the information, since the apparatus (X-ray microtomograph) measures in three dimensions. The "exact" two dimensional information of the particle can easily be sectioned from this three dimensional data. However, the 3D information can be limited by resolution and reconstruction artefacts.

The resolution presented in this work is around 12µm per pixel. Although the available SkyScan1172 system could measure at a resolution below 1µm per pixel, it was found not suitable because of massive computer processing power required for processing high resolution Micro CBT data.

However, some researchers claim that it is possible to determine part of the original three-dimensional information from the two-dimensional information. They state that geometric probability equations provide direct relationships between three-dimensional information and two-dimensional information. (Gay 1995)

When considering information obtained with a Micro Cone Beam Tomograph, the complete distribution of the grains within particles remains intact. One more advantage of this technology is that we are able to consider more than two mineral phases, which will be considered in detail in section 2.6.4. More details on stereology and the main equations are provided in appendix 9.3 and 9.4.

2.4.2.1 Sampling of materials

In addition to stereological bias which is an error made during transformation of one or two-dimensional measured properties into approximate three-dimensional properties (Jones 1987), there is a question of how representative was the sample which was analysed. Any small increment taken from the main ore body could be a sample, but not necessarily a representative one. There is also a need to question the representativeness of the samples taken for microscopic analysis. Such a conclusion will depend on the nature of the analysis in the first place, for example some of the data required for a certain project does not have to represent the deposit or part of the deposit in general. Hence, the representative sample is such a sample which has, generally, the same expected values for certain properties as the original from which it is derived.

Using Micro CBT to obtain three dimensional data excludes the possibility of introducing error of sampling of the particle since we are able to non-destructively analyse whole particles. However, the MLA data is based on sampled material, in this case a section of each particle, and for this reason I would like to consider the implications of this sampling process.

Gy (Gy 1982) had developed a general sampling theory, which is often used to calculate the mass of sample needed to provide a required degree of precision. The theory takes into account the particle size, the minerals that are present, the degree of the liberation of the minerals and the particle shape. Gy's basic equation is:

Equation 2:

$$\frac{mL}{L - m} = \frac{Cd^3}{\sigma^2}$$

Where :

- m is the minimum mass required to provide an adequate sample (in grams),

- L is the lot or the gross mass (g) of the material being sampled,

- C is the sampling constant (g cm^{-3}) for the material,

- d (cm) is the size of the largest fragment in the sampled material, and

- σ is the statistical error that can be accepted in the analytical result.

Since L is generally large in relation to M, there will be:

Equation 3:

$$M = \frac{Cd^3}{\sigma^2}$$

There are also a number of sampling techniques discussed in Jones (Jones 1987). Jones provides guidance for detailed preparation of sample specimen and mineralogical measurement of these specimens.

The operational errors and the statistical errors are the main inaccuracies that can be made by mineralogist who is performing mineralogical analysis of a prepared specimen. Jones (1987) was defining operational errors as mistakes such as misidentification of minerals, the miscounting of the various features, and the misreading of scales. According to him, statistical errors can only be within acceptable limits, which are usually specified as 2σ level, where the standard deviation is calculated as:

Equation 4 (Jones 1987)

$$\sigma = \sqrt{\frac{pq}{N}}$$

Where:

- p is proportion of the selected mineral,

- q = p-1,

- N is the number of observations.

Special attention must be given to sampling and sub-sampling where the analysis are carried out on small samples taken from large bodies of solid rocks or from large masses of flowing mineral pulp.

2.4.2.2 Statistics of limited sampling

Mineral particle studies are most often planed and statistics play an important part in planning, executing, analysing and interpreting data. Classical sampling theory is explained in detail in Cochran (1976), while Thompson (1987, 1991, 1993; 1994) gives details on specific nonstandard problems and how these can be solved using classical theory. The alternative to classic theory is model-based sampling. The theory consists of various methods, and sampling in geostatistical environmental area is described in Cressie

(1991) and Flatman et al. (1988). Model based sampling, although not perfect, may be more efficient as it makes more complete use of the information of the population. (Kern 1995) Kern provided detailed analysis and discussion on various sampling models.

The detailed further equation based on Gy's are presented in a series of publications (1982, 2003, 2004a, 2004b, 2004c, 2004d) which provides calculable confidence. Detailed analysis of publications is also provided in Kern (1995) and Minnitt et al. (2007) . The minimum mass of the material being sampled required is:

Equation 5

$$m = \frac{c * l * g * V_{95}}{\sigma_{FE}^2}$$

Where:

- c is mineralogical factor;

- l is liberation factor;

- g granulometric factor;

- V_{95} is, from empirical mineralogical studies, 95th percentile particle diameter multiplied with shape factor f;

- σ_{FE}^2 is estimated variance of the fundamental error.

Mineralogical factor c is given by :

Equation 6

$$c = \left(\frac{1-a}{a}\right)[(1-a)\delta_m + a\delta_w$$

Where:

- "a" is a decimal proportion of the metal of interest;

- δ_m is density of the valuable phase;

- δ_w is density of the waste phase.

The liberation factor l takes a value between 0 and 1 which depends on the geostatistical characteristics of the mineralization and the nominal size of fully liberated mineral grains. The advantage of this method was direct measuring of the liberation of particle, thus the measured average liberation value was applied.

The granulometric factor is known as the grain size distribution factor and takes values between 0 and 1. Low values for g are used if there is a large range of particle sizes. For narrow range of particle sizes, values close to 1 are commonly used. If the average fragment volume and the nominal fragment volume ratio is over 4, then the g value applied is 0.25 or less. If the average fragment volume and the nominal fragment volume ratio is 1, then g value applied is 1. Medium size range is 0.5.

The shape factor f relates the volume and the diameter of the particles of broken ore to one another. Selected $\pi/6$ for shape factor would transform the cube of the fragment size d^3 into the fragment volume. (Minnitt et al. 2007)

2.5 Review of Models of Mineral Liberation

The importance of liberation in mineral processing has been well appreciated for many years. To investigate, solve and improve operating conditions in mineral processing plants requires reasonable prediction of liberation. The measurement of liberation, its interpretation in terms of mineral preparation technology and important issues associated with mineral liberation had been discussed in detail by Gaudin (1939). In particular, Gaudin described the techniques that can be used to measure the liberation characteristics of an ore. Because of the difficulty of measuring liberation before the development of modern automated techniques, the importance of liberation remained underutilised. The core of the problem is given in Figure 9. Some models are provided as a reference in appendix 9.5 to 9.9.

2.5.1 Modelling the mineral liberation in comminution

Modelling mineral liberation in comminution mostly considers ore to homogeneous because of the complexity of the problem if the ore is considered to be heterogeneous. "Heterogeneity adds to the complexity of the modelling problem in two ways. Initially, the model must now provide the information for the breakage of two phases which may have different breakage and selection functions. At the same time, the model must also represent the liberation distribution of particles formed when parent particles are broken into a range of compositions, liberated progeny and unliberated progeny particles. Figure 9 illustrates the breakage of just three classes of particles in a two-phase ore, with liberated particles of each phase and one composite class of parent particle containing both phases. On the other hand, the challenge at the moment is to focus on predicting breakage from and into many classes of the composite particles." (Evans 2002)
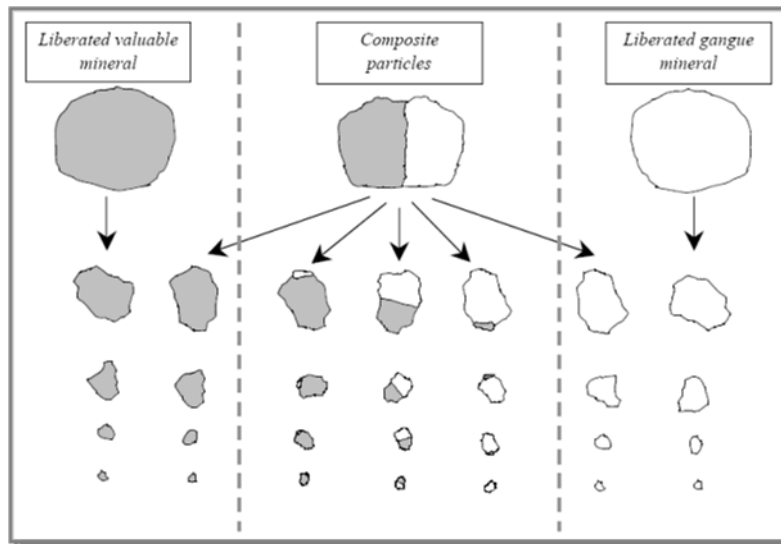
Figure 9: Diagram showing how a composite particle can break into progeny particles with any of a range of compositions and sizes while liberated particles can only break into liberated particles with a range of sizes (from Evans 2002)

Thereafter, the complexity of the models for breakage and liberation increases when the type of breakage is taken into consideration. The breakage of the material may be random or non-random. In random breakage, useful simplifications can be applied to many of the published models to obtain a solution since the fracture pattern of a particle is independent of its mineralogical composition and texture. The underlying assumption in many published models is that the breakage is random.

For non-random breakage, six different breakage conditions have been identified (King and Schneider 1998a). These are selective breakage, differential breakage (Fandrich 1997), preferential breakage (Fandrich 1997), phase-boundary fracture, liberation by detachment (Gaudin 1939), random breakage (Laslett et al. 1990; Wiegel 1965, 1976a, 1976b, 2006, 2010; Wiegel and Li 1967) and boundary region fracture. Preferential breakage is a common phenomenon in those models, resulting in the appearance of the preferentially broken phase in the finer size fractions after breakage. Many (if not most) real ores and breakage processes exhibit some degree of non-random breakage. (King 1987)

2.5.2 King's review of three different approaches to the mineral liberation problem

The fascinating challenge of mineral liberation is to combine mineralogy, comminution and geometry, but Peter King's (King 1987) opinion is that this is difficult and requires some unusual theoretical and practical methods for its solution. As mentioned before, many researchers have tried to find a simple and practical solution to this problem.

However, modern theories of liberation include successive levels of approximation and King's belief is that they are sufficiently accurate to provide good estimates of the liberation spectra that are to be expected when binary ores are comminuted.

King explained the estimation of liberation problem in terms of difficulty to measure unbroken ore texture. King expressed the difficulty in solving the connection between geometry of mineralogical texture and progeny particles. (King 1987) The connection is enabled with this Thesis.

Figure 10 (King 1987) is a stylized representation of the problem and the three possible solution based on different geometrical irregularity of the particles procedures are briefly summarized.

THREE APPROACHES TO THE MINERAL LIBERATION PROBLEM
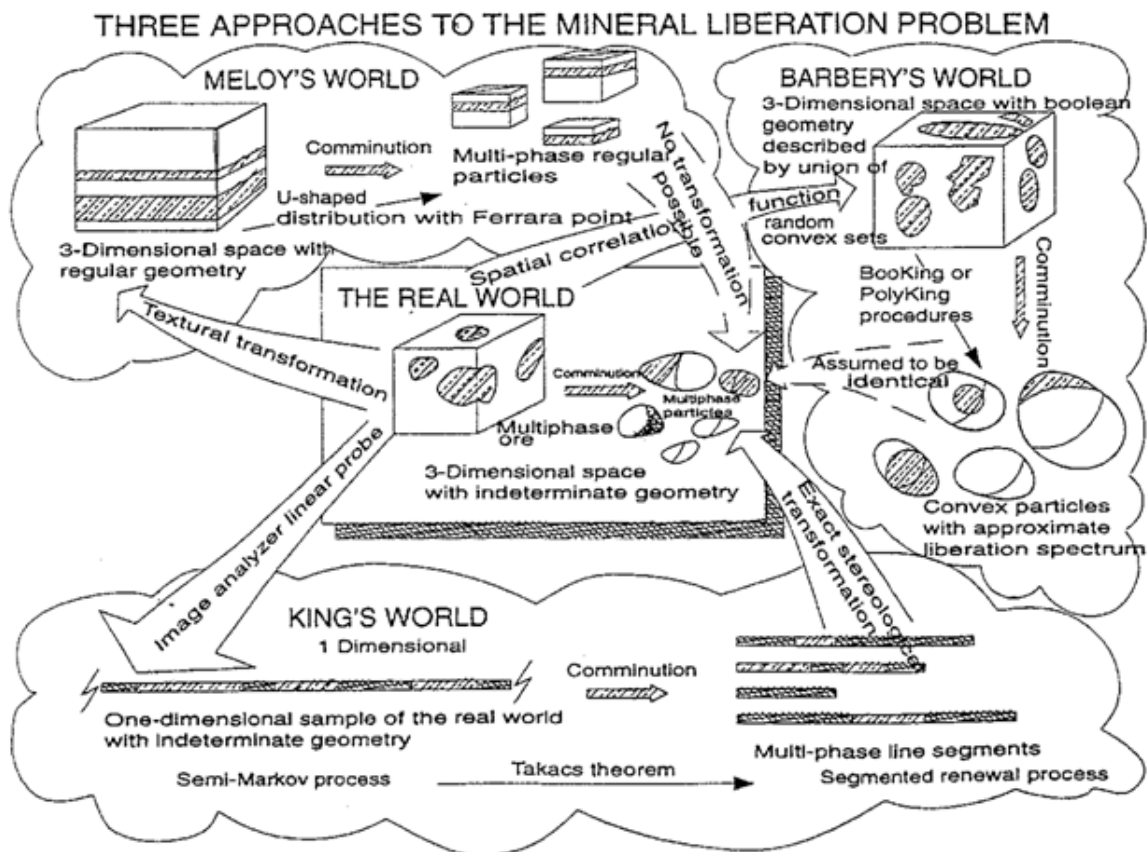
Figure 10: Three different approaches to the mineral liberation problem (from King 1987)

King hypothesized that the solution of the problem of predicting liberation is situated in a different approach to the geometry of the unbroken particles and broken progeny. However, we are now able to measure the undamaged geometry of the parent particles at reasonably high resolution with using X-ray tomography and then evaluate each of the previous models by comparing them with the real world situation.

The geometry of the real world includes a huge range of variations, leading to different approaches to handle this geometry. Some approaches use the assumption that the geometry of the minerals is random and then adopt it to measured reality by appropriate mathematical techniques. Other researchers have used randomly defined geometry. The size of the parent particles is reduced by simulated comminution, and then the model is used to predict liberation.

In Meloy's textural transformations, and the imaginary texture is a simple regular geometric texture with the same phase volume fraction and interfacial area per unit volume as the measured original. This model reduces the size of the original particles of defined simple shape and the final liberation spectrum is calculated using simple geometrical formulas. The size of the progeny particles is smaller than the size of the inclusions. This introduces a problem if we are considering a very fine texture, since it would be very hard to get progeny particles in that small, micrometre scale size range. The model is clearly avoiding complexity by avoiding the orientation of the grains in three dimensions. Because of the loss of the essential information during the original transformation, no back transformation is possible and transformed liberation spectrum is final. (King 1987)

The Meloy model is simple, calculation procedures are easy to visualize. It can be extended to multiphase systems and finally, it is potentially able to analyse non-random fracture patterns but no validations of the results are available so far. However, because of its simplicity it has some further disadvantages (King 1987):

- No back transformation to real world;

- Different assumptions (such as the shape of the particle) give different answers;

- Only limited calibration can be made against real data by use of constants;

- Loss of essential geometric information about the texture;

- Derived liberation spectra can be misleading because there are so many assumptions.

Barbery's method is characterized by the two point spatial correlation function and modelled by a three dimensional Boolean model which is based on the theory of random sets. The parent particle is comminuted into convex particles of varying size for which the linear intercept distribution is known and which is consistent with the fracture pattern in the ore. (Barbery 1992)

Barbery's equation for the degree of liberation in three dimensions is given by Equation 6.

Equation 6 (Barbery 1992)

$L_{3,G}$ = [I-exp(ln(1-p_g)exp(-5.216X))] / [1-exp(ln(I-p_g))]

where:

- $L_{3,G}$ is the degree of liberation at the particle size equals grain size in three dimensions;

- G is grains

- p_g is volumetric fraction at G

- X is size ration D/D80

- D is particle size

- D80 is a diameter of a sphere in which 80% by volume of Poisson polyhedra would fit

The first two moments of the liberation spectrum can then be estimated. Estimates of the two liberated ends of the spectrum are also made and the final spectrum is fitted to a beta distribution. This is also the final answer because no back transformation into the real world is possible.(King 1979; 1982, 1994a, 1994c; Schneider et al. 1991)

Barbery's imaginary model can approximate to reality and can be calibrated against real textures through the spatial correlation function. But it also has its disadvantages (King 1987), such as the inclusion of two moments of the liberation spectrum while others are approximated.

"As the liberation spectrum requires a minimum of four parameters for its description, this spectrum can not be transformed back to real world:

- Particles must be convex;

- Boolean models do not always fit to real textures;

- No theory yet to extend to multiphase system;

- No theory available to handle non-random fracture patterns."(King 1987)

King's Linear Stochastic Method has slightly different approach. It does not use a transformation of the original texture but samples directly using a linear probe that generates a linear intercept distribution for each phase in the ore. The linear intercept is broken into a pattern consistent with the three dimensional fracture patterns in the ore. Linear fragments are calculated using a theorem based on alternating renewal processes due to Takács (1967). By using a stereological transformation, this liberation spectrum can be transformed back into the real world and an estimate of the two dimensional and three dimensional liberation spectra can be recovered. (King 1987)

King said that this model needs no assumptions and can be calibrated exactly against real textures by image analysis of unbroken sections of the ore. It extends naturally to non-random fracture and minerals of different brittleness and to multiphase systems. But, as for the other models, it has some weaknesses (King 1987):

- Relatively complex computation is required;

- The stereological transformation of results is texture specific.

2.5.3 Random liberation modelling and simulation

The mineral liberation model described by Gaudin in his Principles of Mineral Dressing 1939 (Gaudin 1939) was a fundamental model but an extreme simplification of a real mineral system, where two mineral species have cubic shapes which are aligned in such a way that the eight corners of the cube of the mineral one are touching the other mineral cubes corners. This type of the arrangement is known as a Rubik's cube arrangement (Figure 11). Gaudin hypothesised ore texture and progeny particles could be adequately described by cubic particles containing various proportions of same size cubes of various phases, and that the breakage planes are then parallel to the mineral grain surfaces, where as a consequence, the progeny particles are again of cubic shape. The extremely limited computational power was available to Gaudin but the model provides many useful insights.

Here the degree of liberation of the mineral is the percentage of that mineral occurring as free particles in relation to the sum of this mineral occurring in the locked and free particles. We would say that the liberation by detachment had occurred if two minerals had separated during the size reduction process due to their difference in mineral properties. The application of this theory is hard to prove in reality, since it exists only as a hypothesis. On the other hand, if the differences are obvious, we would say that preferential breakage may occur in this instance at the grain boundaries.

It is worth noting that the grid dimension is not necessarily the grain size. In 1939, ore grades were typically much higher than they are now. At volumetric grades higher than, say, 15%, many cubes of valuable material are firmly adjacent distribution of larger grains.

There are three types of composition of the parent particles as the result of such a breakage. First two consist of the same mineral species liberated value or waste, and the third type are locked particles. The last one would have a range of compositions. The disadvantage of this model is that the size reduction used for liberation was not appropriate for low grade ore (lower than 15% by volume).
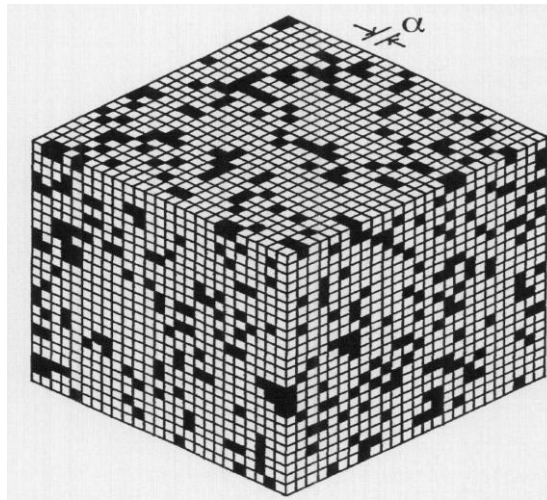
Figure 11: Visualisation of theoretical binary mineral system (from Wiegel (1976))

Wiegel proposed that the original purpose of Gaudin conceptual model was to convey the ideas that help one to understand qualitatively how the composition of the particles produced by size reduction is related to the original mineral grain size, the particle size, and the location of similar or dissimilar grains adjacent to one another in the original grain assemblage being broken. Wiegel's objective from reviewing and reviving the Gaudin liberation model was to describe liberation effects of size reduction with the development of more general quantitative relationships (Wiegel 1964, 1965, 2006, 2010; Wiegel and Li 1967) since the access to greatly increased computing power is available nowadays.

In the early 1960's Wiegel had an access to a mini computer. This allowed for some minimal exploration probably not relevant here. However, his mini-computer had only small fraction of the computing power of a modern mobile phone. With modern computers, these concepts are much easier to explore computationally.

The first difference between these models was in random location of the mineral grains which were defined with binary probability concepts. The second difference was in the position of fractures, which were not parallel to mineral grain surfaces this time. However, they were equally likely to occur at any position in the mineral grain (random fracture). Hence, the random fracture is not occurring in all size reduction processes. Similar concept was used in experimental section in this Thesis, further explained in Chapter 6. The equations which were describing these complex relationships were:

Equation7

$$PA = (1-\varepsilon)^3 VA^{(t+1)^3} + 3\varepsilon(1-\varepsilon)^2 VA^{(t+1)^2(t+2)} + 3\varepsilon^2(1-\varepsilon)VA^{(t+1)(t+2)^2} + \varepsilon^3 VA^{(t+2)^3}$$

Equation 8

$$PB = (1-\varepsilon)^3 VB^{(t+1)^3} + 3\varepsilon(1-\varepsilon)^2 VB^{(t+1)^2(t+2)} + 3\varepsilon^2(1-\varepsilon)VB^{(t+1)(t+2)^2} + \varepsilon^3 VB^{(t+2)^3}$$

Equation 9

PAB + 1 – PA – PB

Equation 10

β/α = t + e = 1/K

where:

- PA= fraction of particles by volume of liberated waste material;

- ε = fraction remainder in ratio β/α;

- VA= volume fraction of waste material in original feed;

- t= largest integer in ratio β/α;

- PB = fraction of particles by volume of liberated values material;

- VB = volume fraction of values in the original feed;

- PAB = fraction of particles by volume of locked values and waste;

- β = particle size (linear dimension);

- α = mineral grain size (linear dimension);

- K = grain size-particle size ratio.

This model was named the Gaudin Random Liberation Model (GRLM).

Although the particle size into which the mineral parent particle is broken in reality is an entire distribution of particle sizes, GRLM assumes that particles resulting from the breakage are the same size. The downside of this model is that both, parent and progeny particles are cubic, which is hardly possible in reality. However, common minerals such as pyrite and magnetite often do occur in small cubes or other block like shapes. That is the reason why the simulations of the processes which are based on GRLM use these calculations for each narrow size fraction separately.

The comparisons of the GRLM with real process of liberation of magnetic iron formations were made in the 1970's (Lynch 1977; Wiegel 1975). Magnetite ore samples were collected of the feed and product from the initial size reduction step in 12 magnetite concentrators operating around the world. The samples, which Wiegel was testing, had grades in the range 15 to 45% magnetite iron and approximate mineral grain sizes of 50 to 2000 μm. Thereafter these samples were screened into closely size fractions and concentrated with high precision laboratory scale magnetic separation using a Davis tube.

The Davis tube (Figure 12) was designed and used to quantify the content of the ferromagnetic fraction in the sample. The test consists of 2.54 cm glass tube which is agitated in an electromagnetic field. An electromagnetic coil is placed on each side of the tube and creates magnetic field whose force can be controlled, thus the separation may be controlled as well. The sample to be tested has to be fine and slurried. The basic process is that ferromagnetic particles are kept on tube walls by the magnetic field and the non-magnetic phase is washed away from the tube. The selectivity of the separation is controlled by the electromagnetic field, the volume of the wash water, agitation speed and the slope of the glass tube. (Mular et al. 2002)
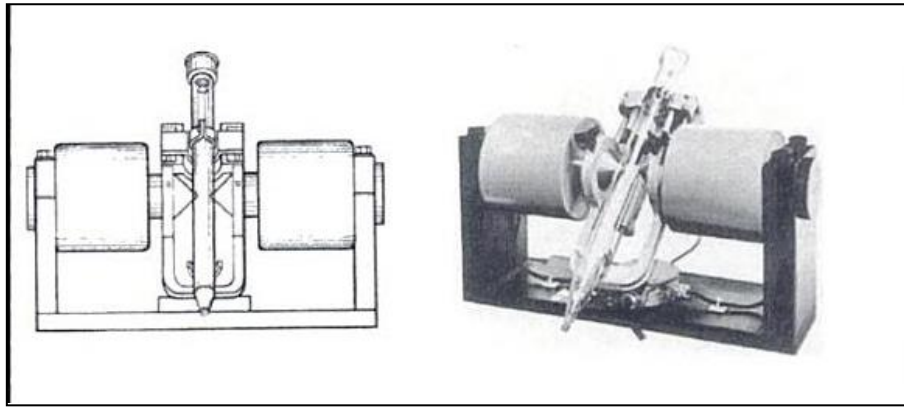
Figure 12: Davis tube tester for measuring ferromagnetic content (Mular et al. 2002)

Small quantities (10-20g) of closely sized particles for testing time of 10-20 minutes were efficiently separated with Davis tube into two classes, those containing any magnetite (liberated magnetite and locked magnetite and waste) and those that are nonmagnetic (liberated waste). Using narrow size fractions reduces the tendency for strings of magnetic particles to entrap nonmagnetic.(Wiegel 2006) Therefore, the assumption was made that the efficiency of the Davies tube in this case is 100%. This assumption was tested by chemical assay.

There was a noticeable increase of the magnetite content in finer size classes indicating the possible preferential breakage of magnetite mineral grains. The explanation of the very unlikely results in the concentrate quantity versus particle size measured in these two tests was explained with the fact that magnetite and waste material behave very differently in grinding process. Although these measured results were different from the simulated, Wiegel's concluded that GRLM is a useful quantitative tool for the explanation of liberation and obtaining an estimate of the 'effective' mineral grain size for a particular magnetite iron ore. There was the need for introducing the coefficient that will help in calculating the breakage rate for each mineral individually. This coefficient was introduced in the following study (Wiegel 1975). Although this model is mathematically convenient, allowing different levels of breakage would probably be more realistic for future liberation studies.

Figure 13 and Figure 14 show how the GRLM could be used for data analysis and for simulation of batch grinding.
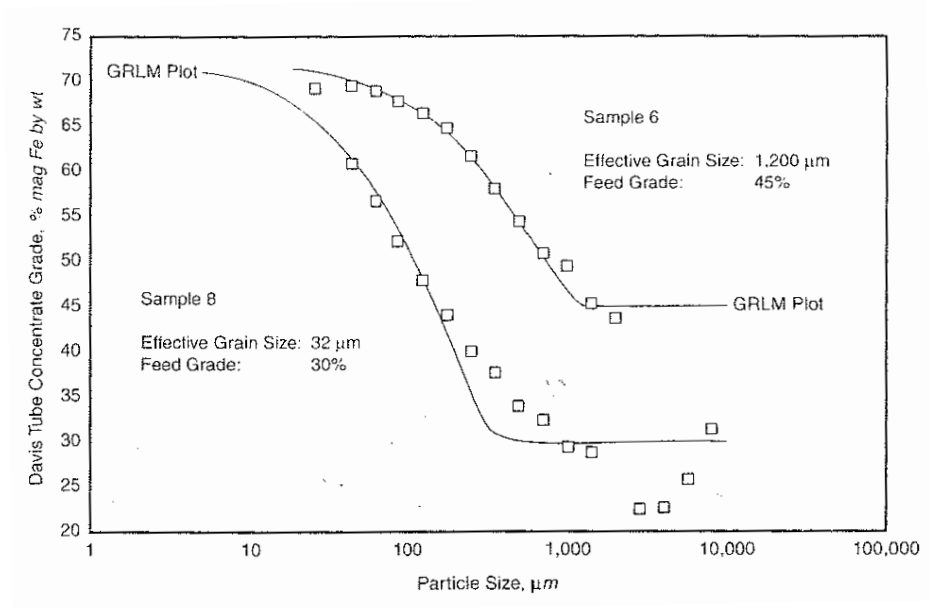
Figure 13: Davis tube concentrate grade versus particle size(from Wiegel 1964)
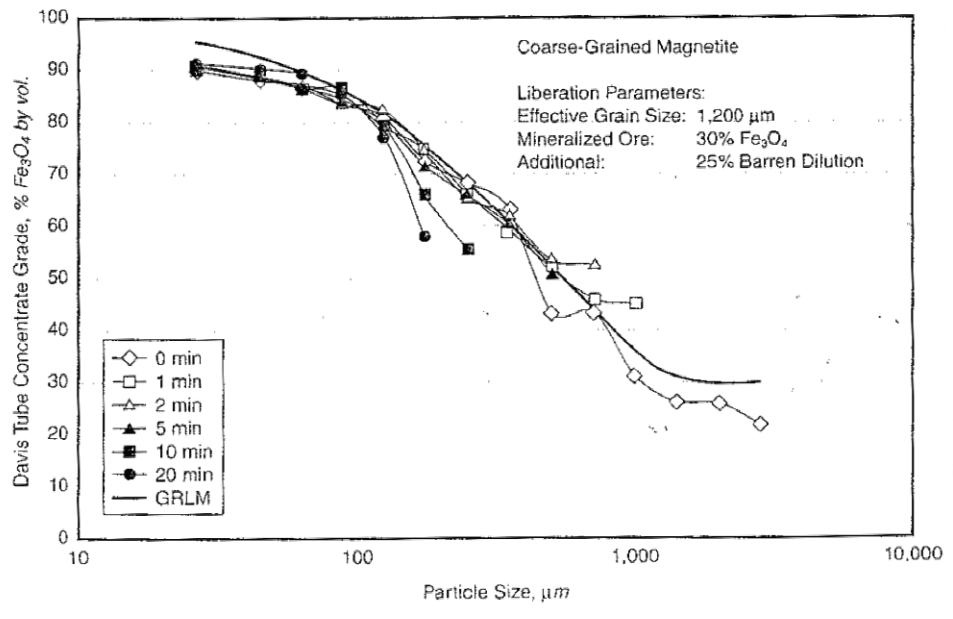
Figure 14: Davis tube concentrate for batch ground sample(from Wiegel 1964)

The next experimental test of GRLM was conducted in 1976 when Wiegel described the gradual size reduction / liberation with the use of GRLM (Wiegel 1976b). Magnetite ore samples were batch ground and product was separated with Davis tube and assayed. There was again evidence that the magnetite was ground more rapidly than the waste,

shown in Figure 12. The concept of a directional coefficient, which came out of this study, described the proportion of material that started in the specific size/composition location and progressed as a result of size reduction to a finer size/composition location. Simulation programs used this coefficient in order to locate particles in the simultaneous process of size reduction and liberation. The assumption was that the each mineral phase has the same breakage function.

Equation 12

$$\sum_{I} V(I,J)Q(I,II,J) = V(II,J+1)$$

Equation 13

$$\sum_{II} Q(I,II,J) = 1$$

Where

- V(I,J)= quantity of particles of size J, composition I

- Q(I,II,J)= directional coefficient, going from composition I to II

- I=composition index in the beginning particle size range , J

- II=composition index in next finer particle size range , J+1

Wiegel used the GRLM to simulate programs for a magnetite taconite concentrator. The simulation included models for hydrocycloning, fine screening, closed-circuit grinding, and multidrum magnetic separation (Wiegel 1976c, 1979).

However, other researchers from all over the world were not satisfied with the information obtained from these tests and thought additional information that could be obtained from such an idealized system. Then a least-square computer program was introduced to

obtain better quantitative measures of those parameters directly affecting mineral liberation (Wiegel 1999b). Those parameters were:

- volume fraction of values in the mineralized ore;

- effective mineral grain size;

- barren waste dilution, defined as contamination by non-mineralised waste.

The parameters can be estimated using the method presented in Chapter 6.

In 1999, Wiegel (Wiegel 1999a) reported on a computer simulation of the breakage of cubic grains (binary system) in a GRLM to generate information on the quantity and composition of the locked and liberated particles. Spacing of the breakage grid was randomised. He created 200 000 particles in order to ensure reasonable statistical confidence. The composition of the particles was divided into 12 volume classes. Each particle created by the simulation was placed in its appropriate composition slot. For a given volumetric feed grade, separate simulations were carried out for grain size-particle size ratios in the range of 0.125 to 32, with the size ratio increasing by a factor$\sqrt{2}$. Because the system has only two mineral components, values and waste, the results are symmetric for values and waste. The 50% range midpoint was chosen to be reasonable approximation of the mean particle composition for each of the ranges. The previous example of the GRLM calculations was now complemented by the inclusion of the comparable locked particle quantity and composition information as shown in Figure 13.

The parent material has 0.25 volume fraction of valuable mineral and a particle linear dimension is 8 times the grain dimension at the beginning. The first size reduction is to 4 grains, then 2 etc. Significant liberation is noticeable by size ratio 1:10. When the particle size is equal to the grain size, 90 % of the waste is liberated.
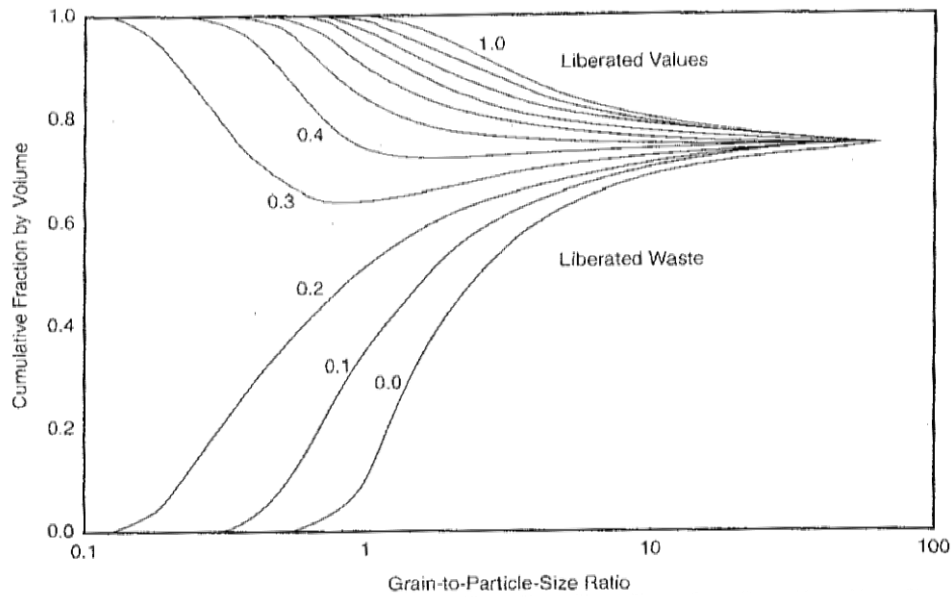
Figure 13: Fraction liberated and locked particles with compositions versus grain size-particle size ratio for an ore with 0.25 fraction values (Wiegel 2006)

The previous history of the parent particle is not considered in any stage of the size reduction and thereafter the assumption was that the same size distribution of particle composition would be generated by breakage.

The overall volume was therefore conserved due to presence of the volumetric balances and there is also one more connotation- particles that are ones liberated stay in that class until the end of the size reduction process. However, the program was not able to predict the proportion of the parent particle volume in the specific composition range. Hence, the total volume of the particle and individual minerals was preserved.

Wiegel (2002) used Equation 12 and Equation 13 to create a linear programming (LP) problem of this distribution phenomenon. When directional coefficients in the calculation are valued 0 or 1, it is by the fact that the once the particle is liberated it remains liberated value or waste. The relationships for the LP are as follows:

75

Equation 14

$$\sum_I Q(I, II, J) = \max imum$$

-from

Equation 14, total volume balances for II=1 to 12:

Equation 15

$$\sum_I V(I, J) Q(I, II, J) = V(II, J + 1)$$

-from Equation 12, directional coefficient balances for I=1 to 12:

Equation 16

$$\sum_{II} Q(I, II, J) = 1$$

-values volume balances for I=1 to 12:

Equation 17

$$V(I, J) \sum_{II} Q(I, II, J) MV(II) = V(I, J) MV(I)$$

Where MV(I) = mean value of a composition range I, or simplified:

Equation 18

$$\sum_{II} Q(I,II,J)MV(II) = MV(I)$$

Although this approach appears to be adequate for simulation of magnetic taconite size reduction/liberation, Wiegel's opinion was that it is limited to original ore feed grades in the range of 15% to 85% values by volume. In addition to this is that the magnetic taconite is usually in the 20% to 40% by volume range. The other values were excluded by the fact that the liberated values or gangue could only be broken into liberated particles of various sizes.

Most of the ore that is currently processed worldwide is low-grade and this model is not suitable for it. That is the reason for expanding the number of composition ranges significantly. Wiegel also suggested that it is worthwhile looking at something akin to logarithmic composition ranges in the low fraction values region. Also, the smallest grain-to-particle size ratio which is currently used is 1/8 and smaller value could be considered. Thereafter, the number of directional coefficients is related to the square of the number of composition ranges and the problem of solving their values will be significantly more difficult. Wiegel also suggested that tests should also be extended to multi-mineral composition particles, not only binary. (Wiegel 2002)

Hsih and Wen (1994) examined the influence of different mineral properties such as hardness on preferential breakage. A detachment factor was introduced as an extension to Gaudin's liberation model. The paper demonstrated a general increase in proposed detachment factor with increase in difference between valuable mineral and gangue phase.

The author has explored Wiegel/Gaudin model in some detail. This work is reported in Chapter 6.

2.5.3.1 Solitary Grain Model (SGM) of a low-grade ore (Wiegel 2006)

This section is also based on the GRLM model. A solitary cubic grain of valuable mineral surrounded by waste grains is considered and fractions generated during breakage can occur in any direction as in the GRLM. The underlying assumption of having cubic parent and progeny particles remains. Because of having only one valuable grain in this model, a number of terms from the GRLM disappear or can be simplified.

The first situation is when solitary grain of values is broken to a particles smaller than the grain size (K>1).

Equation 19

$$PB = VB(K-1)^3 / K^3$$

Equation 20

$$PAB = VB[6(K-1)^2 + 12(k-1) + 8]/K^3$$

Equation 21

$$PA = 1 - VB(K+1)^3 / K^3$$

Liberated values are represented in Equation 19 and liberated waste in Equation 21. Equation 20 is showing three types of locked particles:

- those located along 6 surfaces of the cubic valuable-mineral grain, composed of two grain fragments;

- those located along the 12 edges of the valuable grain, composed of four grain fragments;

-   and those located at the eight corners of the valuable mineral grain, composed of eight grain fragments.

The second situation is when solitary grain of values is broken to a particle larger than grain size (K<1).

Condition: PB=0

Equation 22

$$VBMAX = (\alpha / \beta)^3 = K^3$$

Equation 23

$$K(@\,PA = 0) = 1/((1/VB)^{1/3} - 1)$$

Equation 24

$$PAB = VB(K+1)^3 / K^3$$

For this model there are no liberated values, but there is a maximum values particle composition, when the valuable mineral grain is in full size in one of the broken particles (Equation 23). The liberated waste is following Equation 21, and in Equation 22 the amount of liberated waste is becoming 0. Locked particles are represented in Equation 24.
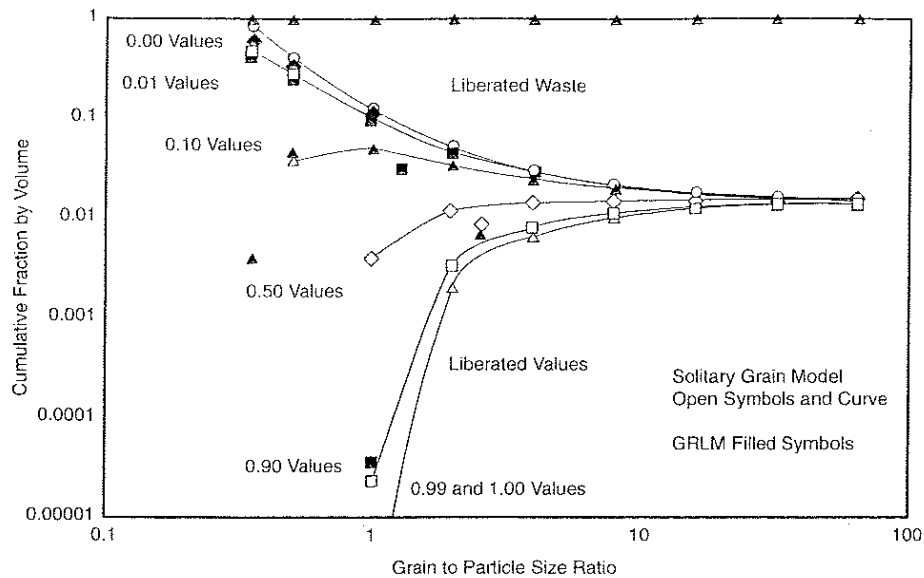
Figure 14: Comparison of GRLM results with SGM calculations for ore with 0.015 volume fraction of values. (Wiegel 2006)

The difference between this model and GRLM was in the K selective function, where it was explained by magnetite having preferential breakage over the gangue. The relationship between those two models is presented in Figure 14. Unfortunately the quality of the image was not very good for comparing them. There is limited data for GRLM, and it is very hard to make judgements (Wiegel 2006). Imaging variables that can affect imaging, at least assumptions of three-dimensional correction, can be controlled using this method (Chapter 6).

2.5.3.2 Comparison of volumetric and section area particle compositions using the GRLM (Wiegel 2010)

The purpose of the model introduced by Wiegel in 2010 was to describe the relationship between true volumetric particle composition and the composition estimates obtained when linear intercepts and areas of the polished section of the particles were simulated. The basis for this simulation was simple set of locked and mineral particles. Random sectioning was introduced, where the particle size was less or equal to the mineral grain size (K≥1). The planes for area sectioning were chosen randomly.

80

Current observation by Wiegel (2010) indicate that the estimated particle compositions based on section intercept lengths are worse than the ones estimated based on sectional areas. Furthermore, they are both very different from the true volumetric composition for 175 binary GRLM Particles (Figure 15). For example, linear intercepts indicated 51 liberated waste particles and 49 liberated valuable particles, where the actual number was 2 and 1 respectively. Because of this great difference, Wiegel did not consider linear intercepts in further evaluation of this model.
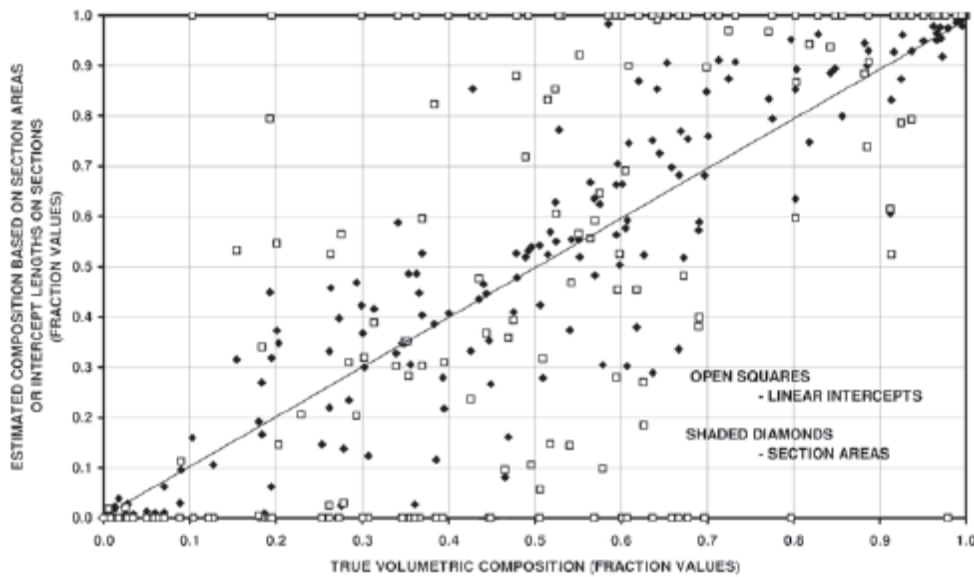
Figure 15: Comparison of estimated particle compositions based on section areas or intercept lengths with true volumetric composition for binary GRLM particles(Wiegel 2010)

The application of the GRLM was tested in Wiegel (1975), where the estimated particle composition was compared with real volumetric composition using Davis Tube measurements. The volumetric feed grade given in Figure 16 is 20 % magnetite. The problem here was that the efficiency of Davis Tube was 100%, meaning that the material which was considered as concentrate assumed all valuable magnetite collection.
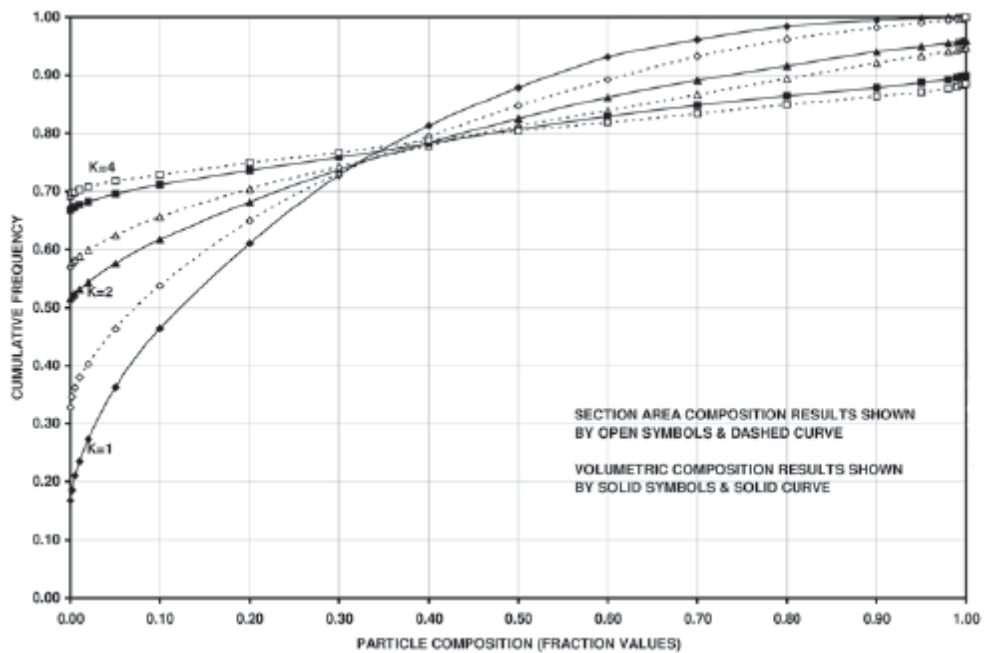
Figure 16: Comparison of cumulative frequency distributions of particle composition for volume and section area data, with VB=0.20, K=1;2;4. (Wiegel 2010)

In principle, the distribution presented in Figure 16, shows that the set of particles having equal size as the mineral grain size has a much wider locked particle distribution than the set of particles whose size is four times smaller than the mineral grain size. This is quite understandable since the possibility of getting more liberated gangue and values is increased in this case. The interesting observation here is that despite the particle size, any set will have about 25% of approximately 35 % locked particles. Hence the estimation of the particle composition by section area is overestimating the degree of liberation, and the difference in magnitude is higher when approaching values where the liberation is more complete.

The difference is less apparent when measuring smaller particles. Wiegel explains this discrepancy with the fact that due to the increasing number of particles which are volumetrically liberated there is much less error in the section area estimate of the composition.(Wiegel 2010)

Wiegel recognised the error which occurs when the liberation information of the particles is estimated by measuring linear intercepts or areas of the particles when dealing with locked

particles. In principle, various correction factors have been developed to reduce errors in this situation (Barbery 1991; Barbery and Leroux 1987; Lin et al. 1995; Miller and Lin 1987; Wiegel 2010).

In 2001, Latti and Adair (2001) developed a relationship between one, two and three dimensional particle information by measuring a number of polished serial sections of real multi-mineral particles and reconstructing the three dimensional data from this information.

Despite the effort to create a physical description by using a large number of simulated particles, one must keep in mind the true particle information and the error associated with those estimates. Hence, the GRLM gives some statistical information about the difference between area and volumetric liberation information, but one must also keep in mind the difference between the GRLM and the real world, where particles are not cubic in shape and the fracture patterns are not parallel to the particle edges, as assumed in the GRLM.

These uses are further characterised by the author in Chapter 6. Chapter 6 provides details of a comparison between estimated composition measured by linear intercepts and polished sections. It also provides a link between the real world particle composition after the breakage and estimated composition using simulated GRLM cubic shape particles.

After the procedure for turning two-dimensional sectional data into three dimensional volumetric data that Wiegel developed was applied, Wiegel concluded that K developed earlier had little effect here. (Wiegel 2010)

2.6   Measurement of mineral liberation

2.6.1 Introduction

There are a number of technologies are used for measuring the degree of liberation of comminuted ore. The techniques that are utilised in this Thesis are CBT (Cone Beam Tomography, SkyScan (2010b)), Automated SEM Based Microscopy – MLA (Mineral Liberation Analyser) and QEMSCAN (FEI 2014), and Optical Microscopy (Leica 2011).

The development of the automated image analysis systems started with the Camebax system at the Royal School of Mines in London (Jones 1987) and continued to QEMSCAN (Laslett et al. 1990) and JK MLA systems (Burrows and Gu 2006a; Gu 2003; Gurnett 2009; Hartner 2012; JKMRC 2003) to FEI projects for plant operation monitoring. The improvements of this new technology led to the automated process of collection of data.

Information about sectional mineral liberation, which can nowadays be obtained from image analysis systems, is widely available and this will probably increase demand for its use in the near future. (Gu 2003; Lastra et al. 1998) The previous problems with SEM image analysis when considering liberation data, such as the speed of the computer and the ability of the software to manage the image, have been overcome by automated systems.

Evans et al. (2011) used an MLA system to collect particle composition data for each size fraction before flotation testing as an input to test the particle surface composition model. Automated SEM Microscopy is commonly used for modal mineralogy, mineral liberation and mineral association data (Miller et al. 1982), clay identification (Haberlah 2011), plant optimisation and modelling (Hartner 2012; Jaime 2009; Morrison 2011; Morrison 2000; Wightman and Evans 2014).

Current observations are that a rapid increase in the application of quantitative measurement of mineral liberation is occurring because of improved availability of highly automated scanning electron microscopy (SEM). This measurement is sectional but can be extended to 3D by progressive slices of the sample. This process is called serial sectioning, where particles are ground finely using fine abrasives, sample blocks are produced and analysed in microscopes. It is commonly used for organic materials that can be finely sliced. (Latti and Adair 2001) The limitations of using this technique are cost and longer processing times which is leading to not so common everyday use in plants, non general use in optimisation and design studies.

More information about these techniques as well as the sample preparation is presented in the sections below.

2.6.2 The use of the optical microscope for measuring liberation

In the past, one of the standard techniques when analysing mineral liberation was the optical microscope. It uses the properties of transmitted and/or reflected polarized light and the changes to that light as it passes through the microscope polarizing filters and can identify the minerals of interest.

It was widely used for identification of minerals where mineral proportions were determined by point counting (Plas and Tobi 1965). Thus mineral textures, particle shapes and mineral associations might be observed by measuring grain sizes using a calibrated eyepiece. (Petruk 2000). The mineral properties used to identify minerals are given in appendix 9.10.

Similar to the other technologies, this technology has its advantages and disadvantages (Burrows and Louwrens 2007). The advantages are that analyses completed with it are relatively economical and quick, easy to set up and maintain equipment on site. In addition to this it has an excellent choice for identifying minerals of similar chemical composition

(for example iron-oxides) and organic material (Plante et al. 2003). It is possible to give high quality image (resolution less than 1 μm), giving the opportunity for the grain size to be measured manually and point counting to be done for statistics (Burrows and Louwrens 2007; Plas and Tobi 1965). Disadvantages are that the operator must be skilled mineralogist, thus the risk of operator errors being harmful for the outcome is very high. It is often very difficult to differentiate subtle but important mineral characteristics (example: pyrite with and without minor impurity, arsenianpyrite, percentage of iron in chalcopyrite can be variable), some minerals have very similar properties under the microscope (Plante et al. 2003). The analysis sometimes may be very time consuming. In order to study thin and polished thin sections a combination of reflected and transmitted light must be used.(Petruk 2000, p.28)

A review of publications on the use of the optical microscope were published by Stanley (1998), Criddle (1998), Jones (1987), etc. Image analysis techniques which are used in applied mineralogy have been described in detail by Lastra (1998) and Petruk (2000). Coal liberation was investigated using automated microscope (O'Brien et al. 2010).

The advantages of Digital Optical Microscopes (DOM) are widely discussed in Hartner (2012). Hartner believes that based on automated image acquisition, high resolution cameras for digital imaging with possibility to integrate multiple optical image layers using advanced image analysis techniques automated microscopy has capabilities beyond expert-driven optical microscopy. In his work, Hartner integrated DOM and SEM based techniques and achieved advanced ore deposit mineralogical characterisation using new image processing methods (e.g. eCognition).

2.6.3 Automated SEM Based quantitative mineralogy

As already mentioned in section 2.6.1, the Mineral Liberation Analyser (MLA) and QEMSCAN are used for identification of the minerals as well as for measuring mineral

grain size, associations, locking and liberation characteristics within a polished section of a sample. The measurement strategy uses two parallel processes namely scanning electron microscopy (SEM) and energy dispersive X-ray detectors (EDX) in order to make useful measurement for metals, process mineralogy, mining, exploration and environmental industries. The software automates control of SEM operations, image collection and analysis, and acquisition of characteristic X-ray spectra. Details on SEM image production and techniques are given in appendix 9.11.

The high - voltage electron beam is produced under high vacuum. This beam can be focused either on an entire sample or on an area of interest only. The average atomic number of the mineral will influence the greyscale level of the back-scattered electron (BSE) image. The main components of the SEM are electron/ion gun, lens system, scan unit with scan generator and detection unit. It generates a beam of electrons in a vacuum which is scanned over a specimen. An image is formed by the electrons that bounce off the surface of the specimen and are collected onto the imaging screen. Electrons react with the specimen to generate X-rays that are characteristic of the elements presented in the sample.

Figure 17: MLA System (FEI 2014)

A BSE image is low noise, high resolution image which is used for mineral identification and quantification. The very stable BSE signal can generate quality high resolution (0.1 - 0.2 µm) images of particle sections. Furthermore, images are analysed using advanced

image analysis techniques, to accurately discriminate the mineral phases within a particle. The most important function of the MLA image analysis are particle de-agglomeration and phase segmentation.(Fandrich et al. 2006)

There is also a setting within the BSE detector that can influence the contrast and brightness. By changing voltage and current on the SEM we are also able to change the shade of the levels of the minerals (Petruk 2000). For the purpose of this research, we have used XBSE (X-ray back-scattered electron) measurement that collects a series of BSE images.

The use of this methodology in liberation field was introduced in 1980's. In 1990's the group of researchers had investigated and followed different mineral phases through size reduction process. (Morrell, Dunne, et al. 1993; Weller et al. 1996) Using the data from two surveys of the circuits, together with QEMSCAN analysis of individual streams, a detailed picture of the liberation and classification of the gold-associated pyrite is presented in Morrell (1993). As mentioned in previous sections, Evans et al. (2013) investigated liberation and association of different mineral species in order to help model the energy consumption in comminution and smelting process (concept "Mill to Melt", 2011) and simplify the presentation of liberation data in order to determine the required and sufficient particle size in concentrators.

Many other (over 20 mining laboratories) use the systems in their daily operations worldwide. Daily monitoring of mineralogy using MLA technology is MineSite systems (FEI 2014) in plant operations is detailed in Dobbe et al. (2013), Goergen et al. (2013) and Martin et al. (2014).

During the sample preparation process, special attention is made to reducing the error in sampling and packing of the particles. Sample section need to be representative of the whole sample population, which is possible using mineral processing sampling techniques or designated laboratory equipment (micro rifflers, micro splitters etc). The weight of the sample need to be optimised in a way that possible setting of high dense component at the

bottom of the sample mould is avoided. Also, if the amount of sample is inadequate, the following problems will occur:

- If the weight of sample is overestimated, the area of the block will be overcrowded with particles, touching of particles will dominate the section and the software will struggle to separate them; these would more likely be reported as a single large particles which will compromise size and liberation information.

- If the weight of the sample is underestimated, the limited number of particles could be measured thus not providing the representative information about the whole sampling population.

Crushed samples are mounted with epoxy resin using standard mixing methods, block surface is cut and polished in order to create a 2D section through the embedded material. The block surface is then carbon-coated and stored in vacuum prior to measurement. (FEI Standard Sample Prep Procedure)

2.6.4 Micro-Cone Beam Tomography (CBT) Measurement technique

2.6.4.1 Overview

The key to this technology is measurement of X-ray attenuation along a line between an X-ray source and an X-ray detector. In order to reconstruct an image of a 2-D cross-section and later into 3-D object, the requirement is to collect the attenuation data along all lines within each cross section. Progress to date has been achieved with a number of different CT designs. (Prince and Links 2006) The overall improvement in the performance of the machines is evident through improved acquisition speed and image resolution.

A single transmission measurement through the object of interest made by a single detector at a given moment in time is called a ray. A series of rays that pass through the object of interest at the same orientation is called a projection or view. There are two types of projection, parallel and fan beam geometry. (Bushberg et al. 2002) In this work we will focus on parallel beam geometry, in which all of the rays in the projection are parallel to each other.

The ASTM standard E1441 (2005) provides the following definition: "Computed tomography is a radiographic method that provides an ideal three dimensional examination technique in the case where primary goal is to investigate planar and volumetric detail of the material. Because of the relatively good penetrability of X-rays, as well as the sensitivity of absorption cross-section to atomic chemistry, CT permits the non-destructive physical and to some extend chemical characterisation of the internal structure of the material. The principal advantage of Cone Beam Tomograph is the possibility of non-destructive acquisition of quantitative densitometric (density and geometry) images of thin cross section of images of an object. Those digital images closely correspond to the way that the human mind visualizes three-dimensional structures and we are able to transform them to any preferred mode. For objects smaller than 10mm in size, the accuracy is approximately 0.1mm at three sigma. For the case in which there is no prior information about the material, CT densities cannot be used to identify the unknown materials clearly. Another potential weakness of the CT imaging is the possibility of the artefacts in the data. An artefact is anything in the image that does not accurately reflect true structure of the object in the part being inspected. Because they are not real, artefacts limit the ability to quantitatively extract density, dimensional or any other data from the images." (ASTM E1441-00 2005)

2.6.4.2 X-ray Image production and characterisation

X-ray cone beam tomography machines have come a long way since their invention. At the beginning these machines were used for medical research only. Nowadays their usage has been extended many other branches of science including minerals.

Micro CBT images do not have as much contrast as SEM images and can be more difficult to analyse. Micro CBT images are better viewed in PDF form.

In principle, the images are produced when a detector image the X-rays that have passed through the object from the X-ray source to the detector. The contrast between components of the scanned rock results from the different attenuation of X-rays by the mineral grains present in the rock as well as the rock matrix.

Ideally, the "monochromatic" source would emit single energy X-Rays. However the emission from the micro-focus X-ray source is a mixture of low and high energy X-Rays. Figure 22 shows an energy spectrum emitted from tungsten at different tube voltages. When polychromatic source penetrates through a solid sample, the low energy photons are removed from the beam preferentially so that the remaining beam energy is shifted progressively higher causing the "beam hardening" effect, discussed in details in section 3.2.3.(Salmon 2005)
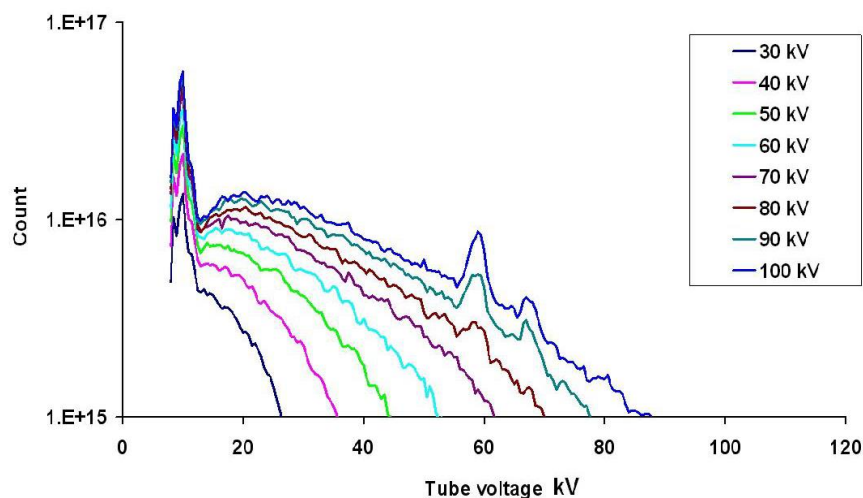
Figure 18: The wide polychromatic spectrum of x-ray energy from the tungsten target of micro-CT scanners' micro-focus sources is a source of the beam hardening artefact. It can be minimised by mathematical adjustment of the reconstruction algorithm, and by correct choice of filter and energy for the x-ray source. (after Salmon 2005)

The tube current of an X-ray source is the number of electrons per second that travel from the tungsten cathode filament to the anode. The definition of the intensity of the X-ray beam is the power incident per unit area and has units of joules per square metre. In

practice the intensity is not uniform across the area. This is known as the heel effect. The maximum power of the tube generated during 0.1 seconds of exposure time is called the tube power rating (kVp). (Webb 2003)

The spectrum of X-rays has a broad range of energies. There are two ways of X-ray due to high energy electrons interacting with the anode. One is Bremsstrahlung radiation and the other is characteristic radiation (Figure 19). When an electron experiences the positive charge force of some heavy atom, in this case usually the tungsten nucleus, it deviates from its path and is accelerated, thus producing a photon (Bremsstrahlung effect or braking radiation, Figure 24).

The outcome of these interactions is the generation of X-rays with the range of energies being emitted from the anode in all directions. Usually around 1% of the energy is converted to X-rays and the rest is converted into heat. The internal filtering shown in Figure 23 occurs when low-energy X-rays are absorbed by the X-ray system within the tube.

The overall Bremsstrahlung intensity is:

Equation 25 (Prince and Links 2006)

$$I = V_{tube}^2 I_{tube}$$

In theory Bremsstrahlung spectrum is given by

Equation 26, and the actual X-ray spectrum considering all losses is presented in Figure 20 (Prince and Links 2006).

Equation 26

$$I_b(E) = Z(E_{max} - E)$$
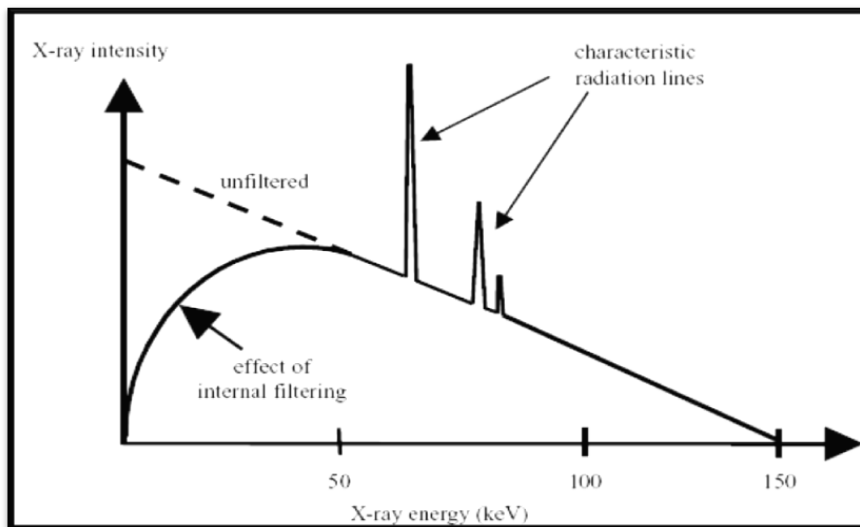
Figure 19: An X-ray spectrum produced with the source of tube rating 150 keV, using a tungsten anode. The dashed line represents low-energy X-rays that are absorbed by the components of tube itself. Characteristic radiation lines from the anode occur between 60 and 70 keV. Unfiltered is theoretical Bremsstrahlung (Webb 2003)
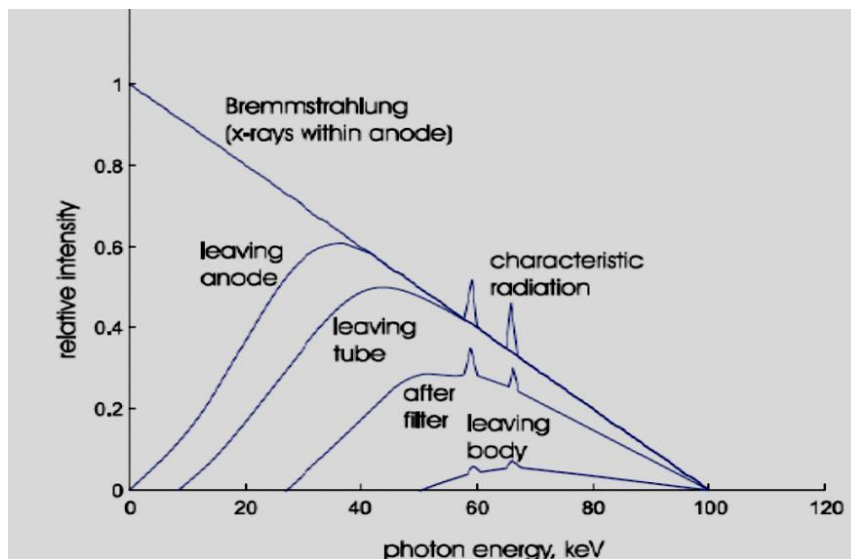
Figure 20: Actual X-ray Spectra (after Prince and Links 2006)

2.6.4.3 Rock X-ray attenuation and their interactions

The contrast between phases in X-ray images of the rocks occurs because of the different attenuation levels of the various mineral phases. Firstly, a proportion of X-rays will pass through the object of interest, in this case the rock, and reach the detector on the other side. This type of radiation is called primary radiation. The other X-rays can be scattered

from their usual path to the detector and this is called secondary radiation. There are two types of secondary radiation, Coherent scatter and Compton Effect. Finally, the radiation can be almost completely absorbed by the mineral grains and it may not be registered at the detector, so it is called absorbed radiation (photoelectric interaction). (Webb 2003)

2.6.4.3.1 Linear and mass attenuation coefficients

In principle, almost any material can be scanned by applying standard calibration procedures since CT scanners measure so-called CT numbers in Hounsfield units. The CT number is defined as:

Equation 27 (Prince and Links 2006):

$$CT\ number = HU = \frac{\mu - \mu_{water}}{\mu_{water}} * 1000$$

Where μ_{water} is the linear attenuation of the water, μ is the linear attenuation of the material tested and HU is Hounsfield units. Hounsfield units are named in the honour of Sir Godfrey N. Hounsfield, a British electrical engineer who invented clinically useful CT scanners. (Hsieh 2009) By definition, water has 0 HU, air -1000 HU, and soft tissues from -100 to 60 HU, 1000HU for bone and could be more than 3000HU for metals, which is a great concern for the reconstruction of X-ray images of rock.

It is known that the same object will give different μ values if scanned in different X-ray CT scanners, since they might have different X-ray tubes installed. The aging of the X-ray tube also has to be considered. This is a required pre - acquisition process when the system is warming up. It is important to set the system to the full power in order to have the highest source energy if required from the beginning of the acquisition.

Hounsfield unit numbers are found to be constant in many different scanners. Hence, quantitative analyses of X-ray transparent materials are made possible by the use of this technique. Because of the growing demand for the use of this technique, manufacturers

94

have been improving the specifications of their machines over time. These modifications have reduced the scanning and reconstruction time considerably.

The attenuation of the intensity of X-ray beam as it travels through the scanned rock is defined as:

Equation 28 (Webb 2003):

$$I_x = I_o e^{-\mu x}$$

where:

- I_0 is the intensity of the incident X-ray;

- I_x is the intensity of the X-ray at a distance x from the source;

- μ is the linear attenuation coefficient of the mineral grain measured in cm^{-1}. It is the sum of all possible interactions μ (coherent scattering, Compton effect and photoelectric interaction).

If we take the log of both sides of the Equation 28, the equation becomes linear:

Equation 29

$$\ln(I_x/I_o) = -\mu x$$
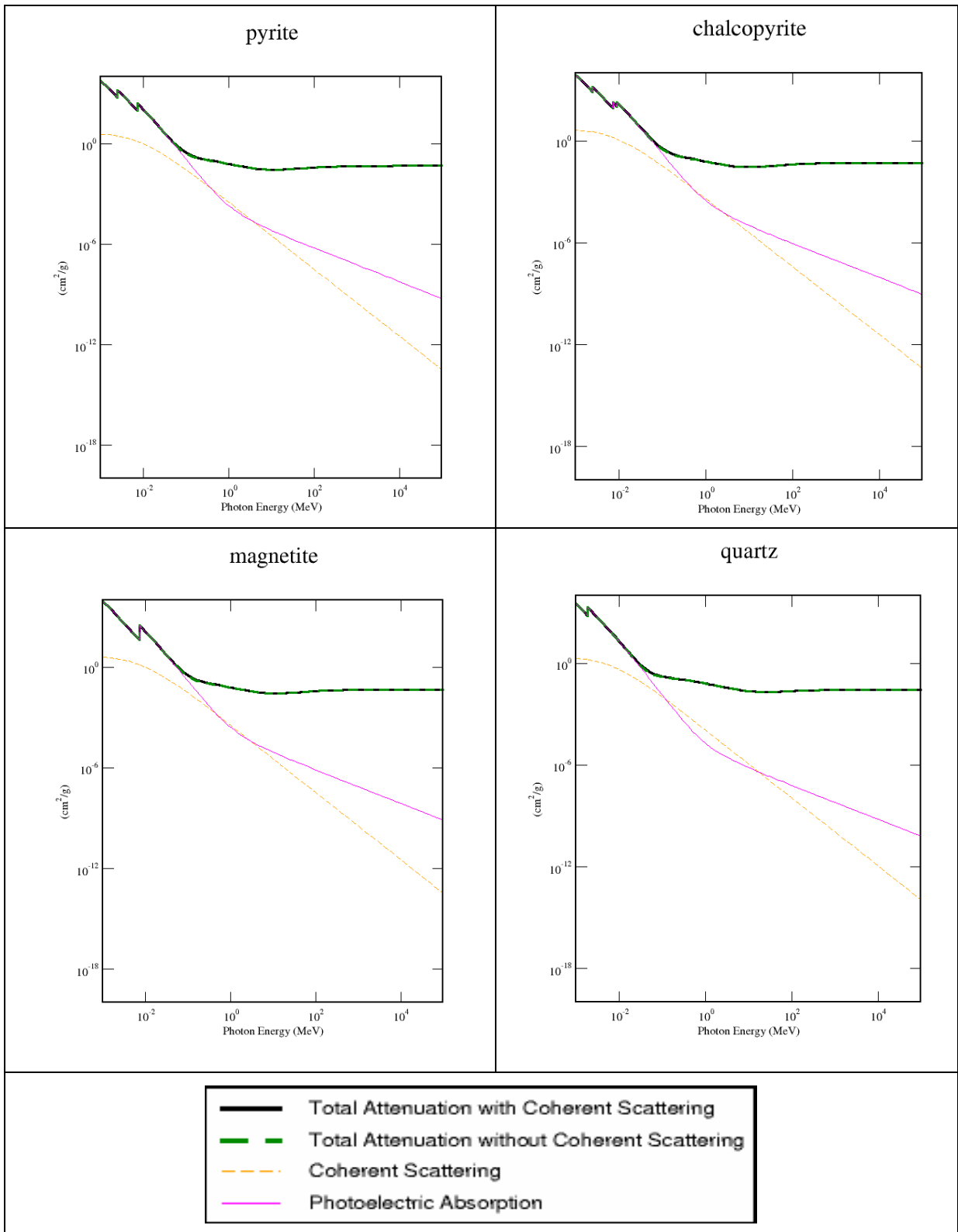
Figure 21: Mass Attenuation coefficients for different mineral grains and their dependence on different attenuation mechanism. Attenuation data sourced from XCOM database (NIST 2011)

It is very obvious from Figure 21 above that the photoelectric interaction contributes most to the linear attenuation coefficients at low energies, whereas the Compton effect contributes at high energies and coherent scattering makes a very small difference or has almost no influence. By multiplying the mass attenuation coefficients with the mineral density we can calculate the linear attenuation coefficients. They will show us that quartz and other gangue minerals will have tendency to absorb the low energy X-rays and make them appear denser than they actually are on the final image. This effect is considered further in section 3.3.

2.6.4.4Visualisation of different phases

X-ray projections of particles are acquired as greyscale images. The SkyScan1072 and SkyScan1172 X-ray Microtomography machines (SkyScan 2010b) can acquire these images (section 3.5). A number of researchers at the JKMRC - The University of Queensland, have used these instruments for research purposes. (Cakici 2009; Keeney 2007)

The best quality standard of the images was achieved with the use of physical tools such as Cu and Al filters, X-ray camera, detectors etc. The computer acquires and stores a series of X-ray transmission images. These images can be reconstructed mathematically. The NRecon reconstruction software provided with the SkyScan system (SkyScan 2010b) was used to generate cross - section images of the particle and three dimensional images of the internal microstructure. The reconstruction program uses a modified Feldkamp algorithm (Feldkamp et al. 1984) with automatic adaptation to the scan geometry. The reconstructed cross sections are then saved in greyscale bitmap (BMP) files. All of procedures mentioned here are discussed in more details in section 3.4.

The conclusion from the initial experimental work was that, in general, special preparation of the samples was not required. The method developed was to mount the samples in Styrofoam as its density value is similar to that of air and it is highly transparent to X-rays. This will not increase noise and it is highly possible that it may act even as a filter for very

low energy X-ray. Mounting the samples in this way helped to prevent any unnecessary movement of the particles inside the sample chamber during the scanning process. This is particularly important as for high resolution measurements the sample and mount must be rigid as any relative movement will smear the reconstructed image.

Visualisation of the internal structure of the sample is possible due to the variations in density and atomic composition of the mineral grains inside the rocks. The contrast between X-ray attenuation coefficients of the phases inside the rocks is represented as variation in the greyscale of the mineral grains. The effective atomic number Z controls the attenuation of the minerals scanned with energies below 100keV, as the dominant attenuation mechanism at low energies (up to 100 keV) is the photoelectric effect which is proportional to Z (Markowicz 1993).

The mass attenuation coefficients used in this research (Figure 22) were calculated from the XCOM Photon cross section database provided by the National Institute of Standards and Technology (NIST 2011). The values are provided by combining experimental results for known atomic specimens (Markowicz 1993). The linear attenuation values calculated by multiplying mass attenuation coefficients for some mineral phases are presented in Figure 23. The Figures provide an insight to the ability to differentiate between different mineral phases in the sample at a set energy level. The linear attenuation coefficients are reconstructed into X-ray CT images. The greyscale of each mineral should be directly proportional to the mineral density/mass attenuation coefficients.
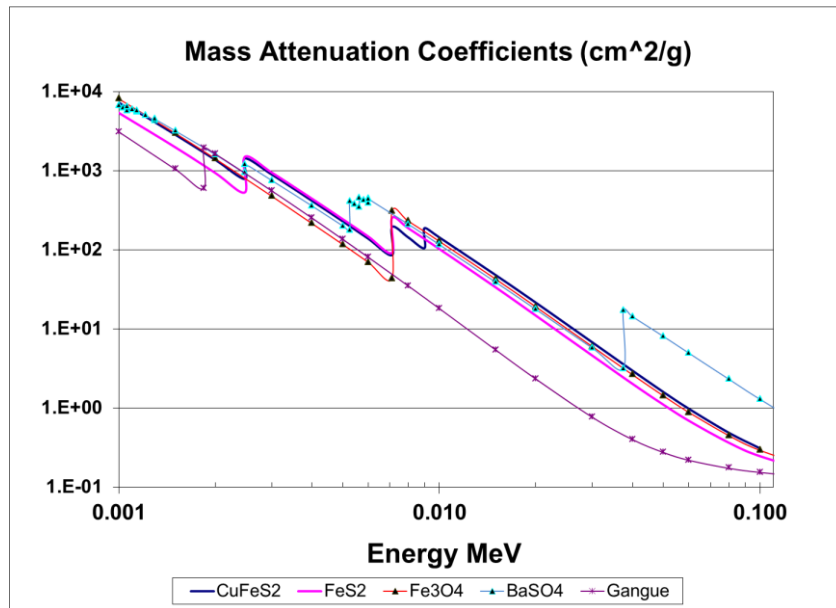
Figure 22: Mass Attenuation Data, attenuation data sourced from XCOM database (NIST 2011)
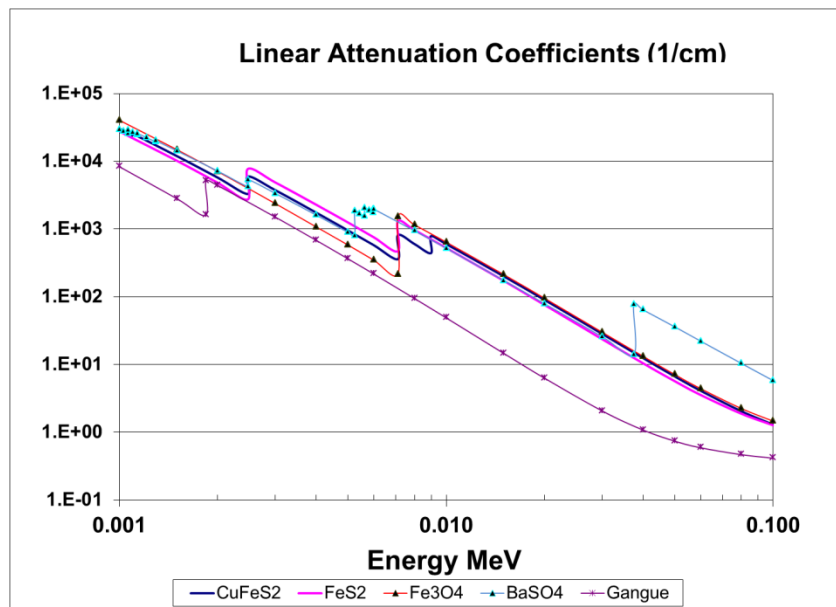
Figure 23: Linear Attenuation Data, attenuation data sourced from XCOM database (NIST 2011)

The samples analysed and reported in this Thesis were from Australian and USA mine sites. These samples contained magnetite, chalcopyrite, pyrite, sphalerite, galena and quartz minerals dominated. All minerals with the density of below 2.7 g/cm^3 were considered as gangue minerals. The image acquired from the SkyScan1072 and 1172 can display three different shades corresponding to each of the three mineral groups present (Figure 23). The darkest shade represents barite if the sample is analysed with X-ray energies of over 80keV.

99

Slightly lighter shades belong to the magnetite, chalcopyrite and pyrite grains and an almost white shade belongs to the remaining gangue minerals. These data indicate that it should be possible to identify each mineral group using higher X-ray intensities. As a measure of accuracy, we have used the measurement of density of each particle as a check on quality. The densities of the particles were calculated from wet/dry weights. The image analysis results were converted to density using the volumetric fraction of each component in order to test the accuracy of the image refinement process.

Although some publications claim they were able to distinguish between sphalerite and chalcopyrite, they failed to present firm validation without incorporating automated mineralogy and QXRD (Quantitative X-Ray Diffraction) techniques.

Ghorbani et al. (2013) investigated the effect of sphalerite leaching in a heap leaching process. The system used was a later technology system then the one used in this Thesis. The energy applied was much higher (225 kV), and the resolution of 3 μm was also higher (compared to 16-19 μm in this Thesis). There was a success in identifying micro-cracks and porosity parameters for particles using this advanced system. But the analysis were destructive and involved crushing and subsampling so that the data could be compared with QEMSCAN data. The mineral data was based on automated mineralogy, where micro-cracks and porosity involved Micro CT.

Ghorbani (2012) a year earlier used similar technique with addition to beam hardening filters applied (linear and quadratic curve fitting). In this study Ghorbani used a dual-energy scanning method for calibration, in order to apply mineral sensitivity properties for better mineral distinction. As this calibration was sensitive to noise, a physical filter (Cu) as well as software corrections were used. He considered three groups of minerals:

1. Gangue mineral group;

2. Pyrite, pyrrhotite and chalcopyrite;

3. Sphalerite and galena.

Although Ghorbani did not accept the difference between pyrite, pyrrhotite and chalcopyrite as sufficient for separation (Ze 22-25), nor between sphalerite and galena (Ze 27 and Ze 78), he did accept the difference between chalcopyrite (Ze 25) and sphalerite (Ze 27). As attenuation coefficients depend on atomic numbers and density, which for chalcopyrite and sphalerite are considered to be similar, using the energies of 130kV and 200kV would not help distinguish the two minerals. It would be beneficial to use the calibration technique presented in Chapter 5 in combination with some other analytical method (chemical assay, QXRD etc), or perhaps considered different grouping of minerals of interest.

The future potential of this technique is that it will rapidly improve with time as the computer technology improves. Reconstruction using the parallel processing power of graphical processing units (GPU) shows promise for rapid reconstruction. Previous instruments had mechanical instrumentation which has now been replaced with digital.

2.6.4.5 X-ray detection

There are a number of detectors used in tomography scanners, but solid-state detectors are the most common. These detectors contain a scintillation crystal in the first stage, typically either cadmium tungstate, sodium iodide, bismuth germinate, yttrium-based, or cesium iodide crystal.(Prince and Links 2006)

During the X-ray interaction with the crystal, photoelectrons are produced which are then excited. This causes emission of visible light when the photoelectrons spontaneously de-excite. This scintillation process results in a burst of light, which is then converted to electric current using an array of solid-state photo diodes. The model of X-ray source is given in Figure 24.

Detectors in microtomography machines detect X-ray photons and the sensitivity of the detectors depends on the photon energy. Detectors or scintillators, may also combine a photomultiplier with the above named components in order to generate a pulse of

electrons for each photon. The size and sensitivity of the detector is very important. X-ray energy is also very important since the high energy X-rays are able to penetrate the particle with much less attenuation than the low energy ones. Consequently, they have a higher chance of being detected than low energy photons. Denser materials absorb more X-rays than less dense ores and therefore they are able to be detected and evaluated while less dense materials are more transparent when X-rays are applied. Very low density materials such as air are almost completely transparent to X-rays.
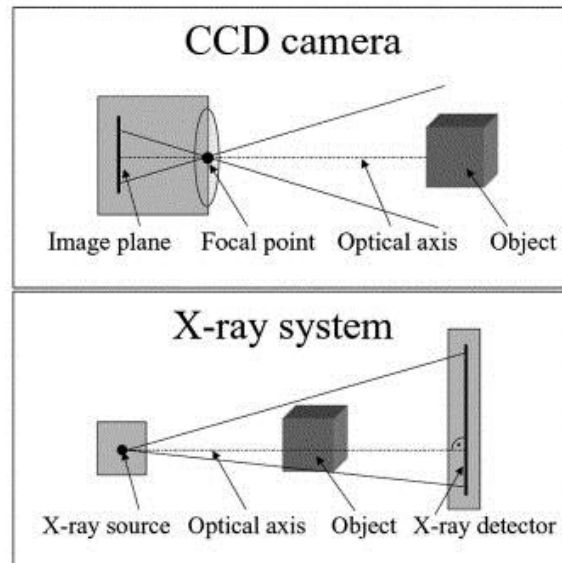
Figure 24: Pinhole camera model, CCD camera projection (top) and X-ray imaging system (bottom) (Mitschke and Navab 2003)

The detector also introduces the noise into the system. This noise must be taken into consideration when starting the acquisition process. To stabilise the detector noise in this work, the function for creating the flat field parameters for known exposure time, rotation step and X-ray intensity has been used. Artefacts in the images are discussed in section 2.6.4.2.

2.6.4.6 Source Exposure time

When establishing the method to measure an ore sample it is recommended to have as much prior information about the ore as possible. For example, an MLA analysis will

102

identify the minerals which are present. This information will assist in the selection of threshold values in the reconstruction process and in setting up the actual analysis process. The importance of this mineral information lays in the fact that inappropriate intensity of the source and incorrect exposure time may adversely affect the image quality and reduce the accuracy of quantitative mineral analysis. Calibration of the measurement and the reconstruction process of each ore to be tested are highly recommended and the method to calibrate the analysis process is discussed below.

If the particle to be tested contains low density minerals, the required exposure time is generally less than when analysing a particle with a high content of high density minerals. The transmission of X-rays is proportional to the exposure time, which may lead to data loss in case where lighter minerals are tested. An example is shown in Figure 25.
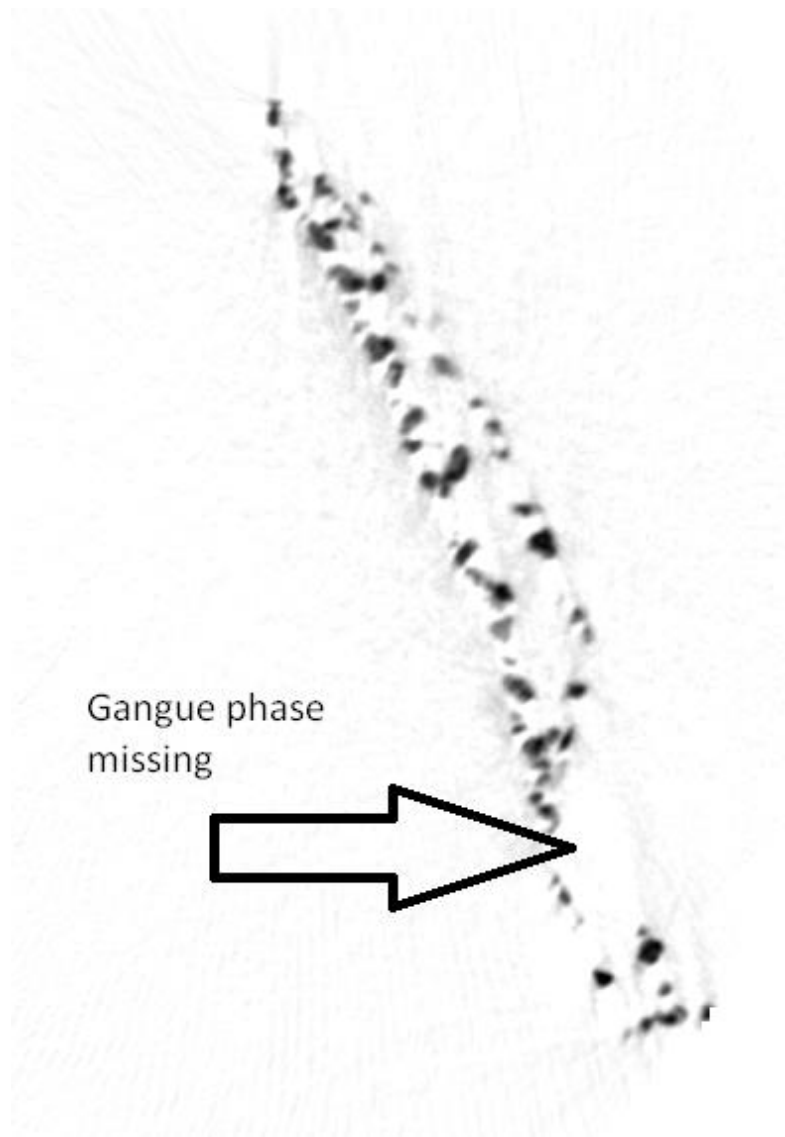
Figure 25: Reconstructed cross section image of the particle analysed with incorrect exposure time, gangue phase missing from internal section

2.6.4.7 Filter selection

Filter selection is an important part of the image acquisition process. A serious problem in reconstruction of X-ray images is the assumption that the beam is monochromatic. External filters are used to reduce the proportion of low energy X-ray radiation in order to reduce the non-linear absorption of the X-ray in dense minerals that will cause problems and false absorption values later in the process. These low energy X-rays do not have enough energy to pass through the object that is scanned and reach the detector.

Different metal filters can be used during the acquisition process, such as Al, Cu, Zn, brass, bronze etc. to change the energy distribution of the X-rays. The application of different thicknesses of the filter is possible. When filters such as these are used, the average intensity of the X-rays gets higher since the low energy X-rays are removed. (Cakici 2009)

Within the X-ray tomography system metal filters are placed in front of the camera. When filters are used, in order to detect and compensate for defect pixels in the detector, longer exposure time and a finer rotation step should be used. (SkyScan 2010b)

The influence of filters has been observed in details in Goertzen (2003) and some results presented in Table 2 and in Figure 26 and Figure 27.

Table 2: Observation of filter influence (Goertzen 2003a)

Beam	Anode	kVp	Filter (inmm)	Tube Current (mA)	Exp. Time (s)
A	Mo	30	0.02Mo + 0.5Al	1.0	2.0
B	Mo	40	0.02Mo + 0.5Al	0.8	1.0
C	W	40	1.0Al	0.6	1.0
D	W	40	2.0Al	1.2	1.0
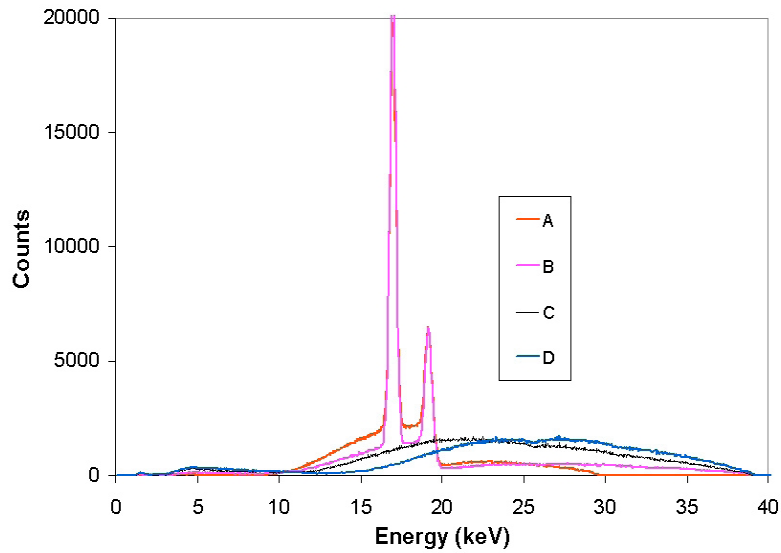
Figure 26: The application of different filters and exposure times, from Table 2 (after Goertzen)
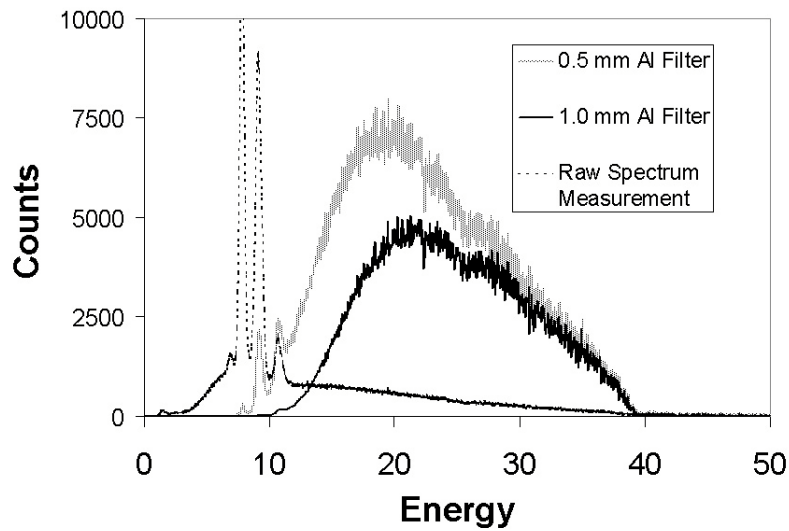
Figure 27: "Energy spectrum for the raw beam and for simulated 0.5mm Al and 1.0mm Al filters. The filtered spectra are multiplied by a factor of 20 in order to be more easily seen on the scale of the plot."(Goertzen 2003b)

2.6.4.8 Image formation

For non-monochromatic X-ray CT systems, the X-ray intensity at any given detector is given by the equation below:

Equation 30

$$I_d = \int\limits_0^{E_{max}} S_0(E)E\exp[-\int\limits_0^d \mu(s,E)ds]dE$$

Where $S_o(E)$ is the X-ray spectrum and $\mu(s;E)$ is the linear attenuation coefficient along the line between the source and detector.(Prince and Links 2006)
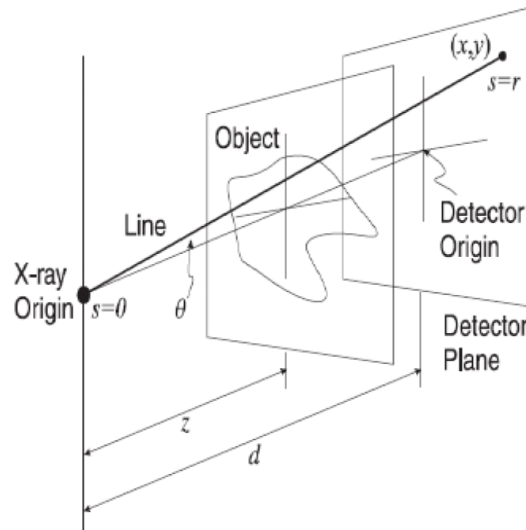
Figure 28: The X-ray projection Geometry (Prince and Links 2006)

The integration of this equation leads to problems in reconstruction if we assume that an effective energy, $\overline{E}$, is producing the same intensity from a monochromatic source as is measured from polychromatic source. Using this assumption simplifies equation 2 to equation 3 but leads to the artefact of beam hardening (see 3.3) as a single energy source is a poor approximation to a broad spectrum:

Equation 31

$$I_d = I_0 \exp[-\int_0^d \mu(s; \overline{E})ds$$

Equation 32

$$g_d = -\ln(\frac{I_d}{I_0})$$

Hence, we are able to say that the basic measurement of the CT scanner is the line integral of the linear attenuation coefficient at the effective energy of the scanner. For this reason, it is important to calibrate the detectors prior to any measurement to generate a reasonable estimate of a spectrum energy I_0. (Prince and Links 2006)

2.6.4.9 Worldwide usage of CBT

As already mentioned, cone beam tomography has been primarily used for medical research, where the main material of interest had a density that ranged between 0.5 and 1.5 g/cc such as water, body liquids or bones.

Micro tomography has been widely used in research. For example, for the characterisation of fibrous structures in textile research (Eberhardt and Clarke 2002; Ketcham 2005), for analysis of archaeological materials (Dooryhee et al. 2004), to determine the origin of rare asteroidal vesicular basalts (McCoy et al. 2006), in geosciences (Ketcham and Carlson 2001; Ketcham and Iturrino 2005; Lin and Miller 1996; Lin and Miller 2001; Miller et al. 2007; Miller et al. 2003) and in modelling processing operations (Evans et al. 2013). It was also used as mentioned earlier in heap leaching process (Ghorbani 2012; Ghorbani et al. 2013). The importance of the Micro-Cone Beam Tomography increased significantly in the field of Mineral Processing and Geology towards the end of the last century.

2.7   Breakage characteristics of ore

The research in the field of breaking ore and coal started in the 1950's. The behaviour of the ore is very important in all stages of mine life, starting from discovering the deposit, prefeasibility stage, feasibility stage, operational and closing stages. The comminution of ore is usually the largest power consumer at the mine site. In the time of climate change, it is paramount to design the circuit in the way that the greatest possible amount of energy applied in comminution devices goes into the proper size reduction/liberation of the ore. It is also very important to avoid any overgrinding during this process.

Thus the importance of properly assessing the breakage properties of the ore is paramount. If well defined, the design of the circuit as well as the optimisation may be straightforward. In principle, there are many tests available for evaluating the hardness of the rocks, but not every one of these may be applied in operational plants. As the hardness is difficult property to define, the test has to be linked with the machine used in the operational plant in size reduction process.

The commonly used laboratory breakage characterisation tests are Bond Ball and Rod tests (Bond 1952; Bond 1954, 1961), JK Drop-Weight Test (Bearman et al. 1997; Kojovic et al. 2008)and SMC Test® (Morrell 2006, 2007, 2008, 2009, 2010), and Rotary Breakage Test (Kojovic et al. 2008; Shi et al. 2009). These are developed on the principals of single particle breakage characteristics. The standard JKDrop-Weight Test provides ore parameters primarily used in the JKSimMet Mineral processing simulator software. Combining these parameters with equipment details and operating conditions will help predict SAG/autogenous mill performance. These parameters may be used in a number of comminution models included in JKSimMet software.

2.7.1 Reduced matrix

The estimation of feed particle properties has been a challenge for many decades. The explanation of the problem is given in Equation 33:

Equation 33 (Keith 2000):

$$p(s) = \int_P k\left(\frac{s}{c}\right) f(c) dc$$

Where:

- f(c) is true particle volume distribution, with c containing three dimensional properties of the interest;

- p(s) is apparent particle distribution (area or intercept based), breakage function;

- k(s/c) is the kernel or conditional probability density in P particle space.

The problem lies in the fact that two different sets of particles can produce the same sections (Cruz-Orive 1976; Moran 1972). This proofs the fact that estimation of particle properties is indeterminate (Keith 2000). This is the reason researchers went from exact solution to likely solution.

The kernel relates apparent particle distribution to true composition, it is a distribution of apparent composition produced by particles with true grade c. When distributions f and p are replaced by vectors, it is:

Equation 34 (Keith 2000):
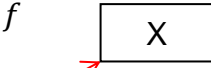
$$f = \begin{pmatrix} f_0 \\ f_1 \\ . \\ . \\ f_{11} \end{pmatrix} \quad p = \begin{pmatrix} p_0 \\ p_1 \\ . \\ . \\ p_{11} \end{pmatrix}$$

Elements of vectors in Equation 34 are proportions of volume of mineral of interest. Then Equation 33 can be rewritten in terms of K square matrix:

Equation 35:

$$p = K * f$$

$$K = \begin{bmatrix} 1 & \cdots & 0 \\ \vdots & \ddots & \vdots \\ 0 & \cdots & 1 \end{bmatrix}$$

In K, 12 columns are the apparent compositions. Hence for 12 sizes and 12 classes (2 liberated and 10 locked) we have 144 solutions for each of the 144 combinations. 144^2 is a daunting number of parameters for breakage of elements. As liberated particles cannot break into locked ones, there are zeros in the first and last column. X area in Equation 35 is locked particles distribution which produce more complicated solutions.

Hence it is easy to say why most researchers use simplified assumptions. They are usually related to the degree of the randomness of the parent texture and of the breakage parameters. These simplifications are considered further in chapter 6.

However if we can measure and classify feed particles into size by texture categories, it is not too difficult to break them at well-defined energy with a suitable breakage device. The progeny can then be characterised in similar manner. This provides a strategy for direct experimental measurement of the liberation kernel.

2.7.2 Rock Breakage (of single particles)

The breakage of rocks highly depends on its behaviour within the comminution device and the amount of energy applied as well as the physical characteristics of the machine. For the purpose of this research, single particle breakage will be used, in which the particles were broken one by one, with an exact input of energy applied.

In rock breakage, there are two main mechanisms. The first occurs at low applied energies (abrasion, tumbling test, (Bond 1952; Bond 1954, 1961)) and the second with high energies applied (single particle impact breakage). For the latter, there are a number of testing devices:

-   Twin Pendulum (Narayanan 1985);

-   JK Drop-Weight Tester (JKDWT) (Napier-Munn et al. 1999);

-   ALICE (Automated Linear Impact Comminution Evaluator) (van Latum 1985, 1995);

-   Mini Drop-Weight Tester (Man 1999);

-   Short Impact Load cell (SILC) (Bourgeois and Banini 2002)

-   JKRotary Breakage Tester (JKRBT)(Kojovic et al. 2008; Shi et al. 2009).

The two machines in common use at JKMRC for this type of the research are the JKDWT and JKRBT.

2.7.2.1 JK Drop-Weight Test

The principle of dropping the particle from a certain height in order to quantity the breakage properties of the particles is well known. Since it was completely impractical to

break the particle with very high energies as it happens in the mills, JKMRC worked on combining machine and ore parameters during the last forty years of time in order to quantify the process properties. This is used for predicting ore behaviour in the plant and very successful process modelling. The ability of testing single impact breakage is possible using the JKDrop Weight Test, whose principle was introduced in 1989 by Morrison and Morrell (Morrell and Morrison 1989) . Here the particles are broken under the impact of the heavy weight, which is dropped from the predetermined height so that the exact energy input level is calculated. The products of the breakage are then collected, sized and the size distribution is then normalised with respect to the particle size. The height of the load, as well as the weight of the load are calculated based on the mass values of the particles. A mass of the particles and the height of the load from which it is dropped are used for calculating exact breakage energy.

The conventional way of expressing the ore breakage at JKMRC is in presenting the t_{10} value, which is the percentage passing one-tenth of the original particle size. It is given as:

Equation 36:

$$t_{10} = A(1 - e^{-bE_{cs}})$$

where :

- E_{cs} is the specific energy (kWh/t)

- A and b are impact breakage parameters.(Napier-Munn et al. 1999)

Using the method of minimising the squared error routine (Whiten 1972) the product of this test are impact breakage parameters A and b are provided which are related to the resistance of the ore to impact breakage. The disadvantage of the test is that there are a general values for A and b provided, covering all five size classes tested.

Figure 29: JK Drop-Weight Tester (JKTech 2011)

The second observation coming from this test is the slope of the energy E_{cs} with reducing the size of particles. It usually follows the trend of decreasing the slope with decreasing the particle since. However, if the opposite trend occurs it may mean that the usual size of the SAG media, 100-200mm range, may not be able to survive. The abrasion parameter is determined from a tumbling test in a small mill:

Equation 37:

$$t_a = t_{10}/10$$

Figure 30 shows the typical JK Drop-Weight Test curve, where A is the highest t_{10} value achieved, and b is related to the overall slope of the t_{10} vs E_{cs} curve. Since the A and b values are interdependent, it is common to report the hardness of the ore as a single value A*b which is a measure of breakage of the ore at lower energy levels.
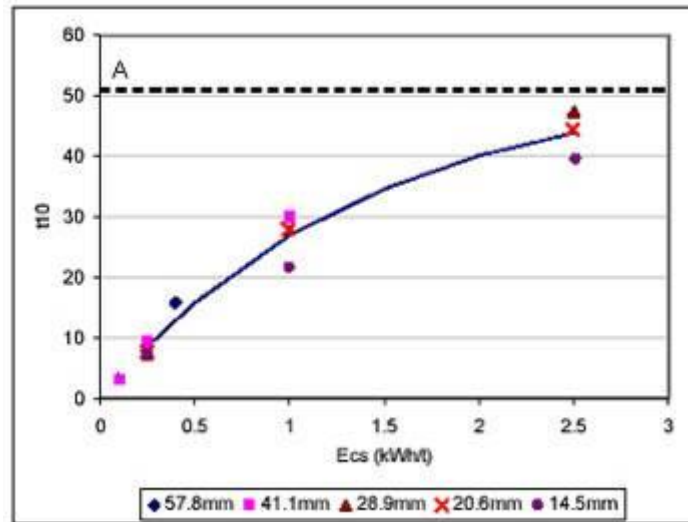
Figure 30: Typical JK Drop-Weight Test Results curve

The impact breakage parameters may be used to design, optimise or analyse a range of operating conditions in comminution plants. It may also be used to determine parameters for new or existing crushers using the JKSimMet model. It has been common rare in the past that the whole deposits were modelled by using Drop-Weight tests results combined with the estimated parameters obtained from SMC Tests explained below. Models in JKSimMet depend on t_{10} value which may be sufficient to generate a full size distribution based on relationship t_{10} vs t_n coming from JK Drop-Weight database.(Narayanan and Whiten 1988)
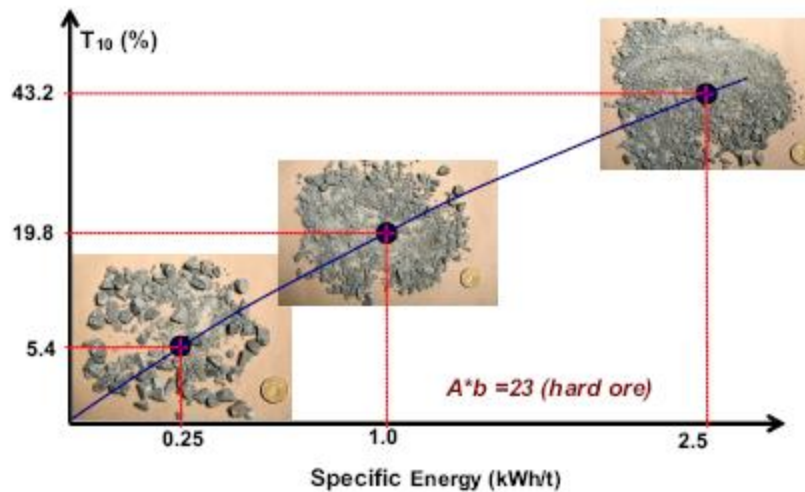
Figure 31: The relationship between produced fines and specific breakage energy for a single particle size (Kojovic et al. 2008)

The limitation of the Drop-Weight Test is the error related to the parameters determined for ore that has higher than normal content of clays. This type of ore is usually brittle and does not experience very much of plastic deformation. Napier-Munn (1996) et al. include detailed information about the JK Drop Weight Test plus information on comminution circuit equipment, operation and modelling. There are more than 30 Drop-Weight Test units operating in JKTech licensed laboratories around the world.

This test was not suitable for application in this Thesis as a set of particles larger in size is required for accurate breakage energy measurements.

2.7.2.2 JK Rotary Breakage Tester (JK RBT)

Market requirements influenced the development of a breakage model which incorporates the effect of particle size and Rotary Breakage Machine, which was commercially available from mid. 2010. The breakage mechanism of the JK Rotary Breakage Tester (JKRBT) is different to the JK Drop-Weight Tester (JKDWT). The particle broken in the JKRBT is in motion during the breakage process, in which case the total energy used for breaking is imported by the rotor and kinetic energy of the particle (single point impact).

Research was shown that incremental breakage is much more present in AG mill operations (Djordjevic et al. 2004) which increases the importance of testing repetitive incremental breakage of the particles at small energies. JKRBT can be used for these tests as the particles feed rapidly into the machine. There is no special fitting of the particle at the anvil, where the computer which controls the rotor speed of the machine helps reduce the test time and increases the test precision considerably. The simulations leading to this discovery were given in Morrell (Morrell et al. 1996) and Djordjevic (Djordjevic et al. 2003).
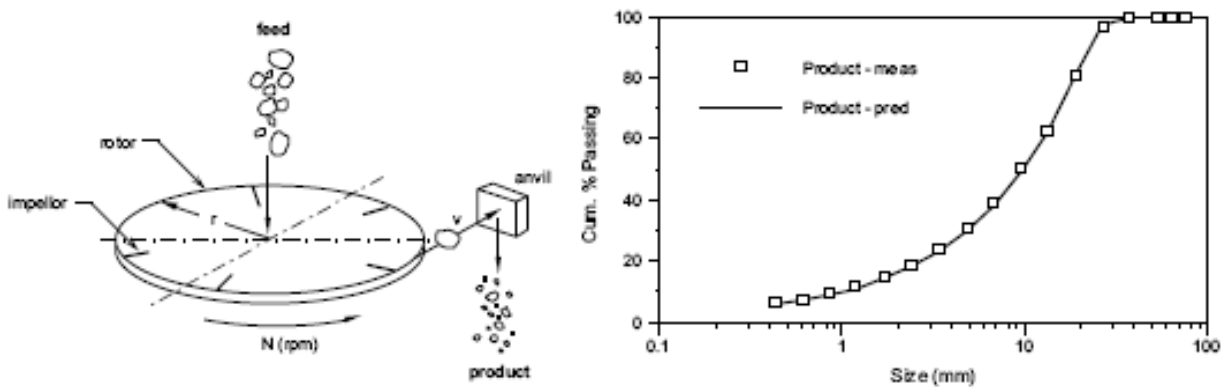
Figure 32: Theoretical representation of Vertical Shaft Impact process and comparison of model prediction for Canica M-100 treating basalt (Kojovic 1996)

This is not the first time this concept was introduced and used (Fuerstenau et al. 1990; Schonert et al. 2002; Vogel and Peukert 2004) however their device was not able to control the input energy as it is in JKRBT, hence the impact velocity was assumed.

Previously it was believed that a machine that breaks rocks using kinetic energy and rotor-stator design may work in very chaotic manner generating biased results, where the particle will receive a secondary breakage at the anvil, the anvil rotor-stator design will influence the actual impact velocities etc.(Van der Zanden et al. 2002)

It has been shown by Morrell et al. (1996), Shi (2002), Djordjevic et al. (2003) and Shi et al. (2003) that the concept is valid by using basic design data on the machine and rock characteristics in useful simulations such as effect of rotor speed. Because of precise measurements of particle velocity and the control of the energy input, the rock

characteristics can be evaluated from the products of the breakage. (Shi et al. 2009) The image of the breakage device is shown in Figure 35.

Figure 33 and Figure 34 show the JKRBT rotor-stator impact system which consists of a rotor with four guiding radial channels, a driving motor and a pulley mechanism, and the surrounding anvils (stator). Underneath the machine there is a container which collects fines generated during breakage. The operation computerised control unit is on the left side of the rotor (Figure 35 and Figure 36). Particles are fed one by one into the vertical tube at the centre of the rotor. The breakage happens as a result of a particle hitting the anvil with a velocity which is a result of tangential and radial velocity as shown in Figure 34.

Equation 38

$$V_i^2 = V_t^2 + V_r^2$$

$$V_{i(theoretical)} = V_t/\sqrt{2}$$

The specific energy of the impact breakage in JKRBT is defined as the kinetic energy per particle mass. (Kojovic et al. 2008)
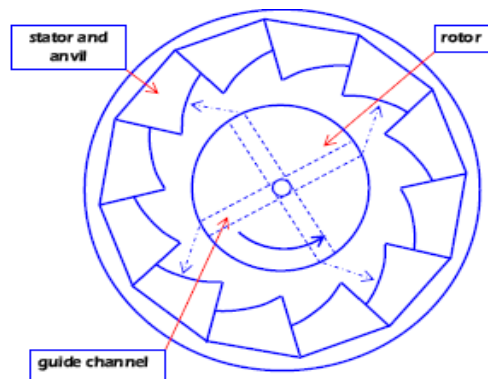
Figure 33: Schematic diagram of impact mechanism of RBT (Kojovic et al. 2008)

Equation 39

$$E_{cs} = 0.5 * m * \frac{V_i^2}{m}$$

$$E_{cs} = 0.5 * V_i^2$$
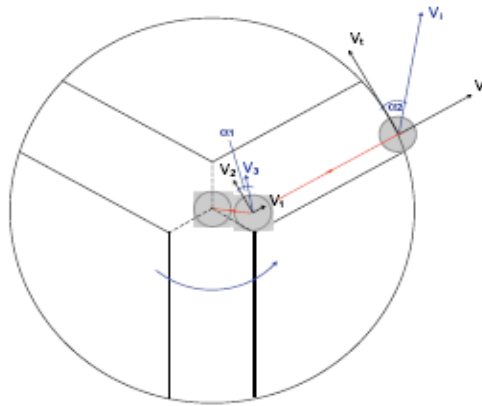
Figure 34: Rotor guide channel entry and exit, velocity components (Shi et al. 2009)

Figure 35: JK Rotary Breakage Tester (JKTech 2011)
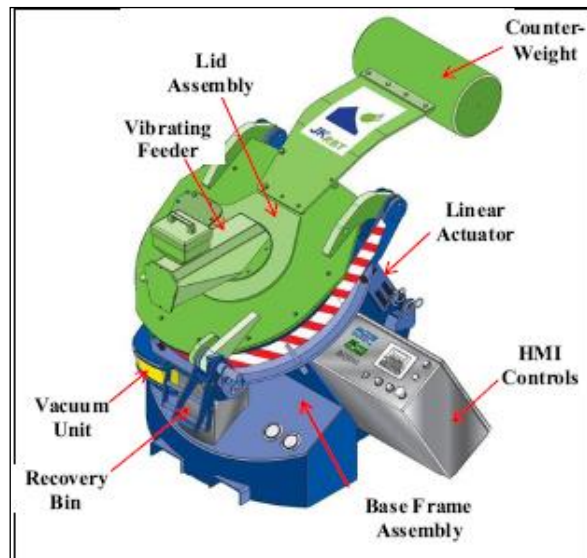
Figure 36: Schematic of the industrialised JKRBT breakage testing device (Kojovic et al. 2008)

The model also recognises the inability of the JK Drop-Weight Test to provide the breakage information of finer particles. It describes the breakage by using material property, particle size and net cumulative impact energy:

Equation 40 (Kojovic et al. 2008):

$$t_{10} = M\{1 - \exp[f_{mat} * x * k(E_{cs} - E_{min})]\}$$

Where:

- M is the maximum t_{10} (%);

- F_{mat} is the material breakage property ($kgJ^{-1}m^{-1}$);

- x is the initial particle size (m);

- k is successive number of impacts with a single impact energy;

- E_{cs} is the mass specific impact energy (Jkg^{-1}) and

- E_{min} is the threshold energy (Jkg^{-1}).

The JK RBT breakage model (Equation 40) was based on a theoretical approach described in Vogel and Peukert (Vogel and Peukert 2004), which uses a generalised dimensional analysis earlier proposed by Rumpf (Rumpf 1973) and a detailed fracture mechanical model based on Weibull statistics (Weibull 1951). All breakage model parameters included in this model are available in JK Drop Weight database. Equation 40 can be converted back into A*b values following the next relationship:

Equation 41:

$$A * b = 3600 * f_{mat} * M * x$$

Equation 40 shows that the model does not depend on particle mass as in JKDWT. It focuses on expressing the breakage properties of the rocks and not the size reduction.

The energy input is directly controlled, but the calculation was modified from the original since it was proven by using photographic analysis that the actual impact velocity in practice is less than theoretical. (Kojovic et al. 2008) Therefore a calibration constant was introduced:

Equation 42:

$$C = \frac{v_{i(actual)}}{v_{i(theory)}}$$ **(Shi et al. 2009)**

Where C is a machine design constant for the maximum possible impact velocity at a given rotor speed and given set of operational conditions.

C varies from approximately 0.85 to 0.95, meaning that the kinetic energy is not completely transferred from the machine to the particle. The trend of increase in the constant with increasing rotor speed is not linear, where C accounts for the friction. Large particles have higher C values, which are resolved by effective rotor radius. It is highly machine dependant and needs to be calibrated for each machine individually. The other rock properties do not significantly influence on the final results. The specific energy is then determined by:

Equation 43:

$$E_{cs} = \frac{0.5 * \left[c * \sqrt{2} * \left(\frac{2 * \pi * N * r}{60} \right) \right]^2}{3600} = 3.046 * 10^{-6} * C^2 * N^2 r^2$$

where:

- r is the rotor radius (m);

- N is the rotor speed (rpm). (Shi et al. 2009)
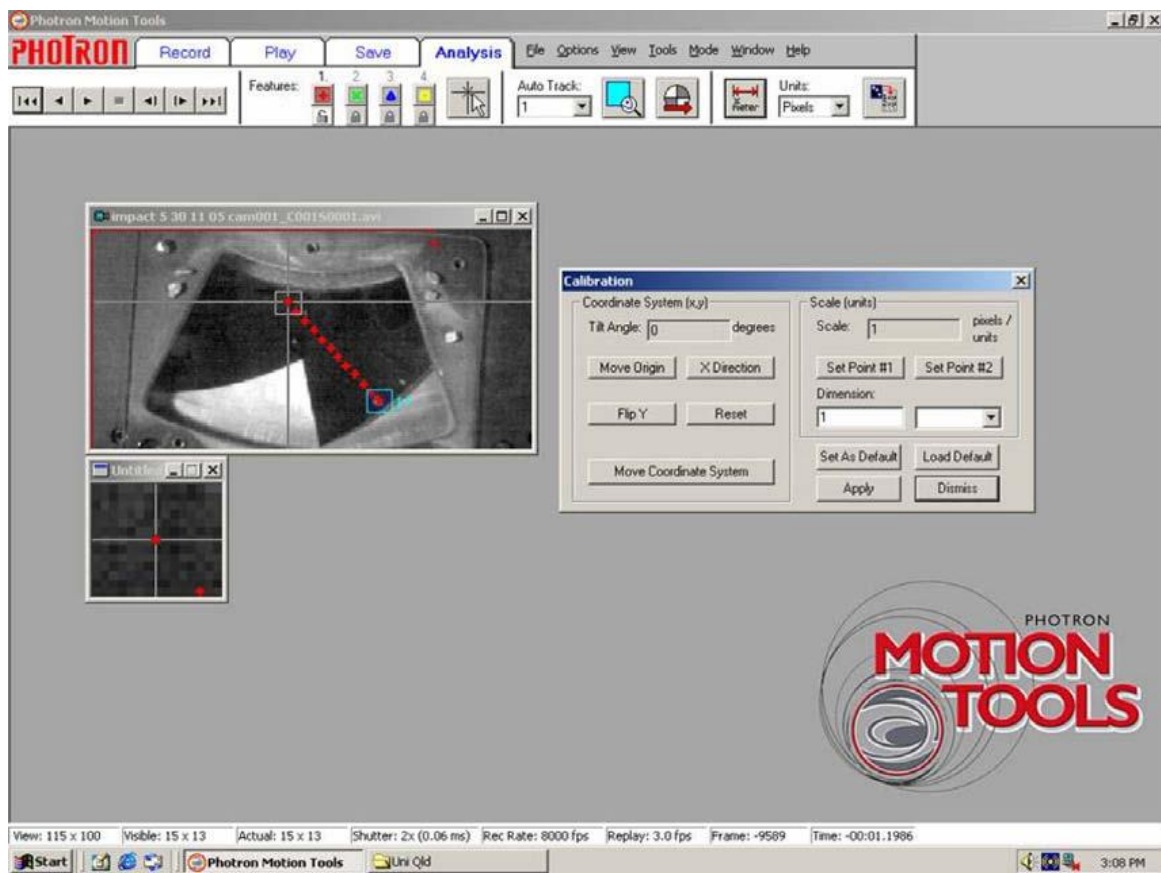
Figure 37: Photron software, processing high speed video data to determine the impact velocity of the particle in JKRBT (Shi et al. 2009)

By examining the high speed video camera data (Figure 37), it was revealed that the particle remained in the contact with the guide channel until the particle completely emerged from the channel. Therefore effective rotor radius should be increased by at least

half of the particle diameter when calculating the tangential component of the impact velocity. Hence the corrected specific energy is then calculated as (Shi et al. 2009):

Equation 44:

$$\mathbf{E_{cs}} = \mathbf{3.046 * 10^{-6} * C^2 * N^2 (r + \frac{x}{2})^2}$$

where x is geometric mean particle size (m).

Based on extensive test work performed on various ores (gold ore, copper/gold ore, hornfels aggregate etc.) using a wide range JKRBT operating conditions (rotor speed, feed rate, feed location) it was confirmed that the JKRBT kinetic energy approach may be applied for rapid particle breakage characterisation. The researchers also tested variations in particle size and shape, particle surface and moisture and solids density.(Shi et al. 2009)
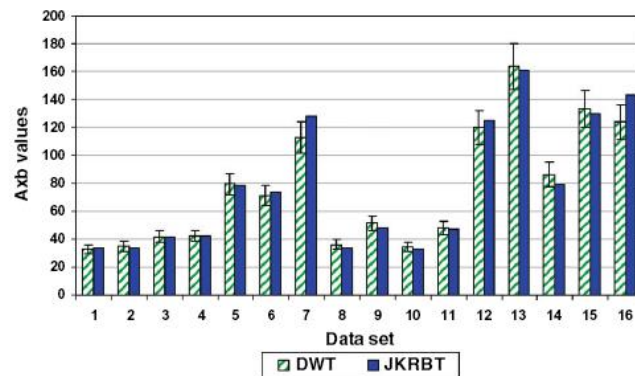
Figure 38: Comparison of breakage parameters A*b determined by JKRBT and JKDWT (10% error bars in DWT)(Shi et al. 2009)

In order to provide an estimate of the JKDWT parameters, there is a calibration procedure of JKRBT data developed in order to translate those parameters from 1-impact breakage mechanism to 2-impact breakage mechanism. JKMRC (Shi et al. 2009) has conducted a validation process in order to obtain the valid calibration factors, since the difference in the breakage mechanism resulted in finer product coming from JKRBT compared from the one from JKDWT. The result of the comparison and calibration process is shown in Figure 38.

However, the requirement is still to provide JKDWT results of the ore when calibrating JKRBT test data, because of the previously mentioned occasional strange ore behaviour, where the coarser phase appears softer than the harder ore phase if the ore consists of two or more different components. The only discrepancy found in the calibration data was to deal with the particle shape, since flat particles broken in JKDWT are consistently broken in the same plane, where the particle broken in JKRBT have random orientation.

To conclude, JKRBT allows the rapid characterisation of the particle impact breakage properties by testing a large number of particles in a relatively short period of time (breaking 1200 particles in approximately 20 minutes). As the specific energy is well controlled in the JKRBT, very high specific energies may be delivered to the small particles tested in this Thesis. Because of its intensive independence of particle mass, the JKRBT was used as the main breakage device in this research.

Repeatability of the RBT data is very high, as shown on Figure 39, which confirms the benefits of the improved control of specific energy.(Shi et al. 2009)
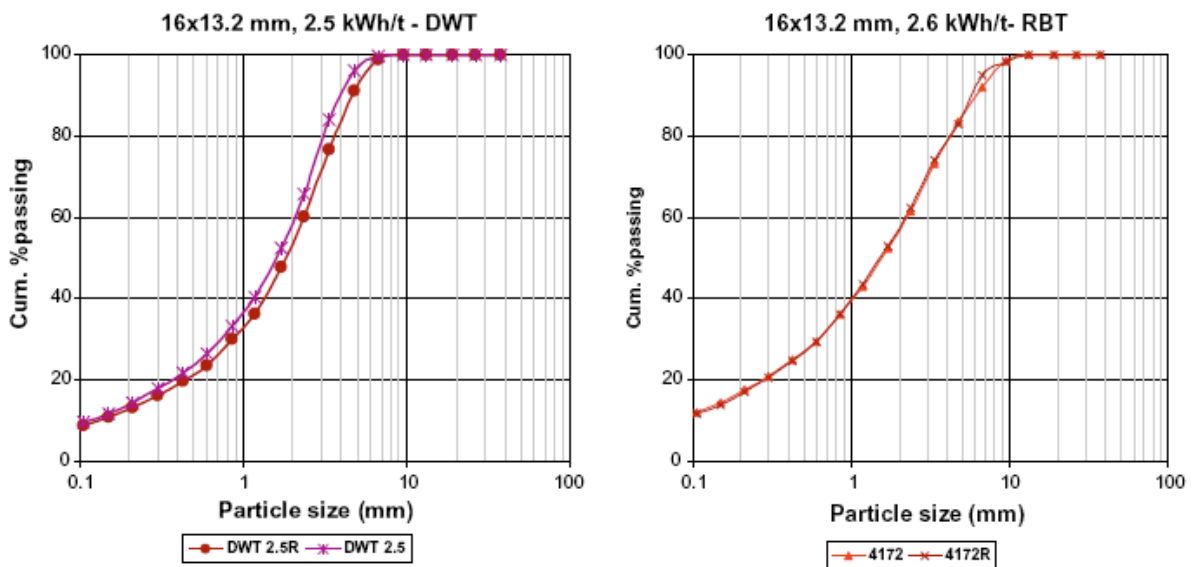
Figure 39: Comparison of repeatability of JKDWT and JKRBT on the same ore and particle size(Shi et al. 2009)

3 Optimisation of Techniques for Characterisation of Liberation

3.1 Overview

Chapter 3 provides details of the development of the experimental methodology used to characterise liberation of the particles before and after breakage. A series of X-ray tomography analyses were performed in order to investigate the three dimensional structure of the mineral grains present in the ore matrix. The following chapter describes the analysis technique and its usage. The most important purpose of the reconstructed tomographic images was the ability to provide three dimensional internal information of the mineral grain arrangement within a range of multi component particles.

3.2 Experimental work at JKMRC (UQ)

The technology was also used at JKMRC where its ability to obtain sulphide content in ore deposits has been tested (Evans et al. 2013; Keeney 2007; Pokrajcic 2010). The data from Pokrajcic's PhD Thesis (Pokrajcic 2010) which was measured in 2007 is given in appendix 9.12. This was part of a case study in which the primary objective was to establish the use of tomography analysis in assessment of an ore body, to provide the macro-texture and meso-texture information and help in identifying the opportunities in early rejection of gangue. The secondary objective of this case study was to determine the separation efficiency of HMP (Heavy Medium Plant).
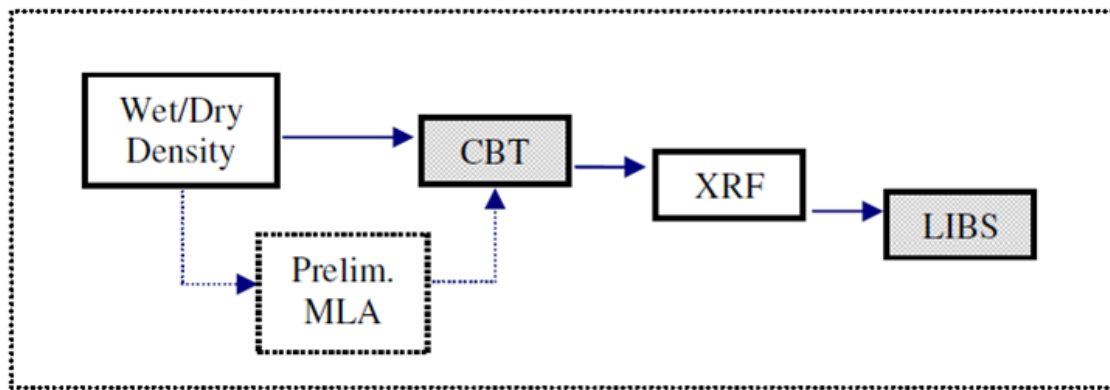
Figure 40: Test work sequence for analysis of Mount Isa lead-zinc ore, (from Pokrajcic 2010)

There was a slight bias in the data acquired in higher density particle, which indicated the problem that the software used for reconstructing the radiograph images acquired in SkyScan1072 had with high dense minerals such as galena, pyrite and sphalerite.

At the time this research was conducted, the apparatus was able to provide the resolution of approximately 18µm, which did not quite serve the purpose of identifying sulphide grains that ranged around 5µm. Ore phases could be hosted in pyritic shales, thus causing differentiation problems, as sphalerite and pyrite have similar attenuation coefficients and thus are indistinguishable from each other in tomography images. (Keeney 2007) This is why it was required to conduct mineralogy analysis of the sample to be scanned in Micro CBT. Nowadays the resolution of the machine is improved significantly, but the mineralogy data is still necessary because of required energy adjustments. The resolution of SkyScan1172 Micro CBT system can be as high as 1µm.

The human factor has to be reduced to the minimum, such as error in deciding what threshold value to be used when calculating volume of the phase. For this reason, we have used eCognition8 image analysis software, where the software has made the decision based on the greyscale of the certain phase. On the other hand, the colour of the mineral phase depends on the attenuation coefficients of the mineral scanned and the energy of X-ray. For further information about the scanning properties, please refer to the section 2.6.4 and 3.7. On details how the problem has been overcome, refer to Chapter 5 and 6.

Since we can follow the liberation through breakage with the development of this new technique that this Thesis is presenting here, our opportunities to better understand liberation and breakage of the ore are increased considerably.

3.3   Artefacts in images

As X-ray tomography systems were first developed mainly medical applications, they were optimised to suit the properties of flesh and bone. The X-ray energy required for penetration of such materials is much lower than for minerals as they are less dense than minerals. The artefacts in reconstruction, particularly beam hardening presented in Figure 41, are caused by the assumption of a monochromatic beam of X-rays and these artefacts become more severe when measuring high density materials. Therefore, for mineral investigations it is very important to adjust the scanning and reconstruction parameters according to the properties of the minerals present.
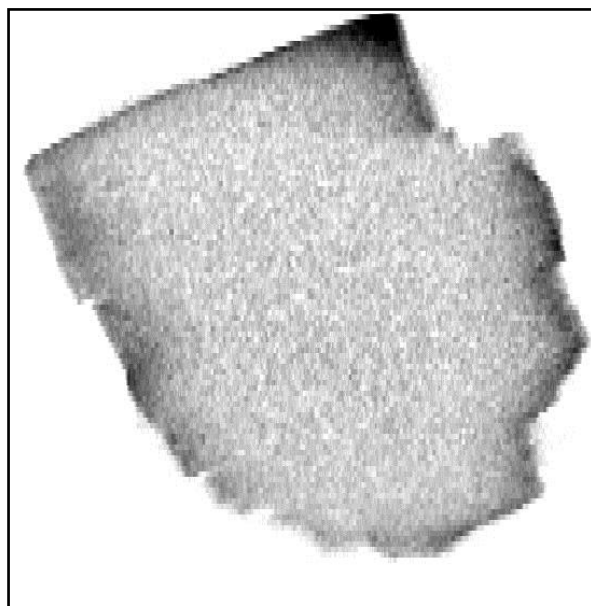
Figure 41: Example of beam hardening

The ideal scan would be the one where the detector detects the primary radiation X-rays, where the energy is equal for all X-rays in the beam (monochromatic beam) and the image

contrast is based only on photoelectric absorption. However, this is rarely the case and the large number of scattered X-rays usually influences the image quality and accuracy. (Webb 2003)

As discussed previously, attenuation by scattering occurs because some of the original energy of the beam is deflected to a new path by some positive energy. Scattering in CT images can be prevented by using a perfectly collimated detector. This detector will reject all photons that are not travelling in a straight line between source and detector. X-ray scatter leads to artefacts in reconstruction since the effect changes with each projection. (Avinash and Malcolm 1988)

The beam dimensions when it reaches the object are often greater than the field of view (FOV), which increases the number of Compton scattered X-rays detected by detector. In order to restrict the beam, the collimator (Figure 42) is placed between the X-ray source and the object, so that the beam can match the FOV.(Webb 2003)
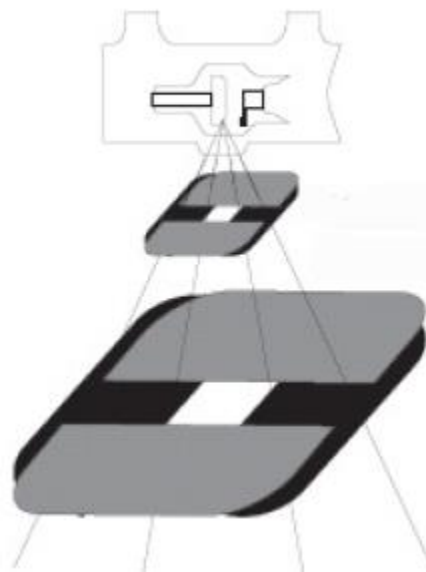
Figure 42: Collimator Beam restrictor (Prince and Links 2006)

However, strong collimation restricts use to a single value of magnification. For repetitive tests, collimation may significantly improve contrast by reducing scatter.

3.3.1 Signal to noise ratio

The detectors respond to the X-rays that reach the detector FOV. However, there are instances where the distribution of intensities is not uniform even when there is no object between the source and the detector. "Quantum mottle" is the main source of noise in this case. It is defined as the statistical distribution of X-rays from the source, that is, the variance in the number of X-rays produces by the source per unit area. (Webb and Kagadis 2003)

The factors that can affect this noise are (Webb 2003):

- The exposure time and the tube X-ray current are linear with the noise;

- The kV_p, (defined as tube power rating) increase introduces the higher level of this noise;

- Filters may reduce the effect of noise since they can prevent some of the X-rays from reaching the detector;

- If the particle size is bigger, there is less chance for this noise to appear since the attenuation will be greater;

- Grid and intensifying screens can also improve this noise.
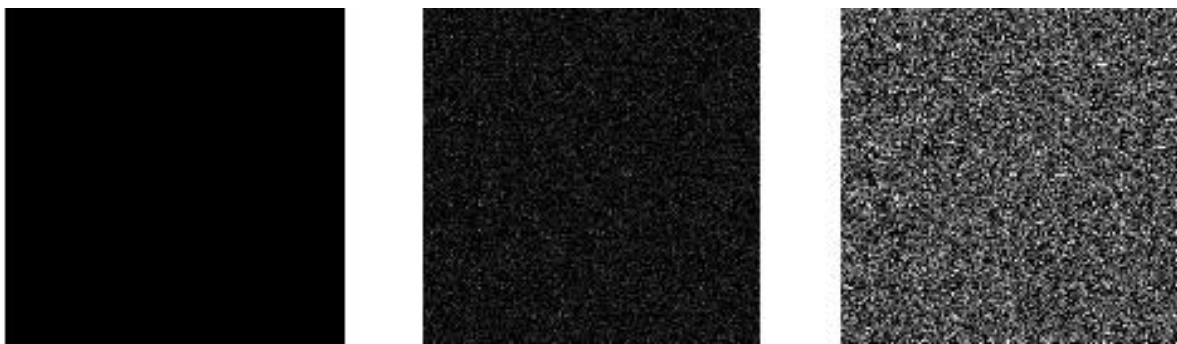
Figure 43: The "quantum mottle" effect increases from left to right, the source was believed to be uniform (Webb 2003)

130

3.3.2 Ring artefacts

As mentioned earlier, third generation X-ray detectors use fan geometry. The transmission measurement is given by Equation 45.

Equation 45 :

$$\ln(g_1 I_o / g_2 I_t) = \mu t$$

Where:

- g_1 is the gain of the reference detector;

- g_2 is the gain of the other detector;

- transmission measurement I_t.

Based on the Equation 45, we are able to conclude that if there is even a small imbalance between the detectors, so that $g_1 \neq g_2$, the µt values that are back-projected to produce the CT image are affected, causing the appearance of ring artefacts. (Bushberg et al. 2002) the ring is generated by the rotation of the sample or the detector.
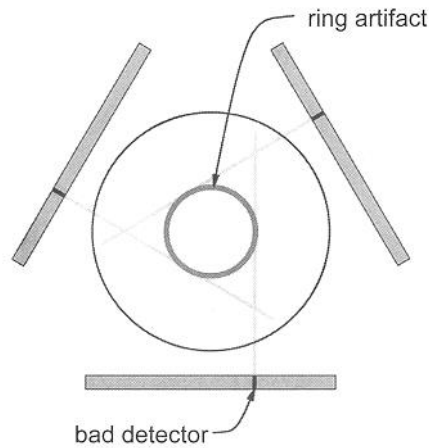
Figure 44: Image of detectors in third generation scanners. Each individual detector gives rise to an annulus (ring) of image information. When a detector becomes miscalibrated, the tainted data can lead to ring artefacts in the reconstructed image later. (Bushberg et al. 2002)

3.3.3 Beam hardening

Higher attenuation of some parts of the material scanned might be caused by photoelectric adsorption or by scattering.

As noted already, higher energy X-rays will penetrate through the particle better than the low-energy ones. Hence the low energy X-rays are more sensitive to density changes inside the particle, and it is common for these rays to be absorbed by the surface of each high density grain inside the particle. When this occurs, such a grain will appear less dense in the centre, and for this circumstance, we say that beam hardening has occurred.

Beam hardening is an artefact that is caused by the assumption that the X-ray beam is monochromatic. This is not realistic as there is a range of energy spread as discussed previously. Low energy X-rays are absorbed quickly as they reach the rock. This makes the mean energy of the remaining X-rays higher. Therefore there will be an increased proportion of the Compton effect in the centre of the mineral grain causing the edge to appear denser and the centre to appear less dense than it is.

This effect has been confirmed by many researchers. In the case of beam hardening, the mean energy associated with the exit spectrum is higher than the mean energy of the incident spectrum. (Avinash and Malcolm 1988; Prince and Links 2006; Webb 2003)
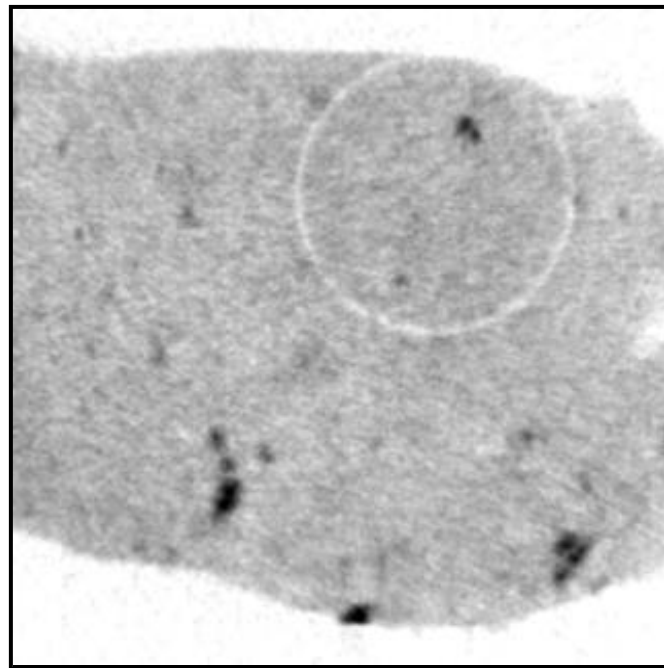
Figure 45: The example of ring artefact

There are ways to reduce the effect of beam hardening. One is to improve the reconstruction algorithm itself. The reconstruction software supplied with the SkyScan system provided the facility to set a beam hardening correction depth from 0% to 100%, with 0% being linear function to 100% being square function. However this algorithm is only adequate for materials between a density of 3-4 g/cm^3. The operator is also able to program a custom correction for beam hardening for use in the reconstruction process. In addition, there is a correlation that can help to reduce the ring artefact. A defect pixel would be the pixel which will have significantly different sensitivity from its neighbours. These defect pixels will be automatically detected by calculating the difference, and the limit for assigning the neighbours average level to the defect pixel. The processing of such artefacts may take considerable time. Therefore it is recommended to process only the slices with visible "hard" rings (SkyScan 2010b). More powerful computers allow greater correction and reduction of artefacts.

X-ray filters are another potential mean of improving image quality since they may pre-harden or post harden the beam before or after it penetrates through the particle. (Ketcham and Carlson 2001) Filtering reduces the spread of X-ray energies but one should be careful when using filters since they also reduce X-ray intensity. Examples of filters commonly used are copper, brass or aluminium and for the purpose of this research we have used post hardening by applying copper and aluminium filters. Based on the Figure 46, one can conclude that beam hardening appears to be an issue when the energy is lower. The same statement has been shown to be valid in similar work (Ketcham and Carlson 2001).
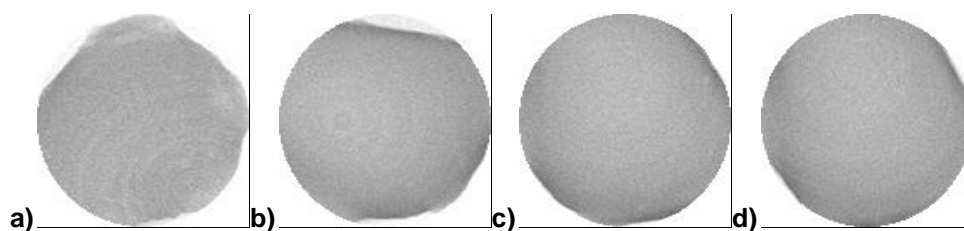
Figure 46: Cross section images, the same section of the particle scanned with different scanning properties: a) the highest energy and highest exposure time, post-hardening filters Cu and Al; b) 25% lower source than in a, post-hardening filters Cu and Al; c) highest source, pre-hardening SiO2 filter plus Cu and Al post-hardening filters; d) highest source, post-hardening filters Cu, Al and SiO2

Another theory that was tested was to introduce pure SiO_2 plates as filters. Please refer to the Figure 46, images a, c and d. The same scanning and reconstruction properties were applied in all three of those scans, with the difference in filters applied as well as their position during the scanning. It appears that SiO_2 filter had worsened the beam hardening effect, in both post-hardening and pre-hardening instances.

The shape of the scanned phase is also very important in considering beam hardening (Ketcham and Carlson 2001). If the particle or grain has a regular shape, it is easier for a human eye to detect the effect of beam hardening. However, if the shape is irregular, which is often the case in scanning mineral grains, it would be very hard to make the decision if the particle has variations itself or if it is demonstrating beam hardening. Consideration should also be made when applying this to multiple cross-sections.

3.3.4 Blurring

Blurring of edges is another common problem occurring in reconstructed images. In this case it is very important to select a threshold value that will represent the real properties of the minerals, such as shape, surface and volume of the mineral grains that are present in the particle. This topic was widely discussed also in medical research when assessing bone parameters in live patients and animals. (Hangartner 2005)
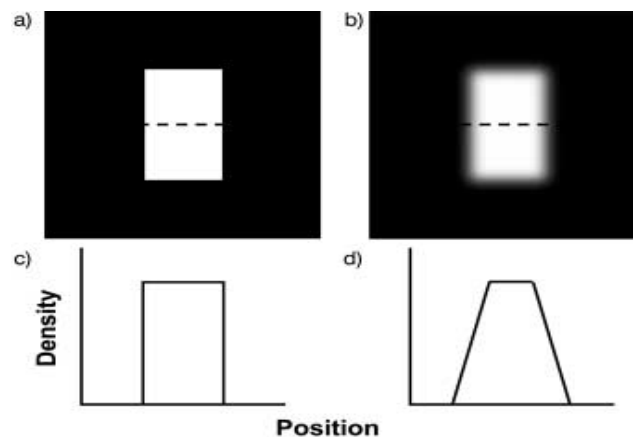
Figure 47: Simulation of blurring through imaging: a) original rectangular block to be imaged; b) imaged block with blurred edges; c) and d) profile along dashed line indicated in figure a) and b), respectively.(Hangartner 2005)

Figure 47 a shows an ideal cross sectional CT image of a rectangular block and image b is the same block image obtained in CT but with convolution with Gaussian convolution filter, which will then blur the image. The difference in profile cuts is presented in Figure 47, images c and d. It is obvious that the sharp edges of the block had turned into sloping edges. (Hangartner 2005)
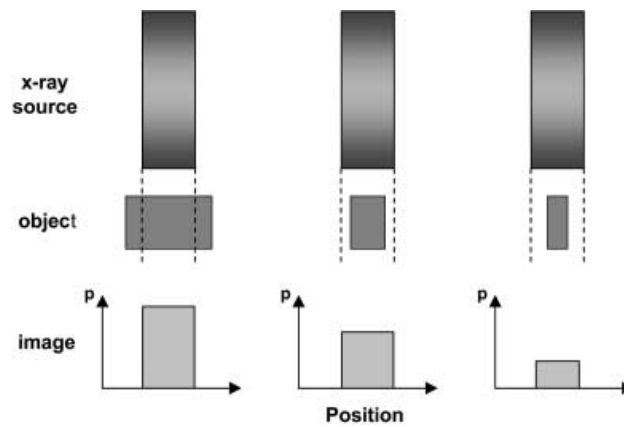
Figure 48: Illustration of recorded image values p in dependence of beam size and object size. An X-ray beam of a given size is imaging objects of gradually narrower widths (left to right). Objects that are smaller than the beam size (middle and right graphs) will not be recorded smaller than the beam size, but they will be recorded with a reduced image value.(Hangartner 2005)

One of the reasons for blurring the image is having the beam size much bigger than the object size. Any structure that is smaller than the beam size cannot be recorded as small as the beam size, as shown in Figure 48. Reconstruction algorithms and the finite resolution of the image matrix are other reasons for blurring of the image. (Hangartner 2005)

The blurring of the image is more apparent at the edge of the object. The distance between the source and the object and the object and the detector influences the blurring as well as the focal size of the beam and the object. The definition of the degree of blurring (penumbra, P) is given in Equation 46 and shown on Figure 49 .(Webb 2003)

Equation 46:

$$P = \frac{f(S_1 - S_0)}{S_0}$$

Where:

- P is the penumbra, the degree of blurring;

- f is the effective focal spot size of the source;

136

- S_0 is the distance between the X-ray source and the object;

- S_1 is the distance between the X-ray source and the detector.
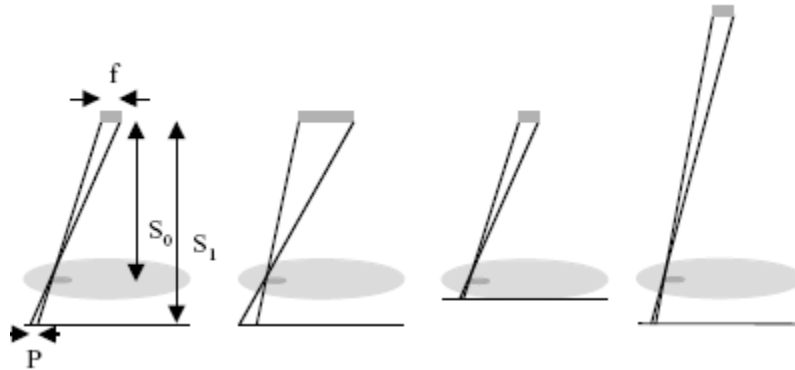
Figure 49: The source focal spot size and the distance between the source, object and detector and varying, demonstrating the degree of unsharpness (Webb 2003)

The blurring effect can be improved by setting the distance between the source and the detector as large as possible and the effective focal size as small as possible. (Webb 2003)

In the instrument used in this research (SkyScan1172), the detector is moves when adjusting the magnification, which improves the image and reduces the blurring effect where needed.

3.4 Image reconstruction

As mentioned in the previous section, detectors are measuring X-ray intensity, I_x. The unattenuated intensity of the X-ray beam is also measured during the scan by a reference detector and this detects an X-ray intensity I_o, the intensity of incident X-ray. For the monochromatic beam, the relationship between these two energies is given in Equation 47, where x is thickness of the object along the ray and μ is the average linear attenuation coefficient along the ray. While the energies highly depend on the machine, x and μ are obviously very dependent on the object of the interest. (Bushberg et al. 2002)

Equation 47

$$\ln(I_o / I_x) = \mu x$$

The above equation clearly states the importance of having rock as an object of interest. The density of the flesh and bones (approximately 1 g/cm^3) usually scanned in medical imaging is far less than the density of rocks (2.6 to +7 g/cm^3). Although the density of the image is independent of I_o, the noise present in them highly depends on I_o.

The process that is very important after the data is acquired is the production of cross section images by applying a reconstruction algorithm. Since these algorithms were developed for medical imaging, it is difficult to create a clear image of the rock that will essentially have less or no noise present. For more information on noise reduction in the X-ray images, please refer to section 3.3.1.

The filtered back projection reconstruction builds up the CT image in the computer by essentially reversing the acquisition steps. During this process, the µ value for each ray is smeared along the known path of a narrow X-ray beam in the image of the object. As expected, the large amount of collected attenuation data are back projected into the image matrix, where areas of high attenuation tend to reinforce each other, as well as low attenuation areas, leading to the construction of an image in the computer. (Bushberg et al. 2002)

The attenuation inside the rock is not as uniform as the reconstruction algorithm assumes, and it would be recommended to correct it in the reconstruction algorithm as the effective attenuation decreases with the increase of distance between from the X-ray source. Imbalances of the detectors need to be adjusted as well. (Webb 2003)
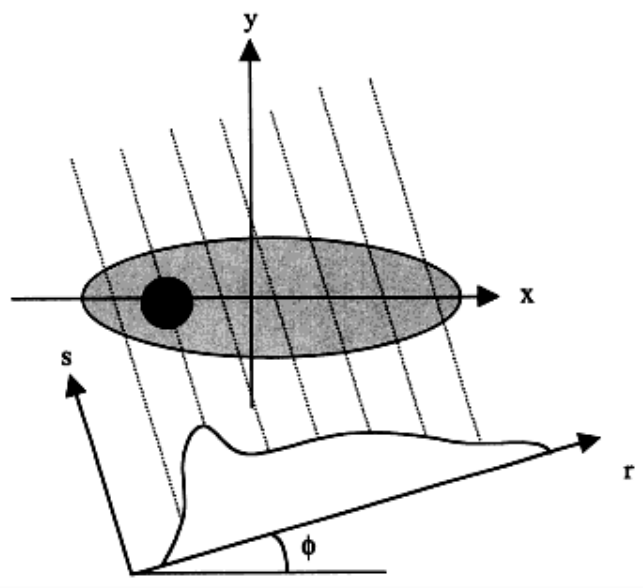
Figure 50: "The coordinate system used for analysing backprojection algorithms. Successive projections of the object are obtained with the detector aligned at different values of the angle Ø(Webb 2003)

Mathematically the object can be presented as a function f(x,y) given in :

Equation 47 (Webb 2003):

$$f(x,y) = \sum_{j=1}^{n} p(r, \emptyset_j) d\emptyset$$

where n is the number of projections. Algorithmic filters can be applied during reconstruction process in order to improve the image and the contrast to noise ratio.
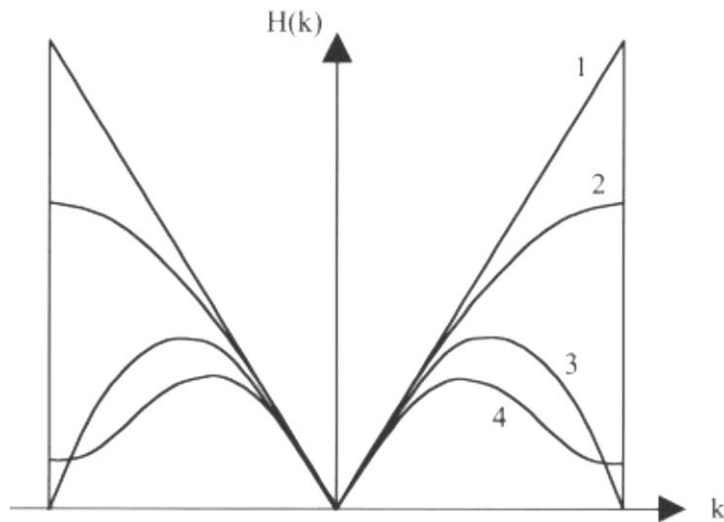
Figure 51: Some common filter functions used when solving backprojection algorithms. 1. Ram-Lak; 2. Shepp-Logan; 3. Low-pass cosine; and 4. Generalised Hamming. H(k) is filter function (after Webb)

3.5   The Instruments

Two X-ray instruments, SkyScan1072 and SkyScan1172, have been used to investigate the three dimensional data of the particles in this research. Each of these instruments was available at JKMRC. The instruments and their specifications are listed below (SkyScan1072 and SkyScan1172 manual supplied with the instruments and available online (SkyScan 2010b)).

a) SkyScan1072 - Desktop X-ray microtomograph (SkyScan 2010b)

- Spatial resolution of 5 μm corresponding to near $1\times10^{-7}mm^3$ voxel size.

- Operating conditions of 20-80 kV / 100 μA or 20-100kV / 0-250μA or 20-150kV / 0-500μA

- X-ray CCD-camera with 1024x1024 pixels resolution in a cooled CCD-sensor with fibre optic coupling (3.7:1 image reduction) to an X-ray scintillator or 768x560 pixels CCD-sensor with optical lens coupling to X-ray scintillator.

- 256 gradations (8 bit grey scale) for analogue camera.

- A typical cycle of data collects 200 to 400 views over 180 or 360 degrees of object rotation.

- The specimen holder with a diameter of 10-15mm can be used for the objects in a size range of 5 to 22mm (Figure 52).

Figure 52: Sample chamber, SkyScan1072 (SkyScan1072 Manual)

b) SkyScan1172 - Desktop X-ray microtomograph (SkyScan 2010b)

- X-ray camera options: high-performance 10 Megapixel (Mp), and the low resolution 1.3 Megapixel camera.

- Cooled CCD sensor with fibre optic coupling to the X-ray scintillator

- Image field width of 68mm (in dual image camera shift mode) or 35mm (in standard single camera image mode).

- A nominal resolution (pixel size) of lower than 1µm is attainable. The pixel size is isotropic and continuously variable from 0.9µm to 35µm.

141

- A scannable height of an object of around 70mm (in single projection).

- Operating conditions of 20-80 kV and 100 μA current while the source working at 20-100 kV and 0-250 μA with a 5µm spot size.

- For the 10Mp camera the X-ray shadow projections are digitized as 1000x575 to 8000x2300 pixels with 4096 brightness gradations (12 bit grey scale).

- The reconstructed cross sections have a 1000 x 1000 to 8000 x 8000 pixels (floating point) format.

Access to both instruments provided an opportunity to investigate the difference between the results obtained on similar samples.

In this study, a single sample was scanned many times to test the outputs of the two available machines. The properties of the particle scanned were as follows: size 14x6x7mm, mass 1.3226 g, volume 431.3mm^3 and density 3.067 g/cm^3. Note that the complete reproducibility test is provided in Chapter 4 while the experimental tests listed in Table 3 are comparing instrument outcomes only.

The SkyScan1072 had limited measurement options compared to the SkyScan1172 instrument. Test 1 and 2 with the first instrument shared similar properties to test 6 using the second instrument. All the other tests with SkyScan1172 were performed in other to generate additional information on system performance and more advanced capabilities compared to SkyScan1072, such as additional filter (copper), better resolution and pixel size.

Table 3: Operating conditions of the scan and reconstruction process

Operating Conditions	SkyScan1072		SkyScan1172					
	Test 01	Test 02	Test 01	Test 02	Test 03	Test 04	Test 05	Test 06
Source (kV/ μA)	74/104	74/104	74/104	100/100	74/104	74/104	74/104	74/104
Image pixel (μm)	16.659	16.659	8.73	14.84	14.84	16.659	16.659	16.06
Exposure time (ms)	4920	4920	885	1180	885	5015	5015	5015
filter	Al	Al	Al	Al+ Cu	Al + Cu	Al+ Cu	Al	Al
Recon. threshold values	0.0264-0.4090	0.0264-0.4090	0.026-0.4907	0.0-0.2483	0.0-0.2483	0.01344-0.2120	0.0067-0.2265	0.0064-0.2215
auto	0.01195 -0.5579	0.12007 -0.5603	0.0264-0.4907	0.007414 -0.3460	0.006768 -0.3159	0.006431 -0.3001	0.006431 -0.3001	0.006187 -0.2887
foam	Yes	Yes	No	No	No	No	No	Yes

The experiments with very similar operating conditions were test 01 for SkyScan1072 and test06 for SkyScan1172.

Figure 53 and Figure 54 show reconstructions using NRecon image analysis software which is used to perform the image reconstruction. This software interface includes a histogram of attenuation of the measured cross section of the particle on the right hand side of the processing window.

From the reconstructed two-dimensional images it is obvious that the image quality (noise, beam hardening effect and gangue definition) was better presented with the SkyScan1172. The observation of images revealed that SkyScan1072 reconstructed image had gangue areas missing and beam-hardening areas around high density mineral phase. The noise is also evident on the grayscale histogram where SkyScan1172 show a much tighter distributions of energy.
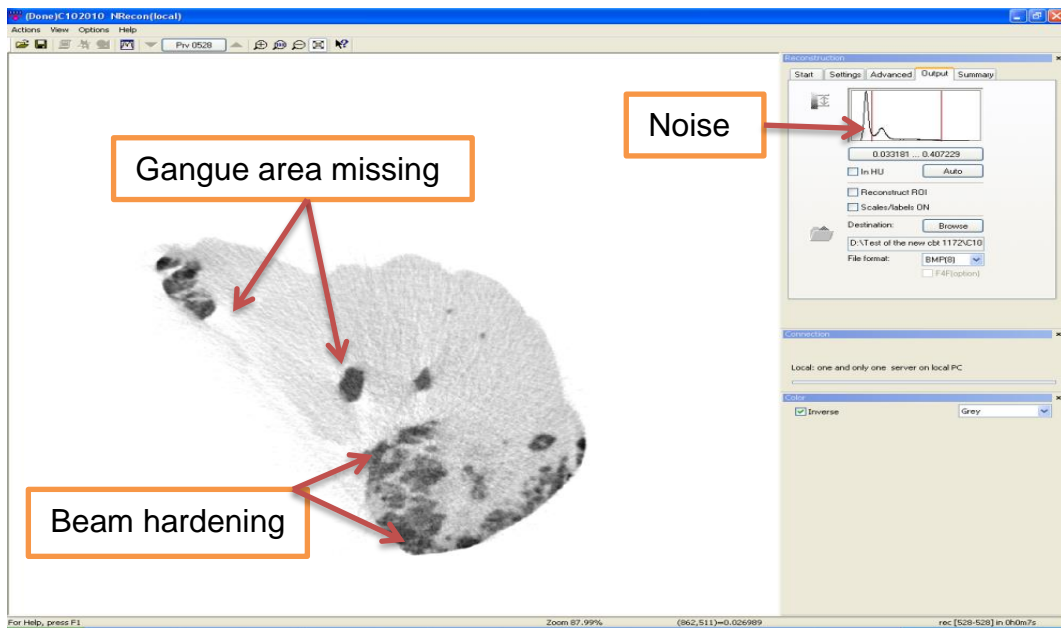
Figure 53: NRecon cross-section image for test01, SkyScan1072
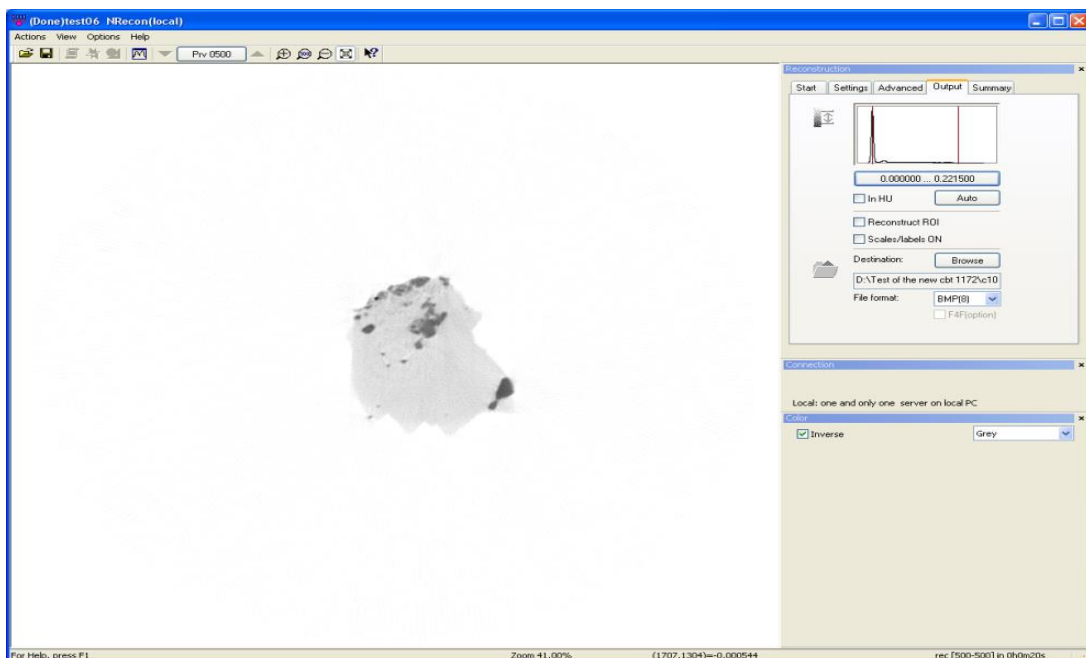
Figure 54: NRecon cross-section image for test 06, SkyScan1172

It was found that the SkyScan1072 was giving statistically similar results compared with the newer model (Table 4). The older instrument has difficulties with the quality of the images, which is understandable since the newer instrument provides the operator with better control of the acquisition parameters. Figure 60 shows some abnormalities of images analysed with SkyScan1072.

Table 4: Volumetric results of the experiments

test	measured		calculated			
	Heavy phase volume (%)	Total volume (mm^3)	Heavy phase mass (%)	Total mass (g) from Micro CBT	Density (g/cm3)	Density (g/cm^3)
1072test01	24.1	432	40.3	1.32	3.06	3.06
1072test02	24.1	432	40.4	1.32	3.05	3.05
1172test01	23.2	428	38.6	1.29	3.00	3.00
1172test02	22.3	433	37.5	1.29	2.98	2.98
1172test03	23.7	429	39.4	1.30	3.02	3.02
1172test04	23.9	434	40.0	1.32	3.05	3.05
1172test05	25.1	438	41.6	1.49	3.08	3.08
1172test06	22.5	430	37.6	1.29	2.99	2.99

The exposure time of around 1 second used in these tests was not long enough to provide adequate contrast between mineral phases. The application of both Cu and Al filters during the acquisition stage was very helpful in removing noise, which was obvious in all scans conducted in the SkyScan1172. The results with improvement are given in section 3.6.2.6, 4.2.1.2 and 4.2.1.3.

3.6 Image analysis software

3.6.1 CTAn

A computer program supplied with the system, CT Analyser image analysis software (or CTAn) (SkyScan 2010b), version 1.10.1.0, was used for analysing the SkyScan reconstructed images. This platform is used to present two-dimensional reconstructed images in three dimensions and can also provide quantitative parameters of the visualised objects. However, the disadvantage of this software is the lack of control of ring artefacts in the reconstructed particle data. The software uses manual settings for thresholding in the segmentation process which introduces operator error in quantitative analysis. For mineral applications these errors may be quite significant.

Even if there is a calibration sample of known density in the same image, it would be quite time consuming to select the area of interest manually and apply different settings to it. An example of this is shown in Figure 55.
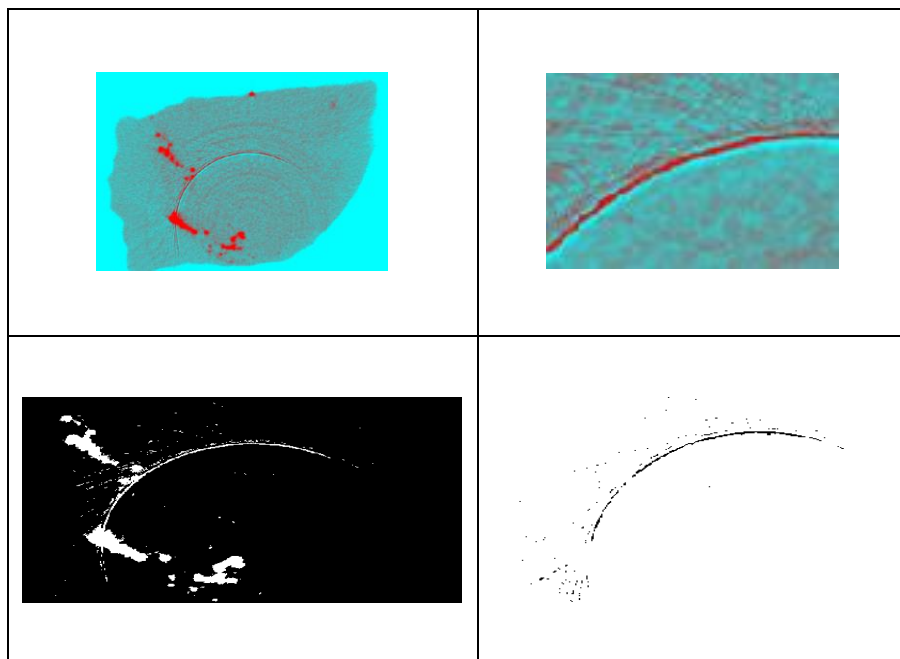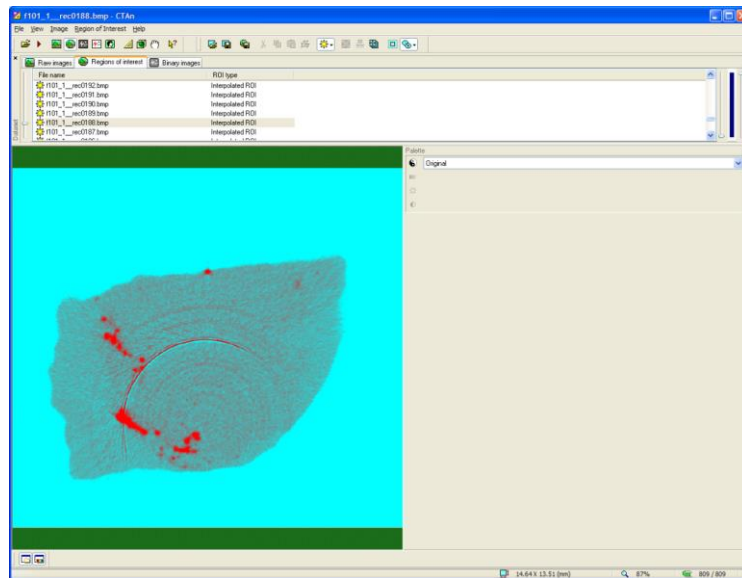
Figure 55: CTAn platform, the software view window, a single cross section of the particle with the presence of ring artefact in colour, selected as bitmap thresholding minerals vs gangue on the left image; thresholding gangue vs background on the right image.

It is difficult, if not impossible to exclude the ring artefact from quantitative measurement in this case. The ring will be selected as mineral phase since its greyscale level is very similar to the greyscale level of the mineral. This is not the only issue here. There is also an area with no grey level assigned to it; this is the area in the immediate contact with the ring. This area will be classified as a background area since its greyscale level is the same as the air.

From the facts above, it is quite clear that quantitative analysis in this case will not provide appropriate results. This platform may be used for binary ores, with known greyscale levels and whose image is clear of any noise. In that case, the analysis should be quick and accurate.

3.6.2 eCognition

3.6.2.1Introduction

Trimble eCognition (previously Definiens) is a software package with multidimensional image analysis applications which can be developed and executed. Explanations of all algorithms applied in process are provided in the Definiens Reference Book (eCognition 2008). Hartner (2012) used eCognition to integrate DOM and SEM images for better understanding and optimisation of geometallurgical modelling and ore deposit characterisation. Evans et al. (2013) used eCognition as part of the workflow for analysing mineral grain size distribution in 3D.

In this work, eCognition version 8 (eCognition8) has been used to analyse X-ray micro tomography images.

The challenge here was to implement an appropriate image analysis procedure (termed a rule set or a process tree) that will be able to provide quantitative mineral data by removing any noise present in the images and by reducing human error in setting the threshold values. Such an improvement of the image analysis process is possible, but variations are necessary for different rocks. The level of variations will depend on the mineral composition of the rocks. For example, if the rock is multi-component, and the combined mineral percentage is high, this will usually lead to higher noise in the images. It is very important to understand the images and to have a project objective before developing a rule set.

During the import of two dimensional reconstructed images into eCognition, a suitable "dsif" file (eCognition combined file) is created inside the workspace folder. This file is used for importing multidimensional image data sets which are represented as a large two-dimensional internal map. The main steps that have to be followed here are segmentation, classification, connection of 2D objects into 3D, and at the end obtaining the required mineral data such as the volume of each individual phase in three dimensions.

3.6.2.2 Rule set structure and purpose

For given variable values (for example known pixel size) and defined image maps, the rule set can remove the background around the rock. The samples that were scanned in this project were usually mounted in Styrofoam, which acts as a filter for many low energy X-rays and does not provide any noise as the air would give around a dense object scanned in an X-ray micro tomography machine. There were occasionally some exceptions where the samples were set in a tube. It is recommended to reduce the resolution when image cleaning process is executed since this may considerably reduce the processing time. When the rock is isolated from the background area, the rule set can focus on segmenting the mineral phases within the rock.

A very important stage in the analysis is filtering, which helped to improve the quality of the images. In some cases, a Gaussian filter was used, which is part of image layer operation algorithms as convolution filter. A convolution filter uses a kernel, with user-defined size values, in this case 7x7x3. Values are defined as pixels. Each pixel value is replaced by the average of the square area of the matrix centred on the pixel. (Trimble 2008)

Equation 49: Gaussian Function (Gauss 1828)

$$f(x) = ae^{-(\frac{(x-b)^2}{2c^2})}$$

where a>0, b, c>0 are real constants and:

Equation 50:

$$a = \frac{1}{\sigma\sqrt{2\pi}}$$

b = μ and c=σ

and σ is standard deviation of distribution.
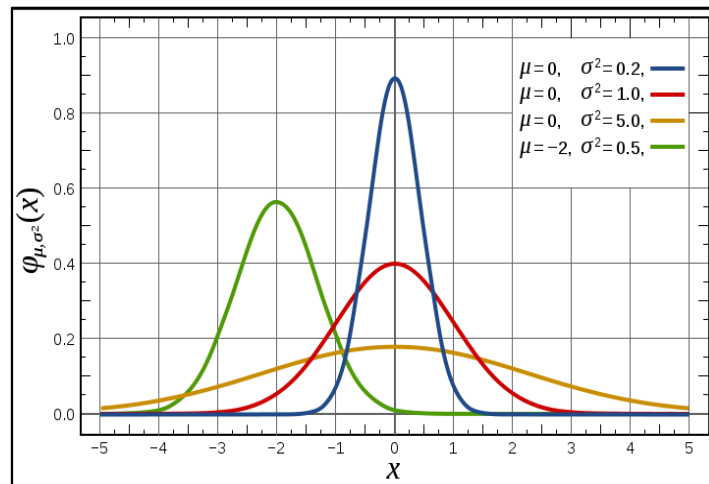
Figure 56:Normalised Gaussian curves with expected value μ and variance σ² (Gauss 1828)

The graph of a Gaussian (Figure 56) is a characteristic symmetric "bell curve" shape that quickly falls off towards plus or minus infinity. The parameter a is the height of the curve's peak, b is the position of the centre of the peak, and c controls the width of the "bell". The two-dimensional Gaussian function is commonly used in image analysis with variation of two separate dimensions as well as rotations. A graph of the Gaussian blur function with the two dimensional domain is shown in Figure 64. The function used in Definiens XD is one-dimensional function with a mean value of zero.

A Gaussian function in one dimension is the probability density function of the normal distribution where in two dimensions the curve is a function of circular Gaussian function is the distribution function for uncorrelated variables X and Y having a bivariate normal distribution and equal standard deviation. If the standard deviations are not equal, the function is then elliptical:

Equation 51: Two-dimensional elliptical Gaussian function (Gauss 1828):

$$f(x, y) = Ae^{-\left(\frac{(x-x_0)^2}{2\sigma_x^2} + \frac{(y-y_0)^2}{2\sigma_y^2}\right)}$$

where:

- coefficient A is the amplitude, $A = \frac{1}{2\pi\sigma_x\sigma_y}$;

- (x_o, y_o) is the centre of the equal area positioned on the pixel, $x_0 = \mu_x$ and $y_0 = \mu_y$;

- σ_x, σ_y are the *x* and *y* spread of the blob.
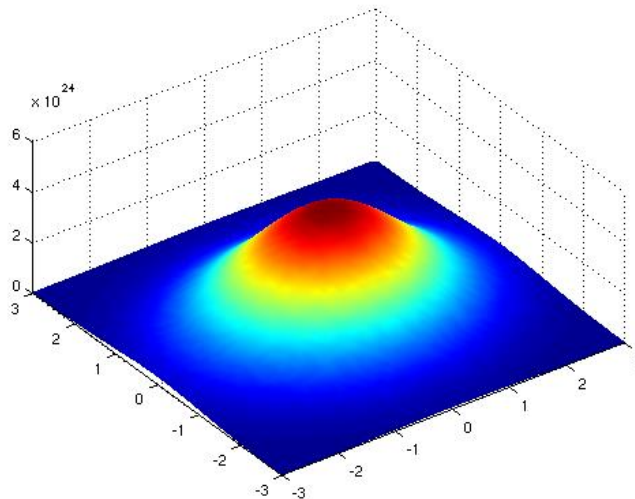
Figure 57: Gaussian function with 2-dimensional domain, where *A* = 1, *x*$_o$ = 0, *y*$_o$ = 0, *σ*$_x$ = *σ*$_y$ = 1 (Gauss 1828)

By using the automatic threshold algorithm during the segmentation process, the rule set can eliminate human error associated with a personal decision for grey scale values of different mineral phases.

Segmentation algorithms are used to subdivide the entire image represented by the pixel level domain or specific image objects from other domains into smaller image objects.

(eCognition 2008) Multi-threshold segmentation is appropriate for segmenting SkyScan images, when user defined threshold values are used for segmenting image. Here we are able to restrict the values of grey scale to be considered.
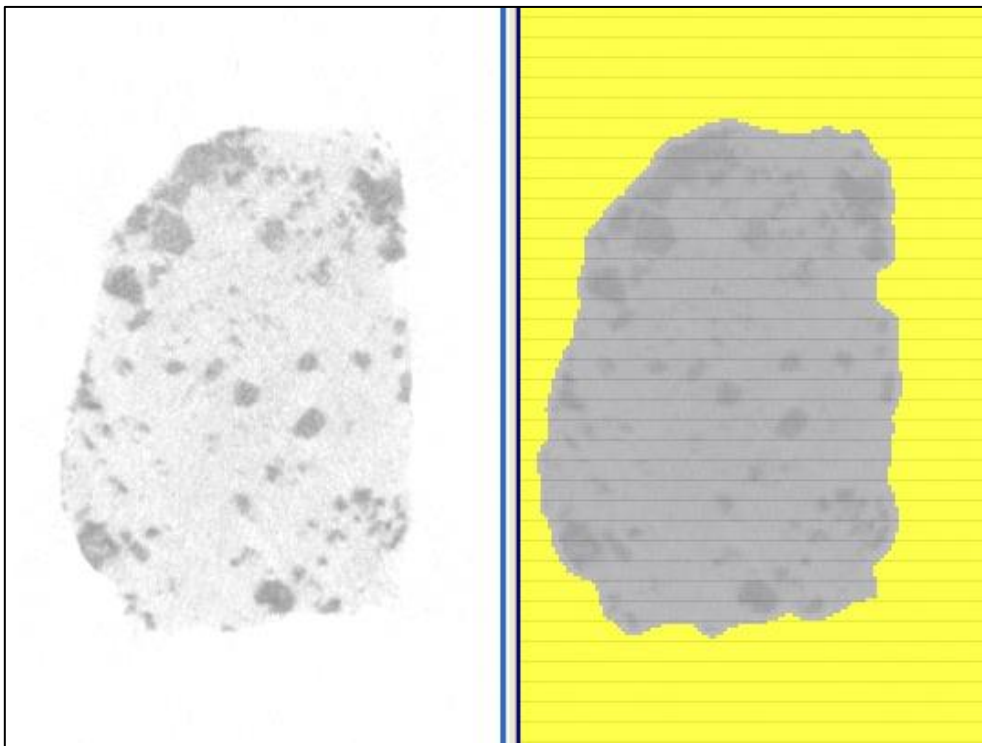
Figure 58: Left image is the main map; right image is reduced resolution map with classified estimated rock area (horizontal lines function of eCognition display and not image feature)

For the purpose of removing the background that is incorrectly classified as rock, an algorithm for shrinking the particle may be found useful. Pixel-based object resizing will add or remove pixels/voxels according to the user defined criteria. Application of the algorithm is shown in Figure 58.

Usually, the "relative area of classified objects" feature is used to find suitable seed image objects. Hence, this algorithm can be used for smoothing the surface of image objects by growing or shrinking in one, two or three dimensions. During the shrinking process, the object is reduced in size by producing coat inside the image object. The operator decides on the coat classification based on the pixels/voxels information. In this case, the coat includes the noise of the image, and will be classified as background. (Figure 59)
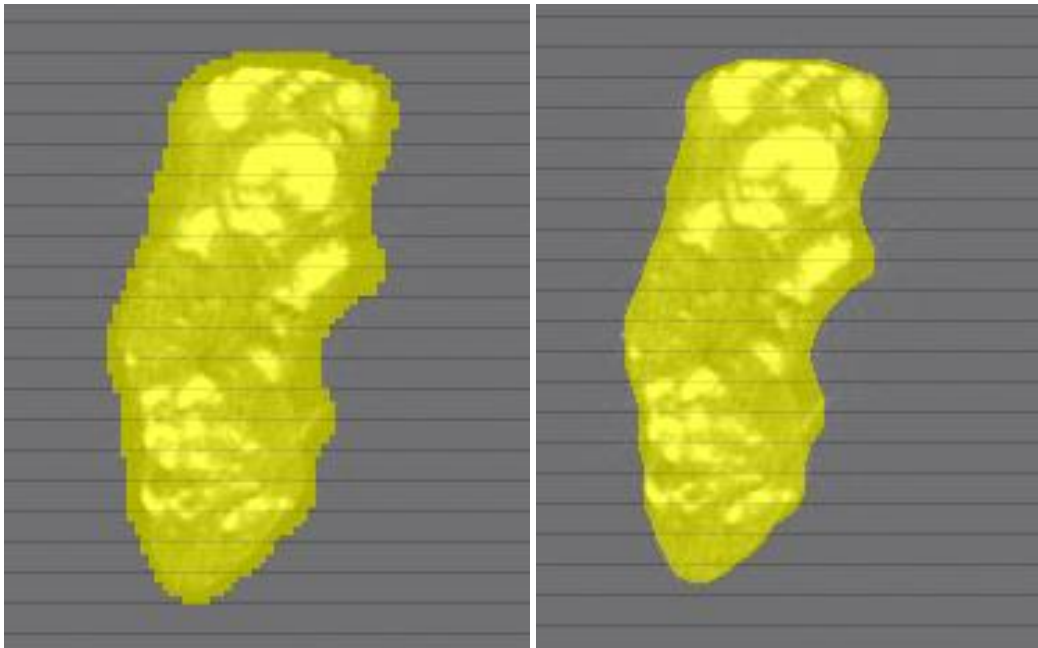
Figure 59: Rock area before shrinking (left) and after background growing (right)

The existing growing area algorithm may be one of the significant rule set components, where the particle or mineral phase boundaries are set for growing. To make sure that the growing of the objects is applied evenly, the value for growing step in vertical z direction is set in a way that it is equal to a ratio of growing steps in x and y direction and voxel dimension. In practice, this means that the background will grow into rock, in all three dimensions equally. Rock area will become background if its mean brightness value is equal or less than the updated absolute automatic rock greyscale value.

The "Candidate surface tension" option is commonly used for smoothing the border of a resized object. Surface tension uses the relative area of classified objects. Figure 60 is provides one example of calculation of relative area. In the tomography image analysis presented here, this means, that the area that has been classified as a rock but has mean brightness value less than 40% of the automatically measured brightness value of rock will be classified as background. Following this, gangue with relative area in background region greater than 0.33 will be classified as background and the balance growing in 3 dimensions will be applied.

The area calculation method is shown in Figure 60.

Class	Area of classified objects	Relative area of classified objects
	11 pixels	$11/25 = 0.44$
	10 pixels	$10/25 = 0.4$
	4 pixels	$4/25 = 0.16$
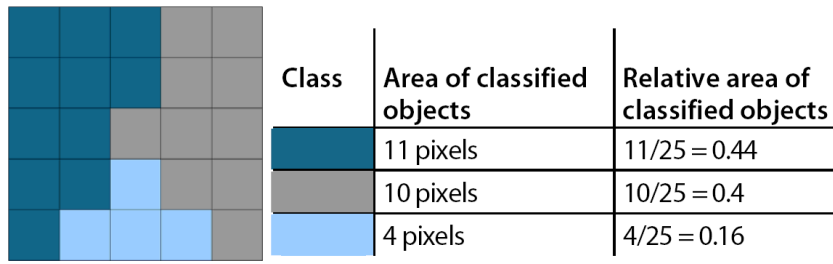
Figure 60: Schematic display of the Relative area of a class within a two dimensional region (eCognition 2008)

3.6.2.3 Classification of mineral phases
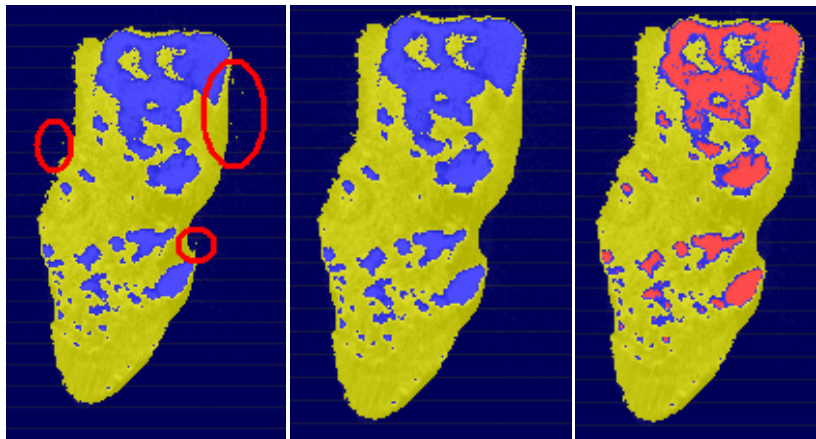
Figure 61: Classifying of minerals, noise removal and high density phase classification (yellow phase is low dense phase; blue and red are high density phase)

The usual approach in this Thesis was to use automatic threshold values for magnetite and chalcopyrite classification. The results of the classification are shown in Figure 61 and in Figure 62. If any ring artefacts were present, they would be removed manually in a short period of time, by changing classification of the phases that had been misinterpreted.
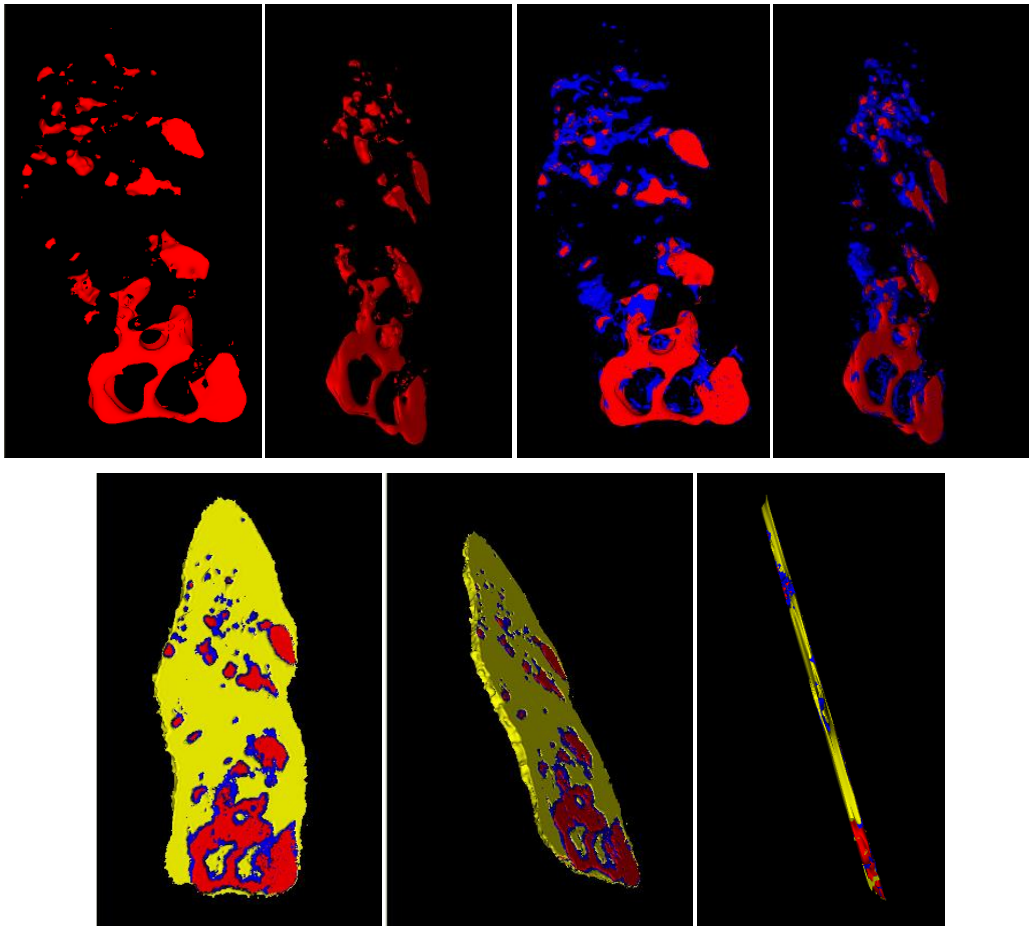
Figure 62: Three dimensional images of the grains, the thickness is 10 pixels (yellow phase is low dense phase; blue and red are high density phase)

3.6.2.4eCognition image analysis conclusion

Once the algorithms in the software are understood together with the mathematical principles built into these algorithms which are appropriate for analysis of tomography images, the process of obtaining the quantitative mineral data from the analysis becomes reasonably straightforward. Chapter 4 shows that the volume of the particles is well correlated with the volume measured in wet/dry analysis of binary particles.

eCognition software was found to be very useful for removing noise around the particle and within the particle as well. It is convenient to apply a rule set to obtain the correct volume of the particle without losing any of the internal data points, which might be lost in CTAn. CTAn allows the user to manually draw the rock border. As the particles usually

have about one thousand cross sectional images, this manual procedure would be very time consuming and impractical. The manual adjustment option is also available in eCognition and was found to be useful in images with touching mineral grains that had to be separated.

In eCognition, mineral greyscale threshold values can be calculated automatically based on histograms, but can also be user defined. However, in CTAn these values are always user defined and therefore it is quite likely that error in these analyses will be greater due to operator error.

3.6.3 Other image analysis programs (Image J + Blob3D)

For various research investigation purposes a program called Image J, version 1.40g was used (Rasband 2010). This image analysis freeware is well known. It has a worldwide community of users since it is in the public domain and is very user-friendly. The platform is built in the way that provides the user with the possibility of using various filters already provided or perhaps building a new filter for a particular case.

"Blob3D" is an image analysis program which may be used for image analysis in three dimensional spaces (Ketcham 2005). Here it was applied for noise removal during the testing stage only. There is also the problem of separating touching mineral crystals in image analysis, and a number of researchers have encountered this problem. Some of them have used data reduction section to remove the area around the crystals and then apply separation process. During the process of erosion, the shape of the crystal may be lost and then the assumption is to be made for this shape to be rebuilt. This may well introduce another error into the measurement as addition to the grey scale level error (Jerram and Higgins 2007; Ketcham 2005; Ketcham and Iturrino 2005). Since Blob3D was not in the public domain and it was at a stage of development when three dimensional

analyses are considered, the decision was made to use another image analysis platform for this research.

3.7 Optimal operating conditions

3.7.1 Overview

A significant improvement in the quality of three dimensional images of the rocks was made possible by manipulating major variables in three areas: image acquisition, refinement and analysis. Even though mineral identification is possible based on grey scale levels in images, errors are introduced by the various artefacts present in tomography images. In order to reduce these effects there are a number of different techniques which can be used to minimise the problems. Freeware "Image J", SEM-based image analysis and eCognition8 software are some of the useful tools.

At the beginning of the acquisition it was necessary to use systematic initial steps that would identify the effect of individual variables on the overall image quality. By doing this it was possible to isolate the individual factors and evaluate their contribution to the image. The operator may reduce or remove some of these effects by changing the operating conditions and controlling them with the tools provided with the machine.

Current observations indicate that rotation step, exposure time, filters and filament current used in scanning can considerably influence the quality of the image. The tools considered here are aluminium and copper post-hardening filters, silica and Styrofoam post-hardening and pre-hardening filters, rotation step, exposure time and sample holder properties. Those properties are controlled by the operator and thus may be modified.

Thereafter, image quality is influenced by a number of effects which are not able to be optimised by the operator, for example rock properties. If particles a few millimetres in size with a high content of a dense component are being scanned, it is highly possible that

the image will exhibit noise due to the high density minerals present. Noise in acquisition can be reduced considerably by applying the previously mentioned acquisition and analysis technique. Images of the internal structure of the particles were successfully acquired in this work. These included images of all mineral grains that were present.

Perspex containers and Styrofoam of different diameters were used as sample holders during the acquisition stage. The rocks were than subjected to 3-dimensional image acquisition process in the SkyScan1172.

The second area addressed was improvement of the reconstruction process. A series of investigations was completed with the various mathematical filters. Using these filters reduces distortions.

Finally, the last process was to investigate several software packages for image analysis. These were CTAn (SkyScan 2010b), Mineral Liberation Analyser (MLA)(Burrows and Gu 2006b; Fandrich et al. 2006; Gu 2003, 2004), ImageJ (Rasband 2011), Blob 3D (Department of Geological Sciences 2004; Ketcham 2005) and eCognition8 (Marpu et al. 2006).

The aim here is to minimise, and if possible eliminate the noise in the images. The limits of currently available techniques are estimation of two dimensions of the particles. The improvement of a novel 3-dimensional measurement technique is an integral component of the analysis of the rocks and will allow measurement of the complete internal structure of the multiphase particles. By using the following technique, one can define systematic methods that will be reproduced when dealing with multiphase particles that consist primarily of magnetite, chalcopyrite and quartz type minerals. However, the process may be adjusted to suit other mineral suites (ore types) as well.

3.7.2 Experimental Method

One of the major fields in the 3-dimensional analysis of rocks with Micro-Cone Beam tomography is the reduction of the noise present in the image due to the assumption of monochromatic beam of X-rays. In order to reconstruct a high quality image that will describe the internal structure of the particles it is necessary to identify the factors that could influence the image.

Artefacts in reconstruction may seriously degrade the quality of the image. There is a need to understand the appearance of artefacts so that they can be suppressed or prevented. On the other hand, the perception of the image quality is very subjective and depends on the information being obtained from the image.

The data given in this section was part of the collaboration work with Ion Gurnett, and some of the data were presented in Ion Gurnett's Undergraduate Thesis (Gurnett 2009).

3.7.2.1 Operating Conditions and image refinement

The measurement in the search for optimal operating conditions for finer particulate material was conducted in the high resolution system within SkyScan-1172 X-ray CT scanner. The instrument was operated under a range of conditions. Nine different size fractions were tested where -2.8mm + 2.4mm was the coarsest one. Cross sectional images of some of the measured particles are shown in Figure 63. The particles were subjected to density fractionation by placing them in a separating funnel with LST (Lithium Heteropolytungstate, of density of 2.75-2.8 g/cm^3) where they were separated into two classes, sinks and floats based on their behaviour in the solution.

Figure 63: Sample A, parent particle (13mm); progeny particles float and progeny particles sink (-2.8mm + 2.4mm)

3.7.2.2 Data Acquisition

Tests were performed in which the voltage was varied with a relatively small exposure time. Once the appropriate voltage level was found, where the required penetration of the particle was reached, a set of tests varying the exposure time were performed. Once the exposure time and voltage had been calibrated, it was decided to optimise the image. This involved various experiments in which the other operating properties were changed. For practical reasons there is a need to compromise between the acquisition and image analysis time and the quality and precision of the image. The ranges of variation for each of the operating conditions are (Gurnett 2009):

- voltage from 65kV to 98kV;

- exposure time from 1.5s to 3.9s with frame averaging;

- rotation step from 0.45 to 1.7 degrees;

- addition of water to the sample holder during the scan;

- with and without filters;

- variation of Perspex tube size from 2mm to 6mm in diameter.

160

The acquisition process in SkyScan1172 has an option to average a number of frames specified by the operator in order to obtain a clearer image. It allows improvement of the image quality by averaging several image frames in every angular position. Increasing the number of frames adds to the quality of the images but also increases the acquisition time.

The purpose of adding water into the sample holder is to decrease the degree of change in density as the X-rays travel through the sample. X-ray filters were also considered as a possible way of improving image quality since they can be used to pre-harden or post harden the beam before or after it penetrates through the particle. (Ketcham and Carlson 2001) Filtering reduces the spread of X-ray energies but care should be taken when using filters since they will also reduce the intensity of X-rays. Examples of commonly used filters are copper or aluminium and for the purpose of this research post hardening filters of copper and aluminium were used.

3.7.2.3 Image reconstruction

CT Image reconstruction gives representative information about the inner image of the particle by measuring or estimating the X-ray attenuation coefficient over the entire cross-section. A series of tests and investigations into mathematical software were conducted on the reconstructed images to define an automated image correction process to provide an additional degree of accuracy on the previously acquired images. This was done in order to achieve realistic and correct characterisation of the mineral groups as CBT does not produce images with as clear contrast as back scattered electron (BSE) in a scanning electron microscope (SEM).

In principle, there are further ways to reduce the effect of beam hardening. One of them would be to improve the reconstruction algorithm itself. The NRecon reconstruction software provides an option to set the beam hardening correction depth from 0% to 100%, with 0% being linear function to 100% being square function (Figure 64). However, this algorithm is only adequate for materials up to a density of 3-4 g/cm^3(SkyScan 2010b).

NRecon also allows the user to generate a code for beam hardening and apply it during the reconstruction process.
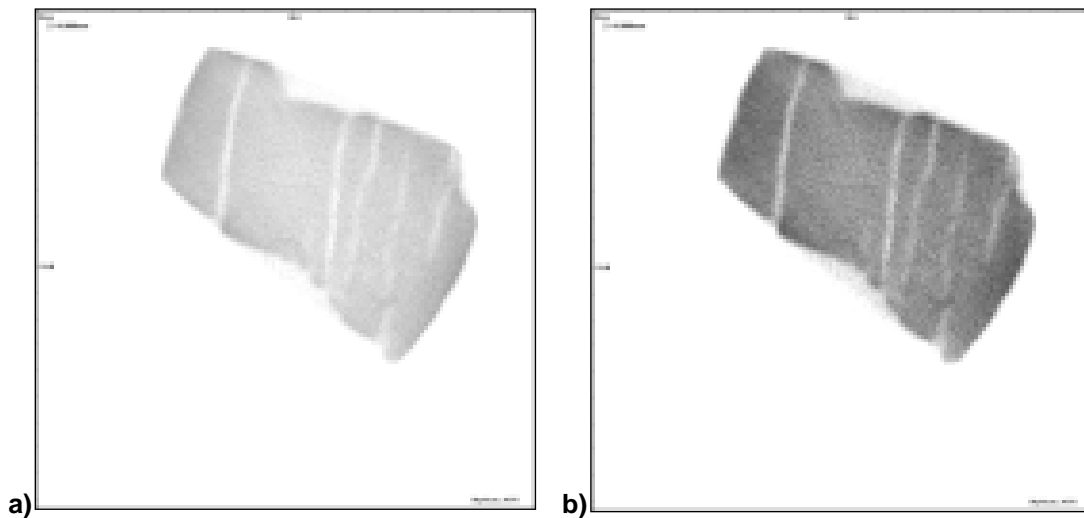
Figure 64: a) beam hardening correction 10% and no ring artefact correction; b) beam hardening correction 61% and ring artefact correction 5

3.7.2.4 Image analysis

Image analysis included processing of the data through various software packages from the refined image (CTAn, eCognition, ImageJ, Blob3D). Full quantification of the volume and the size of the mineral grains was performed during this stage. A series of tests were run within this field by checking the effects of the 'image refinement' processes. This process was highly dependent on comparing the calculated particle density based on the mineral content measured in the images to the sample density to determine the accuracy of the complete process.(Gurnett 2009)

3.7.2.5 Optimisation Outcomes

Accumulation of various cross section images of the particles, some of them being presented in Figure 65 and Figure 66, has proven that the optimisation process performed here was successful.

The volumetric three-dimensional information obtained from the experiments mentioned in section 3.7.2.2 has proven the assumption that the use of low energy X-rays would lead to loss of information. (Gurnett 2009)
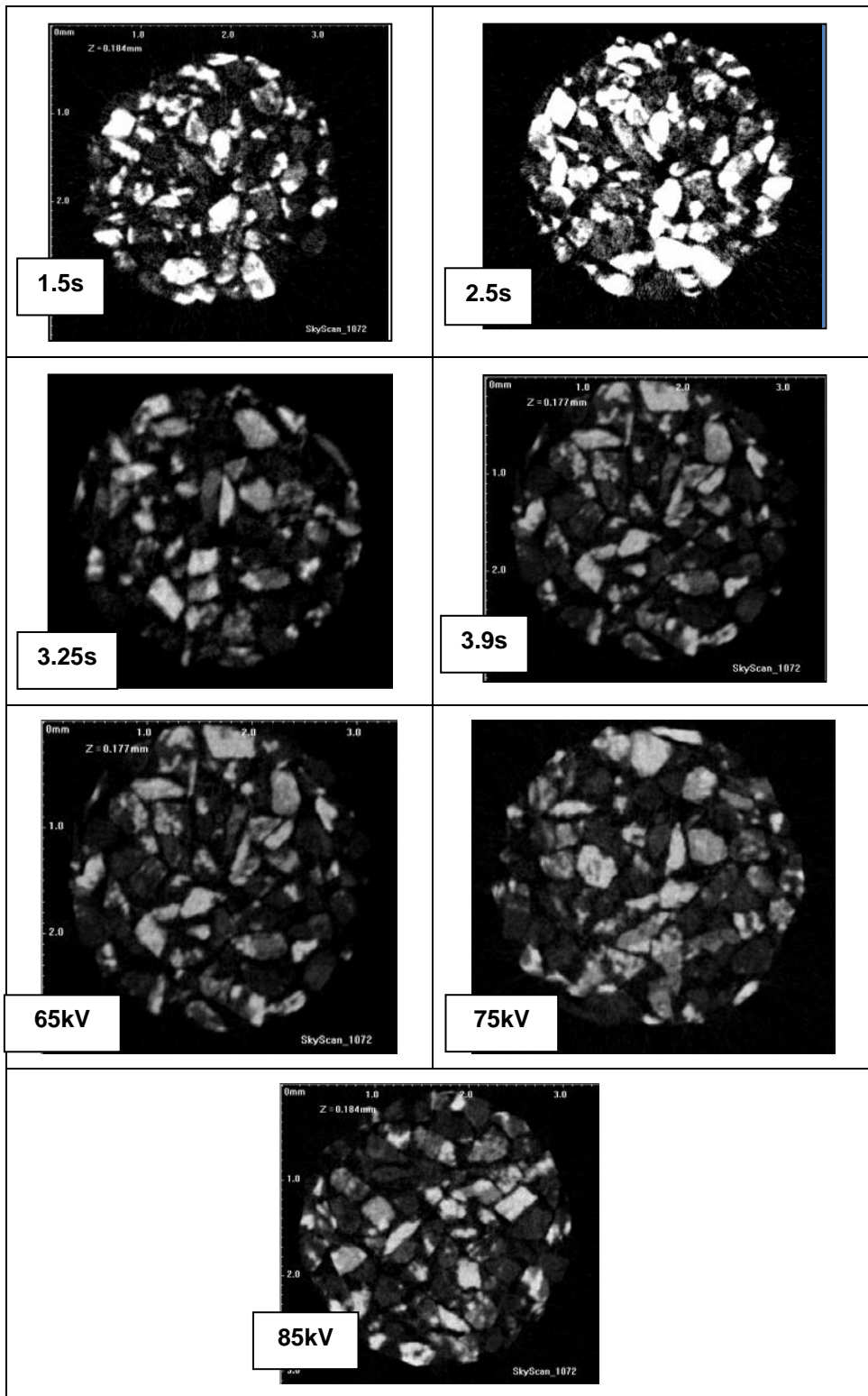
Figure 65: a) Variation of the exposure time 1.5s; 2.5s; 3.25 s and 3.9s. b) Variation of the voltage: 65kV, 75 kV and 85kV (Gurnett 2009)

Figure 65, (a), clearly shows the loss of internal grain information of the particles. As the energy is increased, the internal information improves considerably. Hence we are able to measure the total volume of the particles scanned with an exposure time of 3.9 s. However, we note that this would have to change if the source voltage was changed. Figure 65 (b) shows the images representing variations in source level during the scan process. It is apparent the best results are obtained with 85 kV, where the grain boundaries are clearly delineated and the noise is almost removed completely. (Gurnett 2009)
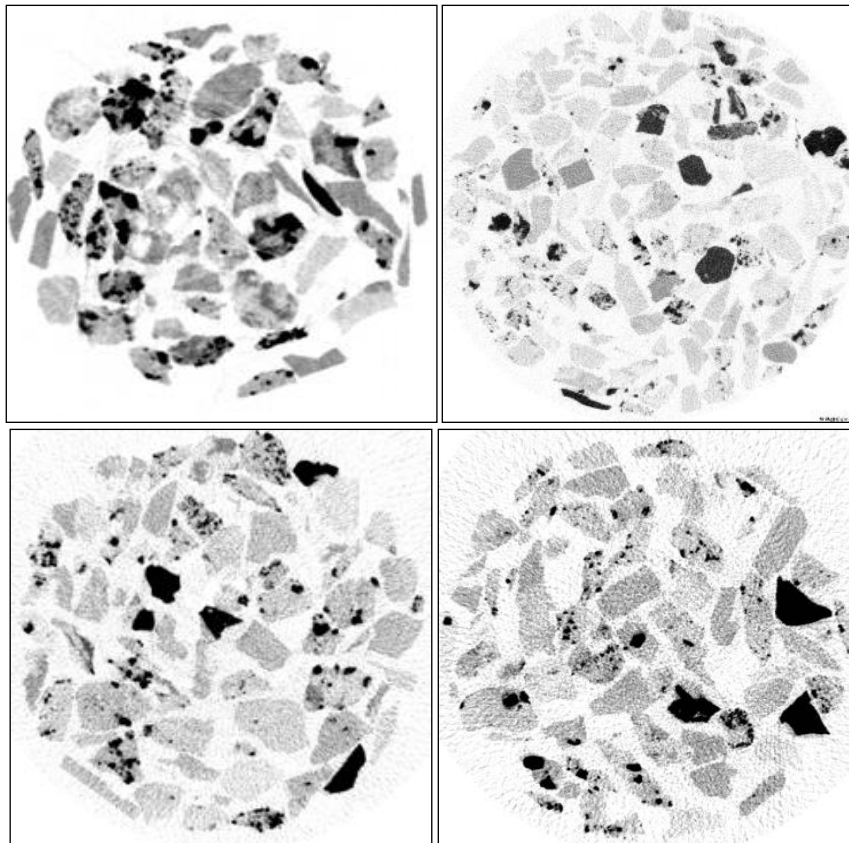
Figure 66: Variation of the rotation step: 0.45, 0.9, 1.35 and 1.7 degrees (Gurnett 2009)

The variation of rotation steps during the scans helped to identify the optimum scanning time considering the quality of the images and the acquisition and analysis time as well. As Figure 66 shows the clearest and highest contrast results are obtained with 0.45 degrees of rotation. It is worth noting that, for this research purposes, there is not a huge difference in the results between this scanning rotation and 0.9 degrees rotation, and considering the doubling in acquisition and analysis time with the smaller rotation step, the decision was to

continue with 0.9 degrees steps in the future scans. The larger rotation steps were not considered as the loss of internal information was higher than acceptable.(Gurnett 2009)

Additionally the routine scans were repeated to test filters of various types in various positions. The outcomes have been discussed in section 3.3.3.

3.7.2.6 Refinement

Testing of the various reconstruction software packages became useful when the optimum acquisition settings were established. The refinement stage of the process was very important as it may reduce the effect artefacts are having on the data quality. The effects of various algorithmic filters were revealed during reconstruction.

When actual data were processed, the removal of noise was not overly successful at this refinement stage. The particle gained volume when the filters were applied, as the initial volume was $7386.07mm^3$ compared with the volume measured when the filters were applied $8161.19mm^3$.

However, some of the difference in volume shown here comes from the threshold set up within CTAn, where the volume is calculated based on the manual greyscale threshold setting of the operator (Figure 67 (b)).

During the segmentation process, if the threshold is set too low (Figure 67a), some parts of the internal structure of the particle were turned into area similar to the area which surrounds particle, thus it will be counted as the air. Hence, the greater problem here is the removal of the internal information which will lead to the significant loss of volume and inaccuracy of the results. A similar issue was discussed in section 3.6.1.
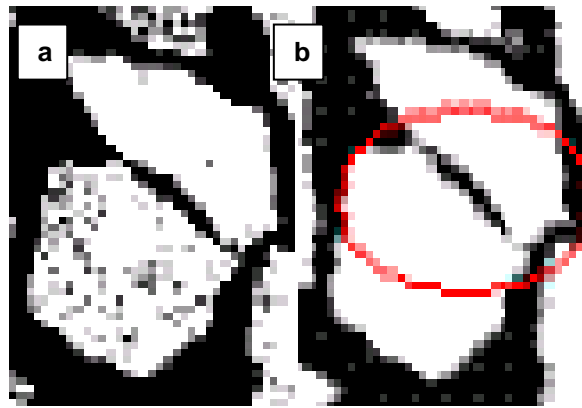
Figure 67: Image in CTAn threshold value set low and high respectively

Indeed quantifying the effect of filters in the noise reduction process is not an easy task. Some example profile lines across the filtered and non-filtered images are given in Figure 68. The quality of the image was improved by implementing some of the filters supplied with the ImageJ freeware. A similar improvement was noted when the images were filtered within eCognition 8.(Gurnett 2009)
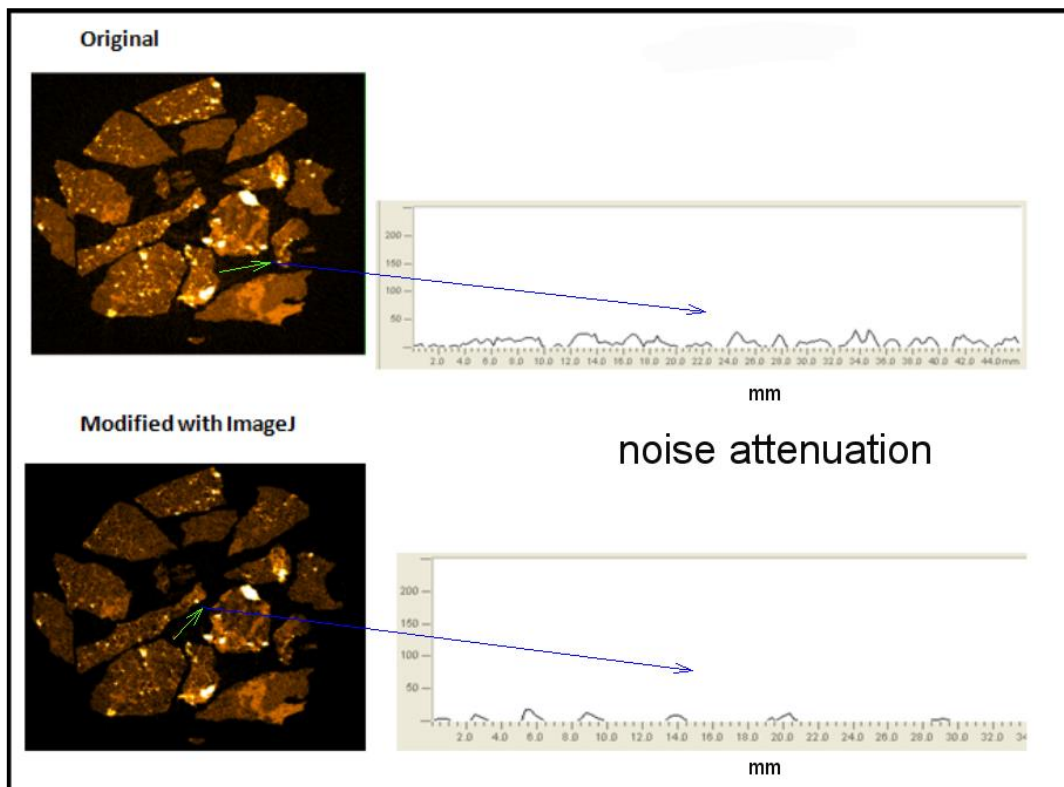
Figure 68: Profile line cuts through the filtered and non-filtered images (Gurnett 2009), image courtesy (Cakici 2009)

One of the filters that was used with ImageJ was the Anisotropic 2D image Diffusion Filter, which is commonly used for noise removal in medical images. This filter smooths the image. However, it also tends to remove the parts of the grains (Gurnett 2009), identified this by comparing the volume of the grains in different analysis process. Total particle volume and back calculated weight, based on the volume of identified mineral phases, were also compared and the results were different. As the results provided had inaccurate grain boundaries, this filter was not acceptable for the purposes of the research presented here.

Gaussian, Gaussian Noise and Sigma Plus filters showed no image improvements, on the contrary, some even generated additional noise when used in ImageJ. An initial minimum filter gave results in noise reduction but was not recommended for segmentation purposes since the total volume calculated before and after filter application was reduced approximately 2% per image, which is considered to be high.(Gurnett 2009)

The image quality level presented in the particles of less than 36μm of the size range was not satisfactory, since there was movement of the particles inside the tube when handling the samples.(Gurnett 2009) An improvement has been made by mounting the fine size fraction samples in Styrofoam, layering them using double sided tape. Further details are given in Chapter 6.
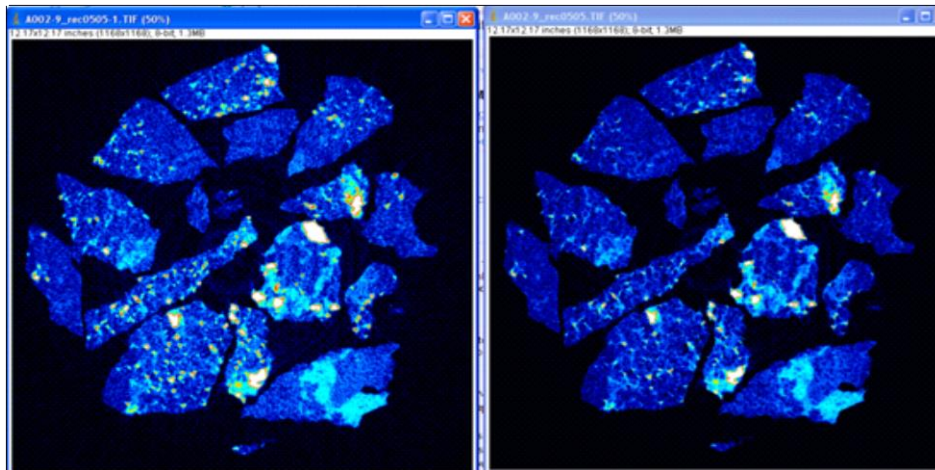
Figure 69: Minimum filter refinement within ImageJ (Gurnett 2009), raw image (Cakici 2009)

3.7.2.7 Variations in image analysis processing

The study presented here focused on the variation between individual software packages during the image analysis process. CTAn is the recommended analysis software that is provided with the SkyScan1172 system. It provides various analysis tools that can be used to identify various features such as volume of the objects of interest, porosity etc. However, in order to use this software package the image needs to be clear of any noise. This program allows the user to draw a profile line through the cross section of the particle, where it shows the level of X-ray absorption of the particle above this line (Figure 68).

Lin and Miller (1996) have suggested clearing the noise from the images by selecting the threshold levels. However, their images were of binary particles containing dolomite and sphalerite phase, and the profile line in the reconstruction showed clear threshold values. Unfortunately this was not the case in the reconstruction software used here. One of possible explanations was that our particles were multi-component particles and contained

mineral grains with very similar X-ray absorption values. Thus it was not possible to set the strict threshold values in the CTAn software.
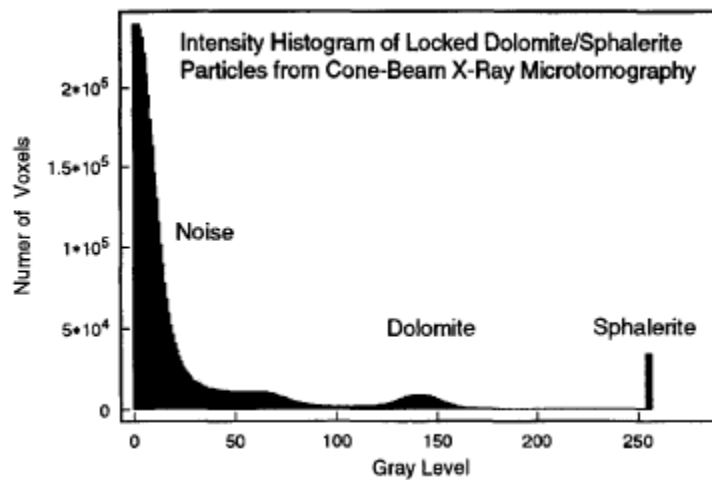
Figure 70: Intensity histogram, dolomite/sphalerite particles (Lin and Miller 1996)

The attenuation level is able to provide us with an approximate level of threshold needed for identifying a particular mineral phase.

An alternative program used for image analysis is ImageJ. As already mentioned, it was found that noise could be removed very efficiently by using a minimum filter. This filter causes greyscale erosion by replacing each pixel in the image with the lowest grey scale pixel value the neighbourhood of that pixel.

One of the most promising software programs for rock image analysis is eCognition 8 software (Figure 71). By using various filters in this software, such as a Gaussian noise filter, the noise was removed completely. Algorithms such as watershed (shrink and grow) may be used for exact grain volume definition and for separating touching particles as well. The algorithms available in eCognition are already known in the image analysis field. (Beucher and Meyer 1993; Lin and Miller 1996; Serra 1980)
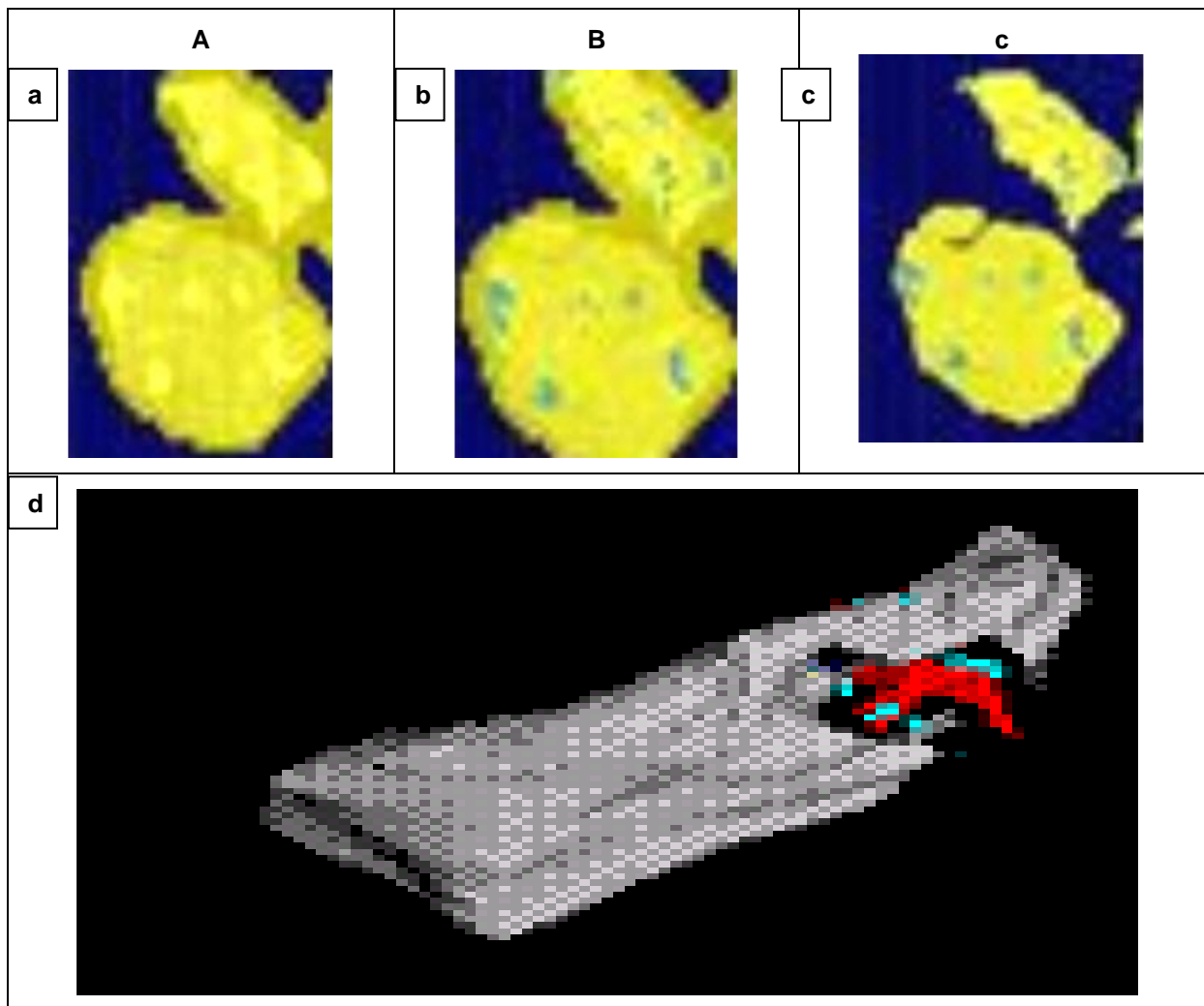
Figure 71: eCognition 8: a) background removed, b) contrast split segmentation, c) noise removed and d) minerals classified, single particle in 3D, chalcopyrite, magnetite and gangue phase

3.7.2.8 Image Quality Conclusions

The refinement process has identified ways of improving the image quality. With the addition of water around the particles (in a Perspex tube) the beam hardening effect was reduced as the contrast between particle and surroundings was increased. Supporting data is given in Table 5.

The use of the filters supplied with the SkyScan system made a certain level of improvement. The copper and aluminium filters used in this case were provided to convert the X-ray beam into a more monochromatic beam and reduce the effect of beam

hardening and ring artefacts. It appears that the SiO_2 filter actually worsened the beam hardening effect, in both post-hardening and pre-hardening instances. Since the particles tested had from 70-90 % SiO_2 phase, the low energy X-ray beam signal has been reduced and the high energy signal was not suitable to identify the gangue phase of the rock.

Table 5: Refined image chemical and mineral weight percentage

	Dense component weight %			chemical assay %		Calculated MLA assay %	
	CTAn	MLA	eCognition (refined)	Fe	Cu	Fe	Cu
Sample1	35.1	28.0	31.6	20.00	1.60	17.19	1.48
Sample2	5.1	7.1	6.6	5.52	0.06	5.13	0.02
Sample3	35.0	39.9	42.0	25.61	3.21	22.22	3.18
Sample4	1.2	0.5	1.5	1.47	0.02	0.30	0.03

Changing the sample holder tube diameter did not change the image quality noticeably and therefore it eliminates the tube size as a problem variable in this case.

The final image quality improves if a smaller rotation step is used as the consequence of having more radiographs for an alignment later in the reconstruction process. Considering the compromise between scan analysis time and image quality, the optimum results were from a scan with 0.9 degrees in each rotation step. However, at high resolutions the measurement sample holder must be quite rigid.

The Gaussian filter within ImageJ made no obvious difference between the filtered and non-filtered image. The Anisotropic 2D Diffusion filter is commonly used to process medical images in order to remove noise (Pilny and Janacek 2006). It was apparent that this filter gives some value by smoothing. Unfortunately, it was also found that the volume of the particles was considerably reduced with the application of this filter. The Gaussian Noise filter within ImageJ contributed to the generation of noise in particle images (Gurnett 2009). However, the same filter applied in eCognition8 gave significantly better

improvement, where the noise was successfully removed and touching objects were detached in three dimensions. eCognition applied the filter in three dimensional space compared to two dimensional application in ImageJ.

The Sigma plus filter used in ImageJ showed marginal improvements in the image quality. The best results were achieved by applying "Initial minimum filter". This filter could improve the border of the particles, but it is not suitable in filtering the complete internal structure of the particle. (Gurnett 2009)
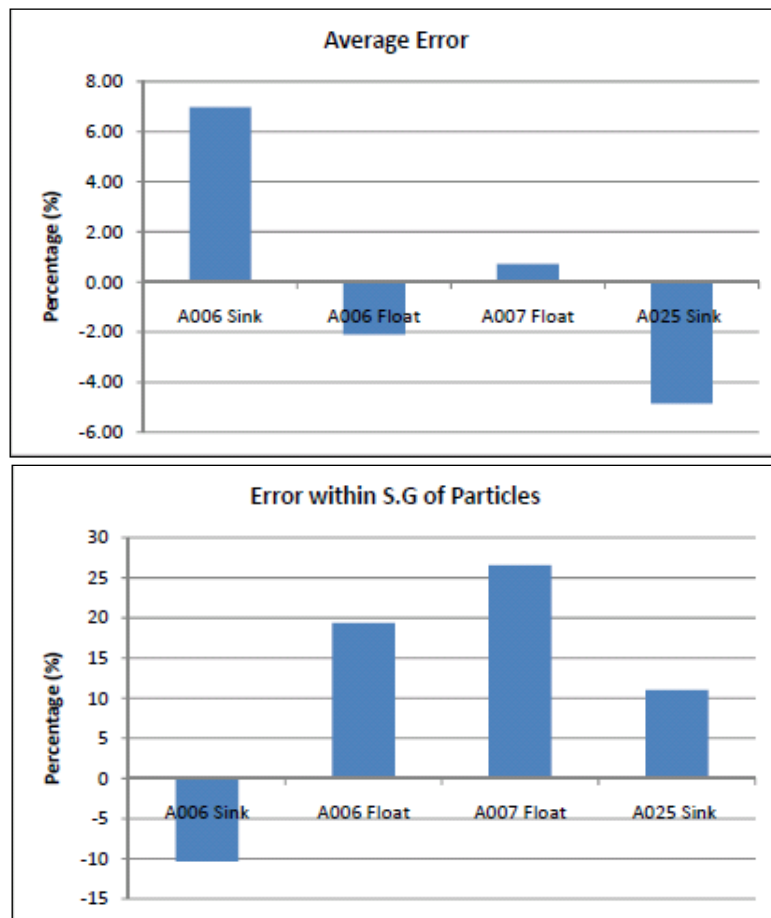
Figure 72: Average errors and density measurement error between two analysis methods, SkyScan and MLA (Gurnett 2009)

Despite the efforts to create an accurate segmented image from the SkyScan, current observations indicate differences between MLA data and SkyScan data analysed in CTAn. The error of some of the tested samples is shown in Figure 72, where the density of the

particles calculated based on MLA data was considered as accurate. As the MLA technique is a well established technique for analysing minerals in two dimensions, identified mineral properties are stored in mineral library files in MLA software. The mineral data for comparison were calculated in MLA software and displayed in the table form in MLA Dataview. The reason for having different observations from CTAn is the involvement of subjective threshold selection during the analysis process which was managed automatically in eCognition software later.

After a number of observations, the overall conclusion was that the use of filters, the increased number of frames averaged and reduced rotation step led to a significant improvement in image quality (Figure 73 and Figure 74). The improvement was noted in all but fine size fraction samples. The movement of fine size fractions (finer than 38µm, Figure 75) happened when samples were placed in Perspex tubes during the measurement process (Gurnett 2009). However the measurement was successful when fine size fraction samples were mounted in layered Styrofoam.

The image condition that produced very high quality data were a rotation step of 0.45 degrees, 4 frames averaged, voltage of 85 kV, current of 98 mA and exposure time of 3.9s. (Gurnett 2009) The decision was made based on the clear contrast between silica and magnetite grains at these conditions.

Based on Figure 46, one can conclude that beam hardening appears to be an issue when the energy is lower. The same statement has also shown to be valid in other similar work (Ketcham and Carlson 2001). By increasing the frame averaging, the scanning time is increased dramatically. It gives the certain improvement of the image but not significantly in comparison with the processing time extension. Therefore the frame averaging was kept at 3 during the experiments.

ImageJ has a high capacity to improve image analysis and filtering. However, a huge amount of time needs to be spent on modification within the software so that it could be used for analysis. The best capacity to perform this type of analysis was by using eCognition 8, where we are able to produce a rule set such that filtering is done

automatically and generates high quality images. From a general perspective, the main conclusions from the X-ray analysis reviewed above are that the image acquired with the SkyScan does have the potential to provide accurate mineral results when combined with image analysis software. To the limits of current observations, the image can be noise free and minerals may be selected and classified precisely in three dimensions.
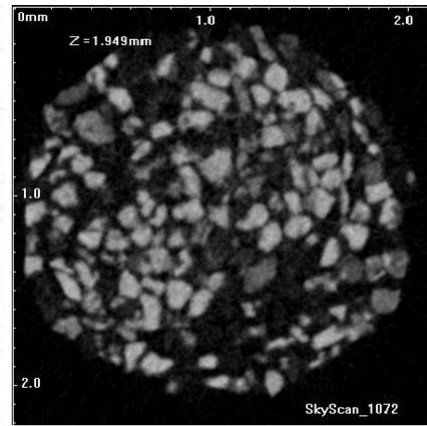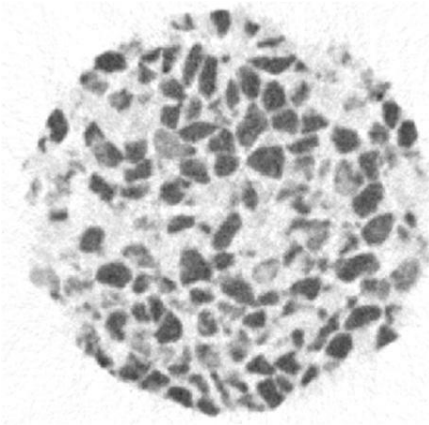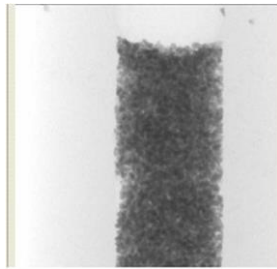
Figure 73: Silica/magnetite ore, -106 + 75 μm, experimental settings defined here, the sample in a tube (radiograph) on left, cross sections on right (Gurnett 2009)
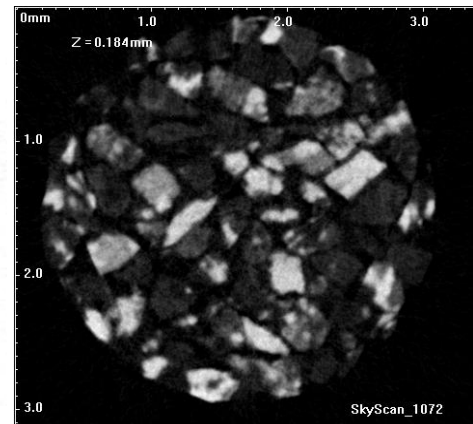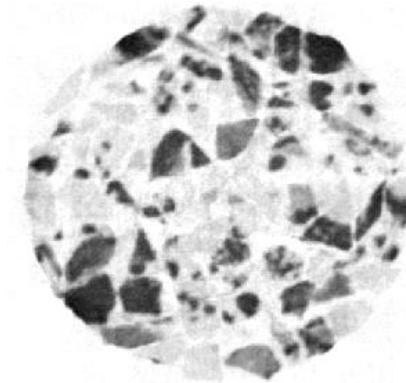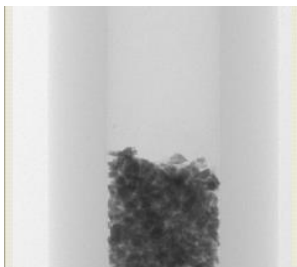
Figure 74: Silica/magnetite ore, -225 +180μm , experimental settings defined here, the sample in a tube   (radiograph) on left, cross sections on right (Gurnett 2009)
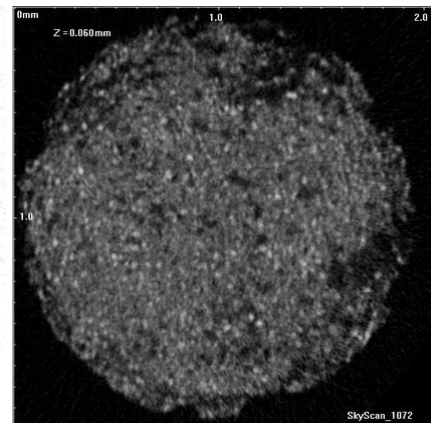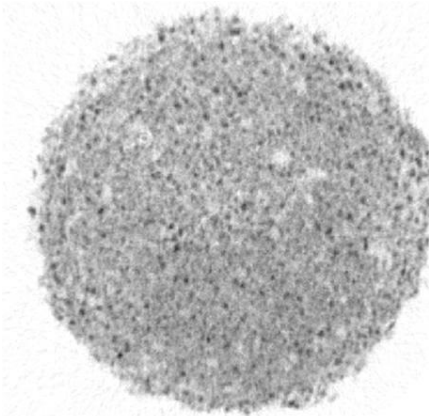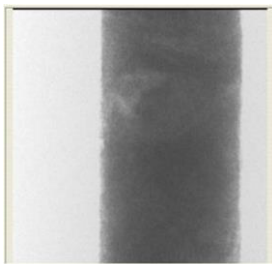
Figure 75: Silica/magnetite ore, -38μm, experimental settings defined here, the sample in a tube (radiograph) on left, cross sections on right (Gurnett 2009)

3.8   QC/QA Assurance

For the purpose of controlling the quality of the analysis of the images acquired in X-ray microtomography machines, tests were conducted on multi-component samples of rock. The particles tested were Mount Isa Lead-Zinc Heavy Media Plant (HMP) samples, where the sink particle was taken from a concentrate and the float particle was taken from the rejected particles in the Heavy Medium Plant (HMP). The size of the particles was -12 +8mm and the ore was rich in galena and sphalerite.

3.8.1 Acquisition Properties

The properties of the scans conducted in SkyScan1072 and SkyScan1172 were very similar (Table 6). The properties of the scans using the same system (SkyScan1072 or SkyScan1172) were equal. The expected outcomes of the seven acquisitions from SkyScan1072 were identical grain volumes from all scans. The same applies to the outcomes from nineteen SkyScan1172 scans. Despite the fact of having equal experimental settings, the results obtained from SkyScan1072 differed (for details refer to the Chapter 4).

Table 6: Acquisition properties of quality assurance control test

Sample Identification	Orientation	Acquisition date	X-Ray Source, kV/μA	Exposure time, ms	pixel size μm	Postalignment
F101_1	↑	26-Aug	100/98	2065	18.956	-1.0
F101_2	↑	26-Aug	100/98	2065	18.956	-0.5
F101_3	↑	26-Aug	100/98	2065	18.956	0.5
F101_4	↑	27-Aug	100/98	2065	18.956	-0.5
F101_5	↑	27-Aug	100/98	2065	18.956	0.5
F101_6	↓	27-Aug	100/98	2065	18.956	0.5
F101_7	↓	27-Aug	100/98	2065	18.956	0.5
F101_11	↑	27-Aug	100/98	2065	17.450	-1.0
F101_12	↑	27-Aug	100/98	2065	17.450	-1.5
F101_13	↑	27-Aug	100/98	2065	17.450	-1.5
F101_14	↑	7-Sep	100/98	2065	17.450	0.0
F101_15	↑	7-Sep	100/98	2065	17.450	-1.0
F101_16	↓	6-Sep	100/98	2065	17.450	-0.5
F101_17	↓	7-Sep	100/98	2065	17.450	-1.0
F101_18	↓	7-Sep	100/98	2065	17.450	-1.0
F101_19	↓	7-Sep	100/98	2065	17.450	-1.0
F101_20	↓	7-Sep	100/98	2065	17.450	-1.0
S101_11	↑	27-Aug	100/98	2065	17.450	-1.0
S101_12	↑	27-Aug	100/98	2065	17.450	-1.0
S101_13	↑	27-Aug	100/98	2065	17.450	-1.0
S101_14	↑	27-Aug	100/98	2065	17.450	-1.0
S101_15	↑	27-Aug	100/98	2065	17.450	-1.0
S101_16	↓	27-Aug	100/98	2065	17.450	-1.5
S101_17	↓	27-Aug	100/98	2065	17.450	-1.5
S101_18	↓	27-Aug	100/98	2065	17.450	-1.5
S101_19	↓	27-Aug	100/98	2065	17.450	-1.5
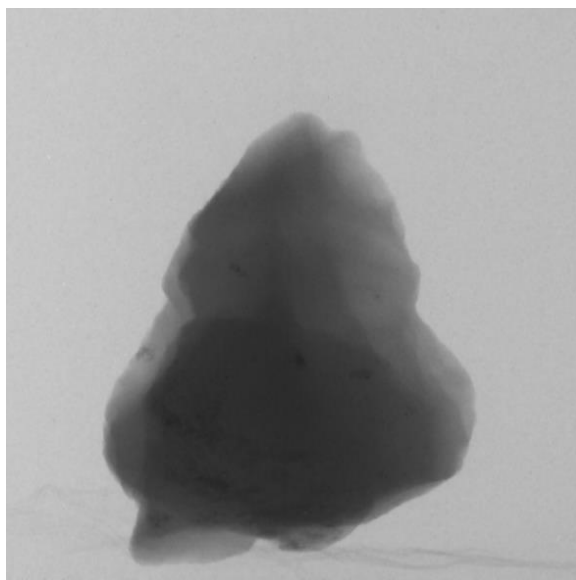
Figure 76: Sample F101, radiograph from SkyScan1072 test scan, orientation ↑
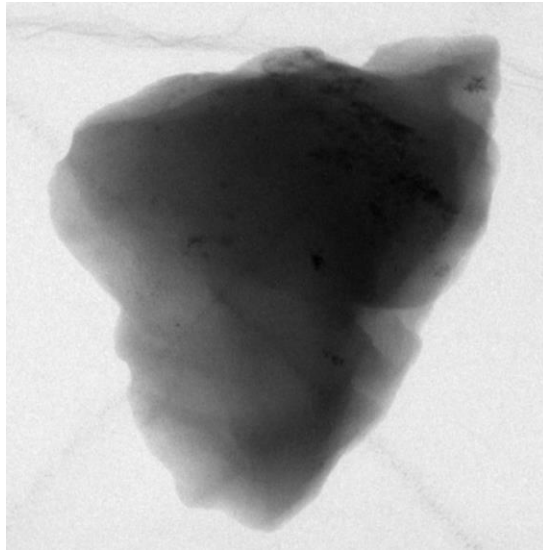
Figure 77: Sample F101, radiograph from SkyScan1172 test scan, orientation ↓

3.8.2 Radiograph grey scale level distribution

The decision at the time was to check if the greyscale of the radiographs differs, since the assumption was that they should give very similar results. Radiographs from specified degrees of rotation are analysed here. The unprocessed (tiff) type radiograph images could be opened with ImageJ hence the complete attenuation/greyscale distribution could be collected and analysed.

The data was presented as grey scale levels in 16 bit images, cumulative and normalised for the acquisitions which were conducted under the same circumstances, considering the orientation of the sample and the acquisition date as well. The date appeared to be important, as the volumetric data will show, since the instrument needs some time to warm up. The statement is also obvious in Figure 78 and more detailed graphs presented in appendix 9.13.

The interesting graphs here are the nine degrees of rotation graphs, which show more discrepancies than the others. As the acquisition progresses in time, the difference between grey scale levels on the same rotation step is reducing considerably. As mentioned earlier (section 2.6.4.3.1), the same particle will give different µ values if

scanned in different instruments, since they might have different X-ray tubes installed or different age of the tube, as is the case here.

The ageing of the X-ray tube obviously influences the acquisition process, as the instrument may not have the highest source energy from the beginning of the acquisition. The source energy "aging" period will depend on the age of the tube and technical capabilities of the instrument. It was obvious that the technology in newer instrument SkyScan 1172 was advanced and that the source stabilisation was achieved earlier than in SkyScan 1072.
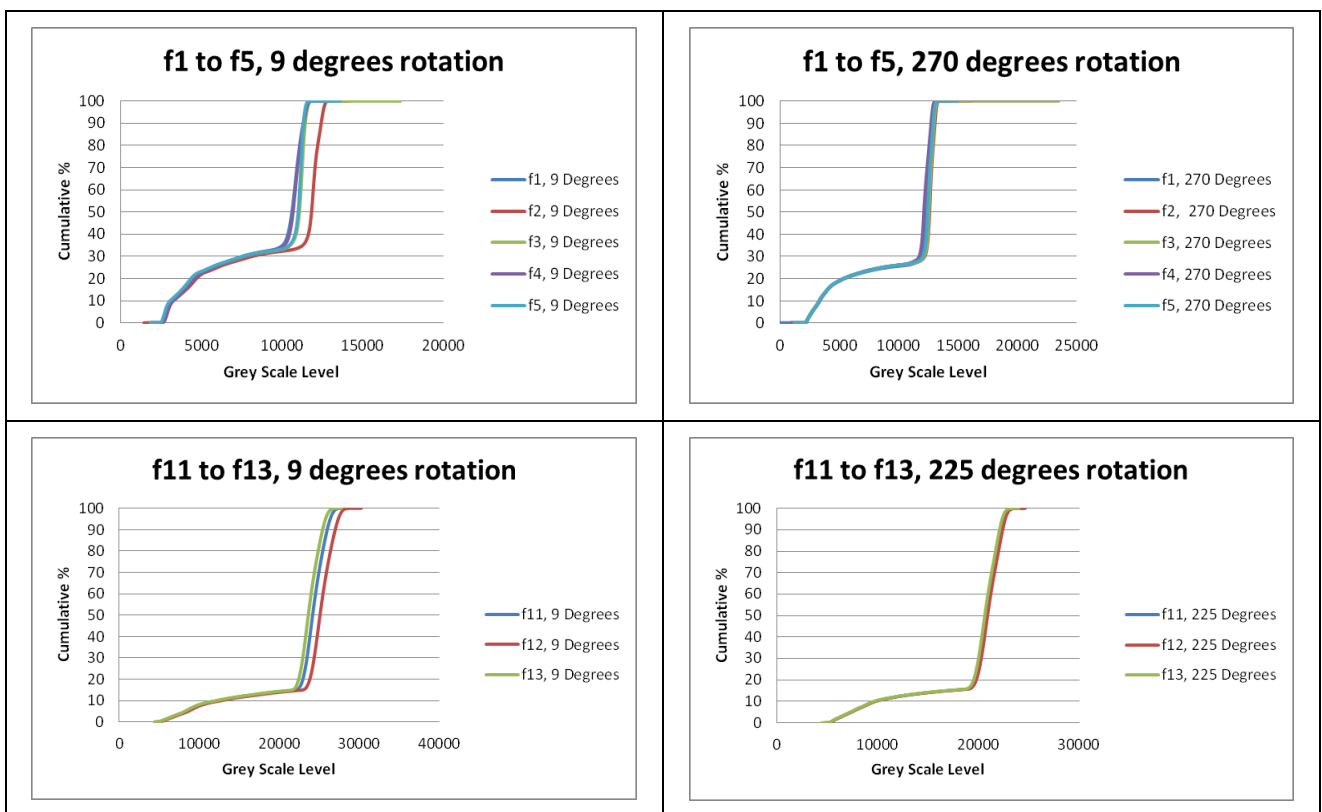
Figure 78: Grey Scale level cumulative distribution showed on radiographs from acquisitions with equal settings, conducted on the same day, of the HMP float sample and using the SkyScan1072 and SkyScan 1172

3.8.2.1 Radiograph grey scale normalised distribution

In principle the presented data did not show any major differences between different radiographs so that a conclusion could be reached. However, the images coming from the instrument SkyScan1072 had an increased level of noise present.
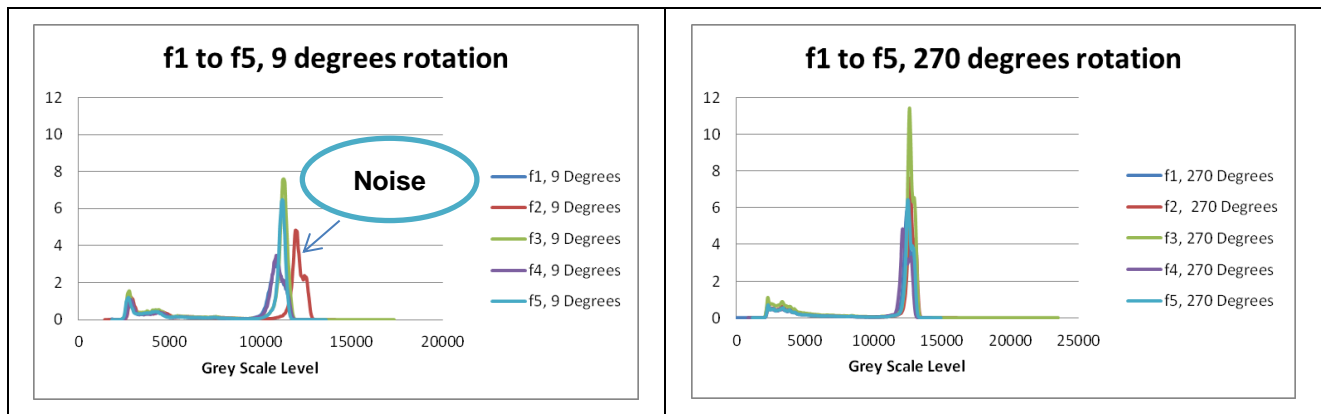
Figure 79: Grey Scale level normalised distribution showed on radiographs from five acquisitions with equal settings, of the HMP float sample and using the SkyScan1172

The indication here was that something was not accurate in the measurement and the aim was to investigate and find the solution. It is very obvious from the graphs in this section that there is greater scatter in data observed in instrument SkyScan1072. The counts in this instrument were very variable in every repeat test, as indicated in Figure 79. The disturbing factor was the inconsistences through the whole duration of the acquisition.

While there was large scatter in the data from the SkyScan1072, the same approach gave much better correlation between radiographs acquired by the SkyScan1172, especially in the field of denser mineral grains, on the left side of the graphs (Figure 80). The similar number of counts was achieved per grey scale level with slight variations noticed during the acquisition initialisation stage.

The variation in the nine degrees radiographs should not be considered as disturbing since the system was in a stage of aging and the requested source level was not achieved at the time to trigger the stable X-ray counts in the area of high dense mineral component. Hence a sufficient number of rotation steps has to be included in acquisition. The number should

be optimised with the quality of data required and the available time. In this case the rotation step was 1 degree, which means that the system will acquire new radiograph image at each step. The system reached the highest source in SkyScan 1172 in the first 10% of acquisition time, after which it was performing well as expected. The results were not impacted by this variation in X-ray counts during the acquisition initialisation (Chapter 4).
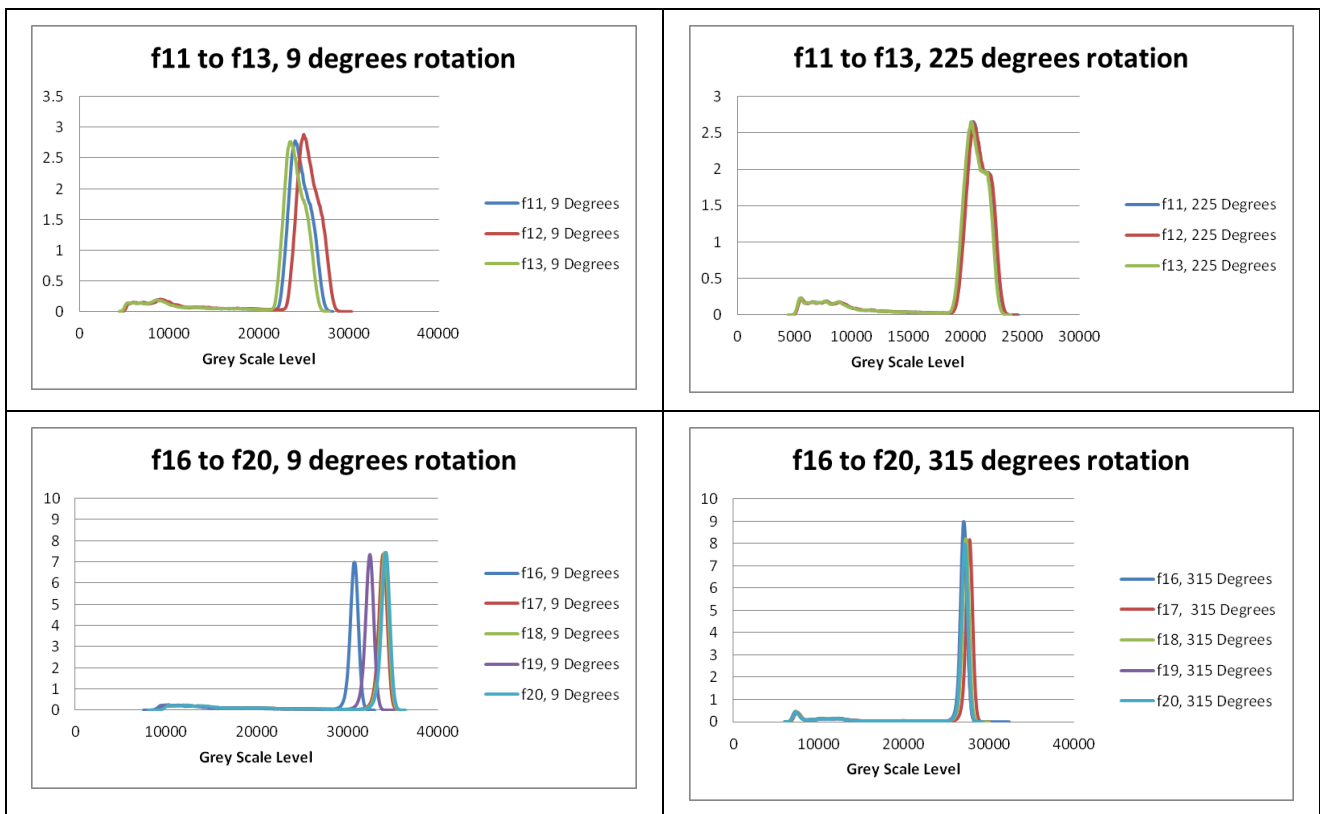
Figure 80: Grey Scale level normalised distribution showed on radiographs from acquisitions with equal settings, of the HMP float sample and using the SkyScan1172

Sink sample repeated acquisitions in Figure 81 and Figure 82 show less scatter than the data from the float sample. The same approach gave much better correlation between radiographs acquired by the SkyScan1172. More details about the data are presented in the section below, with the data per acquisition given in section 3.8.2.1.3.
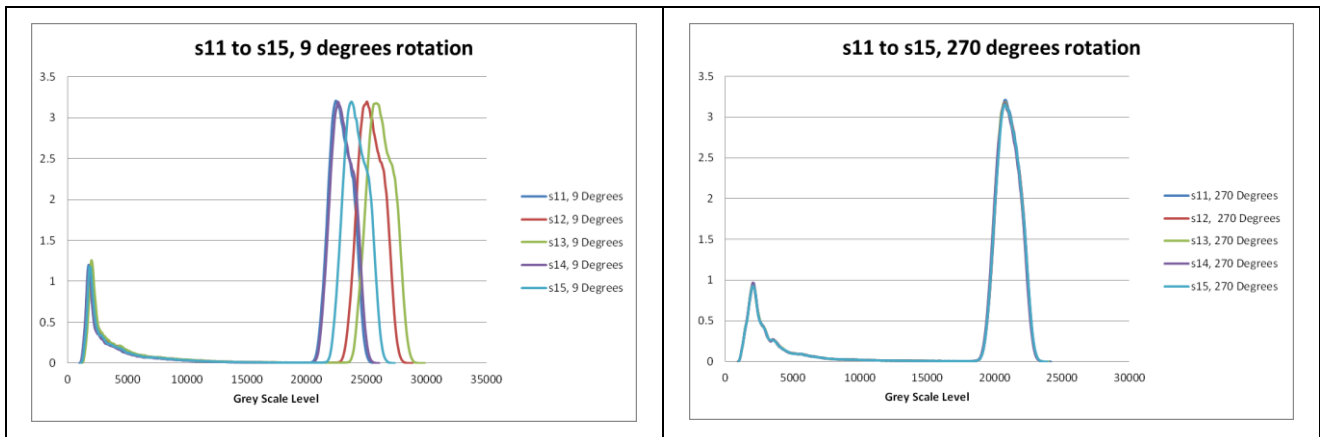
Figure 81: Grey Scale level normalised distribution showed on radiographs from five acquisitions with equal settings, of the HMP sink sample and using the SkyScan1172
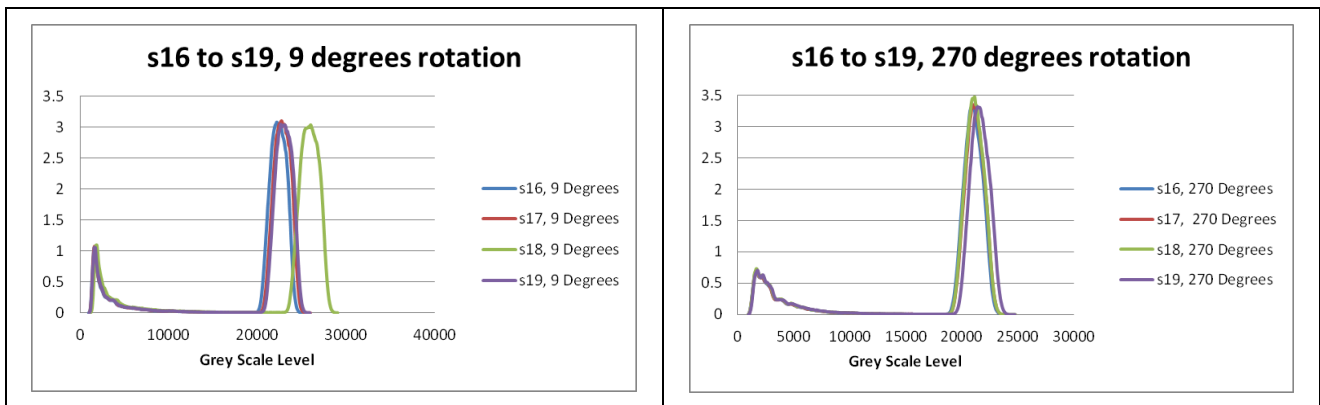
Figure 82: Grey Scale level normalised distribution showed on radiographs from five acquisitions with equal settings, of the HMP sink sample and using the SkyScan1172

3.8.2.1 Summary

To achieve a high standard of quality control X-ray microtomography, the uncertainties discovered here had to be minimised. Hence the whole distribution of the given radiographs will be presented on single graphs in 82 Figure 83 to Figure 85.

Further investigation of the variations in the counts per rotation step was performed and is detailed in the following section. Some of the differences in the number of counts per scan occurred due to differences in postalignment values, sample orientation or different scan day (Table 6). Hence the differences were not sufficient to indicate significant statistical differences in the data generated. The data is shown in Chapter 4.

3.8.2.1.1 Normalised distribution

Figure 83 shows the radiograph grey scale distribution from the acquisitions of the float HMP sample using SkyScan1072. The grey scale levels from the radiograph images are from various rotation angles acquired when the sample rotated on a sample holder during acquisition. The red distributions are acquired at the beginning of the tests, at 9 degrees of the sample rotation.
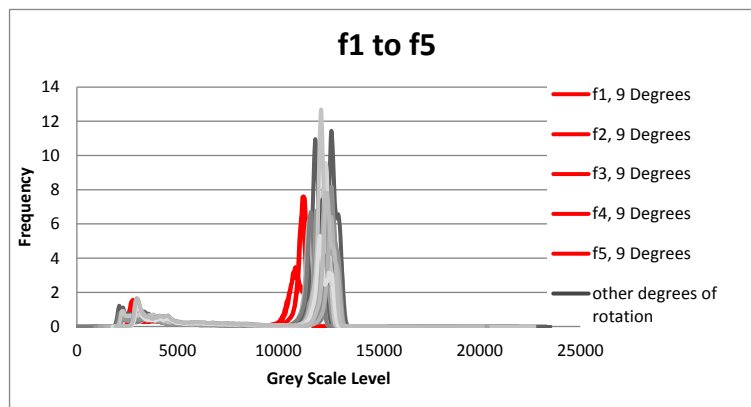
Figure 83: Summary of radiograph grey scale distribution, float sample, SkyScan1072, the data in red from 9 degrees rotation

It is obvious that the distribution of the grey scale levels of the radiographs acquired at nine degrees of rotation were more toward the left side of the graph. This demonstrates that the instrument requires a minimum warm up time before the system is ready for acquisition. As manufacturer's instructions were followed and the recommended 15 minutes of heating ("aging") was performed, this may indicate issues with the system beam emission.

The Figure 84 and Figure 85 show the radiograph grey scale distribution from the acquisitions of the float HMP sample and the sink HMP sample respectively using SkyScan1172 system. Here the nine degrees rotation step radiograph grey scale distributions are also presented as red.

184

It is obvious that the distribution of the grey scale levels of the radiographs acquired at nine degrees of rotation were more toward the right side of the graph. This demonstrates that the instrument was unstable and produced higher beam emission at the beginning of the acquisition. It was stabilised during the test. Details about individual scans are provided in section 3.8.2.1.3. The tube was fairly new in SkyScan 1172 and the aging and initialisation of the instrument helped the beam stabilisation process, presented in grey color lines in Figure 84 and Figure 85.
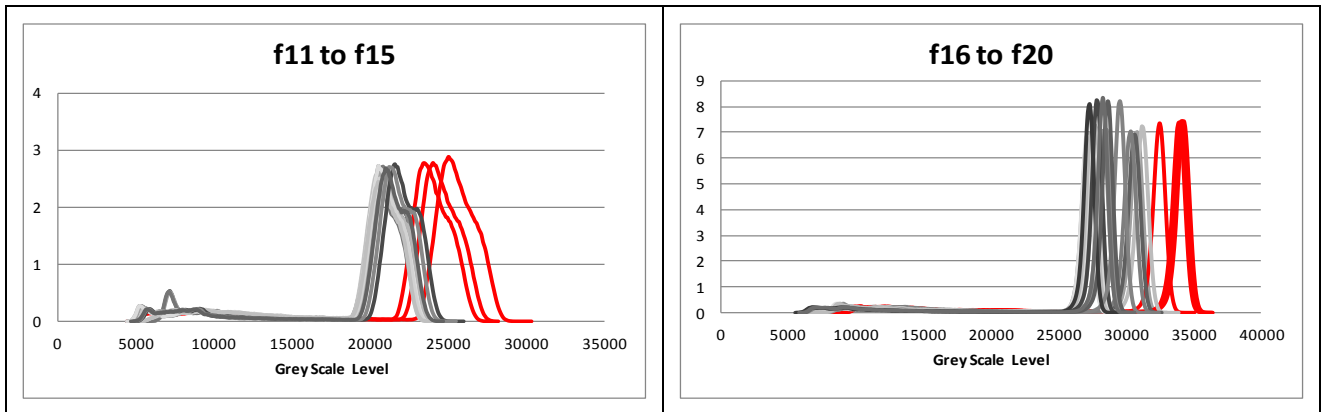
Figure 84: Summary of radiograph grey scale distribution, float sample, SkyScan1172, the data in red from 9 degrees rotation
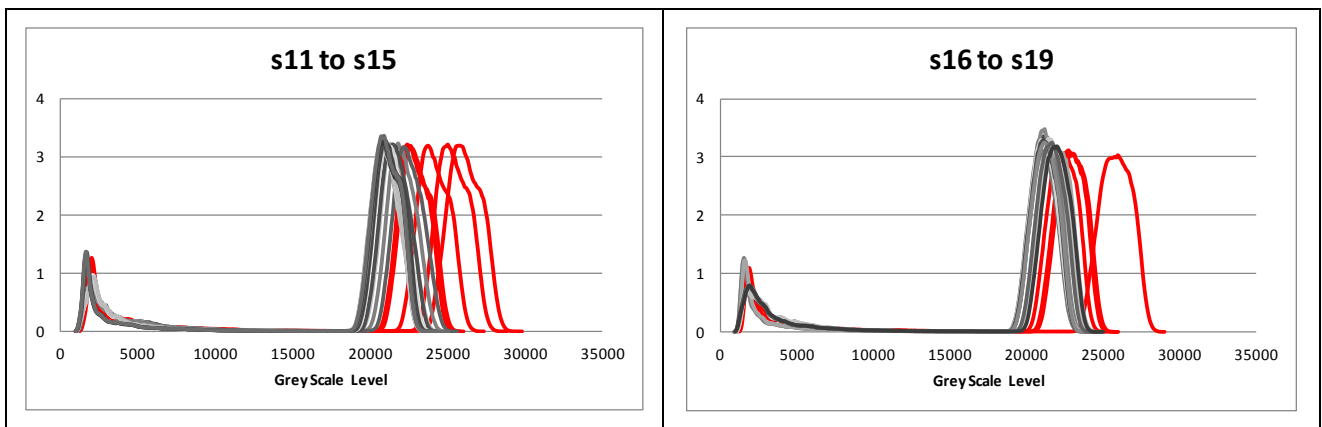
Figure 85: Summary of radiograph grey scale distribution, sink sample, SkyScan1172, the data in red from 9 degrees rotation

3.8.2.1.2 Cumulative distribution

The X-ray data presented on Figure 86 provide clear evidence that there was something wrong with the acquisitions in the SkyScan 1072. The implications of the grey scale levels

185

in the area of dense minerals are having an effect on the final results. A review of the problem identified that the age of the X-ray tube was past the manufacturer due date at the time of use.
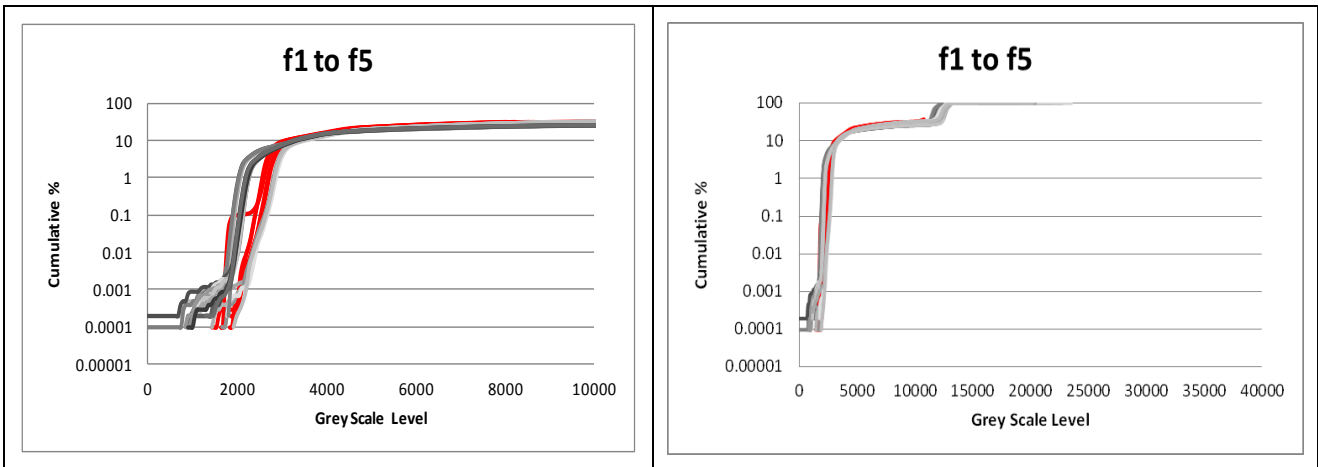
Figure 86: Summary of cumulative grey scale distribution of the radiographs, mineral section of grey scale, float sample, SkyScan1072, the data in red from 9 degrees rotation

This type of analysis may be considered to be a good way of controlling the quality of the results obtained by using X-ray microtomography results, since the radiographs from each rotation step are expected to follow similar trend. Trends from instrument 1172 which has an almost new X-ray tube are shown in Figure 87 to Figure 89.
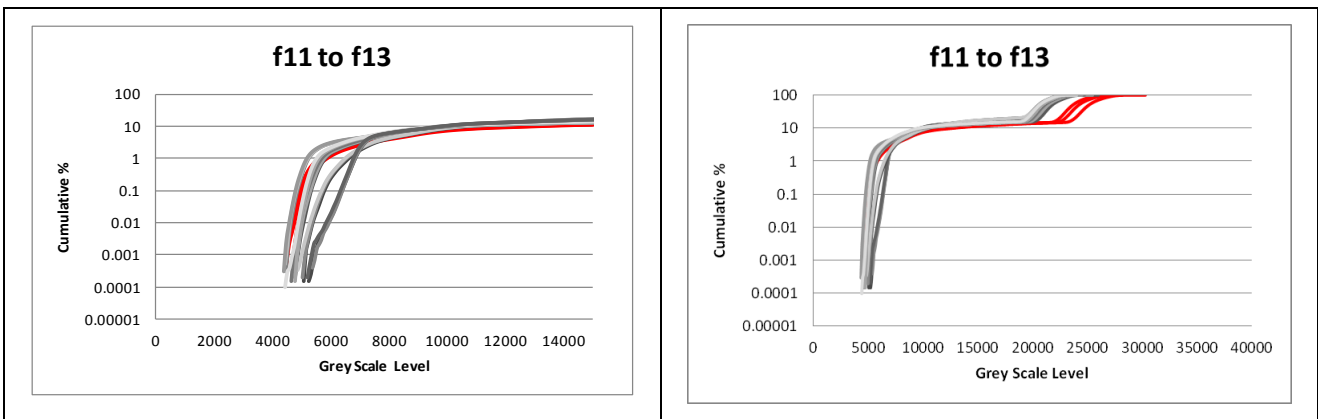
Figure 87: Summary of cumulative grey scale distribution of the radiographs, mineral section of grey scale, float sample, SkyScan1172, the data in red from 9 degrees rotation
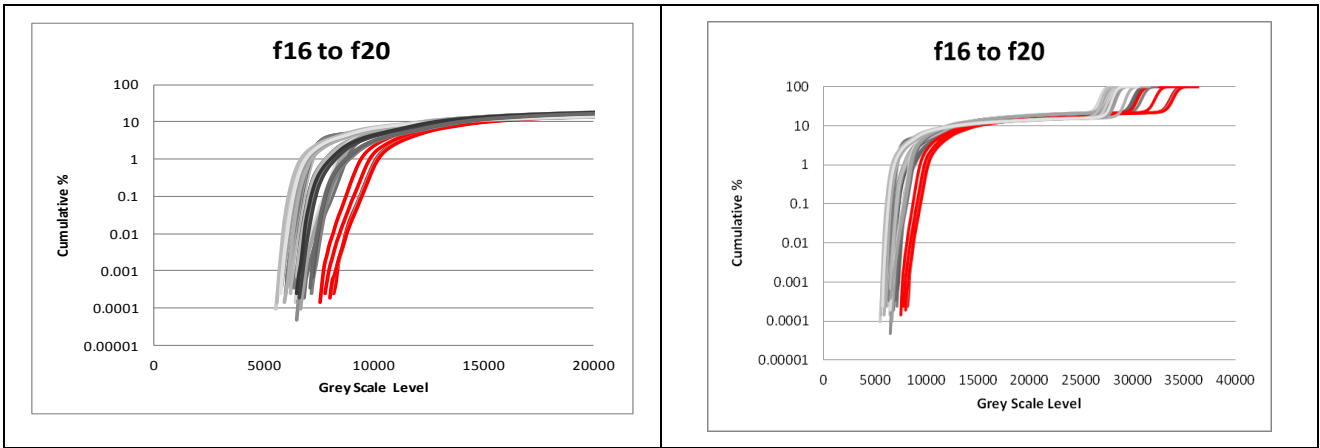
Figure 88: Summary of cumulative grey scale distribution of the radiographs, mineral section of grey scale, float sample, SkyScan1172, the data in red from 9 degrees rotation

In principle, the data from instrument 1172 shows a consistent trend for both the float and sink sample. Current observations indicate that the sample with the higher content of high density mineral (Figure 88 and Figure 89) has less noise than the sample with just a few percent of high density minerals (Figure 87 and Figure 88). More graphs are available in appendix 9.13.
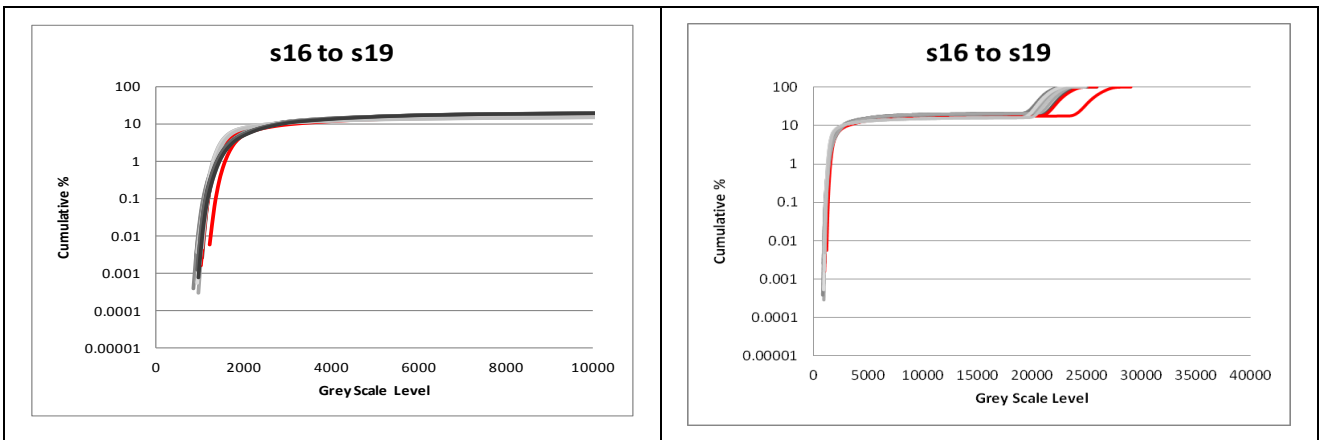
Figure 89: Summary of cumulative grey scale distribution of the radiographs, mineral section of grey scale, float sample, SkyScan1172, the data in red from 9 degrees rotation

3.8.2.1.3 Distribution per test

To investigate the variations of the grey scale counts per test associated directly with the reconstruction software and final volumetric data of the particle being tested, direct

observations of radiographs per test were performed, both in 16 bit and 8 bit images. The important outcome of these analyses is a tool to assess the performance of the X-ray tomography machine, as well as the potential noise in the reconstructed images.

Float Sample SkyScan1072, failed QAQC
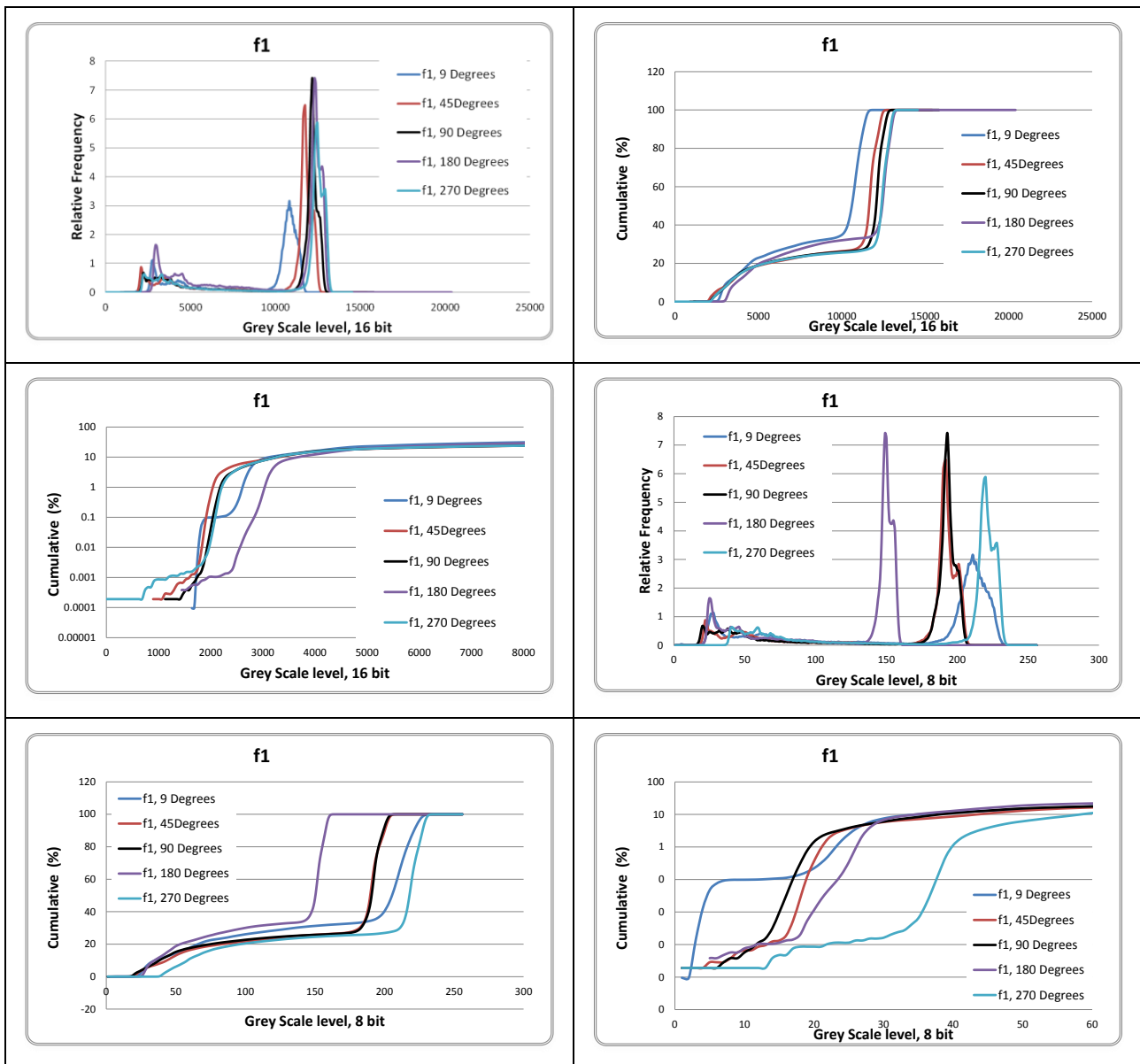
Figure 90: Radiograph grey scale level, normal distribution, cumulative distribution, cumulative log distribution and normal distribution, 16 and 18 bit images, test1

Figure 90 shows grey scale level of radiograph images acquired using the SkyScan1072 system. As mentioned previously, the radiograph acquired at nine degrees of rotation was more towards the left side of the graph. This observation indicated poor source heating before acquisition although the regular aging process was performed.

If the source was monochromatic, the graphs would have complete overlap of grey scale distribution. In this case, regardless of the rotation step, the radiographs would have been the same.

However, it is obvious that the system had trouble stabilising the beam emission, which is clearly visible at 270 degrees and toward the end of acquisition process.

Since the graphs of all other tests performed in SkyScan1072 have shown the same effect in radiograph grey scale level distribution, the use of this machine for further reproducibility studies was considered as unsuitable. The variations of greyscale levels in the area of high dense mineral phase were not acceptable in this research.

This type of analysis is not time consuming. Only a few steps (approximately 30 minutes) are currently involved in acquiring the grey scale levels of tiff images per rotation step. Automation of the QAQC step would help reduce the time even further. The suggested method can be used for instrument performance assurance.

Float Sample SkyScan1172

The variation of grey scale levels here were much less than with the older SkyScan1072 instrument. It was discovered that the variations ranged from 1000 to 1500 in 16 bit images and it is approximately 10 in 8 bit images. The important observation here is that lines are straight lines and not variable as in SkyScan1072. The lines (attenuation) are considered as consistent.

Figure 91 shows the radiograph image greyscale distribution for the float HMP sample acquired in SkyScan1172. As mentioned previously, the effect of aging in this system had the opposite effect to SkyScan1072 system. The beam emission was higher at the start of the acquisition (at nine degrees of rotation) than during the test. The system was stabilised after aging and initialisation, at around 10% of the total 360 degrees rotation.
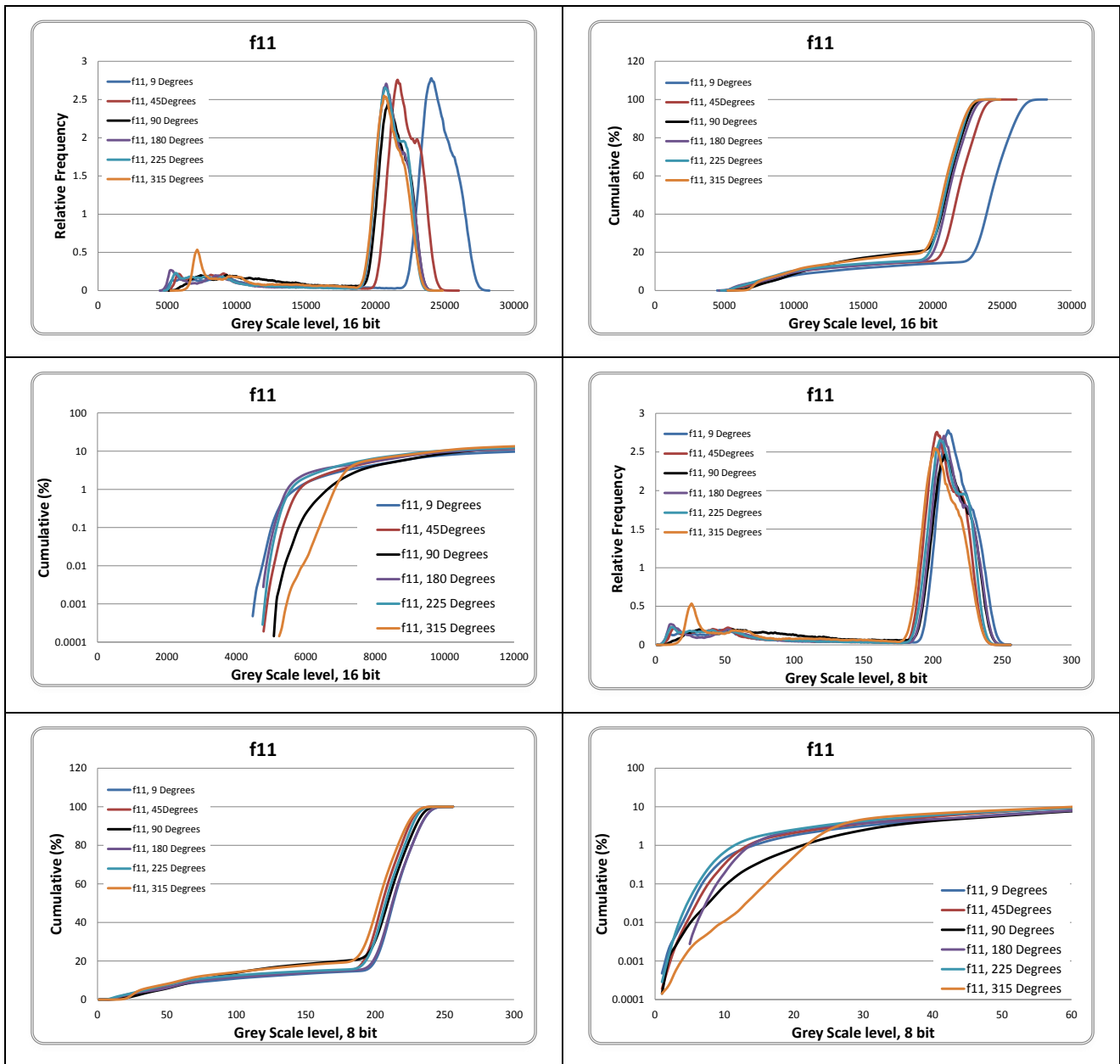
Figure 91: Radiograph grey scale level, normalised distribution, cumulative distribution, cumulative log distribution, 16 and 8 bit image, test11

There is some instability during acquisition due to the fact that float samples contained a matrix of gangue mineral grains with fewer valuable minerals. As already mentioned in section 2.6.4.2, when polychromatic source penetrates through sample, low energy X-rays are removed preferentially by low density minerals causing the beam to shift progressively higher. This higher energy caused issues with fine galena grain absorption and introduced the issues during the reconstruction process. The NRecon reconstruction algorithm assumes a monochromatic beam.

Generally there is less variation in 16 bit images as the available spread of grey scale levels is much higher than in 8 bit images.

Sink Sample SkyScan1172

The combined data from the sink radiograph tests obtained using the SkyScan1172 showed less variation than in the float sample. The graphs below show very good correlation between radiographs acquired from different angle positions. (Figure 92)

The observation is similar to the float sample. The aging caused higher energies at the beginning of the acquisition because of accumulation of energy which was released at the beginning of measurement. The source was stabilised at 45 degrees and continued to be more stable towards the end of the acquisition process. It is clear from Figure 92 that the beam was closer to monochromatic, which is also visible in reconstructed cross section images. The image noise was minimal here.
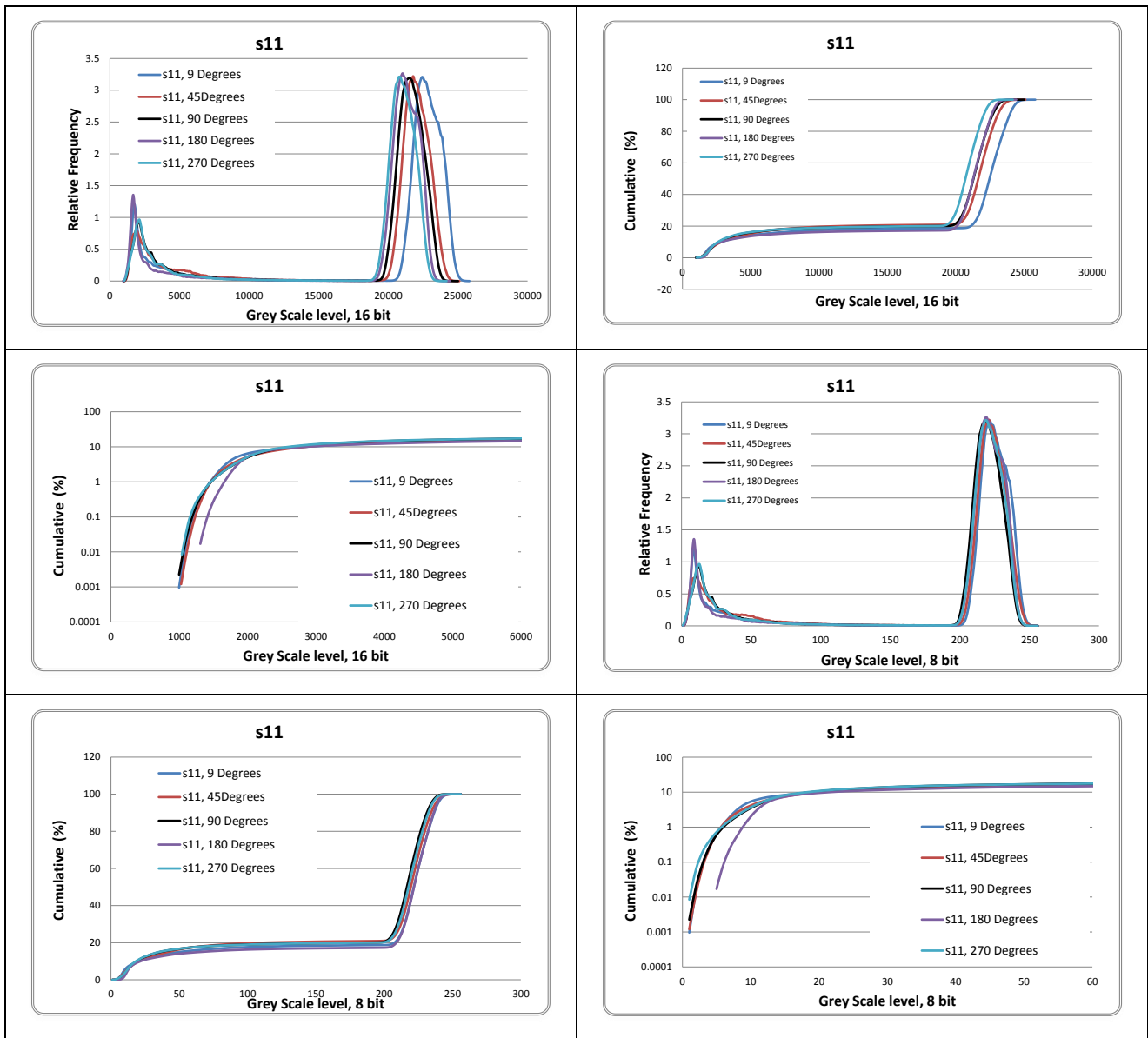
Figure 92: Radiograph grey scale level, normalised distribution, cumulative distribution, cumulative log distribution, 16 and 8 bit image, test11

3.8.3 Conclusions

From a general perspective, the main conclusions from this extensive study of reproducibility of radiographs acquisition processes in two X-ray microtomography machines reviewed above are the following:

- The instrument requires a minimum heating ("aging") each time of five to ten minutes before the system is stabilised, even if the X-ray tube aging process is completed as recommended by the manufacturer. For example, the radiograph on nine degrees of rotation was more towards left side of the graph until the system becomes steadier.

- The tests were repeated a couple of times, and there was no special difference between repeats noticed at longer times.

- Samples with higher contents of high density minerals had a more stable distribution of radiographs. These acquisitions generated images with less noise, especially in the area of denser components. The explanation may be that the matrix of gangue mineral grains with fewer valuable mineral grains was transferring higher energies to the dense mineral grains in the float sample. Hence, the response of the dense mineral grain structure was stronger than in sink particles, causing more ring artefacts than in the sink particle. One way to improve may be to use lower energies in the case where it is known that the dense mineral content is not considerable.

- The SkyScan1172 has shown better performance than SkyScan1072. The scatter showed less spread than in the older model of instrument.

- Radiographs acquired in the instrument SkyScan1072 did not show repeatability in time and rotation, the distribution graph (Figure 90) illustrated the lines not being straight but very inconsistent.

The procedures described here may be useful in defining the accurate threshold values during image analysis process which will be described in detail in the chapter 4 and 5. It is useful in combination with chemical assay and automated mineralogy data.

The radiograph check is thus proposed as a tool for quality assurance of the acquisition process. The above QA/QC monitoring proved to be very effective since the distribution

graphs indicated where the data were inadequate, typically related to images acquired in SkyScan1072. The unusual sample tests were outside the normal distribution trend observed from images acquired with the SkyScan1172.

The images acquired with the system that is not fully stabilised and where acquisition process was not optimised could provide useful qualitative image information. However for quantitative analysis high quality images and reproducibility are essential.

4 Reproducibility of the Tomography Mineral Analysis

4.1   Overview

This chapter describes the reproducibility of the image acquisition and image analysis of rock images acquired using X-ray microtomography instruments. The primary objective of this chapter is to evaluate the reproducibility of the quantitative mineral analysis of the multicomponent particles using microtomography. The secondary objective was to further evaluate the process of quality assurance. This has been discussed in Chapter 3, section 3.8.

The particles tested were Lead-Zinc Heavy Media Plant samples, described previously in Chapter 3. These two multicomponent samples were scanned repeatedly in the SkyScan1072 and SkyScan1172 systems. The sample identified as F101 (float sample) had less content of valuable (high density) minerals than the sample identified as S101 (sink sample). The size of both samples was – 13.2 + 9.5mm. The resolution of the images obtained using SkyScan1072 was 15µm pixel size, and it was lower with SkyScan1172, where the pixel size was 12µm.

After CBT measurement assessment, both particles were pulverised and subjected to XRD and XRF elemental analysis to identify the minerals present in the particles and to determine the percentage of the identified minerals. The reproducibility of the analysis of the above named samples will be detailed here. The results of the XRD analysis are given in Table 7, indicating only the percentage of minerals of relevance for comparison with X-ray analysis.

Table 7: Results of QXRD Analysis

	QXRD Results			
	% by mass		% by volume	
	Float Sample*	Sink Sample	Float Sample*	Sink Sample
Pyrite	1.1	0	0.6	0
Galena	0.2	5.8	0.1	2.6
Sphalerite	0	26.2	0	21.4
Iron Sulphide	0	3.2	0	2.1
Gangue	98.7	64.8	99.3	73.9

*values below detection limits

X-ray powder diffraction (XRD) is an analytical technique mainly used for phase identification of a crystalline material. The detection unit is very low, around 1% of the sample, which is disadvantage of this technique. (B.L. and Clark 2013)

X-Ray fluorescence (XRF) is an analytical technique used to measure the elemental composition of materials. XRF for iron gave 0.41% Fe for float sample and 2.6 % Fe for sink particle (Table 8). Since there was no data available for sulphur, zinc or lead, it was not possible to confirm galena and sphalerite percentage. In calculated CBT results the ratio between sphalerite, pyrite and galena from QXRD was considered.

Table 8: Results of XRF Analysis

	XRF Results (%)	
	Float Sample	Sink Sample
Fe	0.41	2.6

4.2   Experimental Methodology

The float sample particle was scanned seven times using the SkyScan1072 and ten times using the SkyScan1172. The position, as in Figure 76, was used for first five scans in each machine. The sink sample was scanned ten times using the SkyScan1172 machine. No preparation of the samples was required. They were mounted in Styrofoam since it is believed that the Styrofoam will help in defining the edge of the particle. As mentioned in previous Chapter, X-ray absorption lines revealed the noise around the particle. The noise was reduced by implementing this mounting step. At the same time, mounting the sample in this way is recommended when dealing with samples approximately 5mm in size. This provides the flexibility to set up multiple scans of multiple particles and recover the undamaged particles after acquisition.

The experimental conditions were identical for both instruments. However, the image analysis procedures differed due to the differences in image quality, which were discussed in Chapter 3. Table 6 presents experimental conditions of the acquisition part of the analysis, and it is provided on page 176, chapter 3. Radiograph images of the considered particles are shown in Figure 93 to Figure 95.
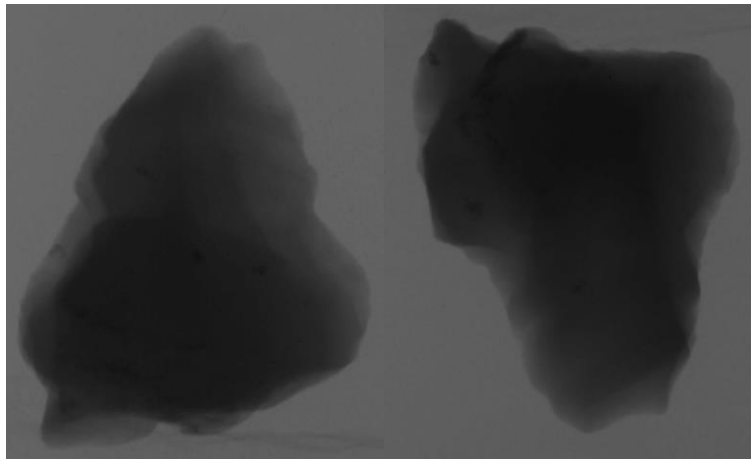
Figure 93: F101 sample, radiograph, SkyScan1072
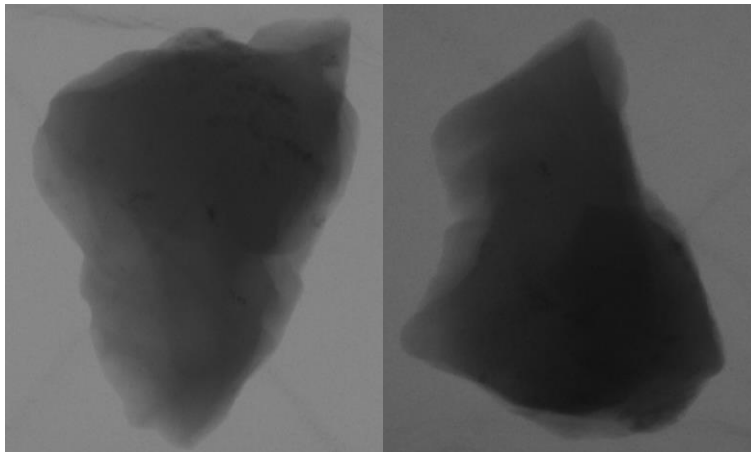
Figure 94: F101 sample, radiograph, SkyScan1172
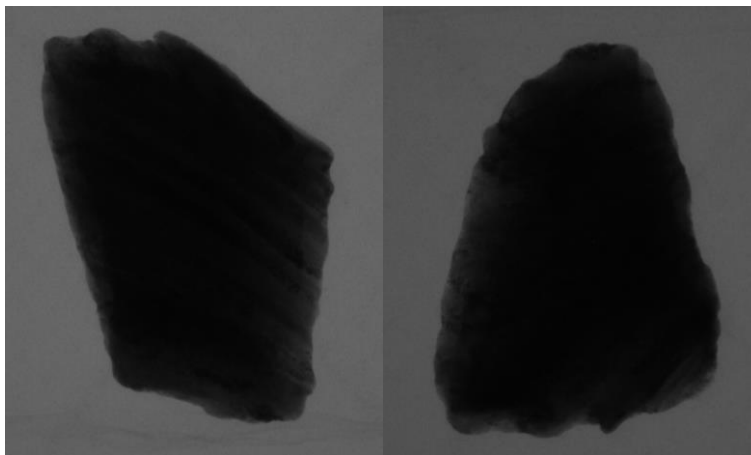
Figure 95: S101 sample, radiograph, SkyScan1172

The samples were positioned in the centre of the sample holder as accurately as possible. Through rotation of the samples prior to the scan, it was confirmed that the samples were entirely visible within the field of view. To reconstruct the image, the image reconstruction

software NRecon was used. The threshold values for the reconstruction process were variable per instrument and sample, as the counts per radiograph were also different as shown in Table 8. The reconstructed images were subjected to image analysis using CTAn and eCognition. The threshold values within CTAn were equal for the same type of test data as they were manually defined by the operator. However the threshold values within eCognition image analysis were automatically defined by the process rule set to provide an automatic threshold function.

Table 9: Photon counts per radiograph for selected rotation steps

Test		Degrees of Rotation/Counts				
		9	**45**	**90**	**180**	**270**
SkyScan1072	**f01**	1048576	1048576	1048576	1048576	1048576
	f02	1048576	1048576	1048576	1048576	1048576
	f03	1048576	1048576	1048576	1048576	1048576
	f04	1048576	1048576	1048576	1048576	1048576
	f05	1048576	1048576	1048576	1048576	1048576
	f06	659308	568480	570152	616044	620500
	f07	671640	567196	631488	683992	633888
		9	**45**	**90**	**180**	**225**
SkyScan1172	**f11**	2096000	2096000	2096000	2096000	2096000
	f12	2096000	2096000	2096000	2096000	2096000
	f13	2096000	2096000	2096000	2096000	2096000
	f14	2096000	2096000	2096000	2096000	2096000
	f15	2096000	2096000	2096000	2096000	2096000
	f16	2096000	2096000	2096000	2096000	2096000
	f17	2096000	2096000	2096000	2096000	2096000
	f18	2096000	2096000	2096000	2096000	2096000
	f19	2096000	2096000	2096000	2096000	2096000
	s11	2075040	2075040	2075040	2075040	2075040
	s12	2075040	2075040	2075040	2075040	2075040
	s13	2096000	2096000	2096000	2096000	2096000
	s14	2096000	2096000	2096000	2096000	2096000
	s15	2096000	2096000	2096000	2096000	2096000
	s16	2096000	2096000	2096000	2096000	2096000
	s17	2096000	2096000	2096000	2096000	2096000
	s18	2096000	2096000	2096000	2096000	2096000
	s19	2096000	2096000	2096000	2096000	2096000

4.2.1 Experimental Results

As discussed above, the particles were subjected to X-ray acquisition in different instruments and the same sets of images were analysed with two different image analysis software programs. Many forms of experimental design were available here. An experimental design was selected with the aim of identifying potential image quality control methods as well as to assist in selecting the next technique for analysing images in the liberation study. The initial experimental design required the same number of experiments in both instrument. However, the issues identified in images acquired by the SkyScan1072 led to the cancellation of further experiments using this instrument.

4.2.1.1 Float Sample Reproducibility, SkyScan1072

In the images acquired by the SkyScan1072 it was difficult to define the mineral grain boundaries in order to set the manual threshold value within CTAn. The results of the analysis of seven scans of the float sample particle are given in Table 10 below. Here the dense component represents the sum of galena and other sulphides.

Figure 96 presents the results obtained in CTAn and compared with XRF analysis of the sample. The results given in Table 10 show that the dense component volume measured in the float sample is underestimated compared to the XRF results. It was assumed that the elemental analysis of Fe using XRF would represent the total amount of dense component present in the float sample, which gave 4.7 mm^3 of dense component. The gangue phase identified was mostly quartz and muscovite, with minor (<0.9%) biotite and chamosite.

There was a variation in the estimate of galena content using Micro CBT and also no Pb assay data to accurately confirm the presence of galena in the particle. Setting the galena threshold was found not to be reliable and therefore it was decided to remove the galena estimate from this discussion.

Table 10: CTAn image analysis results for float sample scanned in SkyScan1072

Test id	Dense component VOLUME (mm^3)	Gangue VOLUME (mm^3)	WHOLE PARTICLE VOLUME (mm^3)
F01	3.11	596.99	600.1
F02	3.13	597.64	600.77
F03	3.15	597.56	600.71
F04	2.86	599.08	601.94
F05	2.99	597.32	600.31
F06	2.95	598.01	600.97
F07	2.83	597.34	600.17
Mean	3.00	597.71	600.71
stdev	0.13	0.68	0.63
var	0.017	0.469	0.401
SE	0.043	0.228	0.211
CoV	4.33%	0.11%	0.11%
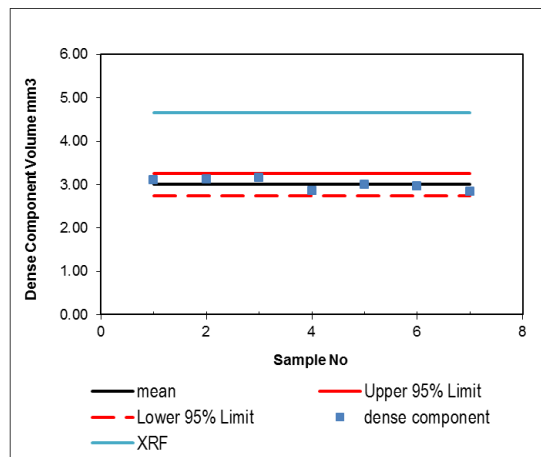
Figure 96 : Float sample scanned in SkyScan1072, CTAn image analysis, dense component mm^3

There was a variation in results observed with downwards trend and it was noted that the counts of photons for runs F06 and F07 were significantly lower than those for F01-F05, as

shown in Table 9. Although the data ranged between confidence limits, it failed QAQC procedure as a quality issue in the acquisition process was revealed.

The same set of images was analysed using eCognition 8. The results of the analysis are given in Table 11 below and the data was also compared with XRF Fe elemental analysis (Figure 97). The same downward trend was observed in the volume of dense component, but higher than with CTAn results. The reason is the operator decision on threshold versus eCognition8 automatic threshold values.

Table 11: eCognition image analysis results for float sample scanned in SkyScan1072

Test	dense component		gangue		WHOLE PARTICLE	
	volume mm^3	n. of objects	volume mm^3	n. of objects	volume mm^3	n. of objects
XRF*	4.67					
f01	5.1	754	593.4	30	600.5	784
f02	5.3	712	595.7	32	601.0	744
f03	4.8	725	596.1	13	600.9	738
f04	4.4	783	595.2	14	599.7	797
f05	4.8	670	595.9	20	600.6	690
f06	4.4	812	596.9	12	601.3	824
f07	4.1	844	596.4	16	600.5	860
mean	4.7	757	595.7	20	600.6	777
stdev	0.4	60.4	1.1	8.2	0.5	57.3
var	0.2	3649.5	1.3	68.0	0.3	3287.6
SE	0.1	20.1	0.4	2.7	0.2	19.1
CoV	9.0%	8.0%	0.2%	42.1%	0.1%	7.4%

note: values based on Fe assay only, lead not included

The results given in Table 11 show that the dense component volume measured in the float sample when images are analysed using eCognition software gave higher results to

the one analysed in CTAn. However, t is not significant with more than 85% confidence, and therefore the methods provided statistically similar results of dense component volume. The observations lie on the average within 9% of the mean. Figure 97 also shows that the heavy component volume estimated from XRF results lie within the 95% confidence limit around the mean of measured dense phase volume.
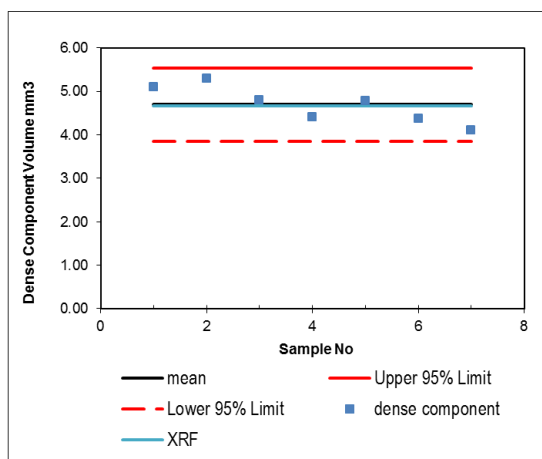
Figure 97: Float sample scanned in SkyScan1072, eCognition image analysis, dense component mm³

The estimate of the volume of the high density component was based on XRF Fe assay only and did not include a lead phase. As galena is present in the sample, the estimated volume using XRF is likely to be bare minimum dense phase volume estimate. Identification of lead phase in this case would not contribute to the volume considerably (it was confirmed with XRD that the volume is far less below 1% but not accurately because of method's detection limits).

4.2.1.2 Float Sample Reproducibility, SkyScan1172

The results of the image analysis of the float sample images acquired in SkyScan1172 are presented below. The segmentation approach applied in eCognition is different from CTAn. CTAn has sharp threshold values defined by the operator. In eCognition the operator defines a wide range of greyscale values for each mineral group based on their X-ray absorption profiles. These values were implemented in the eCognition code together with internal segmentation algorithms to calculate the function of the greyscale for each

voxel and based on this function to assign the voxel to a particular mineral group. Therefore in eCognition the classification value does not depend as much on an individual decision made by the operator as it does with CTAn.

Table 12 : CTAn image analysis results for float sample scanned in SkyScan1172

Test	dense component volumemm^3	gangue volumemm^3	WHOLE PARTICLE volumemm^3
XRF*	4.67		
f11	4.23	599.02	603.25
f12	4.20	598.30	602.50
f13	4.18	596.68	600.85
f14	5.53	608.74	614.27
f15	5.46	607.88	613.34
f16	4.97	606.57	611.54
f17	5.05	606.35	611.39
f18	5.01	606.88	611.90
f19	4.96	607.41	612.37
f20	5.01	607.13	612.14
mean	4.86	604.50	609.36
stdev	0.50	4.57	5.04
var	0.25	20.87	25.43
SE	0.17	1.52	1.68
CoV	0.102	0.008	0.008

note: values based on Fe assay only, lead not included

The results given in Table 12 show that the dense component volume measured in the float sample is overestimated compared to the XRF results, if the iron dense mineral component is assumed to be the only dense phase present in the sample as the Micro CBT data provide the volume of the total dense mineral phase. The results obtained with

measuring the volume of dense phase in the float HMP sample using SkyScan1172 gave similar results to the XRF estimate; t is significant with less than 75% confidence. Reproducibility improved when using CTAn on images acquired in SKyScan1172 rather than the SkyScan1072.

The reconstruction parameter post alignment that was adjusted manually differed amongst the tests, which introduced some difference in the results. The way reconstruction is doing this correction is to overlay the first and 180 degrees cone beam projections, or to overlay pseudo-parallel projections and use the central position for overlaying. Two images may differ due to the cone-beam geometry and magnification factors. (SkyScan 2010a) However, this difference was not considered to be significant and therefore the data obtained was assumed to be reliable regardless of the difference in reconstruction parameters.
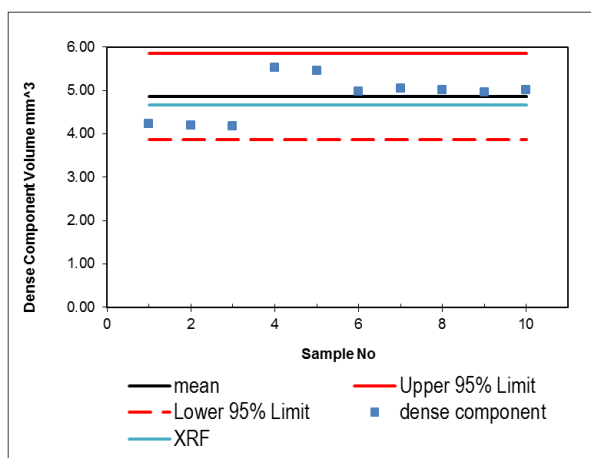
Figure 98: Float sample scanned in SkyScan1172, CTAn image analysis, dense component volume (galena and other sulphides, mm^3)

The results of the eCognition8 image analysis of the same set of images are given in Table 13. The data are plotted and compared with the XRF Fe element analysis data in 99 Figure 100. There are more objects (grains) identified in images acquired with the SkyScan1172 since the image quality and the detectability was better (Figure 99).

SkyScan 1072
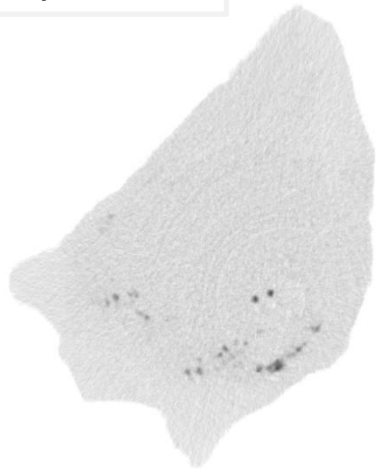
SkyScan1172
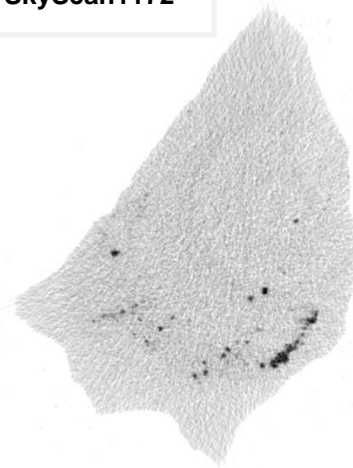
Figure 99: Cross section reconstructed images, acquired using SkyScan1072 and SkyScan1172, float particle

It was also noted that the agreement with XRF results was improved considerably by using eCognition8 on SkyScan1072 cross section images.

As the image analysis was performed on the same reconstructed images, using both method CTAn and eCognition, the variation in final results is visible in both data sets.

Table 13: eCognition image analysis results for float sample scanned in SkyScan1172

	dense component Vol.mm^3	gangue Vol.mm^3	total Vol.mm^3
XRF	4.67		605.5
f11	3.84	596	599.9
f12	3.89	595.5	599.4
f13	3.87	595.5	599.2
f14	5.02	605.4	610.4
f15	4.81	605.1	609.9
f16	4.52	603.6	608.1
f17	4.52	603.8	608.31
f18	4.49	603.9	608.5
f19	4.49	604.1	608.7
f20	4.59	603.9	608.6
mean	4.40	601.7	606.1
stdev	0.41	4.21	4.60
var	0.16	17.69	21.12
se	0.136	1.402	1.532
CoV	0.092	0.007	0.008

The results given in Table 13 show that the reproducibility improved slightly when eCognition was used on the same images analysed in CTAn. However, the dense component volume measured in the float sample is slightly underestimated compared to the XRF results of the iron dense phase. The results of seven tests lie within one standard deviation of 0.41 mm^3 while the other three are within two standard deviation intervals.
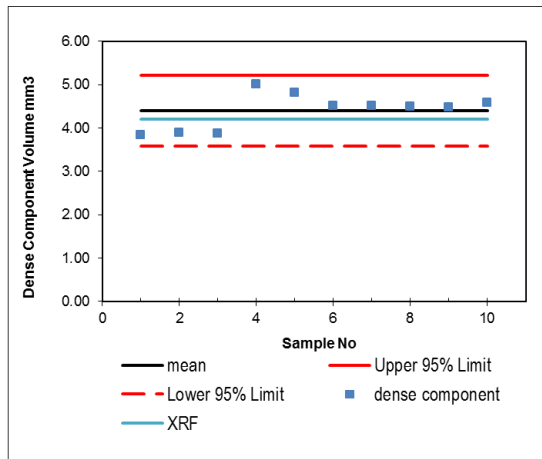
Figure 100: Float sample scanned in SkyScan1172, eCognition image analysis, dense component mm^3
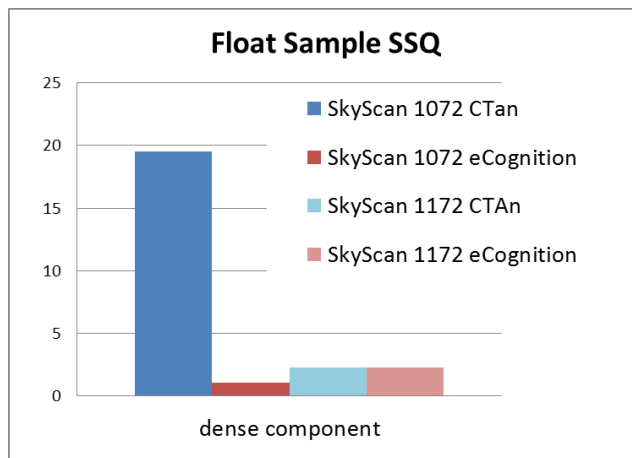
Figure 101: Sum of Squares of the results obtained in CTAn and eCognition for float images acquired in SkyScan1172

Figure 101 shows the statistical difference between different image analysis modes, as well as within results generated with the same method. The variation within identified total volume of the dense component using SkyScan1072 is higher compared with the data obtained using SkyScan1172 system. A single-sided t-test confirmed with over 95% confidence that the results obtained with CTAn and eCognition8 on the same images acquired with SkyScan1072 are different. The t-value indicated that the CTAn results were different from the XRF results with over 95% confidence. Variations were significantly lower with the application of eCognition8 on datasets acquired with both SkyScan1072 and 1172 systems.

211

Table 14: Automatic threshold values defined within eCognition analysis program for Float sample, images acquired in SkyScan1072 and SkyScan1172.

		automatic threshold
	Test	mean_sulphides
SkyScan1072	f01	82
	f02	81
	f03	86
	f04	88
	f05	85
	f06	91
	f07	92
SkyScan1172	f11	146
	f12	142
	f13	143
	f14	136
	f15	139
	f16	141
	f17	143
	f18	142
	f19	141
SkyScan1072	Mean	86.5
	STDEV	3.9
	Var	15.0
SkyScan1172	Mean	141.5
	STDEV	2.8
	Var	8.0

In the SkyScan1072 tests, five out of seven observations lie within 95% confidence limits of mean. The other two lie within two standard deviation intervals. The data from the SkyScan1172 test show that the automatic threshold values lay mostly within 95 % confidence limits, with only two out of nine tests beyond these limits, but still within 2SD limits. The mean threshold values here are very different with the larger scatter of the threshold values defined in CTAn.

4.2.1.3 Sink Sample Reproducibility, SkyScan1172

The same type of analysis was applied to the reconstructed images of the Sink sample. As there was a misalignment identified in the radiographs coming from SkyScan1072, these images failed the QAQC procedure (please refer to Chapter 3, section 3.7.2.1.3), only the data acquired in SkyScan1172 has been analysed.

XRF analysis of sink sample indicated 2.6 % Fe. The ratio between pyrite and sphalerite was based on QXRD data. Therefore calculated volume of dense phase considered to have iron would give 23.9% volume of sphalerite and pyrite combined. As the percentage of lead and sulphur was not available, the accuracy of calculating the volumes of galena, sphalerite and pyrite could not be confirmed. The gangue phase which contained iron was minor compared to quartz. Therefore, the data would be compared to XRD values as the difference between Fe assay measured with XRF and calculated using XRD data is not significant.

Table 15: CTAn image analysis results for sink sample scanned in SkyScan1172

Test	galena	other sulphides	dense component	gangue	total
	Volume mm^3	Volume mm^3	Volume mm^3	Volume mm^3	Volume mm^3
XRD	18.42	166.18	184.60	0.00	707.11
s11	18.31	163.20	181.51	521.25	702.76
s12	18.28	163.07	181.35	524.93	706.28
s13	18.16	160.77	178.93	523.96	702.89
s14	18.16	160.74	178.90	523.54	702.43
s15	18.04	160.27	178.31	524.21	702.52
s16	17.95	163.02	180.97	522.86	703.82
s17	18.11	164.30	182.41	521.90	704.32
s18	17.97	162.47	180.43	523.85	704.29
s19	17.86	160.65	178.52	524.91	703.42
mean	18.09	162.05	180.15	523.49	703.64
stdev	0.15	1.46	1.51	1.27	1.22
var	0.02	2.13	2.28	1.61	1.49
se	0.05	0.49	0.50	0.42	0.41
CoV	0.0083	0.0090	0.0084	0.0024	0.0017

The results given in Table 15 show that the galena and dense component volume measured in the sink sample using SkyScan1172 and when images are analysed using CTAn software was successfully reproduced in repeated tests. All results from the repeats lie within the 95% confidence limits on both side of the mean. However, t is significant with more than 99% confidence, and therefore the methods provided statistically different results than XRD method. The observations lie on the average within less than 9% of the mean. Figure 102 to Figure 104 also shows that XRD results lie outside of the 95% confidence limit around the mean of measured dense phase volume. This indicates that the results are precise but not accurate when compared to the XRD results.
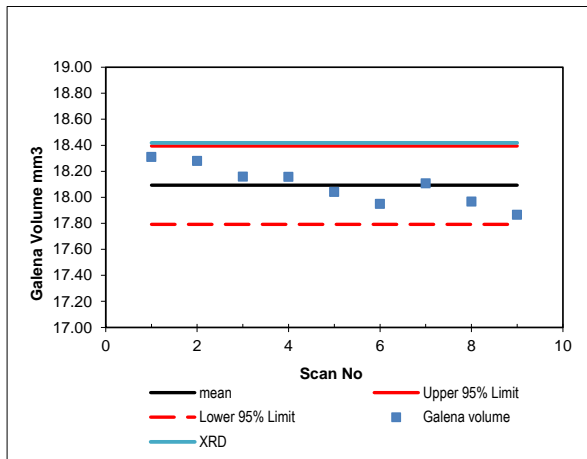
Figure 102: Sink sample scanned in SkyScan1172, CTAn image analysis, galena volume (mm^3)
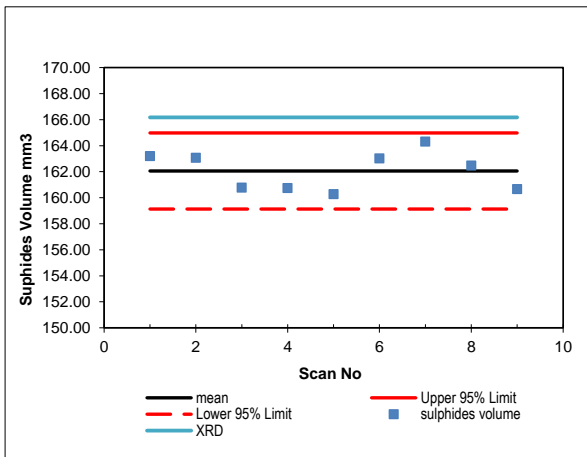
Figure 103: Sink sample scanned in SkyScan1172, CTAn image analysis, sulphide volume (mm^3)
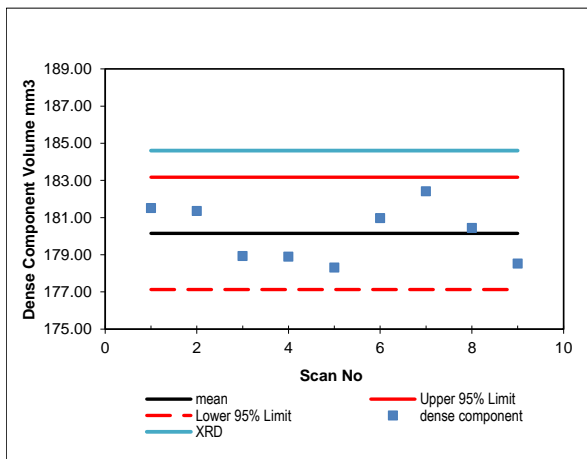
Figure 104: Sink sample scanned in SkyScan1172, CTAn image analysis, dense component volume (galena and other sulphides, mm^3)

The results of the eCognition8 image analysis of the same set of sink images are given in Table 16 and the data was also plotted and compared with the XRD mineral analysis data in Figure 105 to Figure 107.

Table 16: eCognition image analysis results for sink sample scanned in SkyScan1172

	galena	other sulphides	dense component	gangue	total
	Volume mm^3				
XRD	18.4	166.2	184.6		707.1
s11	21.0	164.8	185.8	523.9	709.7
s12	19.0	167.4	186.4	523.4	709.9
s13	13.1	171.1	184.2	525.4	709.6
s14	20.2	163.9	184.1	525.0	709.1
s15	16.0	167.8	183.7	525.6	709.3
s16	15.5	170.4	185.9	523.0	708.9
s17	16.6	171.0	187.6	521.6	709.2
s18	18.5	166.9	185.3	524.0	709.4
s19	17.9	165.4	183.3	525.8	709.1
mean	17.5	167.6	185.1	524.2	709.4
stdev	2.5	2.7	1.4	1.4	0.3
var	6.2	7.3	2.0	1.9	0.1
se	0.8	0.9	0.5	0.5	0.1
CoV	0.14	0.016	0.008	0.003	0.0004

The results given in Table 16 show that the galena and dense component volume measured in the sink sample using SkyScan1172 and when images are analysed using eCognition8 software were successfully reproduced with repeated tests. All results from repeats lie within 95% confidence limits on both side of the mean. Also, t is significant with less than 70% confidence, and therefore the methods provided statistically similar results

to XRD method. All observations except s13 lie on the average within less than 20% (galena volume) and 0.8% (dense component) of the mean.

Test s13 results are within 3SD from the XRD results and investigation revealed a high galena threshold in this dataset. However, considering that the total dense component results showed no significant difference between different tests for both volume and automatic threshold (Table 17). This confirms the fact that the technology needs further development in this field especially in reconstruction algorithm to be able to deal with multi mineral component particles. Higher proportions of the high density component introduced problems in the reconstruction process leading to reconstructed image artefacts which prevented accurate identification of threshold values in the image analysis process and caused greater variation of galena volume within tests.

Figure 105 to Figure 107 also shows that XRD results lie within the 95% confidence limit around the mean of measured dense phase volume. This indicates that the results are precise and accurate when compared to the XRD results.
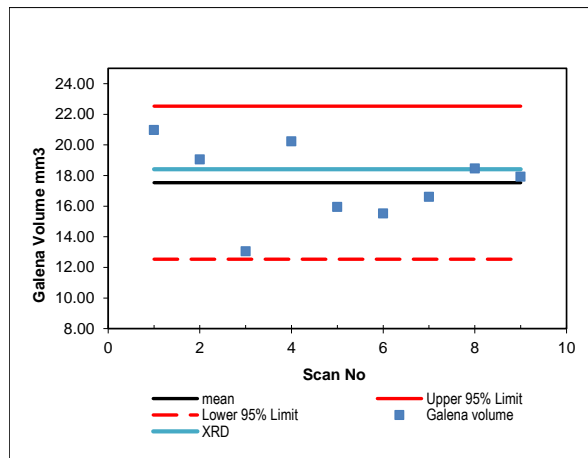
Figure 105: Sink sample scanned in SkyScan1172, eCognition image analysis, galena volume (mm³)
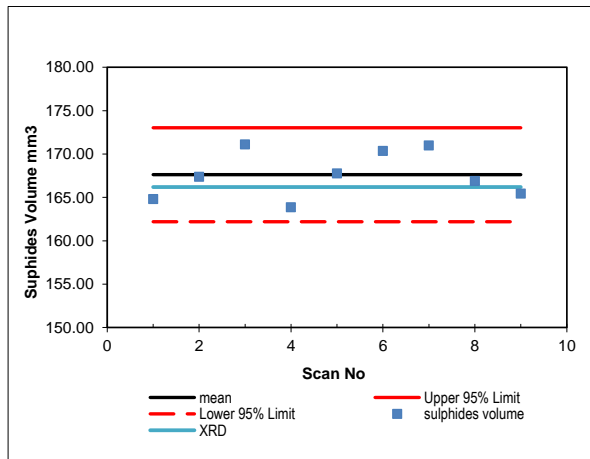
Figure 106: Sink sample scanned in SkyScan1172, eCognition image analysis, sulphide volume (mm^3)
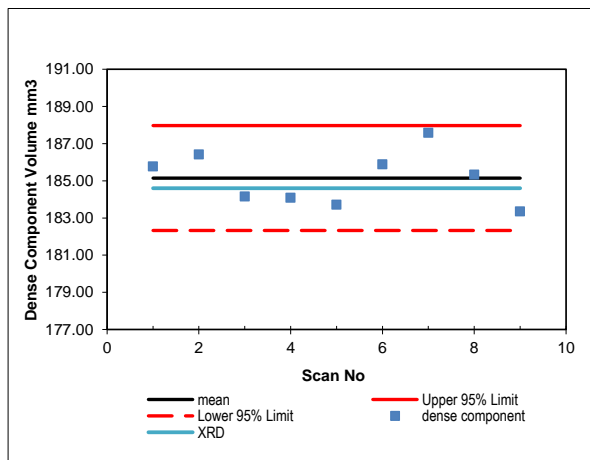
Figure 107: Sink sample scanned in SkyScan1172, eCognition image analysis, dense component volume (galena and other sulphides, mm^3)
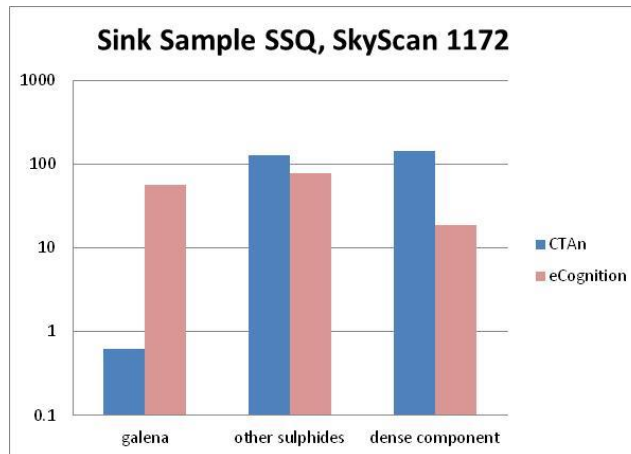
Figure 108: Sum of Squares of the results obtained in CTAn and eCognition for sink images acquired in SkyScan1172

Figure 108 shows the statistical difference between different image analysis modes, as well as within results generated with the same method. The variation within identified total volume of the dense component using SkyScan1172 system was less when images were analysed with eCognition8 than with CTAn. The galena volume results were more variable when using eCognition than CTAn, but still within acceptable limits.

Table 17: Automatic threshold values defined within eCognition analysis program for Sink sample, images acquired in SkyScan1172.

		automatic threshold	
	Test	mean_galena	mean_sulphides
SkyScan1172	11	92	32.3
	12	96	32.3
	13	113	32.3
	14	91	32.2
	15	104	32.2
	16	105	32.1
	17	102	32.1
	18	95	32.1
	19	96	32.1
	Mean	99.4	32.2
	STDEV	7.3	0.1
	Var	54.0	0.0

The variation in threshold values is smaller when the sulphide phase is considered, with all values between 95% confidence limit. This may also mean than the analysis software had no issues identifying the high density mineral phase in the cross sectional images analysed.

4.2.2 Grain Size Reproducibility

The grain size distribution is calibrated by exporting the volume of each grain using the eCognition algorithm. This allows the reproducibility of this data to be collected as a grain size distribution and to be used to estimate mineral liberation by section or volume. The grain size here was calculated as if the grains were cubic in shape, using the classified mineral phase volume from eCognition results tables. Figure 109 to Figure 116 present the grain size distribution of the sulphide mineral group for the float sample, galena and other sulphides for sink sample, analysed using eCognition8 software. Grain size volume distribution is given in appendix 9.14 and 9.15, the example of results table is shown in appendix 9.16 .

The distance between the cross section images was defined as one pixel in the NRecon software. Mineral grains of the high density phase are identified and classified in two dimensional cross-section reconstructed images using eCognition8. The two dimensional classified images in each slice are then connected in third dimension, and the mineral phase properties displayed in three dimensions.

Figure 109 and Figure 110 show the variations in grain size identified in SkyScan images of the float HMP sample analysed in eCognition8, especially in the range of around 100µm, also confirmed in volume distribution of identified sulphide grains. The reduction in grain size with time identified in images acquired using SkyScan1072 confirms the fact that there was a fault identified with the equipment.

The distribution of grain size occurrences shown in Figure 109 indicate that the s19 scan performed in SkyScan1072 did not produce high enough beam energy, and that larger grains of dense minerals did not have potential to show of their full size. Rather than having few thousand galena grains, like in other scans, s19 had over 17000 galena grains identified. The variation in grain size identified in the dense component grain size, confirms that reconstructed images suffered from artefacts of polychromatic X-ray beam, as mentioned in section 3.7.2.1.3. The dense component grain size was very variable (Figure

110) supporting the fact that the eCognition software had issues with identification of these grains, which was also confirmed earlier in radiograph check, section 3.8 and in section 4.2.1.1.
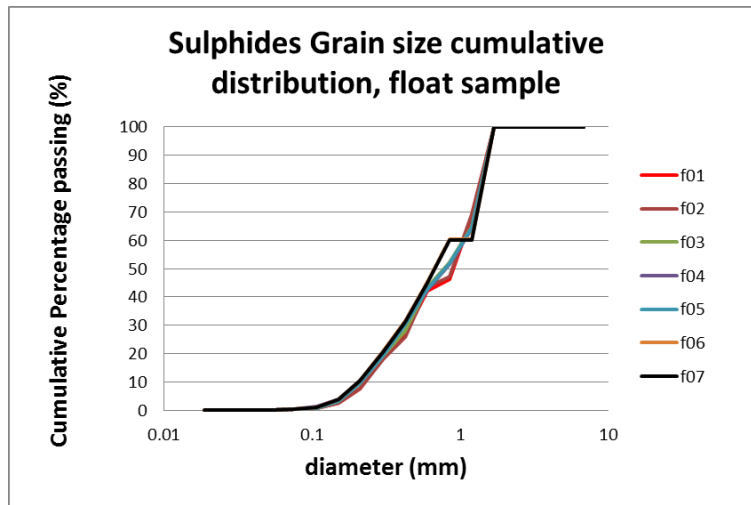
Figure 109: Sulphides grain size cumulative weight distribution for float sample scanned in SkyScan1072
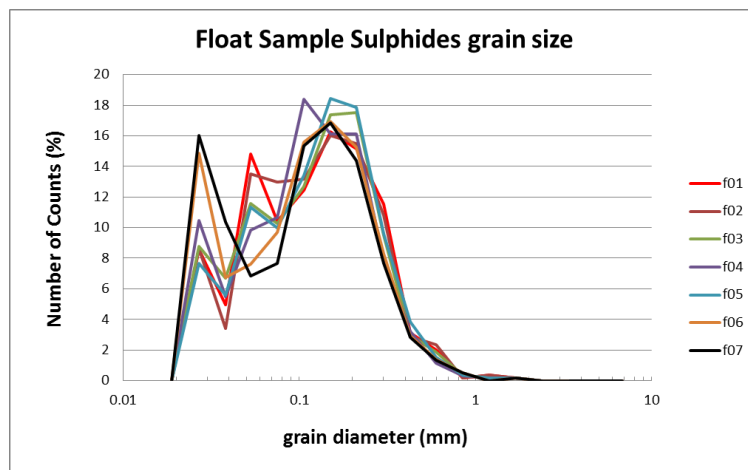
Figure 110: Total sulphides grain size, normalised curve, float sample scanned in SkyScan1072

The results shown in Figure 111 and Figure 112 indicate variation in acquisitions performed on two different days using SkyScan1172. On day 1 tests f11 to f13 were acquired, and tests f14 to f18 were acquired the following day. The variation did not influence cumulative grain size distribution. The difference in final results is not statistically significant as mentioned earlier. The post alignment reconstruction algorithm option was different for these scans which introduced the difference in reconstructed images.
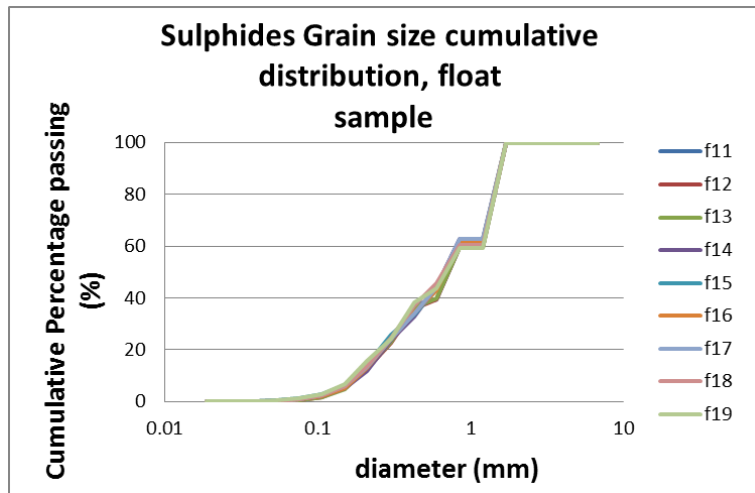
Figure 111: Sulphides grain size cumulative distribution for float sample scanned in SkyScan1172
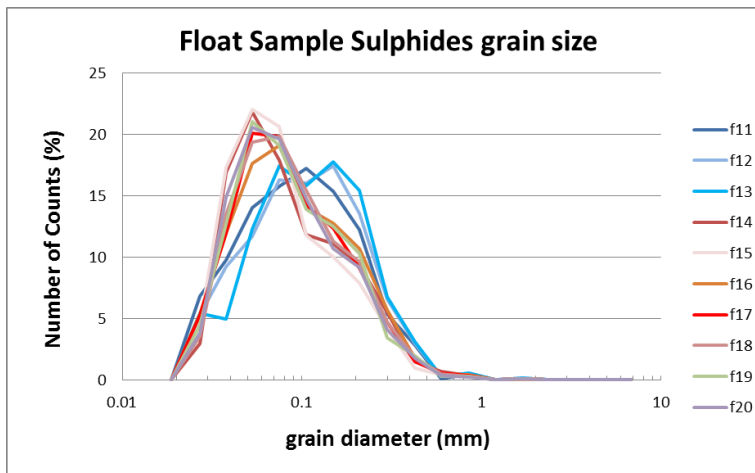
Figure 112: Sulphides grain size, normalised curve, float sample scanned in SkyScan1172

If considering data from equivalent or similar SkyScan1172 acquisitions (f14 to f20 test) and acquisitions from SkyScan1072, it can be concluded that there is significant variation within tests acquired in SkyScan1072. This confirms the issue identified with the data.

The results shown in Figure 113 to Figure 116 show consistency in grain size of identified galena and sulphide phase in the sink sample. The observed variation of sulphide grain size was small, with the tests providing equal sulphide volume and grain size results.

Sulphide grain size is equal for all tests, which means that the data passed the QAQC checks presented in this Chapter.
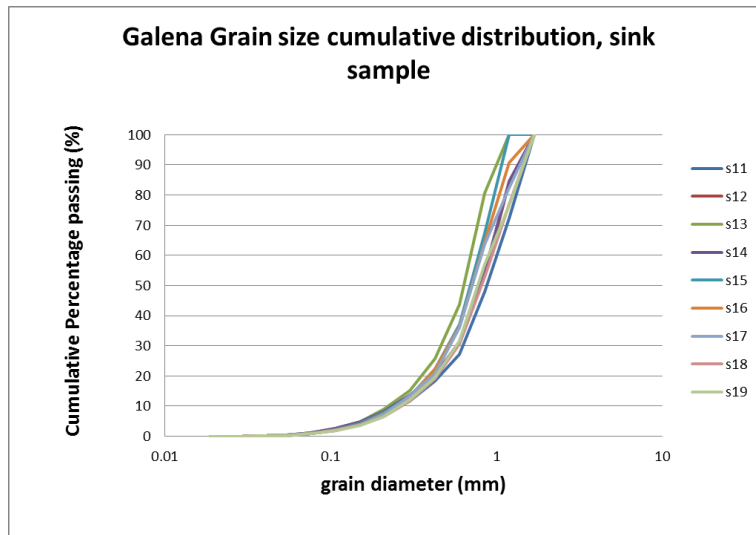
Figure 113: Galena grain size cumulative distribution for sink sample scanned in SkyScan1172
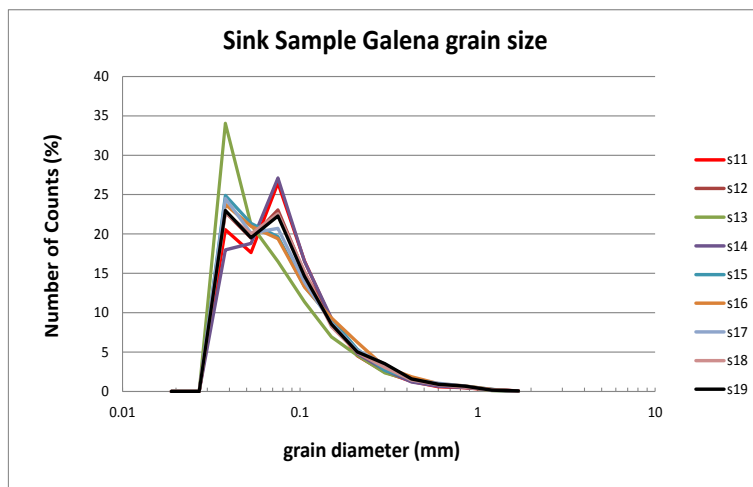
Figure 114: Galena grain size, normalised curve, sink sample scanned in SkyScan1172
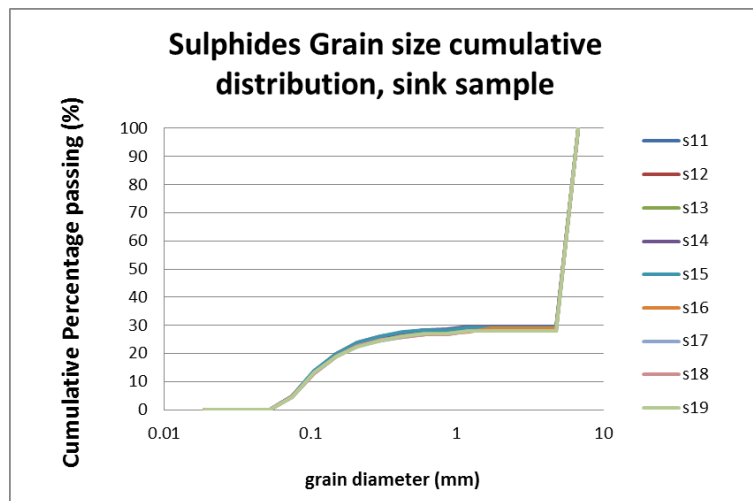
Figure 115: Sulphides grain size cumulative distribution for sink sample scanned in SkyScan1172
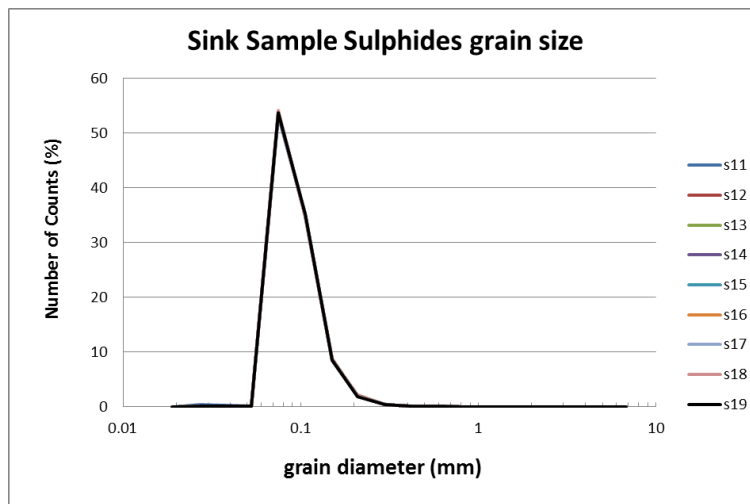
Figure 116: Sulphides grain size, normalised curve, sink sample scanned in SkyScan1172

4.2.3 Operator error

A series of tests was performed to measure the operator error in calculating the volume of the high dense mineral phases within CTAn image analysis software. In total twenty three particles were measured for weight and for volume using wet/dry technique. The same particles were analysed using SkyScan1172 using the same acquisition and reconstruction settings.

The analysis of the cross section images by two operators are presented in Table 18. A Paired Comparison t-test was performed. The observed value of t is significant at more than 99.5% confidence indicating that the two operators gave significantly different results when measuring the volume of two high density mineral phases. This confirms the fact that threshold definition by individual operators when analysing this type of the cross-sectional images was not acceptable. However, the volume of particles measured by both operators was not statistically different from measured wet/dry volume. This indicates that the Micro CBT can be used for measuring total volume as confidence in defining threshold between air or foam and particles is higher than in defining the threshold between individual mineral phases. The results of measuring the high density phases are shown in Figure 117.

224
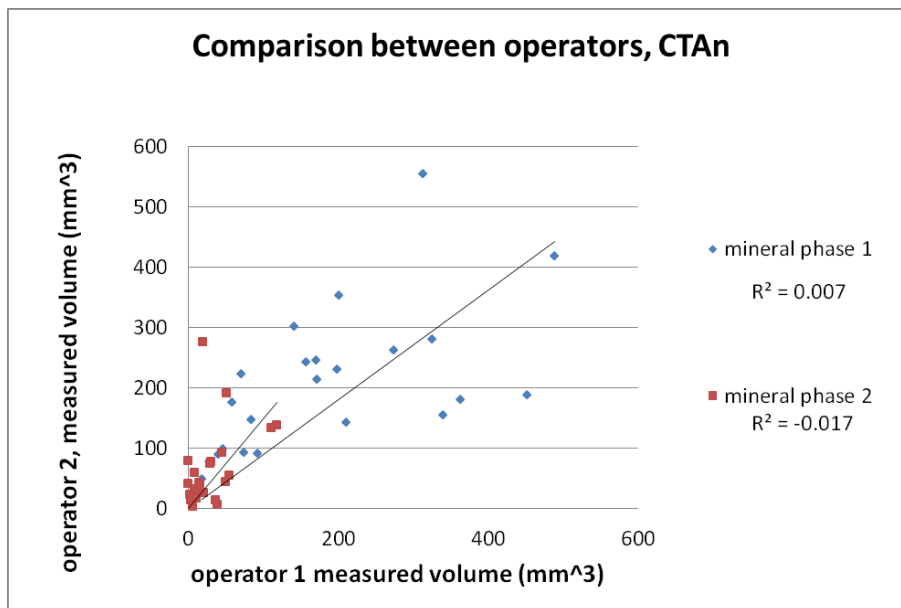
Figure 117: The volume of high density mineral phases, using CTAn

However, when the data has been combined for each operator (wet/dry technique), and the particle calculated weight using mineral densities and the volume measured in CTAn, the results are comparable with measured particle weight (Figure 118). The mineral phase 1 is sphalerite-pyrite-magnetite mineral group and the mineral phase 2 is galena. Although there are differences between individual operators when measuring mineral phase 1 and 2, combined high density phase volume (mineral phase 1 and 2) shows less discrepancies.

The particle volume is calculated using wet/dry measurement technique (ASTM 2009). The particle dry weight was measured on scales, then wet weight was measured by inserting it in the water on scales. These values are then used to calculate bulk densities and volume. The results were then compared with measured volume using CTAn and presented in Figure 119. It is therefore essential to calibrate the greyscale levels within CTAn using some other known technique, as the total volume and weight results can be misleading.
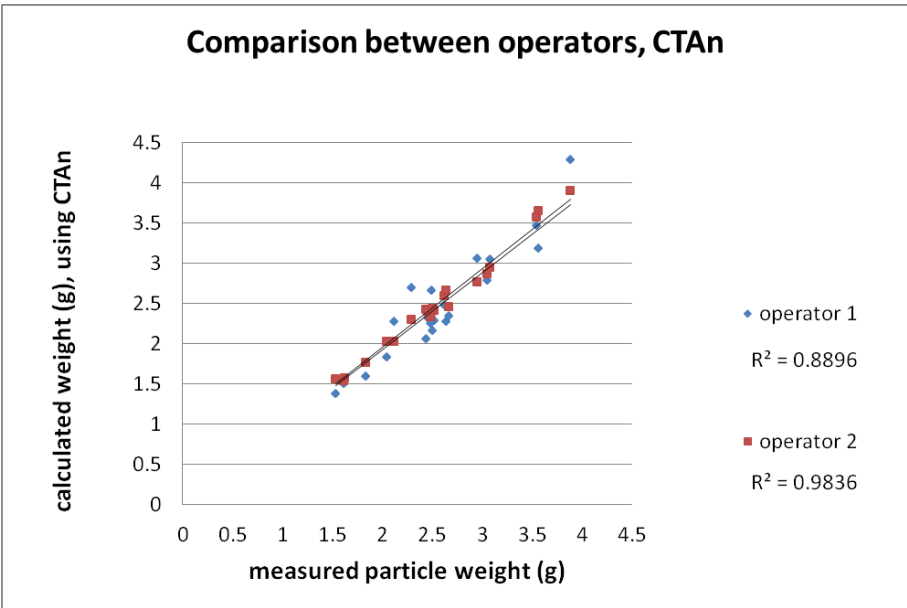
Figure 118: The particle weight measured and calculated using CTAn
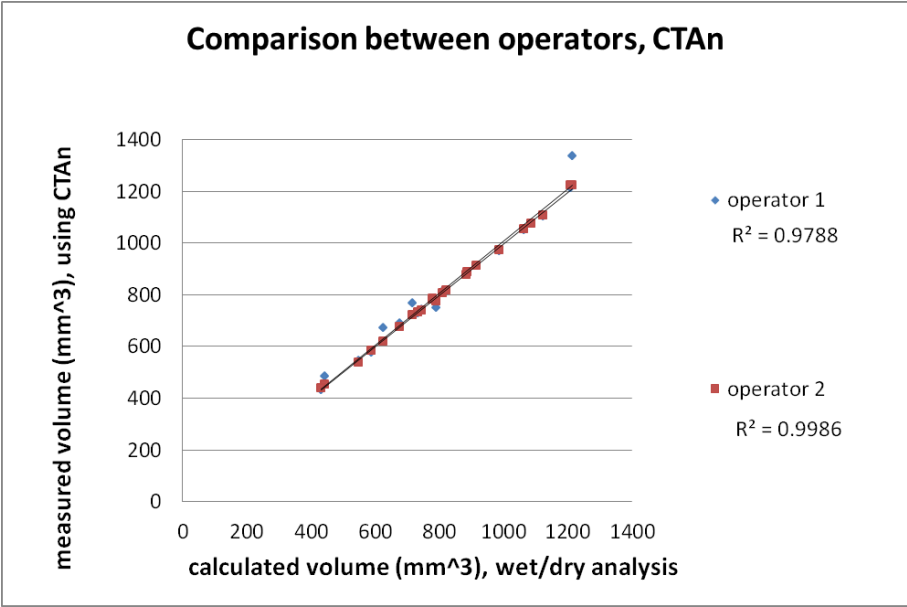
Figure 119: The particle volume measured using CTAn and measured using wet/dry density analysis

Table 18: Comparison of Micro CBT results obtained on the same images by two operators in CTAn

Sample number	Particle mass					Particle volume					Mineral phase volume (mm³) Micro CBT					
	measured	Micro CBT				measured	Micro CBT				Mineral phase 1			Mineral phase 2		
		Operator 1	Difference OP1 (%)	Operator 2	Difference OP2 (%)		Operator 1	Difference OP1 (%)	Operator 2	Difference OP2 (%)	Operator 1	Operator 2	Difference (%)	Operator 1	Operator 2	Difference (%)
1	3.1	3.1	0.98	3.0	4.30	1086.6	1074.0	1.16	1076.2	0.96	210.4	142.9	6.21	5.1	13.3	-0.69
2	3.1	2.8	8.62	2.8	6.10	1123.2	1102.8	1.82	1108.0	1.36	17.6	49.4	-2.83	3.1	13.6	-0.94
3	3.9	4.3	-10.29	3.9	0.49	1213.6	1337.1	-10.18	1124.6	-0.91	488.1	418.5	5.73	117.9	137.6	-1.62
4	2.1	2.3	-7.09	2.0	4.27	626.4	671.4	-7.19	617.9	1.35	325.5	280.9	7.12	39.0	6.2	5.23
5	1.8	1.6	13.03	1.7	3.67	587.2	577.9	1.59	585.1	0.36	84.1	146.6	-10.63	8.9	59.0	-8.54
6	2.6	2.5	5.55	2.6	1.22	779.3	785.5	-0.80	785.5	-0.80	273.9	262.0	1.52	51.0	191.6	-18.04
7	2.6	2.3	13.70	2.6	-0.97	715.0	767.0	-7.27	720.1	-0.72	200.7	353.9	-21.43	19.1	275.3	-35.84
8	1.6	1.5	5.35	1.6	3.54	443.4	486.5	-9.72	451.3	-1.79	171.3	213.6	-9.53	29.8	77.5	-10.76
9	2.4	2.1	15.48	2.4	0.79	713.9	729.1	0.38	733.7	-0.25	141.7	301.5	-21.84	0.2	79.3	-10.83
10	1.5	1.4	9.97	1.6	-1.37	432.8	431.1	0.40	438.8	-1.38	170.2	245.6	-17.43	14.6	42.4	-6.44
11	2.5	2.2	13.68	2.4	2.68	809.8	815.0	-0.64	805.0	0.59	70.3	223.6	-18.93	0.1	41.2	-5.07
12	3.6	3.2	10.48	3.6	2.40	1062.2	1051.5	1.00	1052.8	0.88	312.8	555.1	-22.81	28.7	74.3	-4.29
13	2.3	2.7	-17.31	2.3	-0.37	790.1	749.9	5.09	776.0	1.78	451.8	187.9	33.40	49.2	43.9	0.67
14	2.5	2.7	-6.40	2.4	4.00	820.0	814.2	0.70	817.2	0.34	340.0	154.8	22.60	44.4	92.8	-5.90
15	2.5	2.3	9.43	2.4	4.03	778.5	784.9	-0.82	781.2	-0.35	157.0	242.3	-10.96	54.1	54.1	0.00
16	2.5	2.3	5.44	2.4	2.37	887.4	884.5	0.33	887.4	0.00	45.8	98.34	-5.92	36.6	14.4	2.51
17	2.5	2.2	9.50	2.3	6.17	883.9	878.5	0.61	878.5	0.61	27.7	78.0	-5.69	5.8	2.8	0.35
18	2.6	2.3	11.96	2.5	8.04	916.5	911.3	0.57	911.3	0.57	39.7	89.3	-5.41	1.8	23.2	-2.34
19	3.5	3.5	2.04	3.6	-0.80	1207.7	1212.3	-0.38	1222.1	-1.20	197.9	230.3	-2.69	111.1	133.1	-1.82
20	2.1	2.0	4.36	2.0	4.72	744.3	743.9	0.05	738.9	0.72	92.4	91.9	0.06	10.7	16.8	-0.82
21	1.6	1.5	7.23	1.5	4.99	548.0	546.3	0.31	539.0	1.64	73.9	92.0	-3.29	7.7	32.6	-4.56
22	2.0	1.8	10.31	2.0	0.93	677.3	689.2	-1.76	676.6	0.11	57.7	176.4	-17.53	15.1	37.9	-3.36
23	3.0	3.0	-3.68	2.8	6.53	985.7	969.3	1.66	971.2	1.47	363.2	180.3	18.55	21.0	26.1	-0.51

4.3 Conclusions

This chapter demonstrates that reproducible results can be achieved by using the SkyScan1172 microtomography instrument and analysing images using eCognition8 software. A comparison of the effect of the aging of the X-ray tube revealed that a quality assurance check is necessary when using this type of analysis when scanning rocks. The total distribution of photon counts per rotation step should be considered (discussed in Chapter 3) as well as the consistency of the number of photon counts per sample. The objective is to have the same number of total photon counts per rotation step per sample.

The image analysis software program eCognition 8 provides an opportunity to reduce the operator contributing to the analysis error in defining adequate mineral threshold values. It was found to be very difficult to decide on a threshold value manually by examining the images, as is the case in CTAn. Even the smallest difference in a greyscale threshold value may result in a different mineral volume value and the resulting mineral grain size distribution.

This operator error in calculating the volume of the high density mineral phases within CTAn image analysis software has been assessed. A Paired Comparison t-test was performed. The observed value of t is significant at more than 99.5% confidence, showing that the two operators gave significantly different results when measuring the volume of two high dense mineral phases (Table 18).

Results from the images of Float sample data acquired in the SkyScan1072 system and analysed in CTAn gave consistently lower sulphides volume than calculated from XRF values, as it was not able to detect mineral grains less than 15µm in size. Values obtained with eCognition software on the same set of images indicated improved results when compared to the XRF results. Figure 108 shows the variation in mineral content observed in CTAn and eCognition, where the difference was very apparent in the volume of dense component. eCognition software with automated thresholding provided more consistent

results for this type of the analysis. It appeared that the images acquired in SkyScan1072 and analysed in eCognition gave better results that the one acquired in SkyScan1172. However the result of SkyScan data provided total volume of dense phase and XRF involved only minerals with Fe present in them therefore excluded all galena and sphalerite volume.

The results of the analysis of images of the Float sample acquired by the SkyScan1172 show the variation in results observed on different dates of acquisition in Table 6. Post alignment value difference in the reconstruction algorithm influenced this variation. A similar pattern of variation was noted for both image analysis methods. Another observation here was that a smaller variation in mineral phase volume was recorded in results observed within eCognition image analysis software with automatic thresholding as shown in Figure 101.

It was noted that the counts of photons for runs F06 and F07 were significantly lower than those for F01-F05, as shown in Table 9. This supports the idea that there is a quality issue in the acquisition process. This is one more way of assuring the quality of the acquired image data and that is by controlling the stability of the number of photons counted per radiograph (Table 9). The eCognition software managed to deal well with the count variations by automatically identifying the threshold value to be applied in the analysis process tree. The decrease in greyscale threshold value is noted in Table 14. This procedure helps to obtain more accurate high density mineral volume estimates.

For quantitate analysis chemical assay is recommended as a quality check, which is also common when measuring mineral content using SEM based technologies.

The main conclusions from this chapter are:

1. Large differences in the counts of photons per radiograph per sample indicate poor scan quality.

2. Scans of the same sample performed on different days showed variation in the measured volume of the high density mineral phase. The variance of the same day scans was lower. The measured grain size distribution was also to some extent different for scans performed on different days (Figure 112) but this difference was not significant (Figure 100).

3. The sample with a higher content of high density component had a lower coefficient of variation than the sample with lower content of high dense mineral component. The stability of these images was better. Figure 115 shows the more stable grain size distribution of the high density component.

4. Automatic threshold values defined for S13 in eCognition8 for measuring the galena volume was obviously somewhat different from other tests, giving a different grain size distribution trend (Figure 114). However, the complete volume of the dense phase indicated the correct selection of the second threshold value.

5. The galena grain size distribution was consistent for images acquired in SkyScan1172.

6. The boundary between sulphide minerals and gangue minerals was well defined in images coming from the SkyScan1172 system (refer to Table 14 and Table 17). There was a single greyscale threshold value for sulphides in the Float images, 96, and a mean sulphides greyscale value of 32.2 ±0.1 for the sink sample.

7. The sum of squares of differences between CTAn and eCognition8 results and XRD results on the same particles indicated a problem with identifying the volume of the sulphides with CTAn based on the operator selection of the greyscale threshold value. The results of the high density component volume of Float particle acquired in SkyScan1172 and analysed in eCognition8 were closer to the XRF mineral estimate values than the results acquired in the SkyScan1072 and analysed in CTAn. To analyse images using CTAn, a calibration sample is necessary to define the greyscale threshold values.

5 Quantitative analysis of minerals using X-ray microtomography procedures

5.1   Overview

A method is presented for definition of grayscale threshold values for each mineral present in multiphase particles. It allows a mineral characterisation comparison between the technologies used in an automated Scanning Electron Microscope (MLA) and a Micro-cone Beam Tomograph (SkyScan1172 Micro CBT system). In the present work, a single multiphase particle was analysed with SkyScan1172 at resolutions ranging from 6-14μm voxel size.

During data acquisition, a number of radiographs were collected and analysed to generate three-dimensional tomographic reconstructions. The particle was subjected to precise physical cutting and then quantitative SEM analysis of the two cut surfaces with a MLA system. A detailed comparison of the MLA and tomographic images of the same two layers of the particle was undertaken with eCognition 8 image analysis software. Uncertainty regarding the identity of minerals from radiographs can in part be resolved by calibrating greyscale levels with the MLA. This chapter describes the development of the above method. The following section investigates the variation of X-ray attenuation by mineral grains in three dimensions.

5.2   Introduction

The aim of the present work is to develop a technique which will help to define the threshold levels for minerals within multiphase particles using X-ray microtomography procedures such that the mineral phases identified are defined without any noise or blurring included in mineral grain image.

Before CBT became available, measurements of mineral texture including liberation analysis work was typically based on image analysis of the particle considering only two dimensional (2D) sections of the particle and estimating them in three dimensions (3D) using some form of stereological adjustment. By using the technique outlined here, the complete three-dimensional information about the internal structure of the multiphase particles (low density, medium density and high density mineral groups) can be obtained. This 3D information can generate 2D sections, particle surface liberation, linear intercepts and particle counts as required.

The possibility of measuring the liberation of the particles with the development of the X-ray micro tomography technique was first published in 1996, when Miller and Lin applied the technique to determine liberation spectrum of coal particles. (Lin and Miller 1996) They reported a detailed accounting of grain size distribution, interfacial area, shape features and textural information in coal particles. The difference between Lin and Miller's work and this project is the ability to test high density mineral components in multiphase particles as opposed to low density coal particles and to quantify the variation (or error) in the process. High density minerals produce more challenges in image acquisition and image analysis processes. Multiple high density minerals (in this case chalcopyrite, pyrite, magnetite and barite) introduce a complex intensity histogram which makes selecting threshold values between gangue minerals and image noise as well as between dense minerals and gangue very challenging. The size of the measured particle was greater here than for the coal particles conducted by Lin and Miller (1996).

As mentioned previously in section 2.6.4.4, even with advanced technology (over 2 times higher energy, better resolution, linear and quadratic curve fitting) Ghorbani (2012) struggled to identify different minerals in his work, where he grouped sphalerite and galena although sphalerite properties were significantly closer to chalcopyrite group minerals than galena. In earlier work there was no calibration to confirm the decision of grouping sphalerite and galena mineral grains, and in (Ghorbani et al. 2013) the data was combined with a destructive QEMSCAN method but only cracks and micro porosity was measured using Micro CT. Ghorbani did not attempt to separate minerals with close effective atomic number (Ze values), such as pyrite (Ze 22), chalcopyrite and pyrrhotite, but claimed to separate chalcopyrite from sphalerite although the difference between chalcopyrite (Ze 25) and sphalerite (Ze 27) was minor compared to galena (Ze 78.25) and sphalerite.

The challenge of the present work is to use the calibrated greyscale values of the SkyScan1172 images for groups of minerals as opposed to individual minerals. The publication was presented at SMI RHD conference (Bajic 2010). Several examples of ore texture characterisation have been published in Evans et al. (2012) where MLA system was used to identify minerals in X-ray tomography images.

In this work, the problem has been resolved by taking the image of the same cross section through the particle with X-ray SkyScan1172 (SkyScan 2010b) and MLA (Gu 2003) and analysing those images using MLA Image analysis software and eCognition8 image analysis intelligence software. As the MLA is able to precisely identify a wide range of minerals in the polished section, and the same mineral grains can be located within the tomographic images.

As previously mentioned, identification of mineral groups was based on differences in attenuation coefficients of the minerals. In the ore studied here the first group will be the one with the lowest greyscale values called gangue (greyscale level less than 30 on a scale from 0-255). The second is the valuables group (greyscale between 30 and 75 to 80). The last group consists only of one mineral, barite whose greyscale level is over 75.

The primary objective of this calibration method is to investigate the greyscale level of the mineral phases. The second objective is to investigate the properties of the mineral grains such as shape and volume, in three dimensions. The last but not the least objective is to show the ability of the SkyScan1172 to maintain the shape of the identified mineral grains in virtual sections inside unbroken particles.

The area of identified mineral grains was calculated from SkyScan1172 and MLA images and then compared. There is a difference in greyscale levels between mineral groups and these differences have been accurately determined in this work by calibrating the X-ray microtomography cross section image and the MLA image of the same cross section of the particle. However the technique is only valid for that particular scanning and reconstruction, as it is dependent on properties of the particle, such as density and size.

Image processing was used to achieve a characterisation of each mineral group which was as realistic as possible. This technique enables novel characterisations of the mineral groups since greyscale levels will not be constant per mineral. They will depend to some degree on the size of the grain.

There are a number of factors that can affect the quality of the images. The operator can eliminate or significantly reduce some of these factors. For example, the rotation steps or exposure time may be adjusted as detailed in Chapter 4. However, most of them are highly dependent on the sample properties such as its composition and this cannot be optimised. For example, if the sample size is -13.2 + 9.5mm, with a high content of galena (investigated with the same equipment as used in this research) it would be almost impossible to obtain a clear image with no noise, ring artefacts or beam hardening present because a high volume of galena is essentially impenetrable to low energy X-rays. The reconstruction methods require at least some signal to mark different phases.

Micro CBT has been developed for medical imaging where the energy required for penetrating human tissue (for example flesh and bone) is much lower than for minerals. Therefore artefacts present in reconstructed images are caused by the assumption that the beam is monochromatic. The artefacts are more severe when we are dealing with high

density minerals (for example the likelihood of artefacts occurring increases in this order: gangue – chalcopyrite – galena). The problem with acquiring high density mineral images has been discussed in section 3.3. Although no significant issues have been identified here with artefacts, it is possible to reduce them if not to eliminate them, with the application of this new method.

5.3   Experimental method

SkyScan1172 technology enables the complete internal structure of particles to be estimated from measured two-dimensional shadow images. These images are reconstructed into virtual cross-section images of the particle. The instrument used in this research was SkyScan1172 High resolution desktop Micro-CT (SkyScan 2010b). The measurements conducted were non-destructive and with best resolution of about 1µm with a sample size of 8mm. The following section provides details of the calibration method developed. The experimental scan properties were defined in Chapter 3.

5.3.1 Sample properties and data acquisition

The high resolution SkyScan-1172 X-ray CT scan was used to scan a multi component particle -13.2 + 9.5mm in size using an X-ray energy of 74 kV and 104 µA current for 5.5 s for each radiograph at 9 degrees rotation. The NRecon reconstruction software (SkyScan 2010a) was used to reconstruct cross sections of the particle and then integrate them into a three dimensional internal microstructure. The reconstruction program uses a modified Feldkamp algorithm (Feldkamp et al. 1984) with automatic adaptation to the scan geometry. Cross section images were then saved in bitmap (BMP) format files. In the second stage of the experiment, the particle was cut in half using a diamond saw. Each surface was polished and carbon coated for MLA examination.

Typical radiographs of the original particle and cut sections are presented in Figure 120.
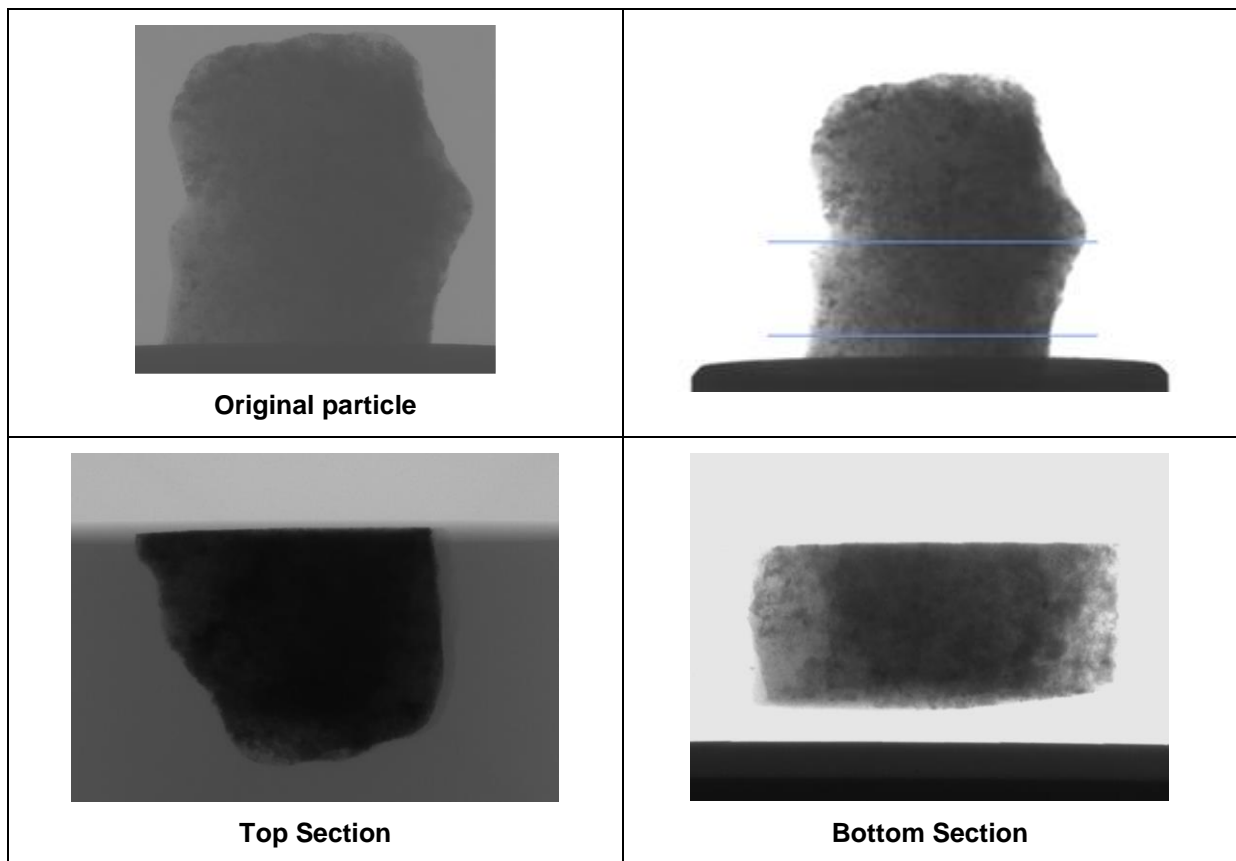
Figure 120: Radiographs of the acquired X-ray tomography scans

For the purpose of this research, the MLA measurement technique called XBSE (X-ray back-scattered electron) has been used. This measurement collects a series of BSE images. Epoxy and background noise were removed during the particulation stage of collecting high resolution images in MLA. In the pre-segmentation phase, grain boundaries are determined based on BSE greyscale differences. Since we have used the cross section of the whole particle in its original size as a polished section, there were no undersize particles to be removed in this stage.

A raw greyscale back-scattered electron image file and a coloured X-ray image file with grains identified from the pre-segmentation were generated with XBSE measurement. The mineral grains were identified offline based on their characteristic X-ray spectra and using well established mineral standards. This classified image was the image compared with the X-ray microtomography image. Figure 121 and Figure 122 show the cross sectional images of the particle before and after cutting and the XBSE classified image of the polished cut.

237
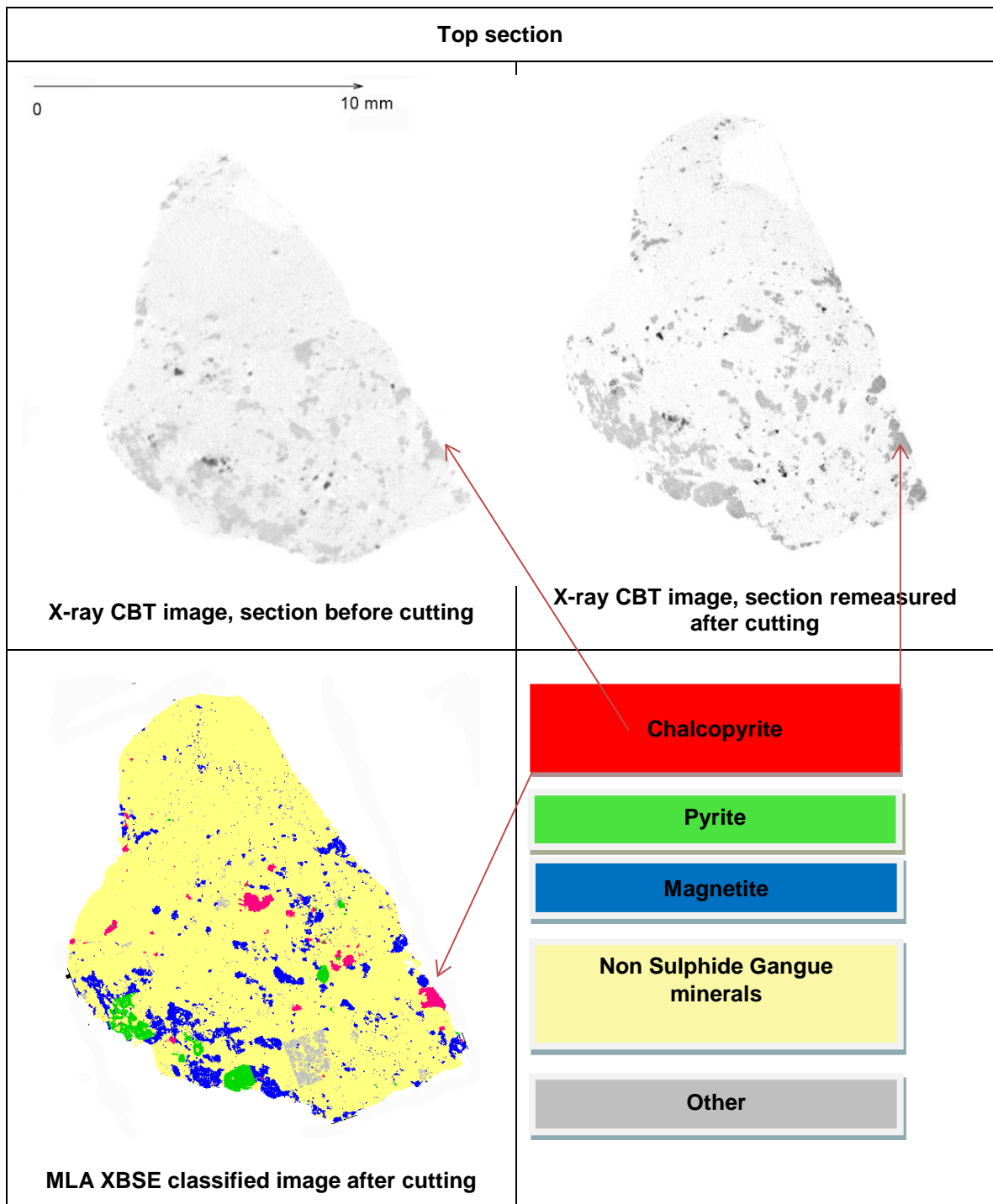
Figure 121: Top section of the particle, virtual cross sections acquired in X-ray CBT and reconstructed with NRecon, and classified XBSE polished section image

238
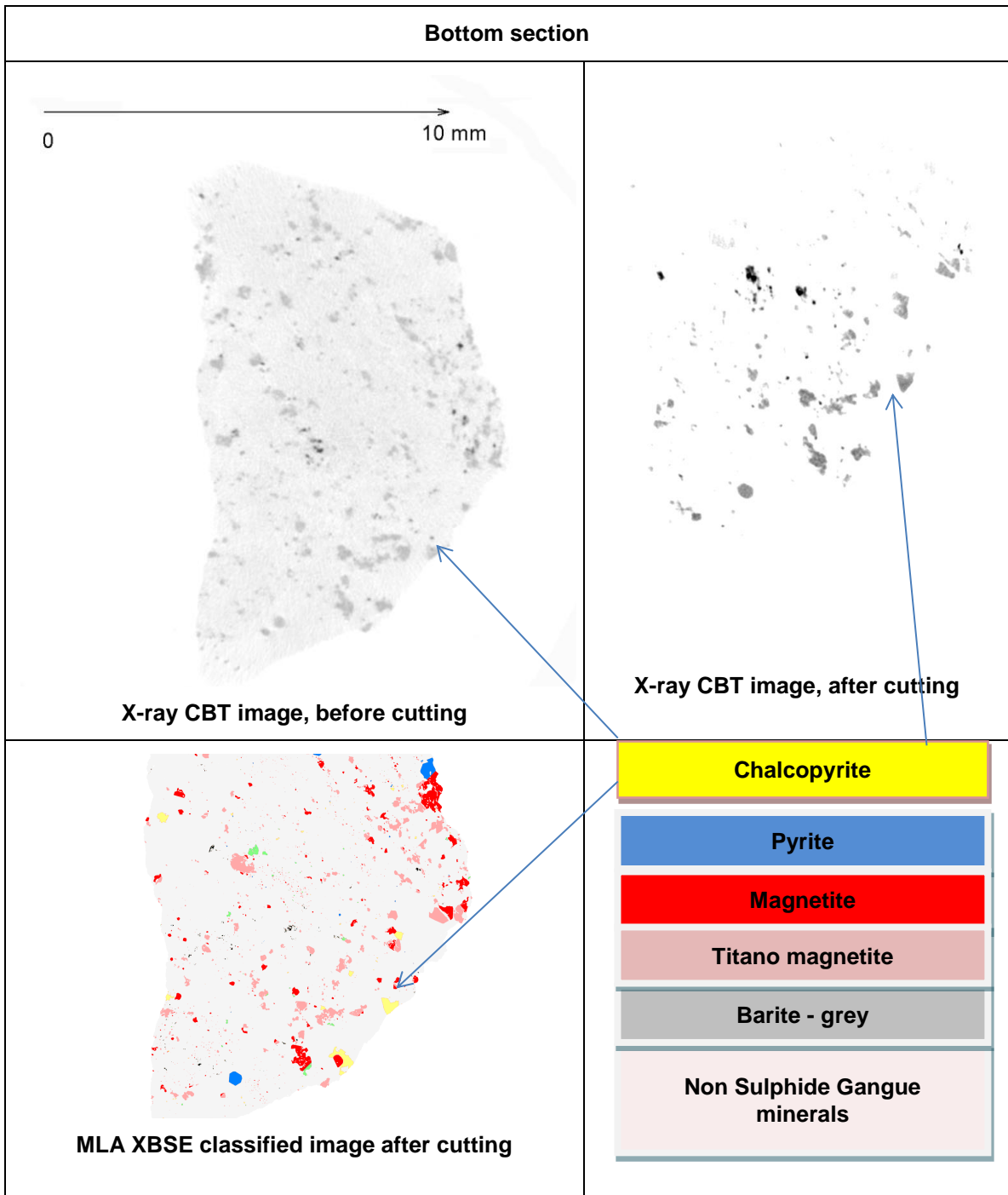
Figure 122: Bottom section of the particle, virtual cross sections acquired in X-ray CBT and reconstructed with NRecon, and classified XBSE polished section image

The two polished sections of the particle showed excellent alignment with the virtual cross section acquired before cutting. The X-ray CBT image in Figure 122 after cutting has a region missing which was the consequence of difficulty to cut and polish as a perfect planar surface. Although great care was applied to the cutting and polishing, a slight

declination of around 5µm was observed. Despite this declination, the shape of the mineral grains can be defined and the sections compared with the XBSE image.

The distance between each of the cross section images shown in Figure 123 is 1µm. the cross section image labelled as 516 is the top surface. As already mentioned, the whole surface could not be seen as part of it was lost in polishing. The image labelled as 515 is 1µm below 516. As the virtual cut lines progress down the particle, more of the area can be seen. The cross section images labelled as 509 and 508 reveal the complete particle section.

cross section 516

cross section 515

cross section 514

cross section 513

cross section line 512

cross section line 510

cross section line 509

cross section line 508
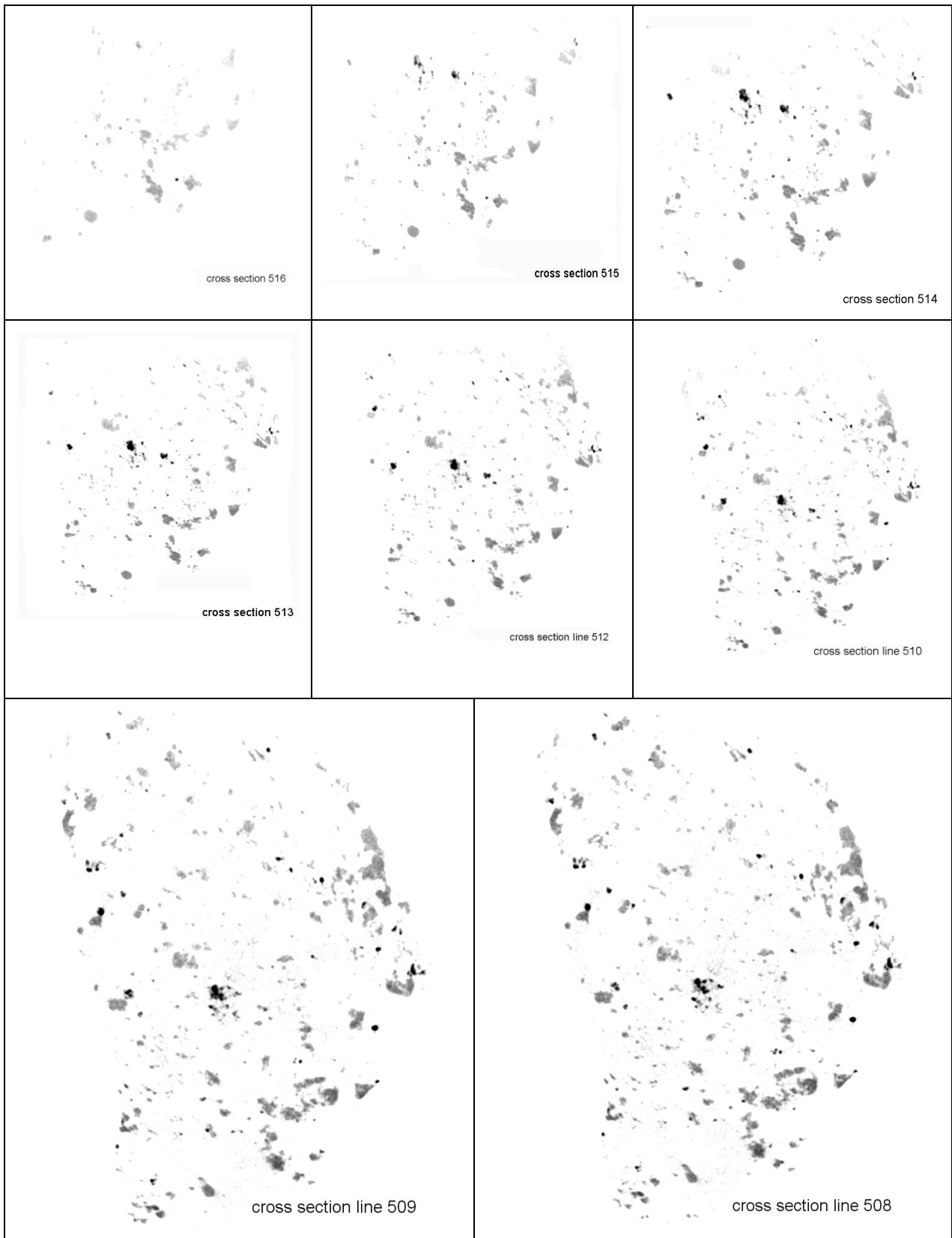
Figure 123: Virtual cross section X-ray SkyScan1172 images of the polished section scan, line516 being the top section

241

5.3.1.1Rock composition

The results of MLA mineral analysis and eCognition 8 image analysis of the MLA image are presented in the Table 19 below. The MLA (sectional) relative error provided here was taken from previous research conducted at JKMRC (Hartner 2012).

Table 19: MLA and eCognition Results Table, % of minerals, cross section of the particle

Mineral	MLA calculated modal mineralogy (%), grouped	95 % confidence limits	
Titano-magnetite	3.54	3.53	3.7
Magnetite	2.14	2.14	2.24
Chalcopyrite	0.06	0.57	0.60
Pyrite	0.51	0.51	0.53
Titanite	0.10	0.09	0.09
FeOxide	0.17	0.17	0.18
Other	92.97	92.83	97.25
Relative error 0.027			

The image analysis programing set used in eCognition was applied to the MLA BSE image and X-ray reconstructed images analysed in eCognition.

5.3.1.2Calibration Method

Figure 124 a, b and c shows the same cross section of the particle obtained with MLA and SkyScan respectively. It is obvious that mineral grains of very similar shape are present in both images. As noted earlier, CBT does not produce images with as much contrast as the BSE image in an SEM. Hence, the shape of the mineral grains observed in the SkyScan1172 was considered to be sufficiently accurate.
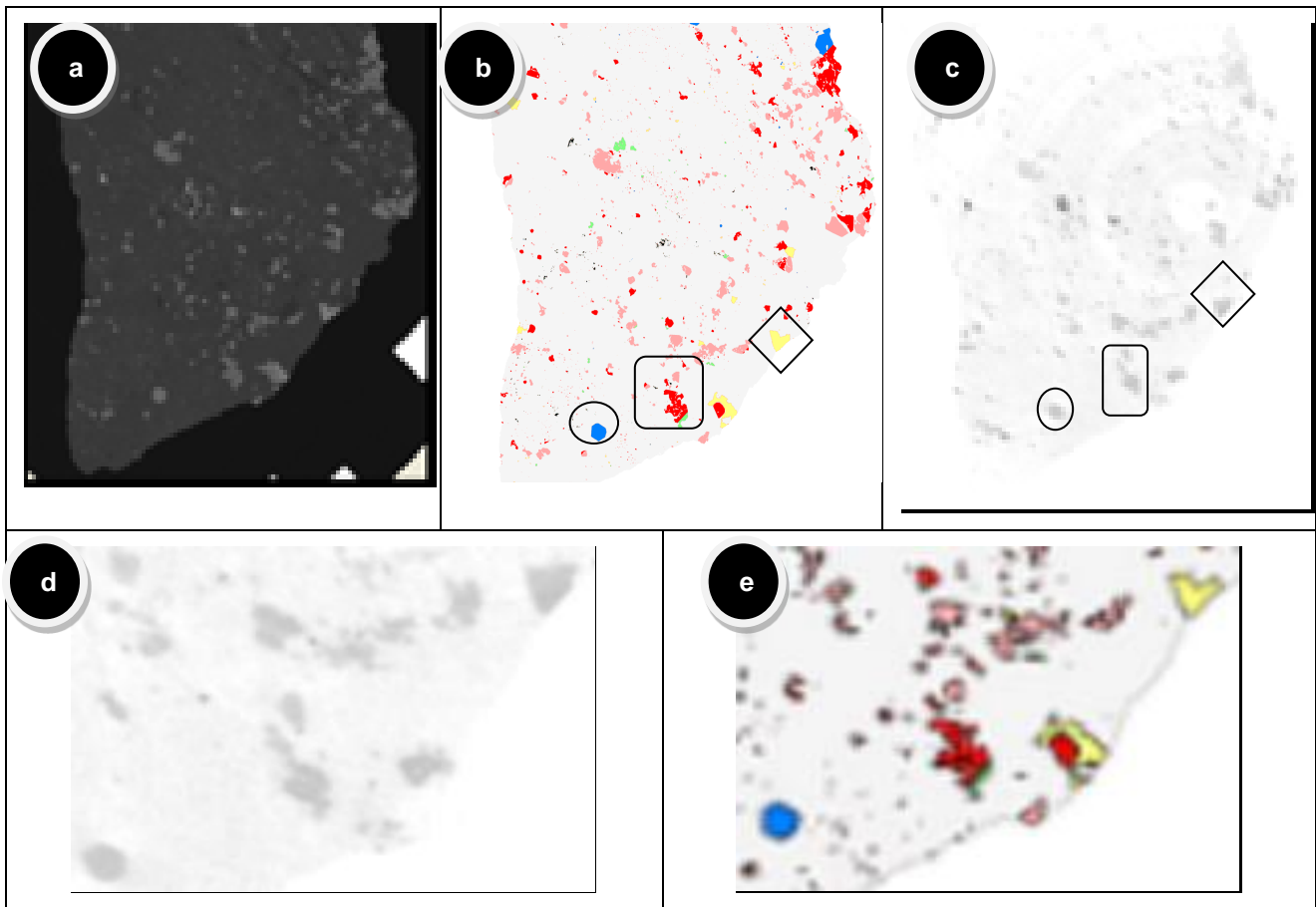
Figure 124: Cross section image of the particle a) MLA BSE; b)classified XBSE image; c)SkyScan1172 reconstructed cross section; d) enlarged section of the SkyScan1172 image c; e) image d classified in eCognition8. Mineral grains presented: magnetite (rectangle, red), chalcopyrite (diamond, yellow) and pyrite (circle, blue)

Note: the quality of the image (e - blurred) is reduced here due to the print and display properties,

5.3.2 Image analysis, problems and improvements

A series of tests and investigations into mathematical software were conducted to define an automated image correction process. The aim here was to create an additional degree of accuracy on the previously acquired images, to achieve realistic and correct characterisation of the mineral groups. As mentioned previously in Chapter 3, SkyScan1172 produces images with less contrast than BSE images in an SEM. For more details please refer to Chapter4, section 4.2.1. Note that Cone Beam tomography images are better viewed as a PDF.

To perform the required image analysis a rule set was developed and implemented in the eCognition8 software. This rule set was able to remove most of the noise from the X-ray microtomography images while retaining the shape and the size of the individual mineral grains. As mentioned previously in Chapter 3, noise was determined by observing histograms from the X-ray absorption profile lines across the particle.

The size and sensitivity of the X-ray detector is very important. As mentioned by Farr (1997), the ideal detector should have high detection efficiency, fast response and a high dynamic range in order to detect both the high intensity and low intensity (highly attenuated) beam passing through a particle in a short period of time. The detector should be stable when voltage and temperature in the measurement chamber varies and be linear enough to accurately detect a signal if X-ray intensity changes. The X-ray energy is also very important since the high energy X-rays are able to penetrate the particle with much less attenuation than the low energy ones. Hence they have a higher chance of being detected than low energy photons.

As previously explained, different mineral phases are able to be separated on the cross section images based on their greyscale level. Denser materials absorb more X-rays than less dense materials and therefore they are able to be detected and evaluated while less dense materials are transparent when high energy X-rays are applied.

To make a high quality X-ray image of a rock, the properties of the acquisition process have to be optimised for a particular set of conditions such that the beam-hardening effect is minimised. Perhaps the major system assumption is that the beam of X-rays is monochromatic. This is not true even if all acquisition settings were set up precisely during the acquisition. (3.8.2.1.3) For this reason interactive image analysis techniques need to be optimised in order to deal with the occurrence of beam hardening. One of the major steps here was the calibration of the X-ray microtomography images with the MLA image which has no beam hardening effect present due to the difference in system methodology.

The grains were compared separately and the difference in the greyscale levels of mineral groups was accurately measured. Uncertainties due to beam hardening and blurring of the rock X-ray images were resolved by means of this calibration.

5.3.2.1 Identification of the mineral groups

The principal aim here was to identify two mineral groups, gangue minerals (quartz, K-feldspar etc) as the first group and sulphides (chalcopyrite and pyrite) and magnetite as a second mineral group in X-ray microtomographic images. During the analysis of the SkyScan images, one mineral phase appeared much denser than the other phases. Based on the MLA data and on calculations of mass attenuation coefficients it was discovered that barite was also present in the particle and that the mass attenuation coefficient of the barite is very high (Figure 125 to Figure 127). The attenuation data were calculated online at NIST webpage (NIST 2011). Hence, barite grains were considered as a third mineral group, which brings the analysis process to the tertiary level.
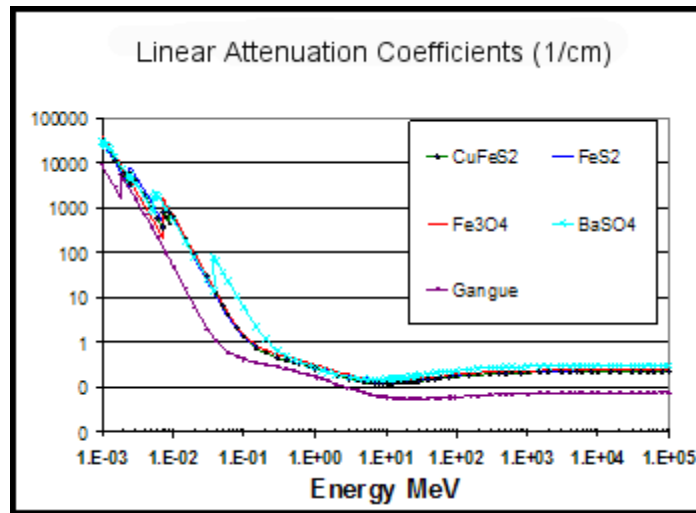
Figure 125: Mass attenuation graph, energy from 1 keV to 100000 MeV (NIST 2011)
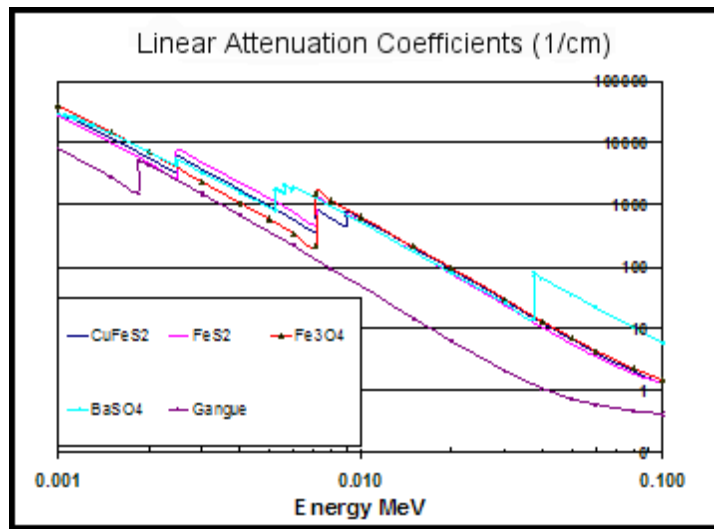
Figure 126: Mass attenuation graph, energy from 1 keV to 100 keV (NIST 2011)
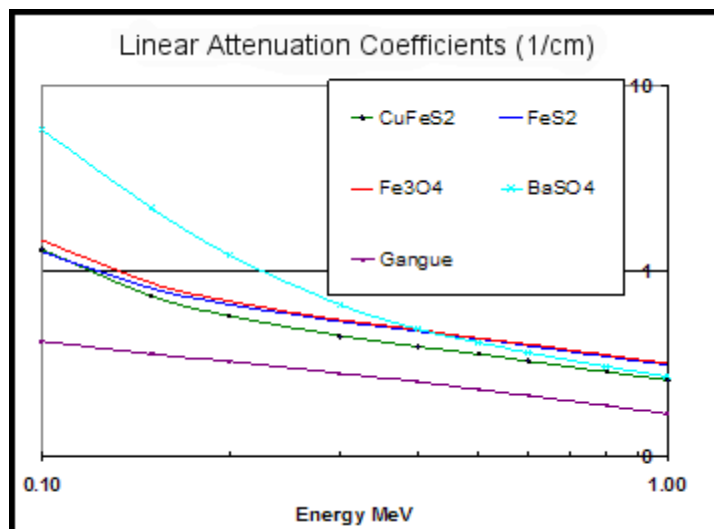
Figure 127: Mass attenuation graph, energy from 100 keV to 1 MeV (NIST 2011)

246
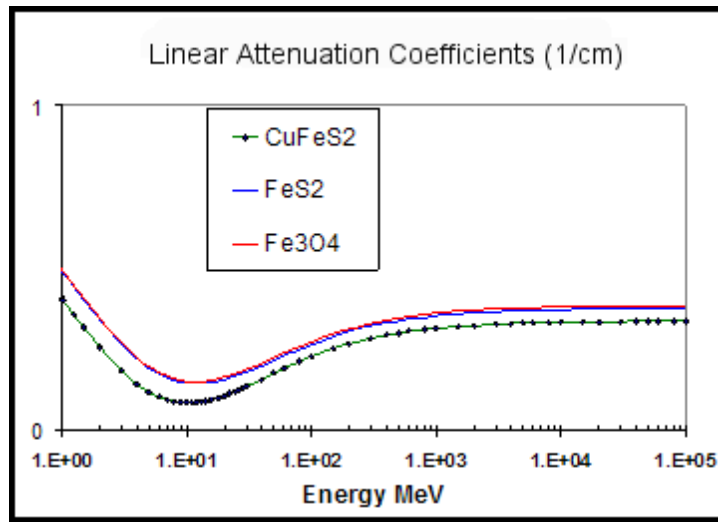
Figure 128: Mass attenuation graph, energy from 1 MeV to 100 000 MeV (NIST 2011)

Figure 126 shows the possibility of separating three groups of minerals with energies between 50 and 100 keV. The gangue mineral group has the lowest threshold value on the inverted SkyScan1172 images, as their mineral attenuation coefficients have the lowest values. The middle group consisting of chalcopyrite, pyrite and magnetite will be easy to separate from both barite and gangue minerals but it will be difficult or even not possible to separate minerals within the group. The third group has a single mineral, barite. Its mass attenuation coefficient is much higher and therefore its threshold value will be the highest.

Figure 126 also shows that it may be possible to distinguish between magnetite, chalcopyrite and pyrite mineral grains using the energies below 10 keV. However, X-rays generated using the SkyScan system with these low energies cannot penetrate through the large particles which have been analysed in this work.

It may also be possible to separate magnetite from pyrite and chalcopyrite with X-ray energies ranging from about 100 keV to 120 keV (Figure 127). With higher energies, up to 100 GeV, it would be possible to separate chalcopyrite from magnetite and pyrite but certainly not possible to identify magnetite and pyrite separately. Figure 128 shows the linear attenuation coefficients and the inability to separate chalcopyrite, pyrite and magnetite using the energy source of more than 1 MeV.

The research is already going into that direction (Iovea et al. 2009; Schena et al. 2002; Zbijewski et al. 2014), but the improvement is needed for reconstruction algorithms. One of the available instruments is Xradia (2014) with dual energy capabilities.

The SkyScan CBT system available at Julius Kruttschnitt Mineral Research Centre (JKMRC) is able to generate energies up to 100 keV. It has been proven with this calibration that magnetite, pyrite and chalcopyrite can be identified as a group but cannot be identified separately by using these conditions.

5.3.2.2 Calibration of the threshold values

The classified XBSE image and the corresponding reconstructed CBT particle section image (see Figure 124 b and c) were overlayed using image analysis software called LeoWorks (EDUSPACE 2010). Figure 129 shows the overlap of the MLA image and X-ray microtomography images. Using this overlap it was possible to identify conclusively the mineral group comprising chalcopyrite, magnetite and pyrite in the X-ray micro tomography image.

Chalcopyrite
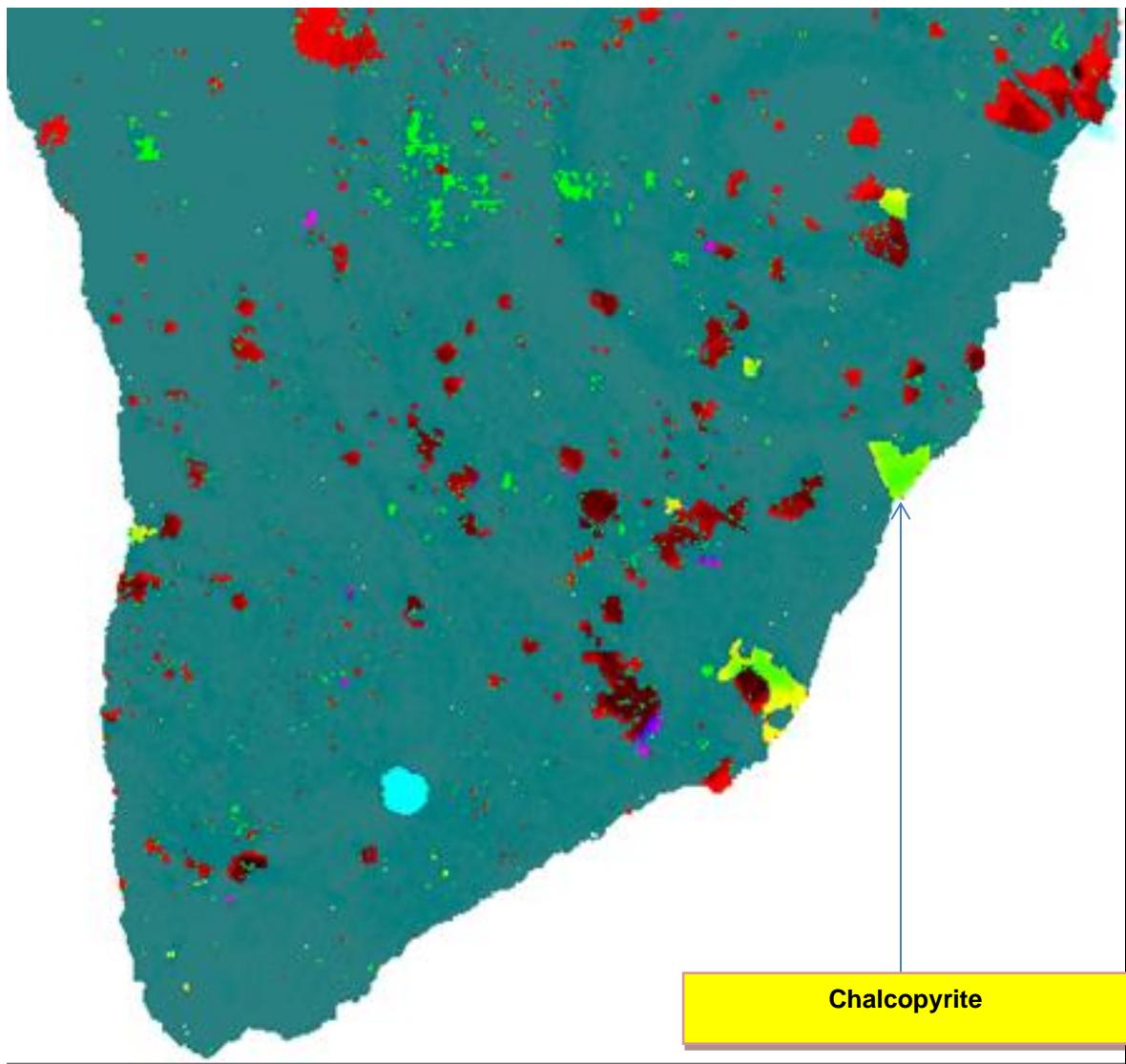
Figure 129: MLA image superimposed over X-ray microtomography image (Figure 137 on Figure 138)

When the MLA image shown in Figure 130 is superimposed, the colour is shaded when there is the clear overlap with the other image, in this case Figure 131.
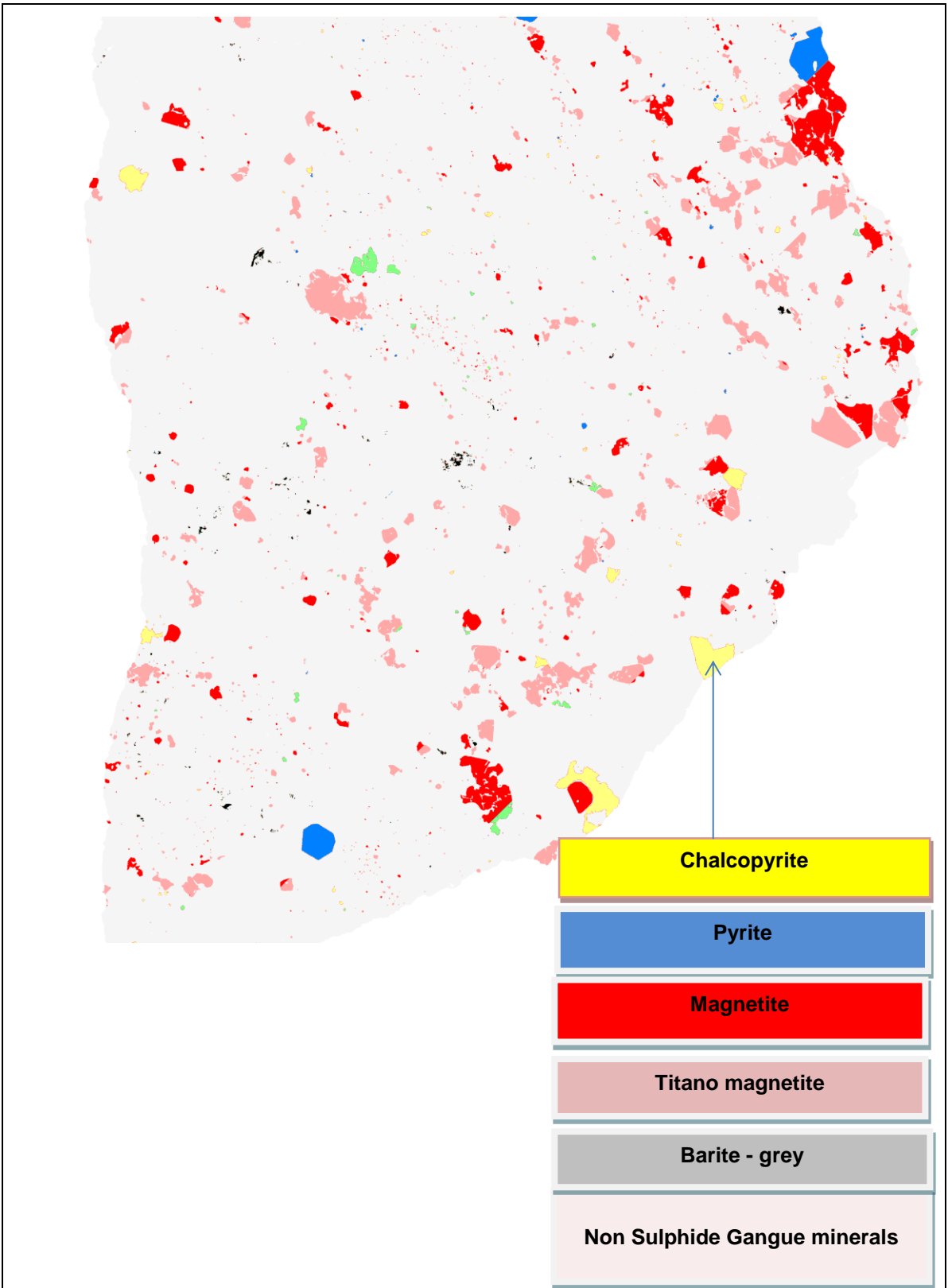
Figure 130: MLA XBSE classified image after cutting
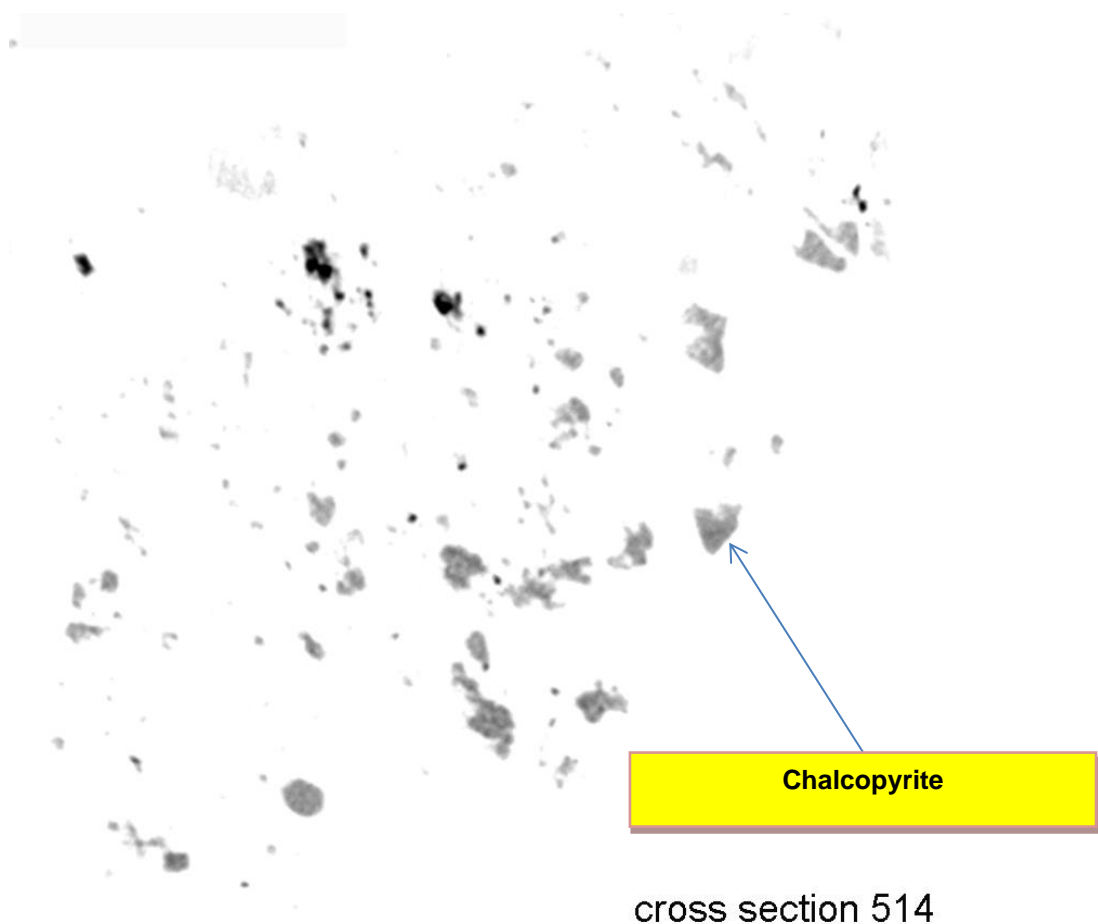
Chalcopyrite

cross section 514

Figure 131: SkyScan1172 reconstructed cross section image, layer number 514
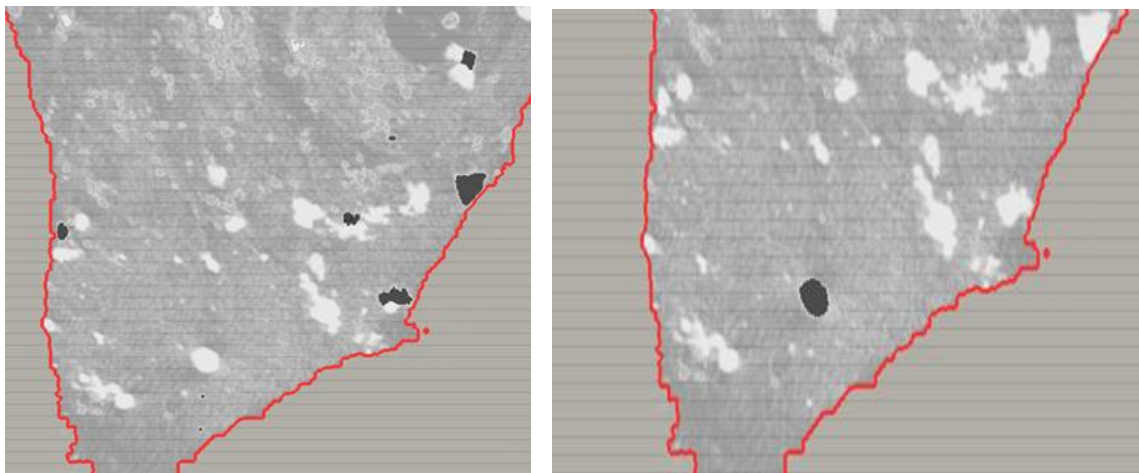
Figure 132: Chalcopyrite (left) and pyrite (right) identified in microtomography image, using eCognition 8, black phase.

251
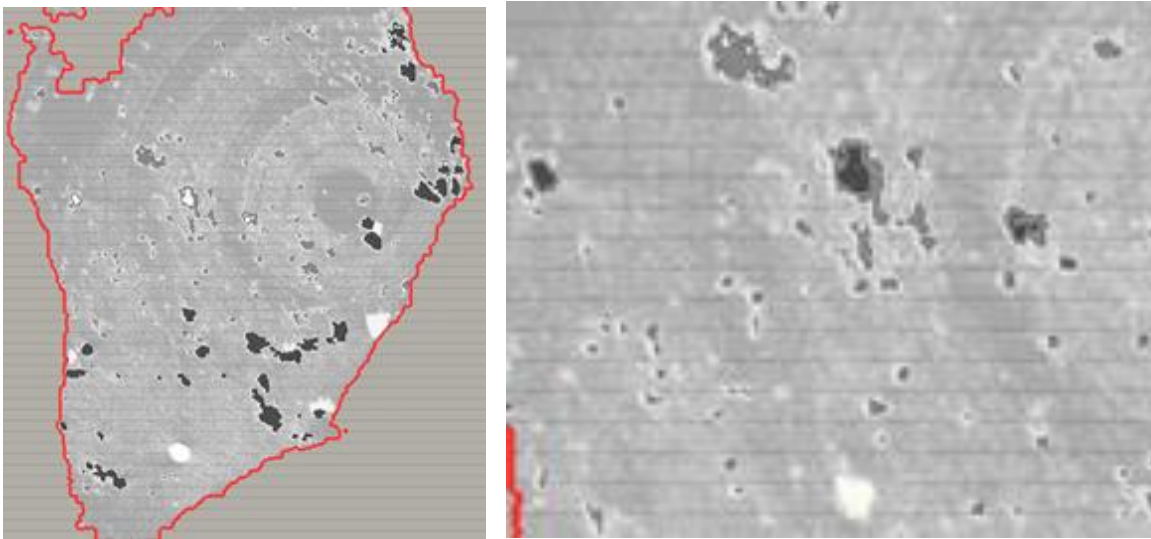
Figure 133: Magnetite (left) and barite (right) identified in microtomography image, using eCognition 8, black phase. Some ring artefacts are also visible

Figure 132 and Figure 133, together with other classified cross sectional images, provide an opportunity to investigate the greyscale values of the mineral grains present in the particle in three dimensions. Grains of the chalcopyrite and pyrite were coarser, barite grains were finely dispersed in the particle while magnetite had a range of mineral grain sizes. That is, there is some scope for identification using textural characteristics, which may provide some application for greyscale calculation within a larger particle.

5.3.2.3 Attenuation profile lines of the minerals

The X-ray microtomographic image was processed in CTAn software (SkyScan 2010a). Each mineral grain was investigated and their greyscale values were compared. Figure 134 and Figure 135 show the greyscale values along the profile line and indicate the maximum greyscale value that each of the mineral grains exhibited in the image. It was clear that chalcopyrite, pyrite and magnetite could not be separated based on threshold values since the levels were very similar (Figure 134). However as Figure 135 shows, the barite grain could be separated as a third phase because of the very high mineral attenuation values. Both Figure 134 and Figure 135 show that the gangue mineral phase attenuation was lower than valuable mineral attenuation values.
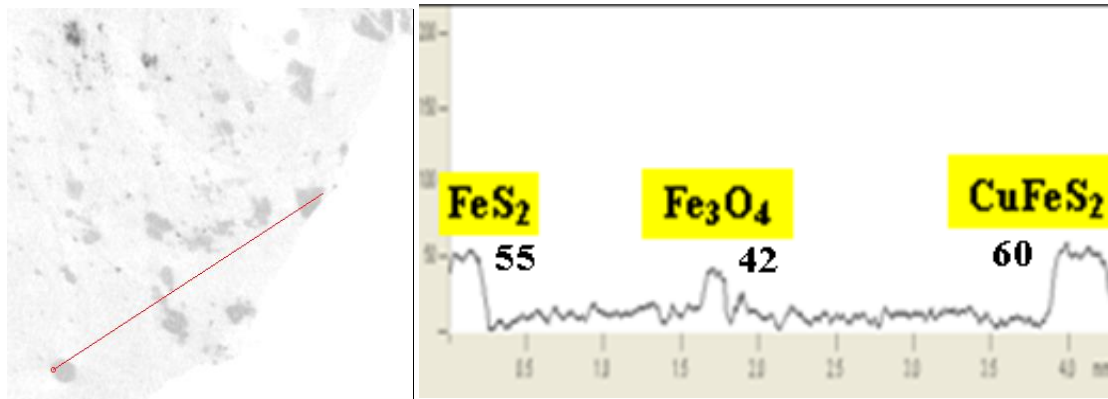
Figure 134: Profile line through pyrite, magnetite and chalcopyrite grains, max greyscale values
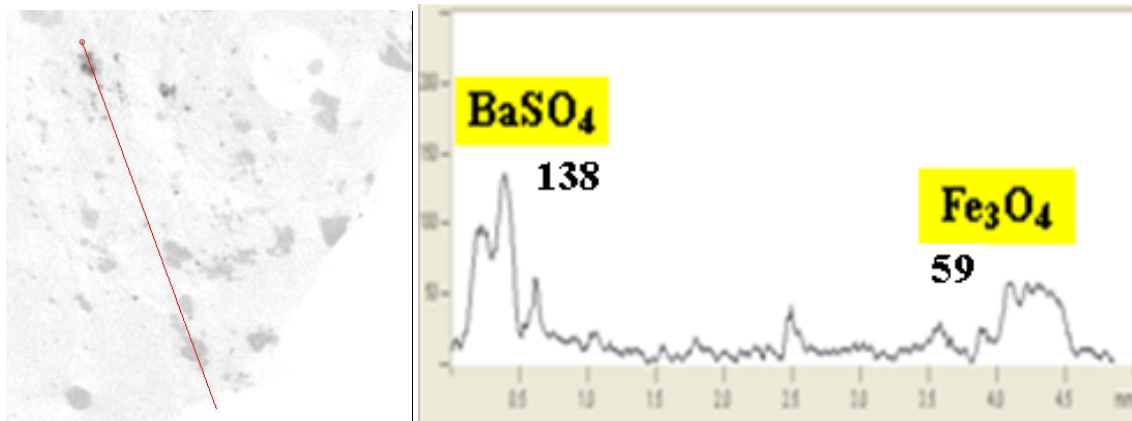
Figure 135: Profile line through barite and magnetite grains, max greyscale values

Figure 136 and Figure 137 are showing individual mineral grains from Figure 134 and Figure 135, where the threshold values within a single mineral grains obtained in NRecon are compared. The data plotted shown in Figure 138 to Figure 141 were obtained from the CTAn software (SkyScan 2010a). After the minerals were identified, it was possible to investigate the change of the threshold values of the individual minerals in three dimensions. These graphs are examples illustrating the variation of the greyscale levels within a single mineral grain. They also show the variations in greyscale levels within the same minerals when the profile line passes through the grain vertically (for example from virtual cross section line 515 to the line 513, Figure 139 to Figure 141).

Size (mm)
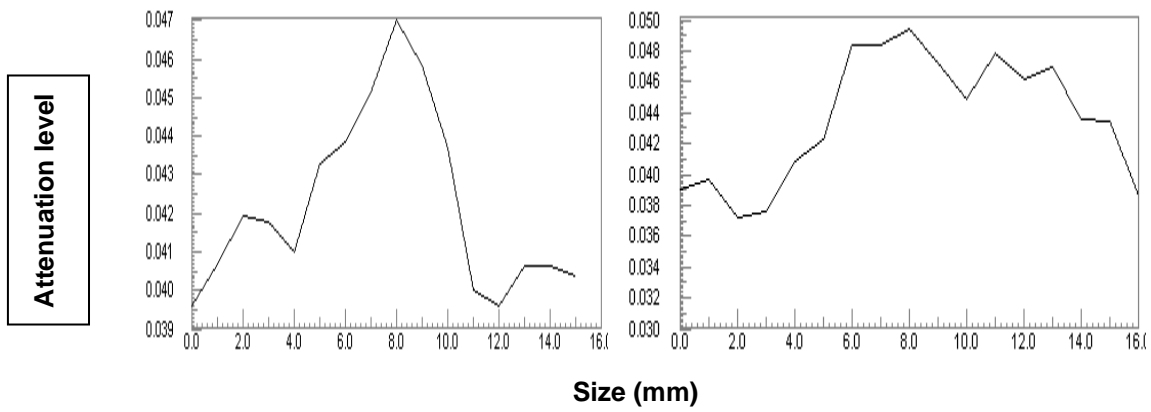
Figure 136: Chalcopyrite and magnetite grain X-ray absorption profile lines for single grains

Size (mm)
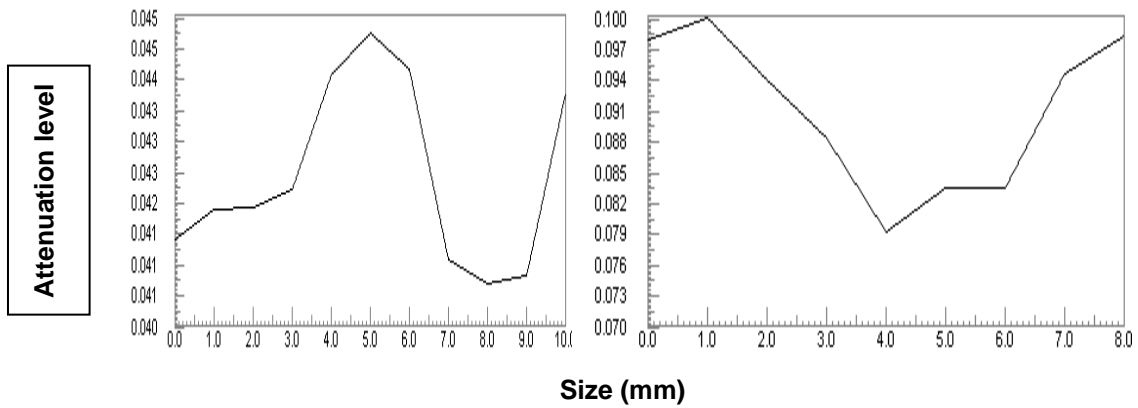
Figure 137: Pyrite and barite grain X-ray absorption profile lines for single grains

Figure 145 is a very good example of the common issue noticed in reconstructed tomographic images. The software is "averaging" the greyscale value at the mineral boundary, where the greyscale value actually presents the average of the greyscale value of the mineral and gangue matrix around that mineral grain.

254
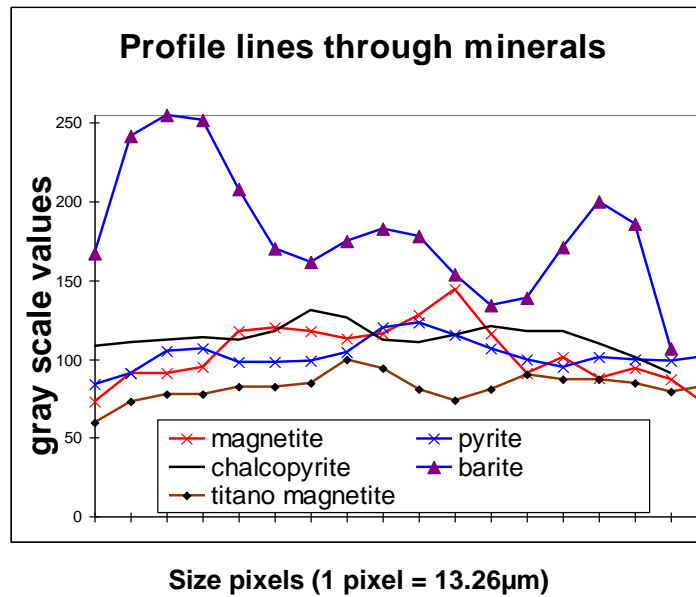
Figure 138: X-ray absorption profile lines across mineral grains

Examination of each image indicates that greyscale level variation exists vertically and horizontally within each mineral grain (Figure 139 to Figure 141). Attenuation profile lines through pyrite and titano-magnetite are presented in appendix 9.17.
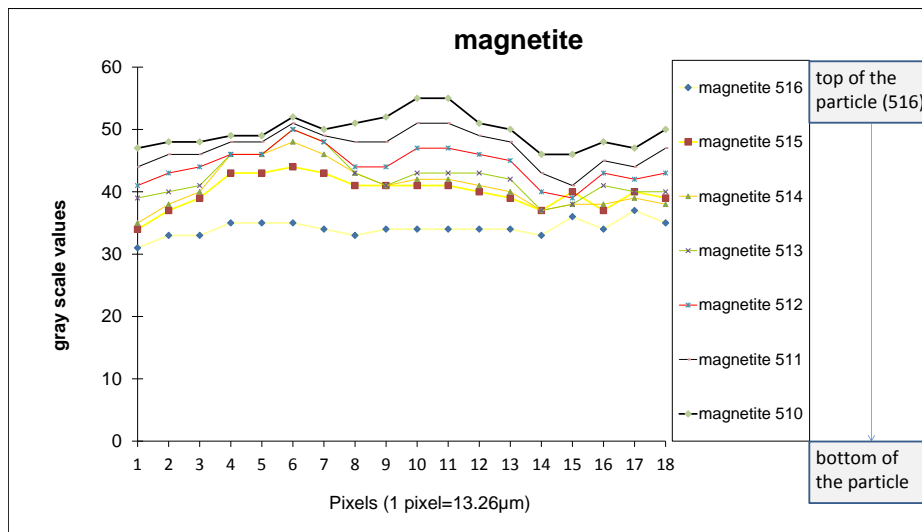
Figure 139: Attenuation profile line across magnetite grain in multiple consecutive 2D sections

A critical criterion for separate mineral identification here would be to achieve measurable differences in mineral attenuation coefficients between chalcopyrite, pyrite and magnetite. This should be possible to achieve using multiple filters in multiple scans but the technique

255

is beyond the scope of this Thesis. Some work has been done in this area by Lin and Miller (2001).
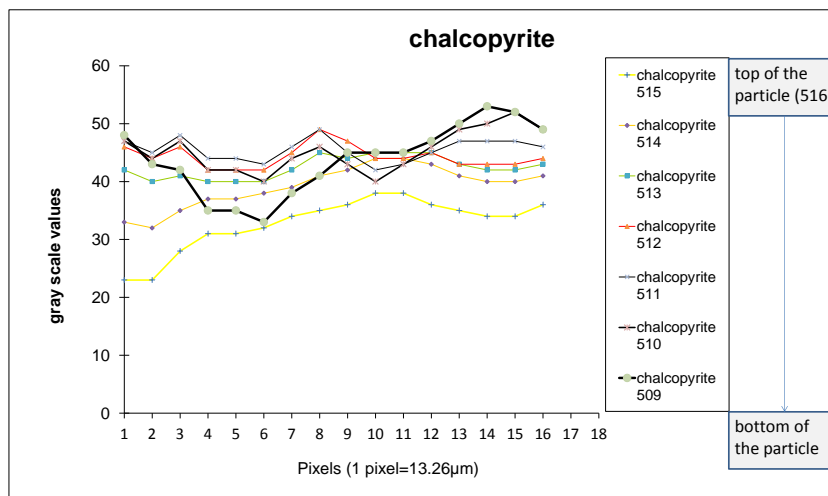
Figure 140: Attenuation profile line across chalcopyrite grain in multiple consecutive 2D sections
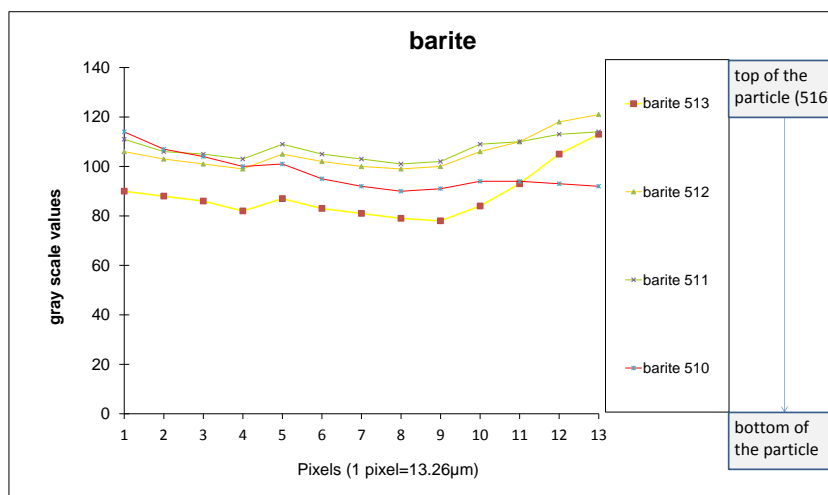
Figure 141: Attenuation profile line across barite grain in multiple consecutive 2D sections

Table 20 to Table 22 below show the greyscale values of the attenuation profile line of the SkyScan1172 image. Barite exhibits a slightly greater variation in these levels which may be a consequence of the smaller grain size. If a grain is smaller, the profile line may show some of the values that do not belong to the grain but to the transition area surrounding the mineral.

This results also prove the point that it is not possible to separate minerals with close Z_e values, such as chalcopyrite and sphalerite claimed to be separated by Ghorbani et al. (2013).

Table 20: Greyscale values from the attenuation profile lines of a magnetite mineral grain

	magnetite			
	min	max	sd	average
516	31	37	1.3	34.1
515	34	44	2.6	39.9
514	35	48	3.6	41.0
513	37	50	3.4	42.3
512	39	50	2.9	44.3
511	41	51	2.8	47.1
510	46	55	2.7	49.7

Table 21: Greyscale values from the attenuation profile lines of a chalcopyrite mineral grain,

	chalcopyrite			
	min	max	sd	average
515	23	38	4.6	32.8
514	32	44	3.6	39.2
513	40	45	1.9	42.4
512	42	49	2.0	44.3
511	42	49	2.0	45.5
510	40	52	3.6	45.3
509	33	53	5.9	43.4

Table 22: Greyscale values from the attenuation profile lines of a barite mineral grain

	barite			
	min	max	sd	average
513	78	113	10.2	84.4
512	99	121	7.1	99.8
511	101	114	4.3	100.6
510	90	114	7.3	92.4
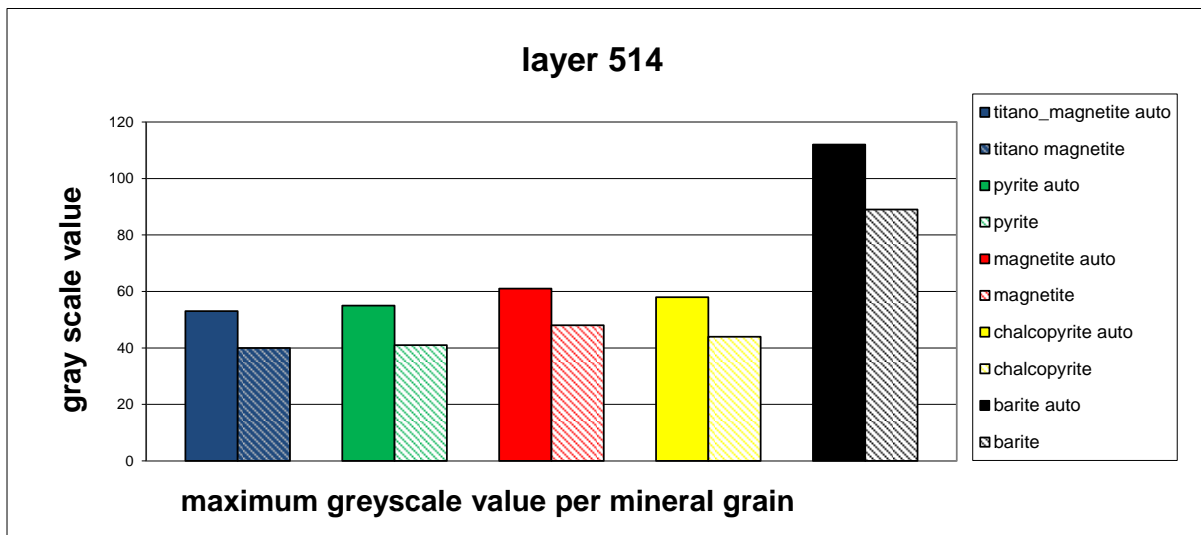
Figure 142: Maximum greyscale values of the minerals, two different reconstruction properties, one software auto selection and one based on operator's selection within NRecon.

Hence, the critical importance of selection of each threshold value is demonstrated again. Figure 142 illustrates the importance of the selection of attenuation levels for image reconstruction. It shows the maximum threshold value of the mineral grains. These values were extracted from the profile lines through the mineral grains.

On the left side are the results of the analysis done with automatic settings within the NRecon software during reconstruction. The right side demonstrates results obtained with manually selected threshold values within NRecon software after the noise is partially removed before reconstruction. It is obvious that barite has higher threshold values, while the rest of the minerals share similar values. When the noise around the particle is removed before reconstruction, the maximum threshold values of the mineral grains will be slightly lower in the reconstructed X-ray microtomographic images.

This clearly shows that the threshold value chosen for reconstruction will influence the final threshold value of the minerals in the image analysis software as well. It is believed that reasonable care should be taken when removing image noise during the reconstruction process. Parts of mineral boundaries may be lost if the noise removal is not appropriately adjusted. It is advisable to use the settings as close to auto as possible and deal with noise removal in the image analysis software.

5.3.2.4 The importance of Greyscale Threshold value

An example of the variation in the volume of the grains when applying different threshold values is shown in Figure 143, user interphase is shown in appendix 9.18. Assuming that the noise of the image presented here has a greyscale value between 0 and 1, then the volume of the particle is about 320mm^3 (Figure 143, a).
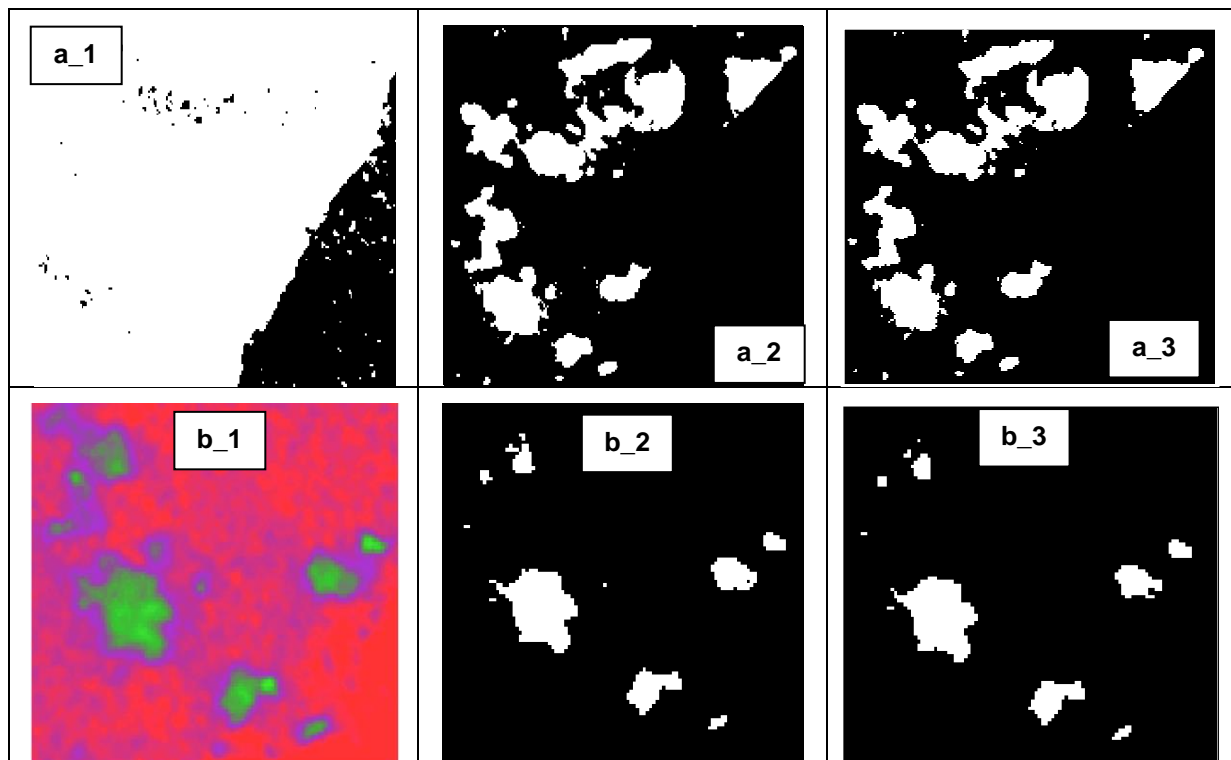
Figure 143: SkyScan1172 image analysed in CTAn: a) cross section of the particle, binary image for greyscale value 1 (a_1), 24 (a_2) and 25 (a_3); b) raw image (b_1) and binary images for threshold 50 (b_2) and 51 (b_3) respectively.

Wet and dry density measurements estimated that the volume of the particle at 219mm^3. This brings the above gangue threshold assumption into question. Considering the mineral of interest threshold value to be 24, a volume of 126mm^3 would be calculated by CTAn. However, if the threshold value is increased by one to 25, the volume is 117mm^3 which is a greater than 4% difference. Figure 143 a2 and a3, b2 and b3, may be used to compare the difference of the grains considered as the mineral of interest. When taking the density of the mineral into consideration, the difference in the measured mass percentage of the

mineral of interest is around 0.5%. This is evidence that the measured volume highly depends on the image quality and its resolution, the presence of noise and operator intervention on acquisition properties and greyscale threshold value.

We can conclude that if the threshold value is too high, the volume calculated will be less than the true mineral volume. If the threshold value is lower than the actual, the volume calculated (assumed number of voxels) will be higher than the true volume of the mineral. On this basis threshold based segmentation is not found to be appropriate for sharp changes in density or X-ray absorption.

5.4   Reproducibility of the results

To test the reproducibility of the CBT results, a sample of a binary rock from a taconite (magnetite and quartz) ore, was scanned in the SkyScan1172 system three times.

The properties of the scans were identical for all three scans. The first two scans were conducted in the same day and the third was done after three days in order to check the variability of the results not only on the same day but also when the machine had not been used for a longer period.

The magnetite and quartz minerals in the test one have very different X-ray attenuation and the CBT contrast was large enough to allow accurate discrimination between the two.

The reconstruction of all three data sets was done with NRecon software using automatic settings. Reconstructed cross section images of the whole particle were then analysed using the CTAnalysis software. Four different greyscale levels were selected as threshold values and all three datasets had the volume of the minerals measured with these thresholds. The results are presented in Table 23 below.

The volume of the mineral phases obtained in test01 and test02 when the same threshold value has been applied per mineral phase are less than one standard deviation from the

mean. The results from test03 when the same threshold values were applied are 1.2 standard deviations from the mean. This indicates different but acceptable variation in attenuation obtained in test03. If the same threshold levels are applied, the confidence in obtained results is reduced.

Table 23: Reproducibility analysis, greyscale levels applied on image datasets are equal

	greyscale intervals			
	1	**2**	**3**	**4**
test ID	**Measured volume of the minerals in mm^3**			
test01	**164.0**	**23.3**	**5.0**	**4.7**
test02	**164.0**	**23.7**	**5.2**	**4.9**
test03	**164.9**	**27.7**	**7.2**	**6.8**
mean	**164.3**	**24.9**	**5.8**	**5.5**
SD	**0.5**	**2.4**	**1.2**	**1.2**

The confidence level is a little reduced when considering the lower greyscale levels, but the results still show acceptably good reproducibility of the analysis. The observations of minority mineral phase identified when threshold level 4 was applied lie within approximately 22% of the mean.

The results presented in Table 24 were obtained by varying threshold levels between datasets, using the operator's identification of mineral grain boundaries. The sensitivity of the machine was different on the third day, and therefore greyscale levels applied in this case were slightly lower than in others. If the operator is deciding on individual threshold values of the minerals during the analysis, the results are more reproducible then when CTAn was used for image analysis. Table 24 suggests that the results do not vary significantly across different scans.

Table 24: Reproducibility analysis, greyscale levels applied on image datasets are slightly different, based on operator's decision

	greyscale intervals			
	1	2	3	4
test ID	Measured volume of the minerals inmm^3			
test01	164.0	23.3	7.1	5.0
test02	164.0	23.7	7.4	5.2
test03	164.1	23.9	7.2	5.5
mean	164.0	23.6	7.2	5.2
SD	0.1	0.3	0.1	0.2

The reproducibility of eCognition image analysis is not in question here since tests have shown that the same code applied to the single image will produce the same output of the mineral data if image analysis is repeated (section 4.2.1.2). Here the importance of the operator's decision when analysing images within CTAn is shown.

5.5 Conclusions

The calibration technique presented in this chapter offers an opportunity to investigate mineral grains in multiphase particles in three dimensions. As particular threshold differences exist when identifying the minerals within X-ray microtomography images, the technique presented in this chapter will improve automatic calibration of greyscale levels of the minerals present in multiphase particles. It also helps to better understand the internal structure of the multiphase particles and to provide better outcomes for application in research in the field of comminution, breakage of the particles and liberation.

Although it may be possible to identify magnetite, chalcopyrite and pyrite as separate mineral grains, it was not possible with the equipment and techniques used for this project.

The main outcome of the work described in this chapter is the non-destructive identification of three mineral groups within multiphase particles which is a big advance compared to previously reported techniques which measure only on binary levels or three groups but using methods which destroy the sample.

In the ore tested here the first group consists of gangue minerals (which includes quartz, K-feldspar etc). The second mineral group consists of chalcopyrite, pyrite and magnetite minerals. The last group is made of single mineral, barite, although this mineral may be substituted with galena, mercury, platinum or some other high density minerals if needed. When making this change, a relatively simple change in the code for analysis is required.

In many cases, when this method is applied to measure ore characteristics in 3D an estimate of the grain size required to liberate gangue may be the most useful outcome of the measurement.

This work shows that it is essential to consider machine, software and particle properties as well as operator decisions when conducting this type of analysis. The significant improvement made by using this method is to follow the properties of the mineral grains with similar threshold values in X-ray microtomographic images through the three dimensions of the particle.

Being able to generate monochromatic high energy X-rays would be very valuable. A more general approach to reconstruction which can account for a broad spectrum of X-rays would also be very valuable and provide an alternative.

The second contribution here is the reduction in the effect of imaging artefacts due to the calibration. The beam hardening artefact can be greatly reduced by calibrating the threshold values of the X-ray microtomography images. The optimisation of image acquisition properties helped reduce artefacts in reconstruction.

Since the same mineral grains were identified within SkyScan1172 images and the MLA, there is clear evidence that greyscale variations within individual mineral grains in three

dimensions are realistic. This information allows the complete internal structure of the multiphase particle to be obtained.

The last outcome here was the discovery of the variations of the absorption levels of the X-rays within single mineral grains in three dimensions. We can conclude that minerals with similar attenuation coefficients will be difficult to separate by an automatic classification process. However, measurements at different X-ray energy levels might resolve some of these challenges.

The current data set provides evidence that, as expected, there is no single greyscale value for each mineral when the particle is scanned in a SkyScan microtomograph. Image analysis software such as CTAn calculates the volume of the mineral phase based on a single value for threshold set up by the operator, which is clearly not the best approach in mineral images.

The way to avoid this issue is to use the algorithm in eCognition8 which automatically defines the threshold values for the each mineral grain present in the image. With this method, the threshold value will not be the single value but the function defined in the code, which will assist by varying the threshold value as appropriate.

Using X-ray attenuation profile lines across the particles, provides the operator with information about the wider spread of grey scale levels within each mineral group. Importing those values into a written code in eCognition8 will help in the segmentation and classification stages of the image analysis process. The program will use those values in the internal algorithms and thus the X-ray absorptions of the minerals within the whole particle define the most appropriate threshold values per mineral group. It will take each pixel or voxel and calculate the value per pixel or voxel based on algorithms and predefined boundaries. Then it will assign the appropriate classification for the defined pixel or voxel or kernel. The type of unit will depend on the type of analysis, for example if it is two dimensional it will consider pixel and for three dimensional image analysis process it will consider voxel or kernel.

6 Parent and progeny liberation analysis

6.1 Overview

The ideas tested and presented in this chapter arise from a long standing issue in investigating the mechanism of breakage when liberation of minerals occurs. For decades researchers have debated in using random or non-random mechanisms of breakage in explaining the way minerals break. To this point, no practical solution has been offered to explain the mechanism of liberation and ore breakage. This chapter describes a method which can estimate the grain size distribution, identify critical grain size for sufficient liberation and thus predict the mechanism of breakage.

It is believed that this type of measurement can help researchers gain better insight in liberation mechanisms.

The testing and analysis methodology used for this research is explained in detail in previous chapters.

6.2 Introduction

A number of particles were analysed with a Micro CBT system at various resolutions. Only some particles were selected for the mineral characterisation and liberation analysis presented in this chapter. All of the particles were analysed with the SkyScan1172 Micro CBT system. The reconstruction of two-dimensional radiograph images was performed using NRecon software. The reconstructed two dimensional images were then analysed in

eCognition8 image analysis software, programing rule set is presented in appendix 9.19 and different features shown in appendix 9.20 to 9.23. Particles were split into three categories based on their content of high density component. In the present work, eight multiphase particles were analysed with the Micro CBT system at resolutions in 6-14µm in range. A detailed analysis of four particles will be presented, plus the grain size distribution analysis of remaining four particles.

The ore selected for this investigation was a binary magnetite-quartz ore. The reason for selecting this type is the simplicity in having only two mineral components in the image analysis. In previous chapters, a new method was presented for definition of greyscale threshold values for each mineral present in multiphase particles. This method allows calculation of the measured liberation kernel and then compares values with the predicted liberation kernel generated using a published mathematical model.

The selected particles were analysed using the SkyScan1172 Micro CBT system and their grain size distributions were measured before breakage. The same particles were then subjected to breakage at a precise energy input using the JK Rotary Breakage Tester. Progeny particles were carefully sized and each size fraction subjected to the same analysis as their parent particle.

The set of images generated when the parent particle was measured by Micro CBT was cut into virtual 100 and 50 pixel cubes. Images of these cubes were then analysed with eCognition8 image analysis software and their volume and liberation were compared with the measured volume and measured liberation of progeny particles. This strategy simulates a random breakage pattern.

Most of the published liberation models ((Austin and Luckie 1988; Barbery and Leroux 1987; Laslett et al. 1990; Mehta et al. 1990) consider the breakage mechanism incorporated in models to be random. Cutting the particles into cubes supports the assumption of a critical particle size at which liberation begins, but also investigates the influence of density difference and interfacial minerals forces on breakage.

One has to bear in mind that texture (that is the distribution of mineral grains within the matrix) of the ore will influence the way the particle breaks. If the texture is fine, and grains are randomly distributed, it is believed the liberation distribution for any size fraction of progeny particles will be similar, only size reduction process will occur. Based on this research, this statement is true only for coarser than critical size fractions. The work presented here revealed liberated low and high grade fine fractions of progeny particles when the parent grain size was examined as fine simulated breakage.

The core of the issue of quantifying liberation is when the texture is largely coarse and the minority mineral phase is more or less concentrated in clusters. Whether or not the breakage is going to be random at that time, will depend on the nature of the minerals, their mineralogical properties, hardness, physical properties of minerals, cleavage etc. This concept was tested and supports this assumption.

If the minority mineral phase hardness differs from the majority mineral phase, breakage may occur along the mineral boundaries. Here the bond between different mineral phases is weak and the fracture will be intergranular. (Lawn 2004)

Hsih and Wen (1994) presented an extension of the Gaudin liberation model by incorporating a detachment factor. For much larger particles this model used binary magnetite silicate particles, which were also considered in this Thesis. The findings of this paper were that there was a general increase in the detachment factor with increased strength of the mineral . Gangue strength and mineral-gangue interfacial area are believed to be the governing factors in liberation by detachment. Hsih and Wen considered two types of liberation, transgranular fracture and liberation by size reduction. This is reasonable but the texture was not considered to be a factor, only the state of the interface between the grains. If the grains of the harder minerals had strong intergranular connection, we would have both types of liberation occurring.
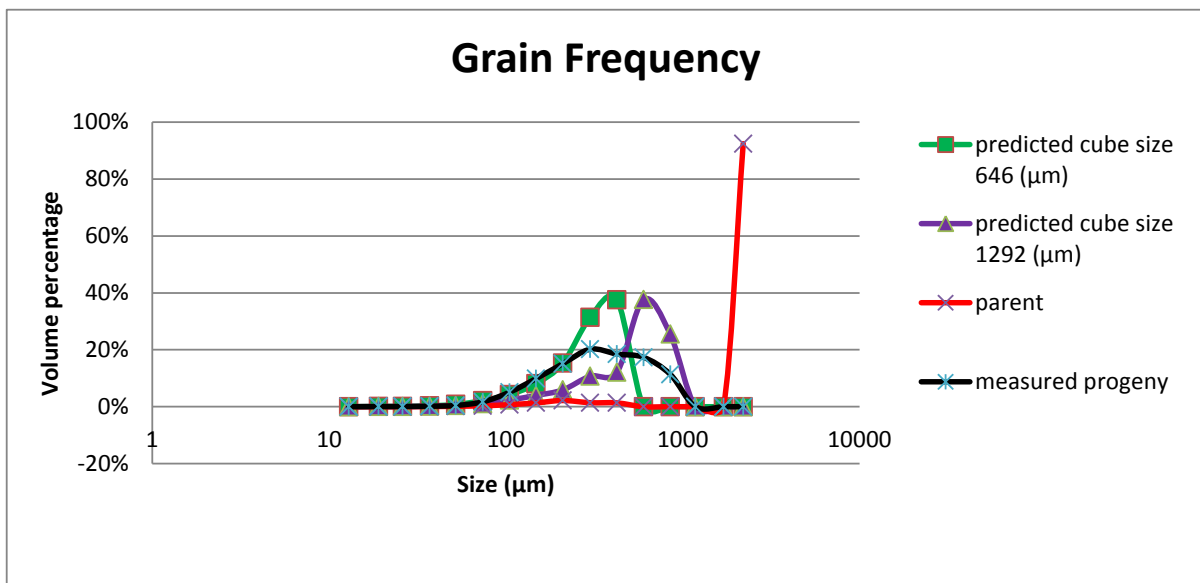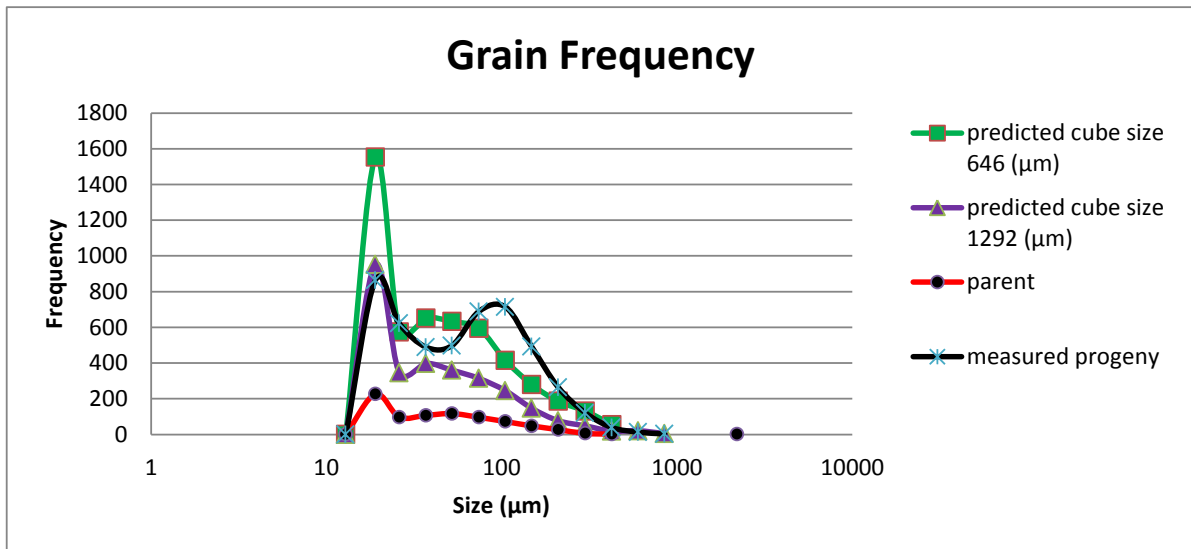
Figure 144: Measured and predicted grain size, before and after breakage

The double peak visible in the graph given in Figure 144 for measured progeny grain size shows the heterogeneous nature of the rock (Gaudin 1939). This was also visible in the work that Berube and Marchand (1984) published on iron ore. It is evident that the large clusters of iron grains may break into clusters of grains, and not as the random breakage model suggests, into evenly distributed sizes. Figure 144 is also shown in Table 43, appendix 9.24.

Moen et al. (2006) investigated variation in liberation of similar ore types with different origins, where they proved the influence of both heterogeneity of the rock (mineralogy) and grain size on liberation. The genesis of the rock plays a very important role and can control the way both gangue and minerals are going to be liberated.

Ferrara et al. (1989) presented variations in rock texture and its influence on liberation. If we could carefully plan the steps of comminution and consider the texture of the ore and the way it can be liberated, the degree of liberation can be considerably increased. Hence the focus is on weakening the grain boundaries in carefully planned comminution steps, and the relevant techniques are given in Wills and Atkinson (1993), Clarke and Wills (1989), Wiegel (1975), Forssberg et al. (1988), Andres and Bialecki (1986), Mazurkiewicz and Rakowski (1995).

The aim of this work is to establish a method for measuring liberation in three dimensions and apply it to identify the nature of breakage of particles that consist of two mineral phases with different hardness parameters, with introduction of mineral composition and mineral grain size distribution considerations by measuring both parent and progeny. This process establishes the relationship between progeny size distribution and liberation to parent grain size distribution and liberation, and thus presents a way to characterise the liberation kernel.

The following section provides a proof of concept for experimental strategy to address two important problems in characterising liberation kernel. The first is optimised methodology to non-destructively measure valuable mineral phase in the parent material before breakage. The second is relating the liberation distribution of progeny particles produced by parent particles.

6.3   *Experimental method*

This chapter presents results from experimental work presented earlier using three dimensional (3D) mineral liberation identification techniques. The goal of the experimental

work was to develop and demonstrate the technique for identifying iron ore mineral grains matrix inside gangue matrix. The technique can be applied to many fields of research and should considerably improve understanding of ore breakage mechanisms, especially when dealing with complex fine grained ores.

Parent particles were sized and their weight and density were measured using wet lab measurement techniques. The particle size selected was – 4.75 + 3.36mm. Particles were then scanned in the SkyScan1172 Micro CBT system (SkyScan 2010b) and the iron mineral grain matrix was reconstructed using the eCognition8 image analysis technique presented earlier. (3.6.2)

The measurement and image analysis technique developed in previous research presented here, permitted successful identification of very fine grains (less than 20 μm), leading to characterisation of breakage mechanisms and liberation relationships.

6.3.1 Sample composition

The particles selected for liberation matrix calculations are given in Table 25 and their progeny size distribution shown in Figure 145 below. Four particles are presented in this Chapter. The JK Rotary Breakage Tester was used to break the rocks at an exact energy input.

Table 25: Particles selected for liberation kernel calculations

Particle ID	KE001	KE002	KE003	KE004
JKRBT rpm	1839	2797	2797	2691
JKRBT energy (kWh/t)	0.4	1	1	1
initial mass (g)	0.2271	0.1990	0.1542	0.1964
Liberation by volume (%)	27	44	20	40
texture	fine	coarse	coarse	coarse

Figure 146 shows the parent particle (KE001) radiograph and its characteristics are given in Table 26. This particle was broken using JKRBT set 0.4 kWh/t energy. The progeny particles radiographs of each size fraction are shown in Figure 147. Particles were mounted in Styrofoam and there were no movements of the particles noticed in acquisition. Finer size particles were mounted in multiple levels using double sided sticky tape.
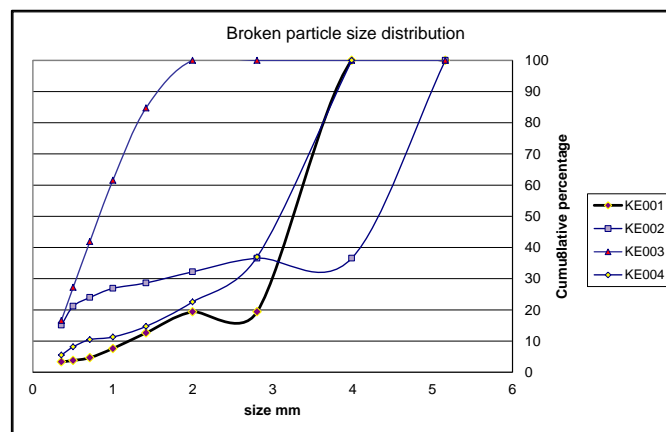
Figure 145: Size distributions of measured progeny particles

The particles selected had different grain size distributions (Figure 148). The grain size defined here was equivalent to equal volume cube edge, as eCognition8 displays results in a cubic pixel size.

272

6.3.2 Data acquisition

The liberation matrix of parent particles was evaluated by scanning particles in the SkyScan1172 X-ray Micro CBT system before breakage. The process of image acquisition was straightforward, using the steps already explained in the earlier chapters. Following controlled breakage using the JKRBT, the progeny particles were carefully collected, sized and scanned in the Micro CBT system.
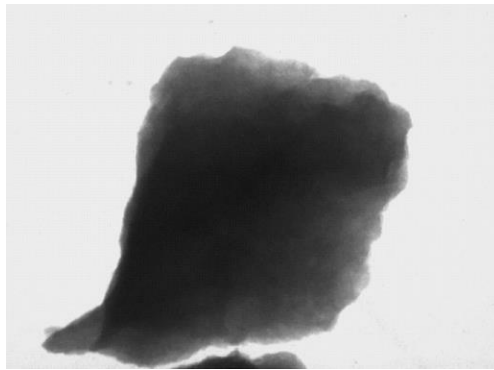
Figure 146: Radiograph of the parent particle
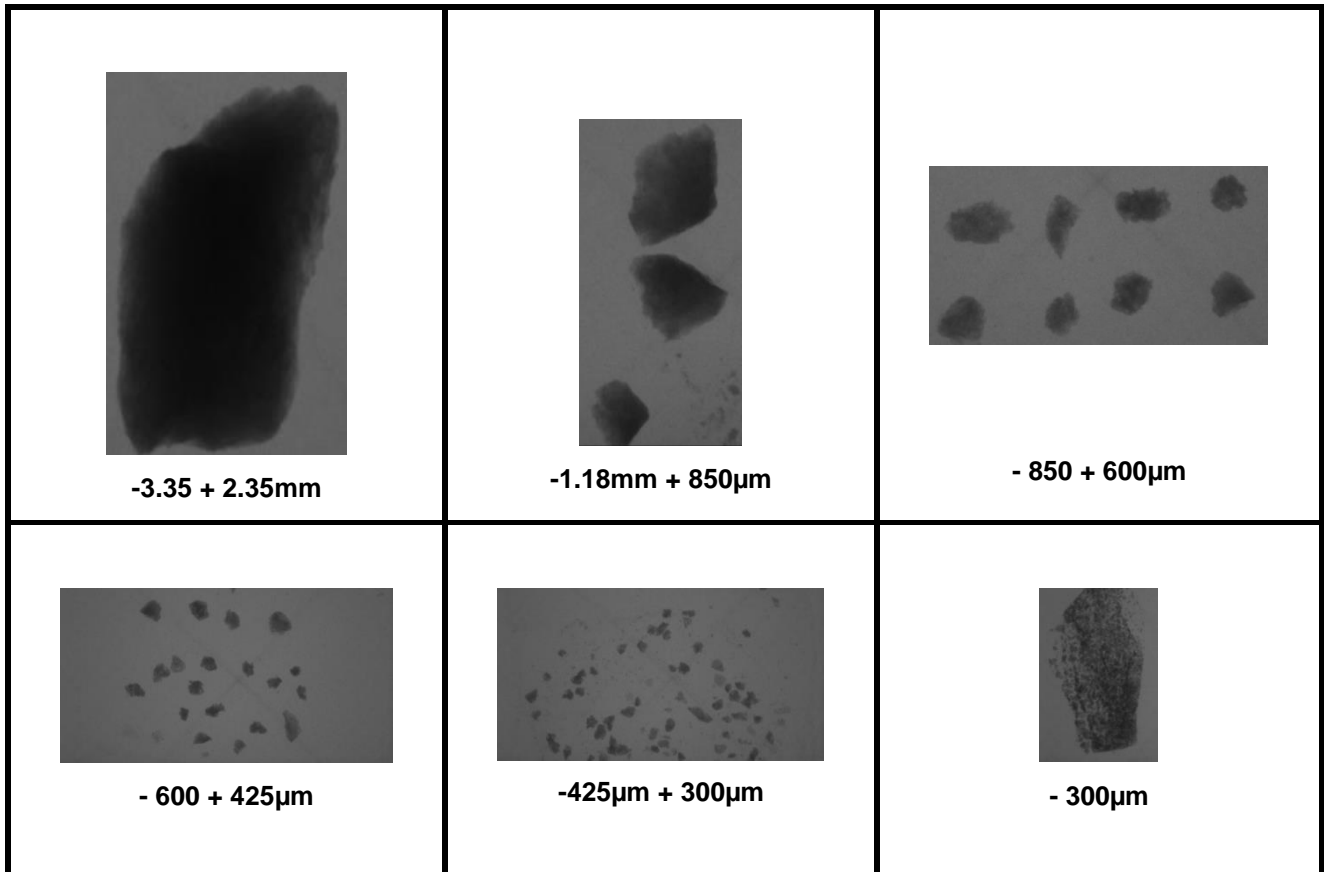
Figure 147 : Radiograph images of measured progeny generated by breakage in JKRBT, particle KE001

Table 26: Parent characterisation, KE001

Volume	57.41mm^3
Weight	0.23 g
Iron phase volume	15.9mm^3
Iron phase percentage by volume	27.67 %

6.3.3 Rock texture and breakage

An interesting feature of particle identified as KE001 is that it broke in thousands of fine particles and a single large progeny particle which contained just over 80% of volume of the parent particle. The liberation of the coarse progeny was identical to the parent particle liberation.

Table 27 : Progeny size distribution and image acquisition properties

Sample identification			KE001				
			initial mass (g)	0.2271			
JKRBT rpm		1839	mass lost in breakage (g)	0.01298		t10	1.051578
JKRBT energy kWh/t		0.4	cumulative %	energy	exposure	rotation step	pixel size
Size (mm)	mass (g)	%	passing	(kV/µA)	time (ms)	(degrees)	(µm)
-4.75 + 3.35	0.000	0.00	100				
-3.35 + 2.36	0.173	80.61	19.39	74/104	790	0.7	12.2
-2.35 + 1.7	0.000	0.00	19.39				
-1.7 + 1.18	0.015	6.77	12.62	74/104	790	0.9	12.9
-1.18 + 0.85	0.011	5.01	7.61	74/104	790	0.9	12.9
-0.85 +0.6	0.006	2.94	4.67	74/104	316	0.9	12.9
-0.6 +0.425	0.002	0.89	3.78	74/104	316	0.9	12.9
-0.425 + 0.3	0.001	0.47	3.32	74/104	316	0.9	12.9
-0.3	0.007	3.32	0.00	74/104	316	0.9	12.9
total	0.21412						

Table 27 shows progeny particle size distribution for KE001 parent particle and it also shows the acquisition properties of each size fraction.
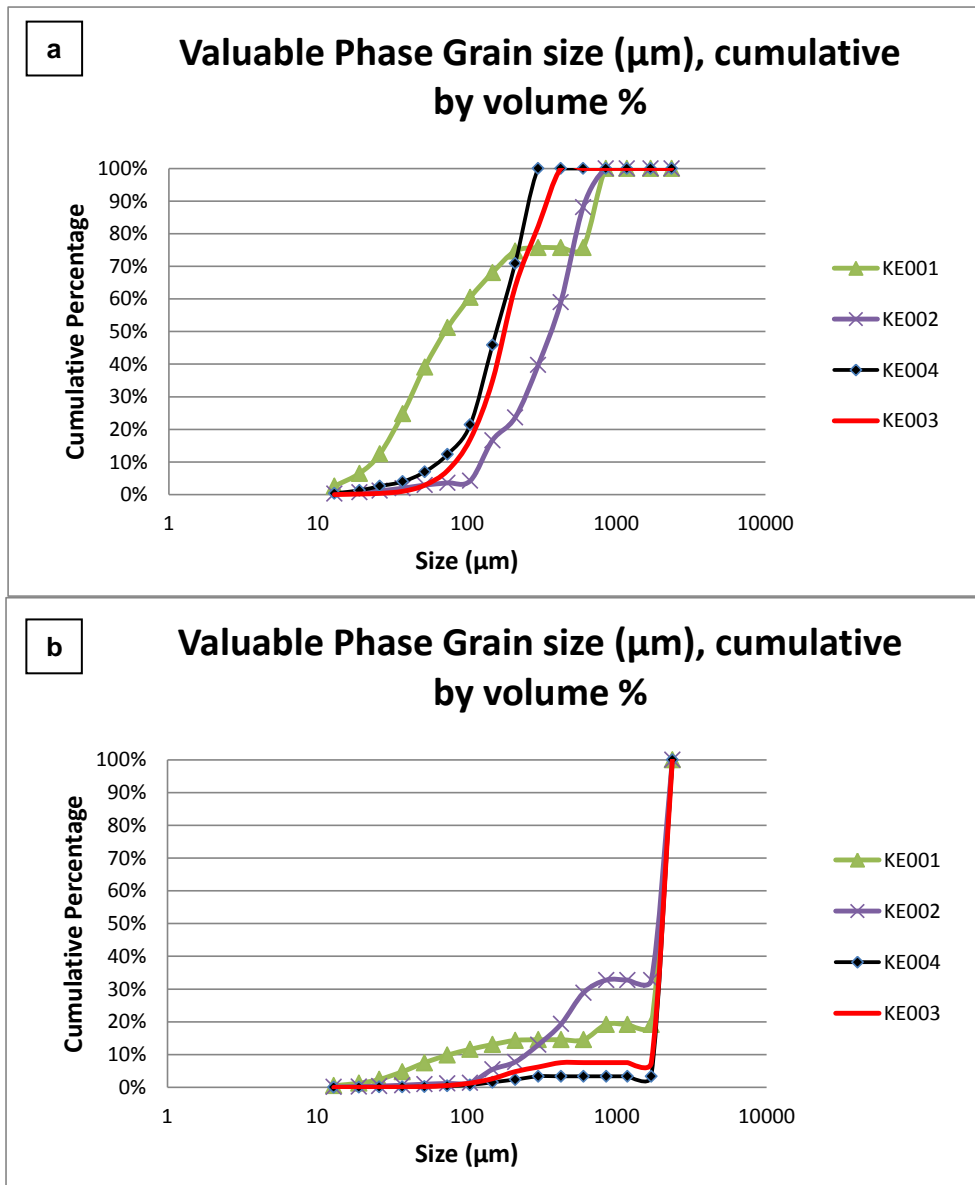
Figure 148: Grain size distribution of parent particles, iron phase, a - without the largest grain (over 2200µm) note: particle 002 to be included before submission

Each of the parent particles analysed had a cluster of grains (around 2200µm). Figure 148 presents the size distribution of measured grains in the parent particles which were characterised, including the largest grain cluster in "b" figure, and without the cluster in "a" figure. Three dimensional images of the grains are given in Figure 149 to Figure 151.
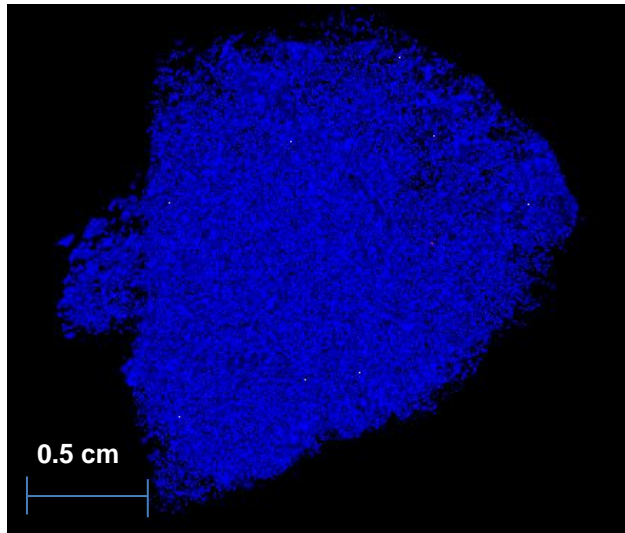
Figure 149: Particle KE001, Iron phase grain cluster, three dimensional views from eCognition8
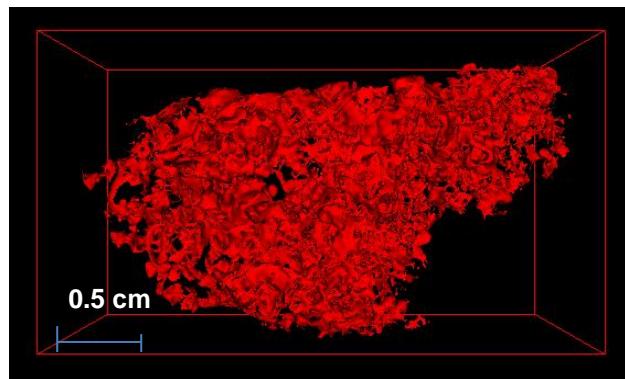
Figure 150: Particle KE003, Iron Phase grain cluster, three dimensional view from eCognition8
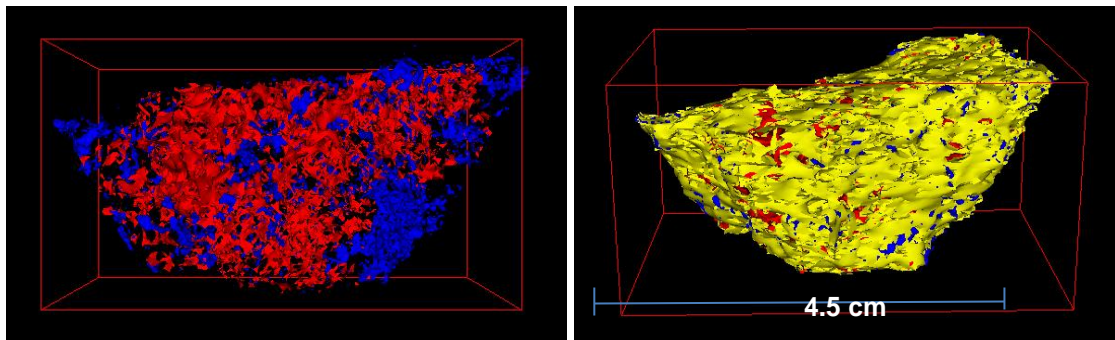
Figure 151: Total Iron phase grains and complete KE003 particle, three dimensional views from eCognition8, average image quality
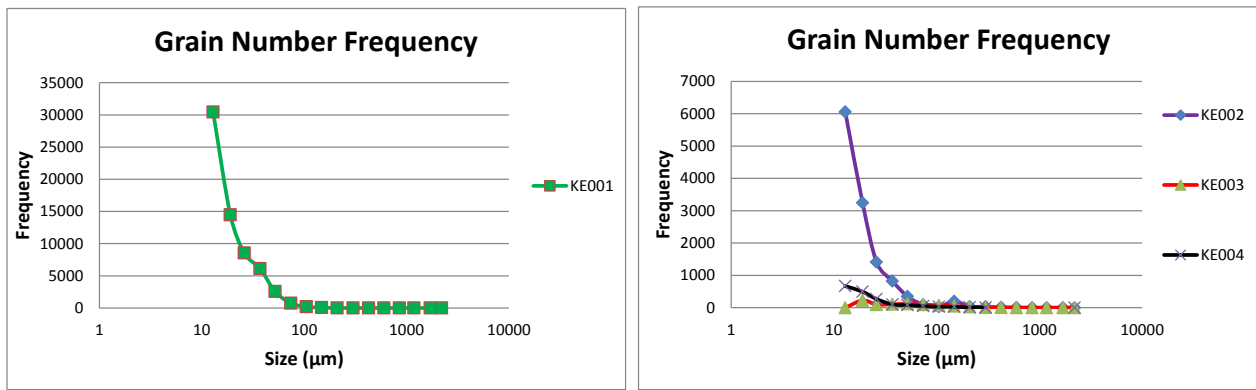
Figure 152: Parent particle iron phase grain size frequency

The parent particle iron grain size frequency for KE001, KE002, KE003 and KE004 is shown in Figure 152. Particle KE001 had finer iron phase grain size; KE002 had a mixed texture while KE003 and KE004 had coarse grained texture.

There was excellent agreement (over 93% recovery) between the measured mineral phase volume in the parent particle before breakage and the progeny particles after breakage. This also demonstrated that acquisition and image analysis rule set properties were adjusted correctly for each of the particles considered (Table 28 and Table 29).

Table 28: Measured and simulated total volume and weight

ID	Parent volume (mm^3)	Progeny volume (mm^3)	Parent weight (g)	Progeny weight (g)	Simulated 100 pixels cube volume (mm^3)	Simulated 50 pixels cube volume (mm^3)
KE001	57.4	53.9	0.227	0.214	57.6	57.6
KE002	46.8	43.5	0.199	0.160	46.6	46.9
KE003	51.1	48.7	0.154	0.147	50.1	50.4
KE004	55.22	54.4	0.196	0.187	56.4	55.6

Table 29: Measured and simulated iron phase volume

ID	Parent iron phase volume (mm^3)	Progeny iron volume (mm^3)	Simulated 100 pixels cube iron volume (mm^3)	Simulated 50 pixels cube iron volume (mm^3)
KE001	15.9	15	16	15.7
KE002	21	20.6	20.8	20.7
KE003	10.8	10.2	10.9	10.9
KE004	22.1	21.2	22.5	22.3

There is the difference between measured parent iron phase volume and the measured progeny iron phase volume because of a minor loss of weight during the breakage in RTB. Simulated cube iron phase volume difference to the measured parent iron phase volume was less than 1% (Table 30).

Table 30: Measured and simulated relative error to parent measured iron phase volume

ID	Progeny iron volume	Simulated 100 pixels cube iron volume	Simulated 50 pixels cube iron volume (mm3)
KE001	-5.7%	0.6%	-1.3%
KE002	-1.9%	-1.0%	-1.4%
KE003	-5.6%	0.9%	0.9%
KE004	-4.1%	1.8%	0.9%

6.3.4 Image analysis

An example of a rule set image analysis is shown in Figure 153. As already stated, the basis for the image analysis rule set was developed in previous sections. Each of the progeny particles were segmented and mineral phases classified according to a set of rules defined in eCognition8. Thus, the results of all collected particles were combined after which the grain size distributions were compared between broken particles and the parent particle. The findings were that the rule set classification provided very similar results. An example of a rule set is given in 9.18.
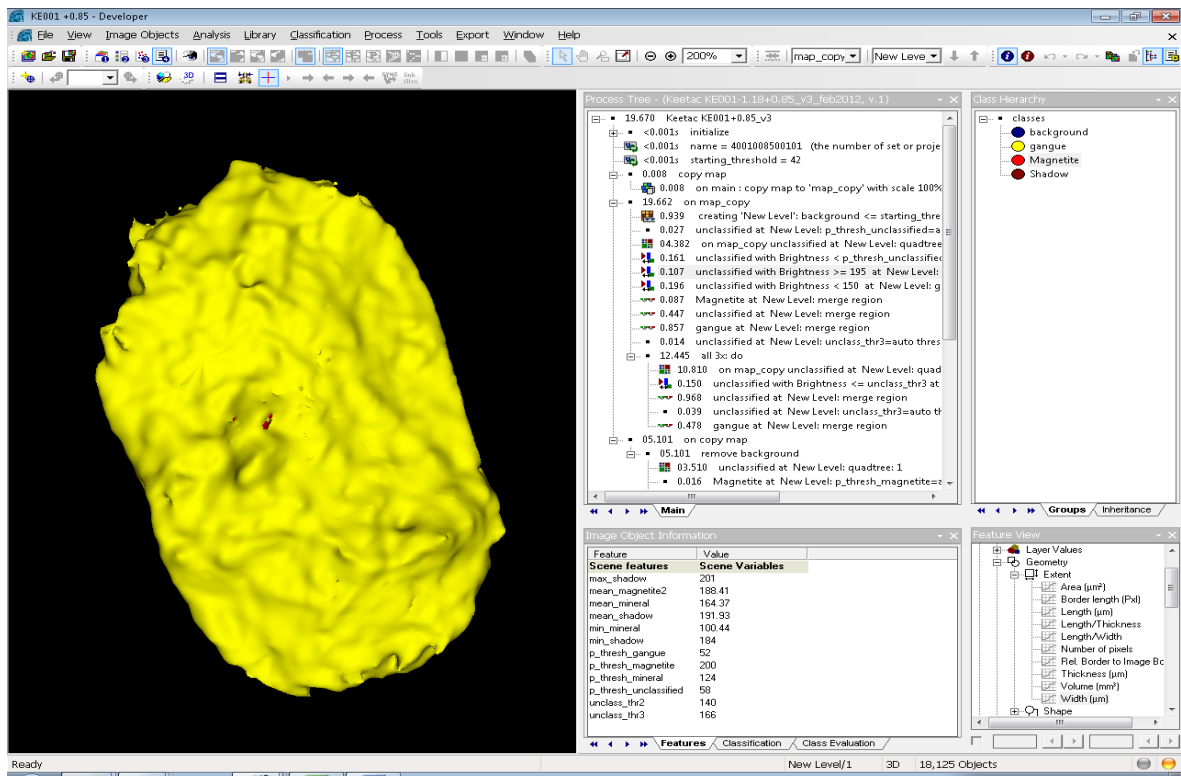
Figure 153: Screenshot of eCognition8, programming rule set on the right, image analysis result three dimensional view on the left.

Based on the image quality, the starting greyscale levels were set for background removal and identification of the high density phase, since these two represent the extreme greyscale levels (less than 3 and more then 140). Layers of two dimensional images were reconstructed and then segmented into squares whose greyscale difference would not exceed 5. Low valued squares were classified as gangue phase. For the remaining of unclassified phase, an automatic threshold function decided on the iron phase greyscale level and classified it using the linear model into gangue and iron phases. appendix 9.22 explains how particle connection is achieved in three dimensions.

Several functions were used to remove any unrealistic phase in the background segment (such as reconstructed image noise removal). No ring artefact effects were noticed in the selected particle images. The programmed rule set connected two dimensional classified gangue and iron mineral grains into three dimensional objects. The volume of classified iron mineral and gangue grains was obtained in table form as well as their positions and shape.

Parent particle bitmap images were cut into virtual three dimensional cubes using the CTAn software. The number of cubes generated and the number of total particles measured is shown in Table 31. Each of these cubes was then analysed in eCognition8 using the rule set applied to progeny particles. The cube edges for this analysis were 100, 50 and 25 pixels for particle number KE001, and the bitmap images of the cross sections of the cubes are given in Figure 154. Figure 155 presents a 3D view of the internal and edge cube classified in eCognition8. The internal cube is the cube which has no contact with the particle surface, and the edge cube is positioned at the particle surface.

Table 31: The number of measured particles

ID	Number of particles			
	100 pixels cubes	50 pixels cubes	25 pixels cubes	progeny
KE001	89	408	2284	525
KE002	69	356	*	2660
KE003	66	376	*	2640
KE004	73	403	*	4772

*note: only KE001 was analysed with 25 pixels cube due to very time consuming manual process

1292µm   646µm   323µm
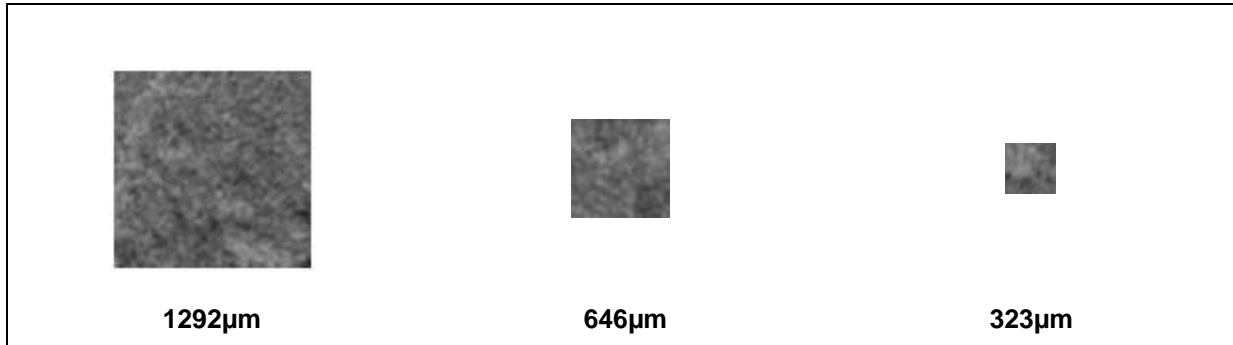
Figure 154: Cube cross section profiles, bmp images, 2000 x zoom

The reason behind this analysis was simulation of the random breakage of parent particles into cubes, as per Wiegel (1975).

Internal Cube - 3D	Internal Cube – Gangue phase	Internal Cube – iron mineral phase

1.292mm

Edge Cube – 3D	Edge Cube – gangue phase	Edge Cube – iron mineral phase

1.292mm
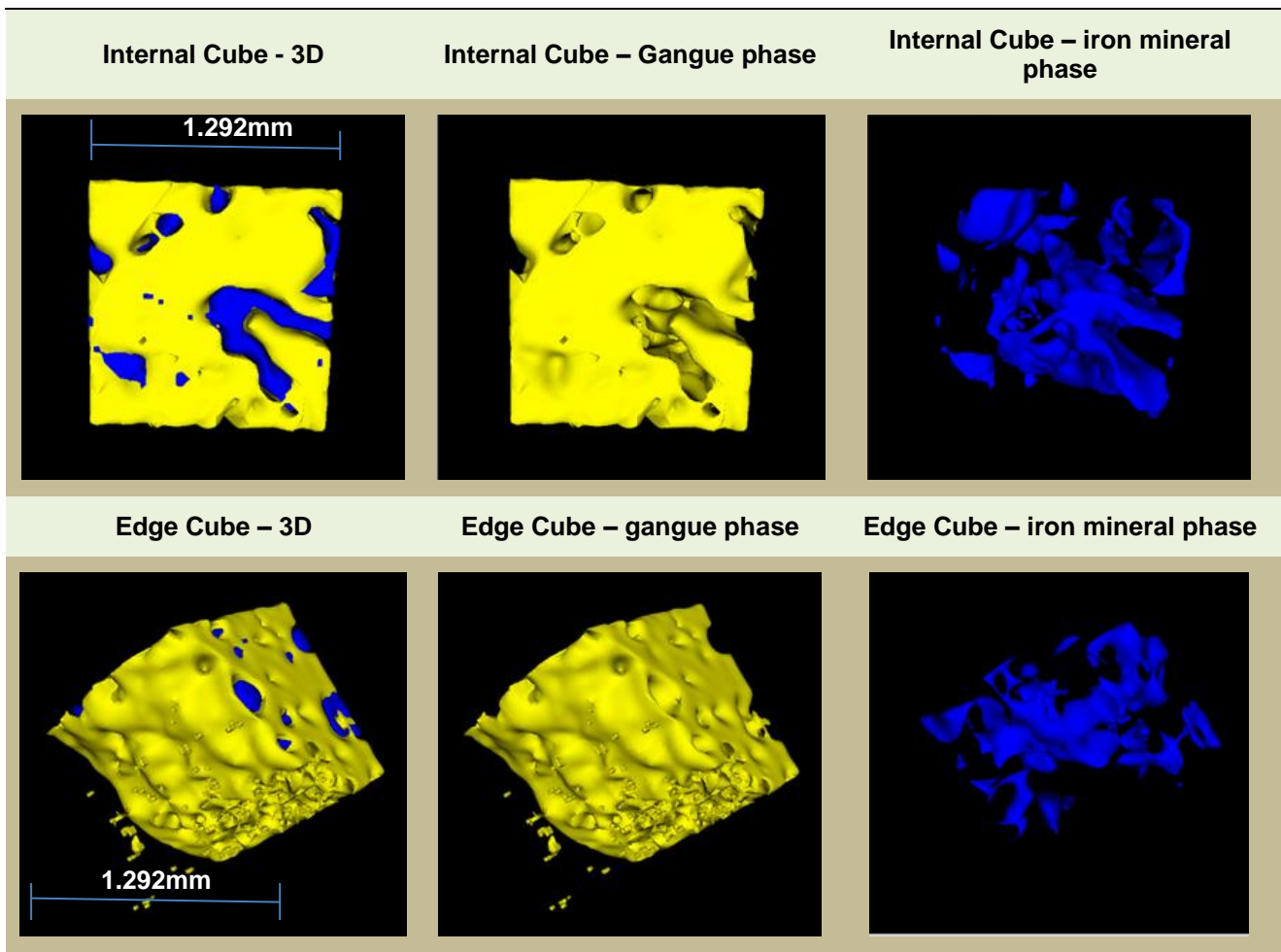
Figure 155: Simulated progeny cubes classified in eCognition8, average display quality

6.4   Results

The results generated in this section were quite complex and it was a challenge to find the way to transform the data into understandable form. Many of tables and graphs are based on ideas given in the liberation literature. Iron phase grains varied in size between 13-2350µm, and thousands of progeny fine particles had to be loaded and processed one at the time in image analysis software. This was a time-consuming process.

6.4.1 The number of particles required

To ensure that 95% confidence interval gives an estimate of the grade with relative error of 10% in analysis of the similar ore as analysed in this Thesis, it is recommended that at least 52 particles be analysed. Details are provided in Table 32, based on section 2.4.2.2.

Table 32: Detailed sampling parameters

a	The decimal proportion or fractional concentration of the metal of interest	0.46
c	Mineralogical composition factor	4.69
g	granulometric constant (medium size range)	0.50
f	shape factor	0.50
R	average grade (%)	33.40
d	particle size (cm)	0.40
v95	95th percentile of the diameter (cm^3)	0.032
K	constant	0.78
l	liberation factor (average from data)	0.33
p	precision	0.10
σ_{FE}^2	estimated variance of the fundamental error	0.0025
m	required sample weight (g)	10.03
m_n	average particle weight (g)	0.19

6.4.2 Raw results, parent

The parent particle analysed in this section had just over 27% of valuable iron phase, indicating around 73% of gangue minerals which were grouped in a single phase. Liberation distribution per size fraction of the measured progeny particles is provided in Table 33.

Table 33: Parent and measured progeny liberation per size table, volume (mm^3), percentage of parent particle volume and the number of particles

Particle volume (mm^3)

liberation class	Parent 3.989	2.812	1.416	1.001	0.714	0.505	0.357	0.251	0.176	0.125	0.088	0.062	0.044	0.031	0.022	0.016
0.05					0.8363	0.2262	0.2429			0.0013	0.0026	0.0009	0.0018	0.0004	0.0004	0.0008
0.15				0.4000	0.3700	0.0335					0.0015	0.0007				
0.25	57.40 / 44.15				0.2070	0.0617			0.0043	0.0048	0.0028	0.0004				
0.35		1.7533			0.0340			0.0039	0.0072		0.0008					
0.45		1.9985	1.4411	0.1441	0.0768	0.0742	0.0217	0.0069	0.0062	0.0011		0.0001				
0.55			0.3792	0.3187	0.0446		0.0116	0.0121	0.0064	0.0012	0.0002	0.0001				
0.65			0.4625				0.0336	0.0058	0.0057	0.0008	0.0006	0.0001				
0.75							0.0506	0.0184	0.0110	0.0049	0.0011					
0.85						0.0382	0.0840	0.0438	0.0170	0.0054	0.0014					
0.95						0.0632	0.0951	0.0293	0.0399	0.0113	0.0015	0.0008	0.0001			
Sum mm^3	57.4 / 44.15	3.7518	2.6827	1.8760	0.4768	0.4184	0.2967	0.1246	0.0994	0.0317	0.0077	0.0029	0.0005	0.0004	0.0008	
									53.9218							

Percentage of parent volume

liberation class	Parent 3.989	2.812	1.416	1.001	0.714	0.505	0.357	0.251	0.176	0.125	0.088	0.062	0.044	0.031	0.022	0.016
0.05			0	0	1.551	0.420	0.450	0	0	0.0024	0.0049	0.0018	0.0033	0.0008	0.0007	0.0014
0.15			0	0.742	0.686	0.062	0	0	0	0	0.0027	0.0013	0	0	0	0
0.25	100.00 / 81.88	0	0	0	0.384	0.114	0	0	0.0079	0.0088	0.0052	0.0007	0	0.0001	0	0
0.35		3.252	0	0	0.063	0	0	0.0073	0.0134	0	0.0015	0	0	0	0	0
0.45		3.706	2.672	0.267	0.142	0.138	0.040	0.0128	0.0114	0.0020	0	0.0001	0	0	0	0
0.55		0	0.703	0.591	0.083	0	0.022	0.0225	0.0119	0.0023	0.0004	0.0002	0	0	0	0
0.65		0	0.858	0	0	0	0.062	0.0108	0.0106	0.0014	0.0012	0.0002	0	0	0	0
0.75		0	0	0	0	0	0.094	0.0342	0.0203	0.0091	0.0021	0	0	0	0	0
0.85		0	0	0	0	0.071	0.156	0.0811	0.0315	0.0100	0.0027	0	0	0	0	0
0.95		0	0	0	0	0.117	0.176	0.0544	0.0739	0.0210	0.0029	0.0014	0.0002	0	0	0
Sum (%)	81.88	6.9578	4.9752	3.4790	0.8842	0.7760	0.5503	0.2311	0.1844	0.0587	0.0143	0.0053	0.0011	0.0007	0.0014	

Number of particles

liberation class	Parent 3.989	2.812	1.416	1.001	0.714	0.505	0.357	0.251	0.176	0.125	0.088	0.062	0.044	0.031	0.022	0.016
0.05					4	4	2			1	5	5	20	12	36	242
0.15				1	1	1					2	2				
0.25	Parent / 1				2	1			1	2	5	2		1		
0.35		1			1			1	3		3					
0.45		1	2	1	2	1	1	1	3	2		1				
0.55			1	2	1		1	2	3	2	1	1				
0.65			1				2	1	3	1	2	1				
0.75							3	3	5	6	5					
0.85						1	4	6	9	7	6					
0.95						2	6	6	19	18	5	7	2			
Sum	1	2	5	10	10	6	17	21	48	48	31	30	15	36	242	
									522							

The first table demonstrates the size reduction step and distribution of parent volume in each liberation size class after the breakage. It lists the volume measured in each composition range with the grain size particle size ratio progression of the $\sqrt{2}$. There were ten liberation classes defined. The 0-0.05 class was defined as liberated waste (from 95-100% gangue by volume) and the 0.95-0.1 class was defined as liberated value (from 95-100% magnetite by volume). Other classes were locked values and gangue ranging from 5-95% values (liberation class 0.1 to 0.9). The parent particle volume was 57.40mm^3, size 3.98mm and it was placed in 25-30% (0.25) liberation class as it was 27% liberated based on dense mineral phase content (magnetite). After breakage, the progeny particles were

screened and each particle was analysed in three dimensions then placed in liberation class based on the measured dense component volume. The coarsest progeny particle had a volume of 44.15mm^3 (2.81mm) and it belonged to the same liberation class as its parent particle. There was a loss of 0.013g from the original particle mass in the breakage stage, which resulted in a volume of 53.92mm^3 for the measured progeny particles.

The second table shows the same data expressed as percentage volume. It shows that over 99% of the parent particle is distributed in the coarser progeny particle compositions, while only 1% finished in the finer composition classes and was distributed towards the liberated limits. In the case of this particle, most of the progeny coarse particles were distributed around the parent liberation class and towards liberated gangue.

The last table shows the number of particles measured in each liberation size class, with the frequency increasing towards liberated value or gangue in finer size fractions.

The parent results provided here are the first unknown in the kernel equation, the feed true particle volume distribution with three dimensional properties of the mineral of interest. The progeny results are the second unknown in the kernel equation, the true particle distribution or breakage function. As mentioned earlier, this is a useful experimental strategy concept, and the representative feed sample with all size fractions would need to be measured for optimal kernel characterisation.

6.4.2.1 Comparison of line and area liberation to volumetric liberation data

Parent particles were analysed for liberation estimates using the attenuation profile line and area methods applied in CTAn. Five cross section (virtual) images were randomly selected. Each of these areas was analysed for area liberation after which ten profile lines were selected for line liberation. The process is schematically presented in Figure 156, and results for one particle given in Table 34 and Figure 157. The results for the other particles data are presented in appendix 9.25.
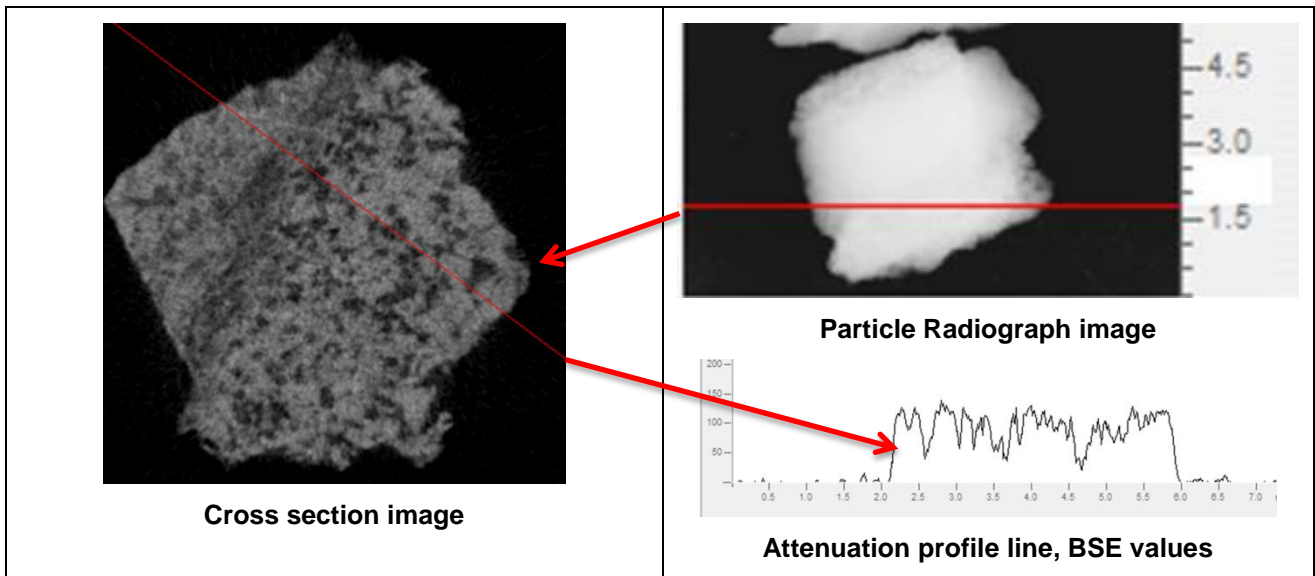
Figure 156: Line and Area liberation measurement

The results show that line measurements are accurate but imprecise which implies uncertainty and reduced confidence in results. For area liberation, 95% confidence limits were +/- 10.9%, and for line measurements these were +/- 3.9% for KE002. This does not mean that the line measurements were providing better results as line measurement had ten times higher number of degrees of freedom. For the line measurement t is significant with over 90% confidence for KE002 and over 99.9% confidence for KE004, and therefore the line method is not giving the correct volume liberation data. The standard deviation was higher than 10% for all but KE003 measurements. This method provides a powerful strategy for testing stereological corrections.

Table 34: Liberation information in one, two and three dimensions, particle KE002

	Liberation per area (%)	Line Liberation per profile line/per area (%)								
Particle three dimensional volumetric liberation 44.9%										
Area 1	37.7	47.9	34.8	30.8	41.5	59.1	53.0	46.9	46.7	38.9	46.4
Area 2	44.7	53.3	50.2	44.9	49.2	57.1	43.8	61.6	43.0	49.8	45.7
Area 3	49.8	41.3	60.1	52.3	67.8	51.4	60.9	52.2	74.5	55.1	49.1
Area 4	19.0	17.7	27.4	30.3	12.3	32.9	33.6	26.7	24.7	36.4	23.8
Area 5	28.6	27.4	25.6	24.2	42.0	21.6	12.6	27.9	31.3	32.8	34.4
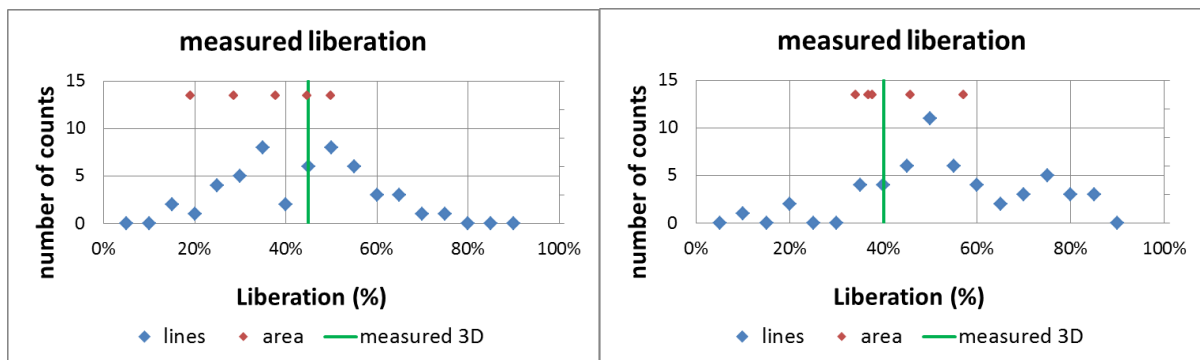
Figure 157: Number of counts of liberation range in line liberation and area liberation measurement (calculated to volume %) and three dimensional volumetric measurement, KE002 and KE004

The data presented here gives the emphasis on sampling and how important the sampling for area liberation measurement is. If the particle was crushed and sampled for area measurement, the data would high likely be more precise and closer to the real three dimensional composition.

6.4.2.2 Comparison of particles less than 300µm between MLA and Micro CBT

A comparison of MLA and Micro CBT data has already been presented in Chapter 5. The size fraction passing 300µm has been subjected to Micro CBT liberation analysis. This process identified 494 particles which were then analysed in the MLA. The graphs comparing the results from the two methods of analysis are shown in Figure 158.
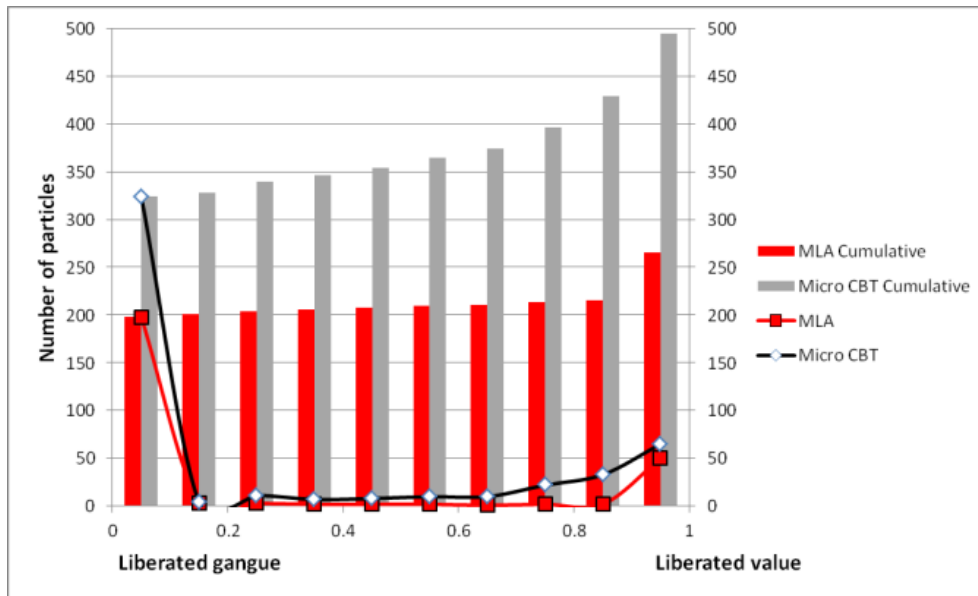
Figure 158: Comparison between MLA and Micro CBT analysis on -300µm size fraction

The sample preparation process for Micro CBT does not involve any physical damage to the particles. However the sample preparation process for MLA includes mounting of particles in resin and polishing. Although special care was taken during the manual polishing, some of the particles have been lost and the total number of identified particles in the MLA sample was 265.

The correlation between two datasets is considered to be acceptable. The difference is significant with 75 % confidence, which means that the measurements modes statistically give similar results. The data processing of Micro CBT images was very time and labour intensive, due to the inability of the available rule set (programming within the eCognition software) to separate touching particles and provide particle by particle data. It is recommended that the MLA or other SEM based two dimensional analysis be used for finer size fractions.

6.4.3 Random breakage model prediction and discussion

This section compares the measured liberation of broken parent particles and liberation simulated by cutting the parent particle reconstructed Micro CBT two dimensional images into different size cubes. The modelled cube size has geometric limitations because of already set size of 25, 50 and 100 pixels cube edge (323µm, 646µm and 1293µm). This limitation is very important as it does not allow simulated particles to belong to more liberated gangue or value unless the grain size of the mineral phase is similar or greater than simulated cube size. While this model has its geometric limitations it is still able to provide estimates of the distribution of the mineral species in the locked particles.

The breakage model presented here differs from Wiegel and Li (1967) in that the geometric arrangement of mineral grains, as they are not presented in terms of breakage pattern dimensions but rather their true volume dimension. The grains presented here are not of the cubic uniform shape and in lattice like arrangement. Fracture patterns are parallel but there is no dependence on mineral grain arrangement. The similarity is uniform predicted progeny size.

It is believed that cubes convey the ideas that help one to understand how the composition of parent particles relates to the original mineral grain size, the particle size and the location of individual grains. It can help develop the relationship to describe liberation effects of size reduction. This approach isolates size reduction from particle composition. The cube concept helps keep size reduction constant so that liberation can be assessed. This is a way of assessing grind rates and providing more information of actual breakage modes.

In an ideal system, grains with shapes based on actual progeny might be used for simulated breakage. However, this approach is beyond the capacity of the currently available software and can be considered as possible further work.

The models presented here are suitable for investigating iron formation deposits. It is important to find the size at which magnetite is sufficiently liberated from its silicate matrix. Also if the ore is coarse grained magnetite, it would be reasonable to reject fine liberated gangue.

Magnetite ore of 50-75% magnetite (37-52% Fe) is currently considered feasible. It is not uncommon for magnetite ore to be present in two liberation forms in deposits. The first type is coarse size grained consistent with inherent silica and the second is finer size (Figure 159). The type of liberation directly influences the design of the flow sheet. (McNab et al. 2009)
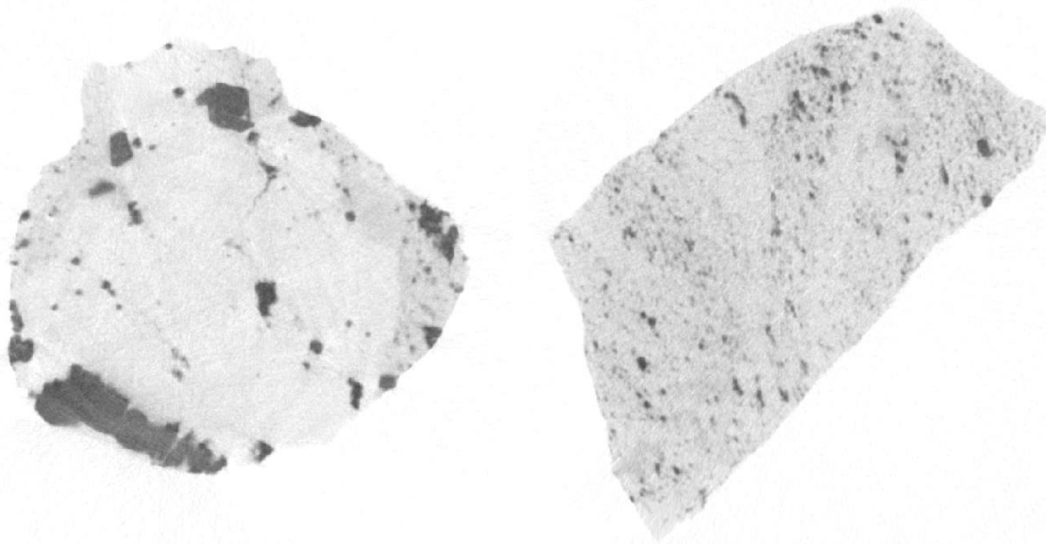
Figure 159: Magnetite ore from a single deposit, different textures - coarse and fine size grained, SkyScan1172 reconstructed cross-sectional image

For magnetite liberation, surface data is not of the same importance as for copper or lead/zinc ore deposits since magnetite separation is based on magnetic properties and not on flotation physical-chemical properties.

Also, association of copper with pyrite is important in copper ore processing if selective flotation is present as the first stage of separation. As copper minerals cannot be separated from pyrite using this technique, the application could be in processing

flowsheet designs where initial separation is collective copper pyrite flotation-gangue rejection, then selective copper pyrite flotation. However, these flowsheet suffer from difficulties of depressing pyrite as once activated grain tends to stay activated.

For selective Cu-Py flotation, feed particles can be analysed for group copper/pyrite liberation, products can be analysed for group mineral liberation in three dimensions then calibrated with two-dimensional mineralogical data for separated copper pyrite liberation. However, if the quantities of pyrite are insignificant and if there is no need for pyrite to be separated (especially in cases where gold is associated with pyrite), the method presented here can find readily applications in the industry. For large scale applications, development of process automation is needed to enable large number of particle analyses and improved statistical information.

The data are presented in multidimensional space, and although many display modes have been approached, it is difficult to present the data in a clear, simplified and understandable form. The presented data could find readily applications in iron ore flowsheet design.

6.4.3.1 Data presentation, family of curves

The approach of presenting a family of curves to represent a complete process is well-known and has been used at JKMRC for many years. The method presented in Figure 160 was developed at JKMRC (Whiten 1972) and it is used to describe the size distribution after a breakage event. The parameter t_{10} is defined as percentage passing one tenth of the original parent particle size. Thus t_2 is percentage passing half of the parent particle size and t_4 is the percentage passing quarter of the original parent size. Using the model presented in Figure 160, one can relate the energy applied during breakage and use it to predict the size distribution in future events using different energies. Each particle line on provides a breakage function.
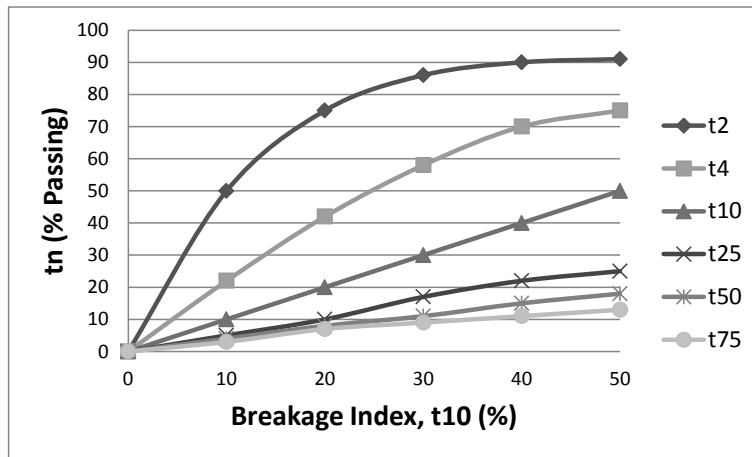
Figure 160: t vs degree of breakage, t_{10} (after Narayanan 1985)

A similar concept can be used to present liberation data. Weedon and Napier-Munn (1990) presented a relationship between particle size and progeny size ratio (L) using cumulative percentage liberated smaller than that progeny particle size. Figure 163 uses the same idea and the data generated in this Thesis.

The model using the L parameter concept is used to predict size by size liberation of each mineral phase (Weedon 2001). However it is based on two dimensional cross sectional QEMSCAN data. Feed data has not been measured and the distribution of breakage parameters has been fitted to feed.
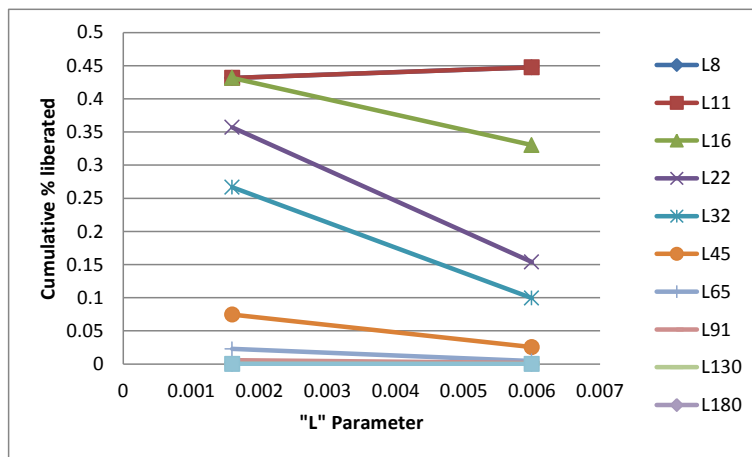
Figure 161: Example of a family of "L" lines from measured progeny liberation (after Weedon and Napier-Munn 1990)

6.4.3.2Measured progeny

Figure 162 shows the Gaudin Liberation model (Wiegel 1975) and actual measured lines of constant liberation for the particle KE001. Here the grain size was kept constant, and particle size was varied. A change of grain size would only impact the grain to particle size ratio, and not the shape of the curve which is constant.

The lines of constant liberation show the relationships over the entire liberation size spectrum, the data related to the proportion of liberated waste and liberated values particles, and locked waste and values particles. It defines the relationship for the magnetite silicate binary mineral system among the volumetric proportion of value and relates it to size reduction progeny to particle size to grain size ratio.(Wiegel 1976a, 2006)

Examination of the graphs indicates that the liberation pattern for this type of ore is not linear, exponential or logarithmic, but very variable depending on the particle size. The GRLM shows a significant downward trend for liberated values toward the coarser size fractions, which is not visible in the measured liberation.

Figure 162 is a very powerful graph which shows liberation for each size fraction and the data can be used to reject waste in the size reduction process in magnetite processing plants. Table 35 provides the details on grain to particle size ratio for a given particle size. For a given ore, if the particle of a known size and liberation is broken, progeny particles 125 µm in size (from the table K=0.42) would be around 30% greater than 95% liberated, 70% would be over 70% liberated value, around 10% of progeny would be liberated waste. For finer progeny particles of around 30 µm in size, over 70% would be liberated waste.

The measured liberation shows that this ore liberates well at around 104µm (0.5 grain size to particle size ratio) and again at 50µm, which could be indication where classification of this ore type should happen in the field. There is reasonable agreement between models and measurement in the range of finer progeny particles where liberation, as expected, proves to tend towards fully liberated particles, gangue or valuable.

Figure 162, liberation by size fraction graphs, were compared to the real data generated using the method presented here. They were seen as maps (signatures) for a particular ore, where at each particle progeny size the full liberation distribution can be predicted, in this case measured. Including the measured mineral volume in a specific composition range will bring the insight into the liberation of particular ore.

The number of liberation classes is not extended in this Thesis, but it is possible to be achieved. The selected liberation class values were matching Wiegel liberation classes in order to enable evaluation of the random model concept. The idea was to present a simplified model that is already common and used in the industry.
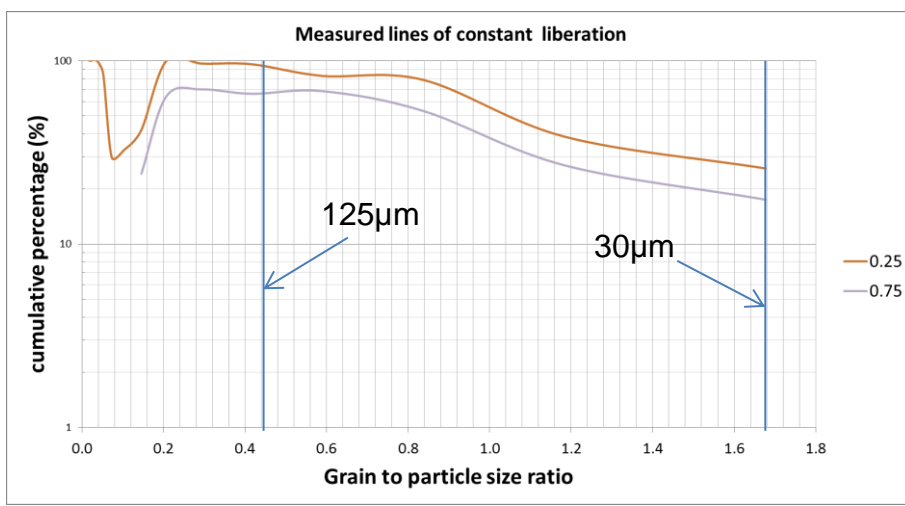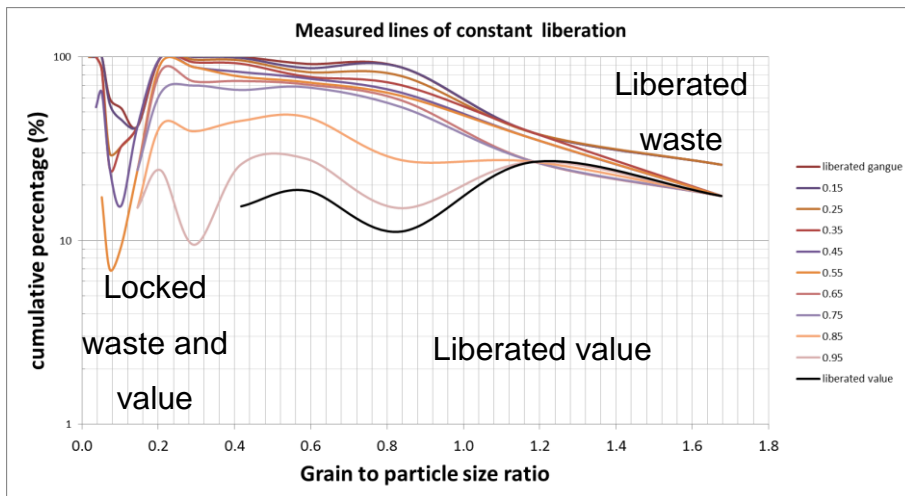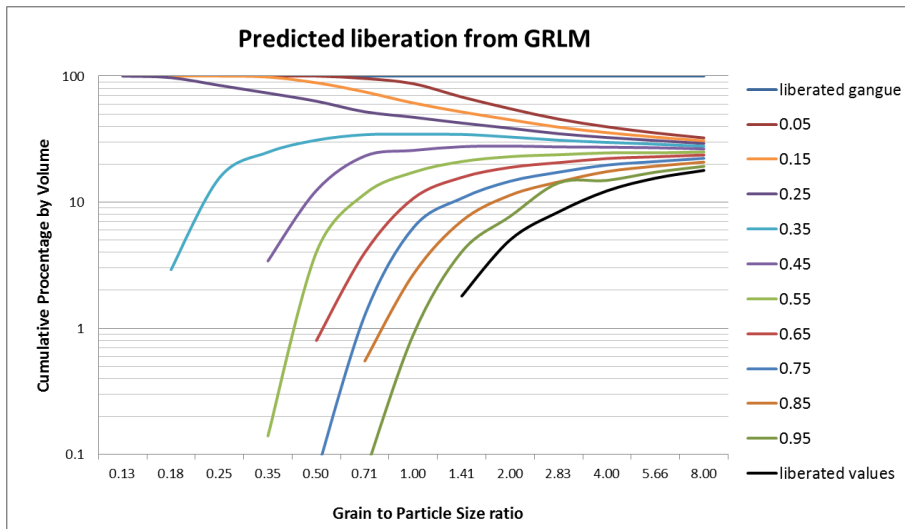
Figure 162: Predicted liberation from GRLM Wiegel (up, average grain size 0.054mm) and measured lines of constant liberation (bottom two graphs, average grain size 0.052mm), KE001

295

Table 35: K is grain to particle size ratio for a given particle size (average grain size 0.52mm)

K	0.02	0.04	0.05	0.07	0.10	0.15	0.21	0.29	0.42	0.59	0.84	1.19	1.68	2.34
Size (mm)	2.89	1.42	1.00	0.71	0.50	0.36	0.25	0.18	0.125	0.09	0.06	0.04	0.03	0.02

A key concept in analysing three dimensional liberation data obtained from measuring progeny particles is that the broken particle size distribution could be correlated with its mineral grain size distribution, grain position in gangue mineral matrix and reasonably predict liberation. It is practical to consider the porosity and rock type influence on prediction. However, research of this type is beyond of the scope of this Thesis.

Figure 162 and Figure 174 present graphs with measured lines of constant liberation for particle KE001 and KE002, with other particle data provided in appendix 9.26 and 9.27. This is a simple way of relating size reduction process to liberation. If a single particle of a known size and liberation is broken, and if progeny particles of known size are examined for liberation, a full map of liberation per size can be obtained. This map contains the measured degree of liberation of progeny and it does not require a complicated model.

If the grain size is changed, the lines will respond by moving along the axes, and there is no need for model adjustments for grain size adjustments.

On an industrial scale, if a larger number of the same texture particles is measured, the low particle number noise noticed in Figure 162 may be reduced or completely removed.
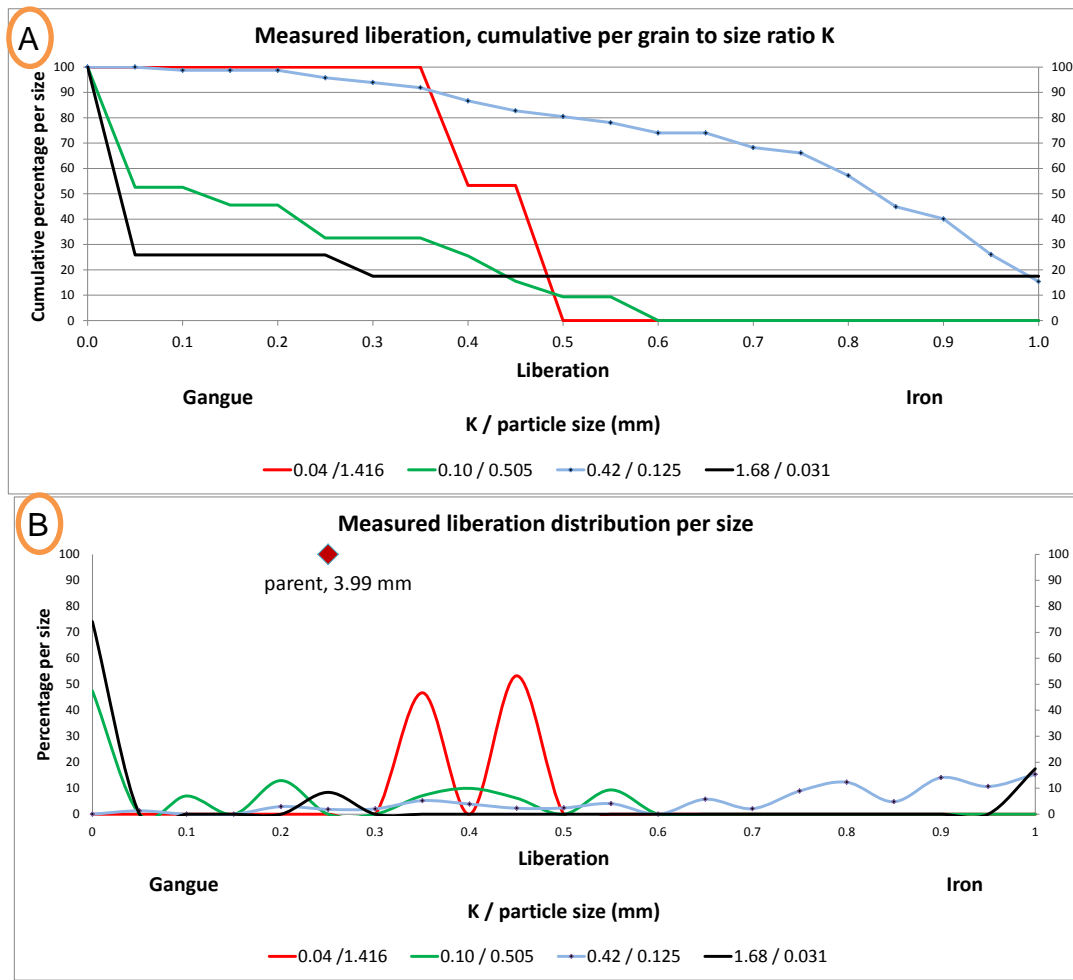
Figure 163: KE001 progeny particle composition at a given size or grain to particle size ratio

Figure 162 can be replotted in terms of particle composition per size fraction. Perhaps the best way to consider the map is to present the lines of constant liberation in liberation per size fraction or particle to size ratio form as in Figure 163 (cumulative percentage volume A and volume percentage B). If one wants to see how the 125μm progeny particles would be liberated, a cross section line through Figure 162 at the point 0.42 (K from Table 35) would provide particle composition of around 15% liberated value and about 70% of that fraction would be more than 70% liberated value (Figure 163, A, blue dotted line). The distribution of volume percentage per size is given in Figure 163, B. It is reasonable that with finer size liberation percentage increases, which is also presented on the graph (505μm particles had under 50% liberated gangue where 31μm particles had over 70% liberated gangue).

6.4.3.3 Simulation of random breakage

The difference between the particles identified as KE001 and KE003 is in their mineral grain size distribution and the energy applied in the breakage event. The first is set has one large cluster of grains and thousands of very fine iron phase grains (Figure 152). The second particle KE003 also had one large cluster of iron phase grains, similar in size to the KE001 grain cluster. However the remaining 65 % of the grains were coarser then KE001 grains as shown in Figure 164. Data from the parent grain size distribution analysis is presented in Table 36 and Table 37.

6.4.3.3.1 Valuable phase volume distribution

The energy applied to break particle KE001 was 0.4 kWh/t, and to break KE002, KE003 and KE004 energy of 1.0 kWh/t was applied. It is believed that this large progeny particle from particle KE001 would most likely have been broken the same way its parent particle broke if a higher energy was applied.

Table 36: Parent particles grain cumulative distribution by volume, with and without grain cluster

Parent particles					Parent particles				
Valuable Phase Grain size (µm), cumulative by volume %					Valuable Phase Grain size (µm), cumulative by volume %				
Grain Size (µm)	KE001	KE002	KE003	KE004	Grain Size (µm)	KE001	KE002	KE003	KE004
13	0.5%	0.1%	0.0%	0.0%	13	2.6%	0.3%	0.0%	0.4%
19	1.3%	0.2%	0.0%	0.0%	19	6.5%	0.7%	0.2%	1.3%
26	2.4%	0.4%	0.0%	0.1%	26	12.5%	1.2%	0.4%	2.6%
37	4.8%	0.6%	0.1%	0.1%	37	24.8%	2.0%	1.0%	4.0%
52	7.5%	1.0%	0.2%	0.2%	52	39.1%	2.9%	2.9%	7.0%
74	9.8%	1.2%	0.6%	0.4%	74	51.2%	3.6%	7.4%	12.3%
105	11.6%	1.4%	1.3%	0.7%	105	60.5%	4.2%	17.0%	21.4%
148	13.1%	5.5%	2.6%	1.5%	148	68.0%	16.7%	34.9%	45.9%
210	14.3%	7.7%	4.8%	2.4%	210	74.6%	23.6%	63.7%	70.9%
300	14.5%	13.0%	6.2%	3.4%	300	75.7%	39.8%	82.3%	100.0%
425	14.5%	19.3%	8%	3%	425	75.7%	59.0%	100%	100%
600	14.5%	28.9%	8%	3%	600	75.7%	88.2%	100%	100%
850	19%	33%	8%	3%	850	100%	100%	100%	100%
1180	19%	33%	8%	3%	1180	100%	100%	100%	100%
1700	19%	33%	8%	3%	1700	100%	100%	100%	100%
2350	100%	100%	100%	100%	2350	100%	100%	100%	100%

298

Table 37: Parent particles grain volume, with and without grain cluster

Parent particles					Parent particles				
Valuable Phase Grain size (µm), volume %					Valuable Phase Grain size (µm), volume %				
Grain Size (µm)	KE001	KE002	KE003	KE004	Grain Size (µm)	KE001	KE002	KE003	KE004
13	0.50%	0.08%	0.00%	0.01%	13	2.58%	0.25%	0.00%	0.39%
19	0.75%	0.14%	0.01%	0.03%	19	3.93%	0.43%	0.18%	0.92%
26	1.14%	0.16%	0.01%	0.04%	26	5.95%	0.48%	0.20%	1.27%
37	2.36%	0.26%	0.05%	0.05%	37	12.30%	0.80%	0.62%	1.41%
52	2.74%	0.31%	0.14%	0.10%	52	14.30%	0.95%	1.89%	3.00%
74	2.33%	0.22%	0.34%	0.18%	74	12.12%	0.66%	4.48%	5.36%
105	1.78%	0.21%	0.72%	0.30%	105	9.29%	0.65%	9.60%	9.06%
148	1.45%	4.07%	1.35%	0.82%	148	7.57%	12.44%	17.92%	24.49%
210	1.27%	2.28%	2.17%	0.84%	210	6.59%	6.96%	28.79%	24.98%
300	0.20%	5.29%	1.41%	0.98%	300	1.07%	16.14%	18.65%	29.14%
425	0.00%	6.30%	1.33%	0.00%	425	0.00%	19.24%	17.68%	0.00%
600	0.00%	9.55%	0.00%	0.00%	600	0.00%	29.15%	0.00%	0.00%
850	4.66%	3.88%	0.00%	0.00%	850	24.29%	11.84%	0.00%	0.00%
1180	0.00%	0.00%	0.00%	0.00%	1180	0.00%	0.00%	0.00%	0.00%
1700	0.00%	0.00%	0.00%	0.00%	1700	0.00%	0.00%	0.00%	0.00%
2350	80.81%	67.24%	92.46%	96.64%	2350	0.00%	0.00%	0.00%	0.00%
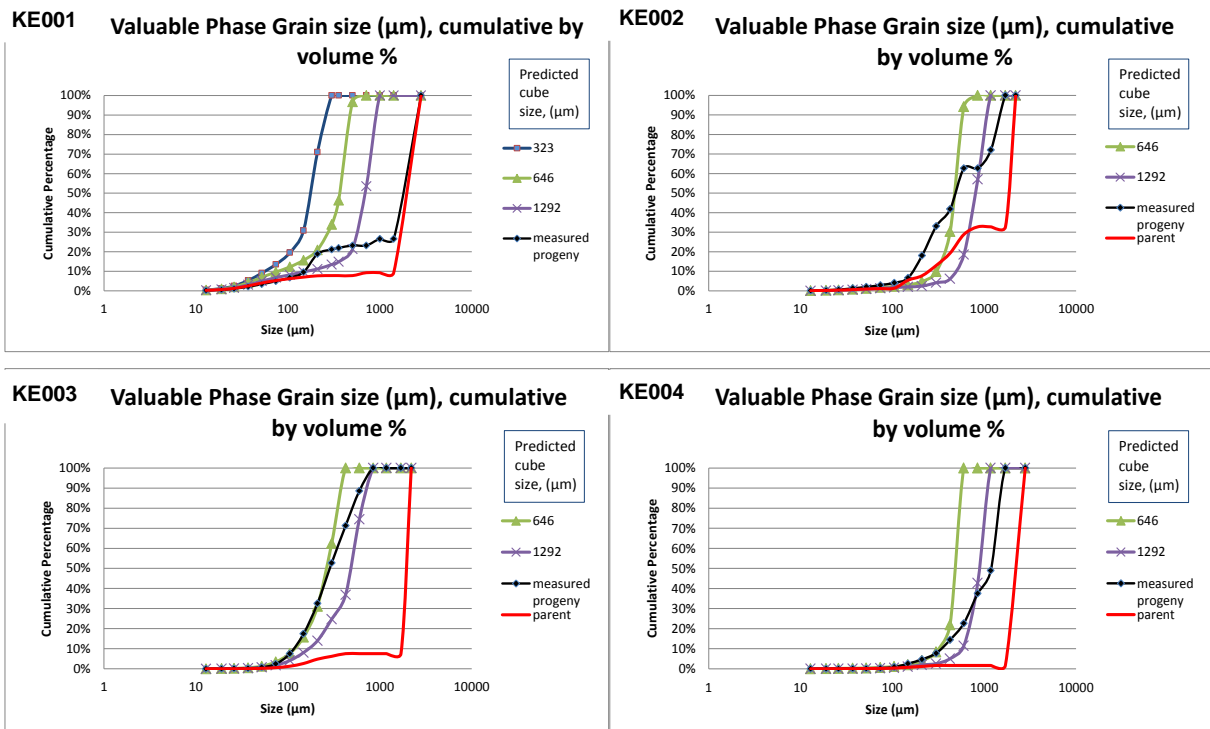
Figure 164: Iron phase grain size distribution per volume, predicted and measured progeny and parent KE001, KE002, KE003 and KE004

As the cluster of grains has an irregular shape, predicting liberation by applying a random breakage cube fracture pattern applies to some extent, but it fails to predict the much faster liberation of valuables at coarser size fractions. Figure 164 presents the cumulative distribution by volume of iron phase measured in simulated random breakage cubes and progeny and parent particles.

As mentioned previously, random simulated breakage has its geometrical limitations. For coarser cubes, grains remain almost intact as the simulated progeny size is coarse and there is less chance for the fracture pattern to go across iron phase grains. With a reduced simulated cube size, the chance of breaking iron phase grains is increased. However, with a fine cube size there is a geometric limitation on estimating large iron phase grains, as they are larger than the fracture pattern size and have 100% chance of breaking. Thus grain size measured here is geometrically limited to cube size. Figure 164 in a table form for KE001 is given in appendix 9.28.

6.4.3.3.2 Measured progeny and simulated cube liberation

Hsih and Wen (1994) suggested incorporating a detachment factor in their liberation model. The work presented here supports the idea that it is not only size reduction that controls liberation, but the ore type properties as well. This can be explained by intergranular weak bond (Lawn 2004; Lawn et al. 1977) where the fracture goes rather between different minerals than through a single mineral phase as seen in Figure 165.

Figure 165 shows all particles and cubes measured in three dimensions for iron phase volume, going from coarse cube on the top graph to the fine cube on the bottom graph. This figure shows the iron phase volume percentage (liberation class from liberated gangue 0 to liberated iron phase 1) for each progeny (predicted and measured) on y axes and progeny size in mm on x axes.

The apparent bias of simulated breakage towards liberated gangue can be explained through texture. As the texture was disseminated finer, many of simulated fine cubes will have some iron phase, depending on the grain position within particle matrix. This leads to an underestimating of the liberation of iron phase because of the previously explained geometrical limitations of cube breakage, where liberation is influenced by inability to break iron formations to size at which particle would appear to be more liberated. Hence estimation of locked low grade gangue would be appropriate. It is obvious from Figure 165

300

when considering measured liberation that the liberation was influenced not only by size reduction but also by intergranular weak bond between the iron phase and gangue.

Understandably, with a coarser simulated cube size than the iron phase grain size, the liberation of gangue would be underestimated. This is all plausible in terms of interfacial area weakness compared to mineral grain forces. The data in Figure 165 supports this. The geometrical limitations focus around cube size, and do not allow for faster iron phase liberation.
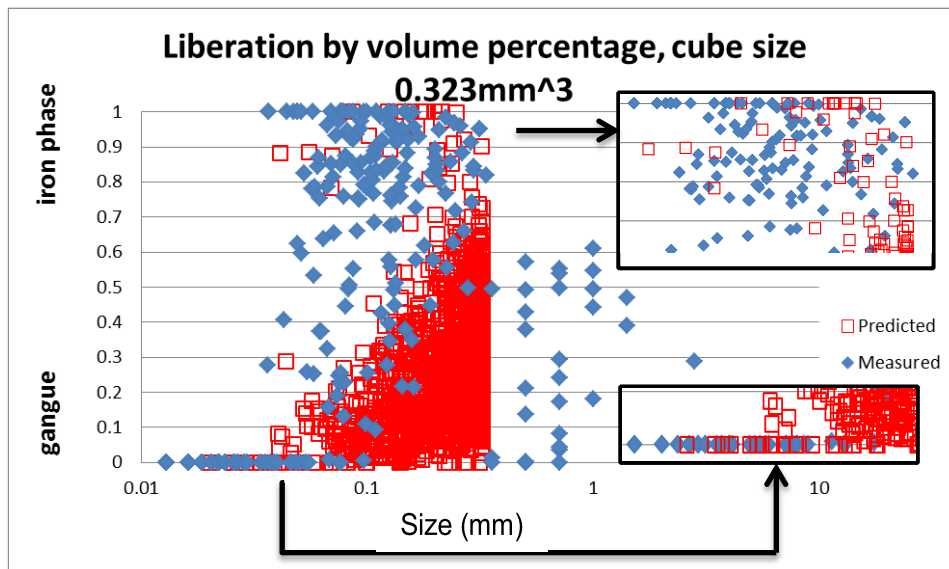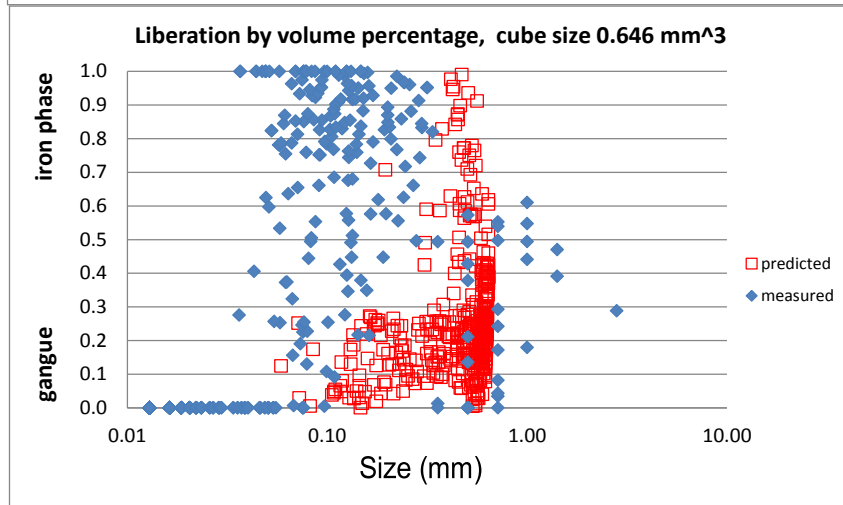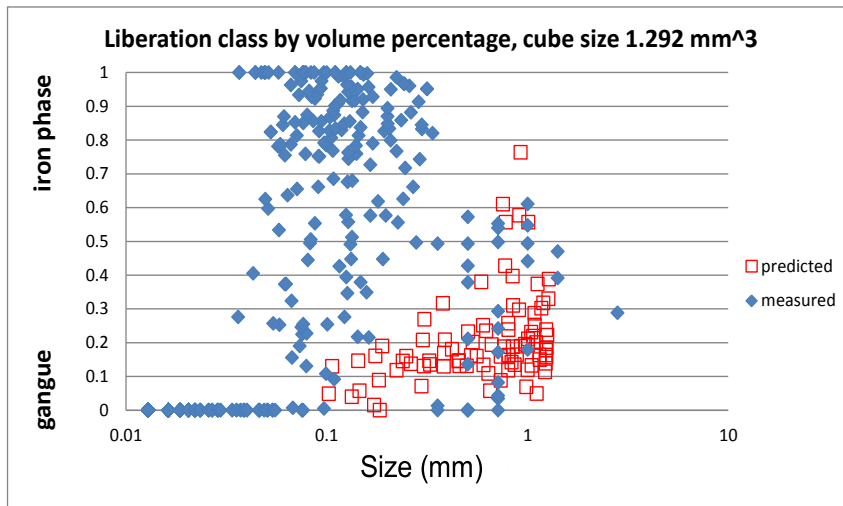
Figure 165: Measured progeny and simulated breakage of parent particle with 1292, 646 and 323µm³ cube size, particle KE001
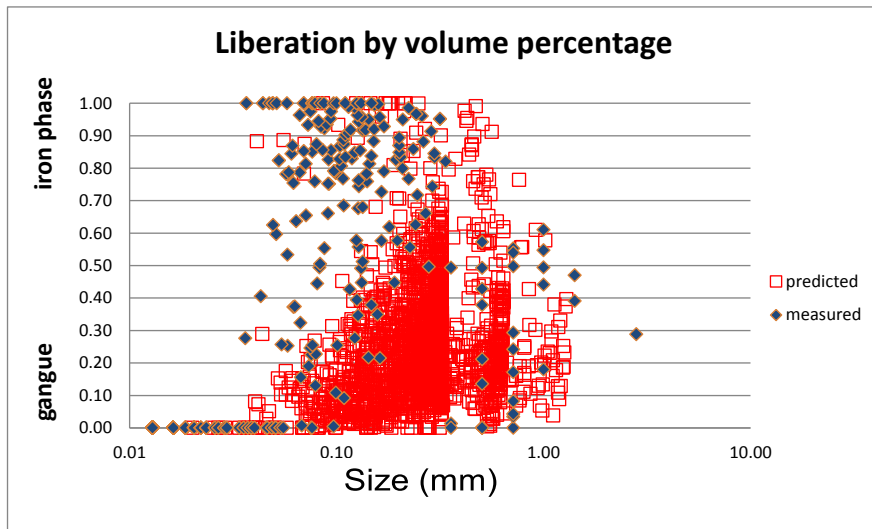
Figure 166: Measured progeny and simulated breakage of parent particle, combined three different simulations with 1292, 646 and 323µm³ cube size, particle KE001

The iron phase tends to break into finer particles, but there is still a strong correlation between the simulated coarser cube breakage (1292 and 646µm³ cube size) and that measured in the range of coarse low grade particles. The correlation is not so strong in high density particles. Figure 166 presents the data for the measured progeny particles and combines the three sets of simulated breakage data from Figure 165. All particles from the simulated cubes are presented, so care should be taken if any future test analysis is to be performed on this set.

The situation when considering a coarser texture is exactly the opposite. As the cube size is coarser and closer to the grain size, it does predict the coarse liberated fraction reasonably well, but fails to predict fine liberated fraction. Figure 173 clearly demonstrates that random breakage of a coarse ore texture and coarse fracture pattern will only result in narrow liberation values, closer to the parent liberation. If a fine fracture pattern is used to simulate breakage than due to the coarse mineral grain size, there is a high probability that the liberation will be overestimated. The lower error is possible when there is a natural tendency in the ore to break along interphase boundaries, thus when both liberation by size reduction and liberation by detachment occur together.
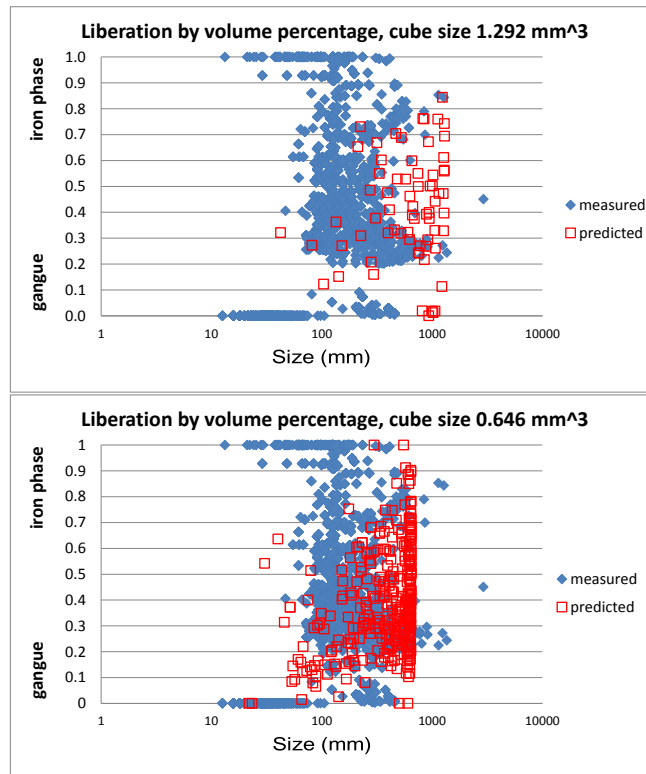
Figure 167: Measured progeny and simulated breakage of parent particle with 1292 and 646µm3 cube size, particle KE002

For the analysed particles, it is obvious that preferential breakage is occurring when liberation of the valuable phase is considered. For coarser breakage, using the 1.292mm^3 simulated cubes, only some liberation happens and size reduction would be dominant. It would be hard to predict the full liberation distribution using only this approach. However, if combined with simulation using cubes with 0.646mm^3 in size, the predicted data will be closer to the real progeny liberation distribution. Figure 167 shows the measured and simulated liberation when particle KE002 is considered, KE003 and KE004 are shown in appendix 9.26 and 9.27. There is a high variance due to the small numbers of particles in some liberation classes with a single parent. With several parent particles (of similar texture) the variance can be expected to decrease. (section 2.4.2.2)

As mentioned previously, the ore tested here was magnetite-silicate binary ore. Care should be taken when considering other ore types, such as sulphide ore (chalcopyrite, pyrite, lead/zinc). It is reasonable to accept that other mineral species would behave differently during breakage. However, there are no constraints to apply the same method in characterising liberation kernel for other ore types. It is possible to combine high density

minerals in a single valuable group. Further development should be considered if dense mineral phases are to be evaluated separately.

6.4.3.3.3 Model comparison

As mentioned previously, the data presented here is multidimensional data and representing it was a difficult task. Many approaches have been made in presenting the data and also in comparing it with already published ideas and models.
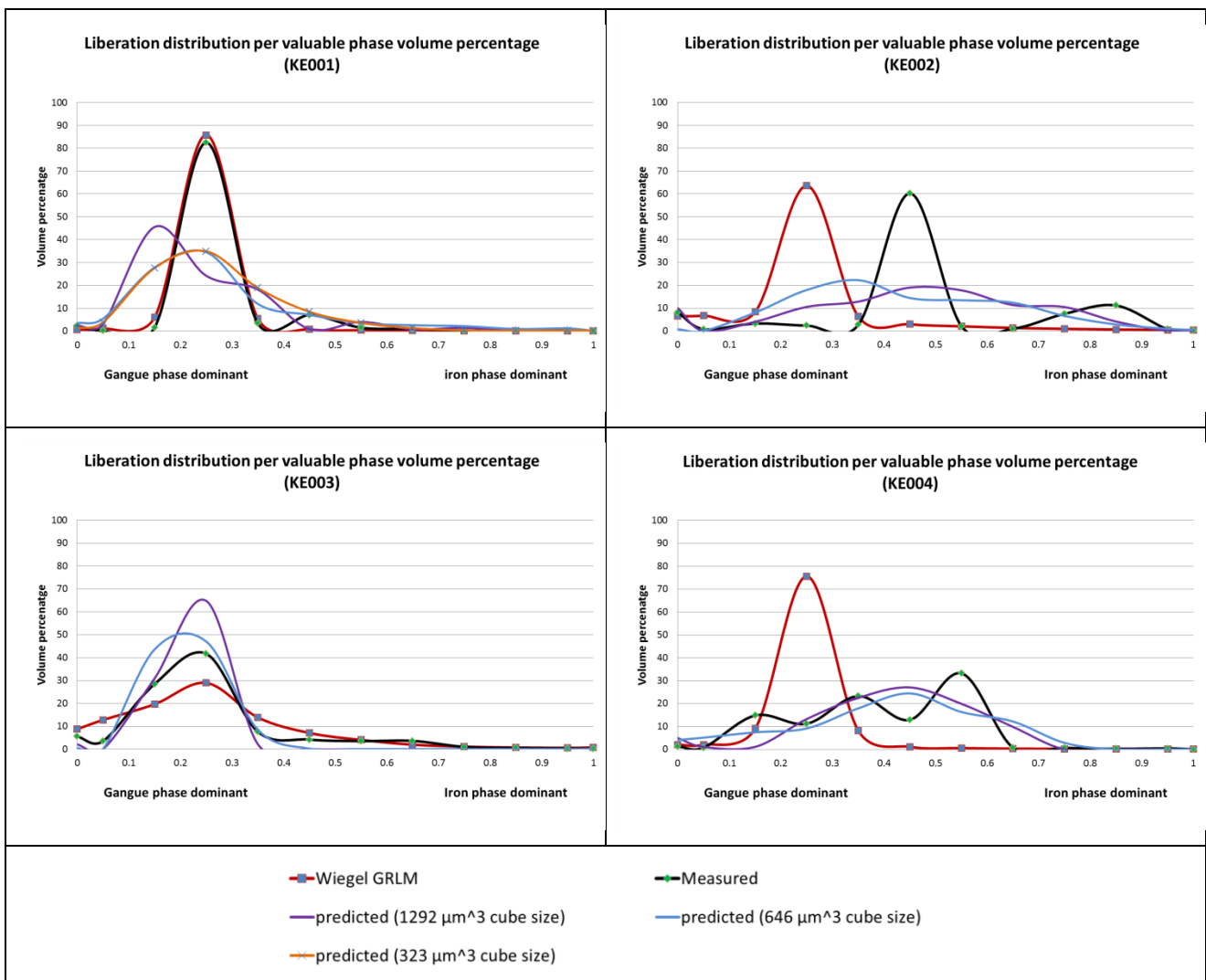
Figure 168: Liberation distribution comparison between Wiegel GRLM, predicted random breakage and measured true liberation

Figure 168 gives the liberation distribution calculated using volumetric percentage and the Wiegel GRLM, measured progeny and predicted random model breakage using 100 and 50 pixels edge cube size (25 pixels for KE001). The data presented here indicate that true particle liberation happens at faster rates than predicted (KE002 and KE004). The GRLM tends to overestimate gangue liberation if a particle was broken with higher energies. Predicted random breakage liberation had issues predicting valuable phase fast liberation, due to its geometrical limitations and inability to incorporate a detachment factor.

Figure 169 presents the data in cumulative form. For low energy breakage (KE001), the GRLM clearly aligns with measured liberation. Although the differences between predicted liberation and measured are not considerable (Table 38), these are less aligned with the measured data. It is important to state that the same set of images was analysed in all three simulation cases.
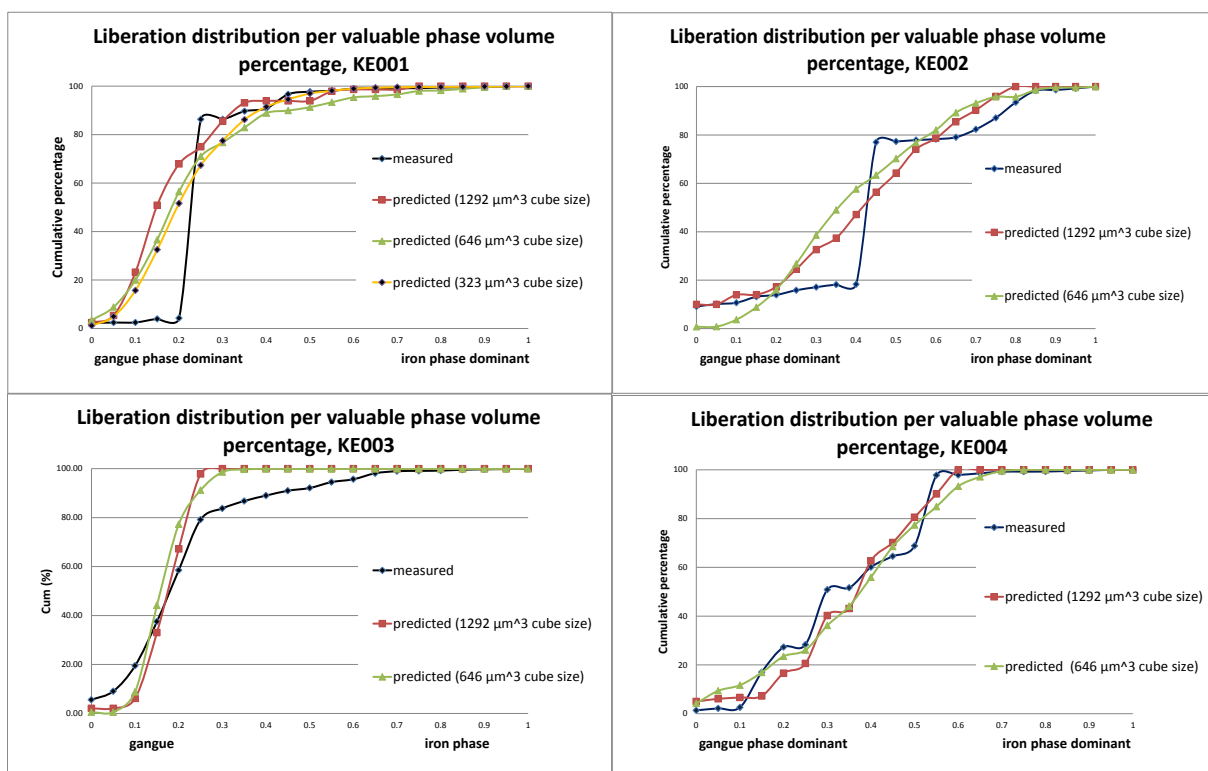
Figure 169: Cumulative liberation distribution by valuable mineral phase volume percentage

If considering a liberation distribution using all 12 liberation classes, when comparing the predicted liberation from the GRLM and the measured liberation x^2 is insignificant for

KE001 and KE003. Predicted values are closer to measured values in KE003 where x^2 is insignificant. The statistical test was based on differences between distributions using volumetric units of the valuable phase.

In industrial processing grouped liberation is more important than widely spread liberation classes. For example the data is analysed in a way that liberated gangue is considered a particle with less than 25% by volume iron phase and liberated value particle with more than 75% iron phase by volume. The data presented in this form is given in Figure 171. The coefficient of determination was found to be in high 90-percentile range for most except for predicted GRLM in KE002 and KE004 particles, 50 pixels cube prediction for KE002 and 25 cube prediction from KE001. Further testing is necessary to determine the differences between different ore textures and the influence of breakage energy on liberation. The study is enabled using the method presented in this Thesis.
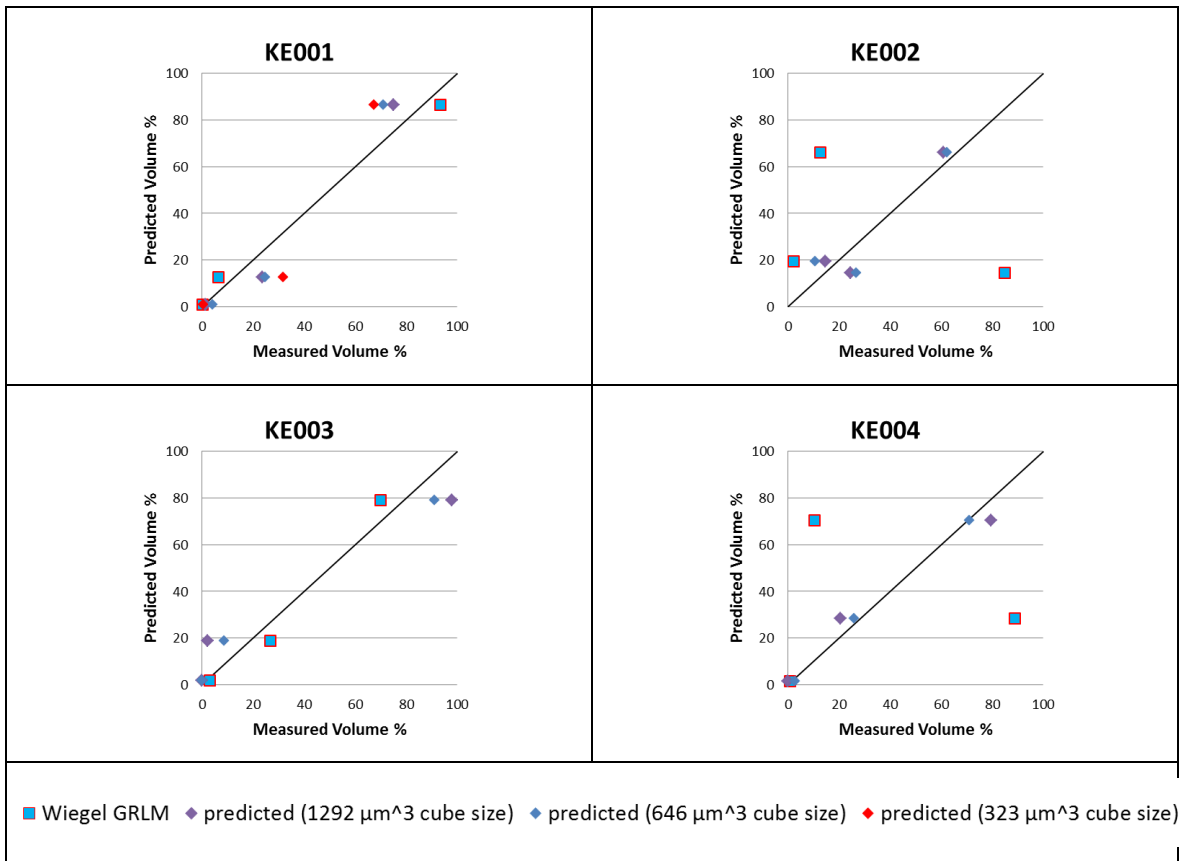
Figure 170: Grouped liberation by size matrix

Table 38: Volume percentage per liberation class

Liberation class	Wiegel GRLM	Predicted			Measured
		1292 µm^3	646 µm^3	323 µm^3	
KE001	Volume percentage				
0-25	93.3	75.0	71.1	67.4	86.3
25-75	6.5	23.6	24.8	32.0	12.7
75-100	0.2	1.4	4.1	0.7	1.0

Liberation class	Wiegel GRLM	Predicted		Measured
		1292 µm^3	646 µm^3	
KE002	Volume percentage			
0-25	85.0	24.5	26.8	14.5
25-75	12.6	60.9	62.4	66.0
75-100	2.4	14.6	10.8	19.4

Liberation class	Wiegel GRLM	Predicted		Measured
		1292 µm^3	646 µm^3	
KE003	Volume percentage			
0-25	70.0	97.8	91.2	79.2
25-75	26.9	2.2	8.7	18.9
75-100	3.1	0.0	0.1	1.9

Liberation class	Wiegel GRLM	Predicted		Measured
		1292 µm^3	646 µm^3	
KE004	Volume percentage			
0-25	88.9	20.6	26.1	28.3
25-75	10.3	79.4	71.0	70.3
75-100	0.8	0.0	2.9	1.4

6.4.3.3.4 Liberation distribution – family of lines of constant liberation

As already mentioned (6.4.3.2, page 295), each vertical line in Figure 171 represents a complete liberation distribution expressed as cumulative volume percentage passing. Therefore it is believed that for a known ore type, and known energy, the methodology used to generate data presented in this Thesis can be used to predict the liberation distribution which would occur at any reasonable degree of breakage. Thus, it can be used to characterise the liberation kernel.

Figure 171 shows the random breakage liberation model using simulated cubes. It was generated using the predicted liberation by size simulated data as presented in section 6.4.3.2. The model incorporates K (the grain size to particle size ratio) and presents how liberation by size class would distribute if breakage occurred in a given mode. A limitation of these models is the pre-set progeny particle size, which restricts the model to estimating liberation at finer particle sizes. The variability of the liberation fraction with size is clearly visible in Figure 171.

Figure 171 can be replotted in terms of particle composition per size fraction. Examination of the lines of constant liberation in liberation per size fraction or particle to size ratio form as in Figure 172 gives the opportunity to relate the size and liberation distribution of measured progeny particles to the liberation of the parent particle.

As the cube size decreases, the same size class will be more liberated (Figure 172). For example, 125µm particles will have approximately 25% liberated gangue in coarser cube breakage then 45% with middle cube size. Fine cube size had only 20% of 125 µm particles as liberated gangue because of ability to show finer size distribution and therefore liberation of 44µm particles at 65% liberated gangue range. This is a valid representation of liberation rate.
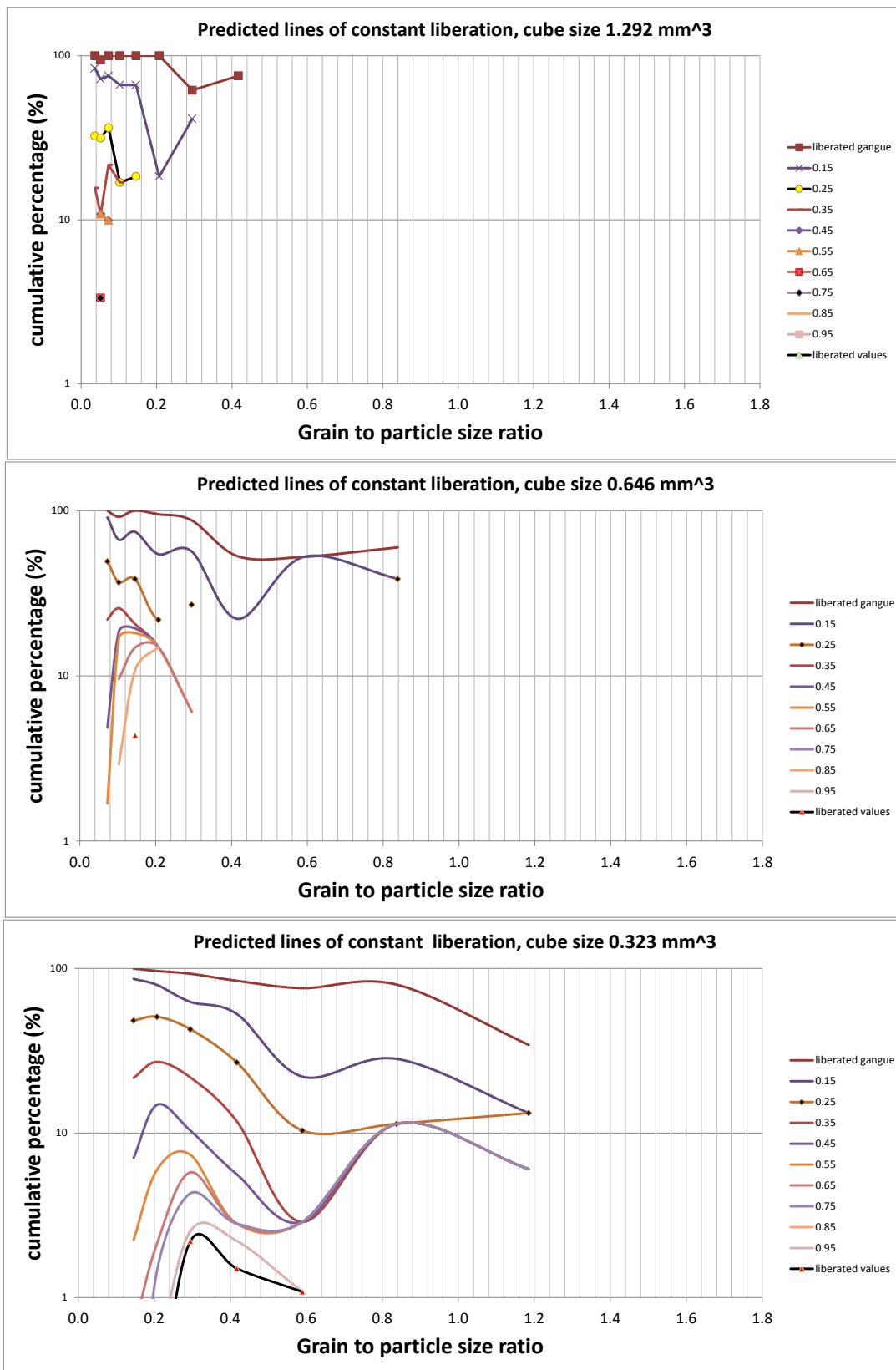
Figure 171: Predicted lines of constant liberation, KE001 particle, using 100 pixels[3], 50 pixels[3] and 25 pixels[3] simulated cubes
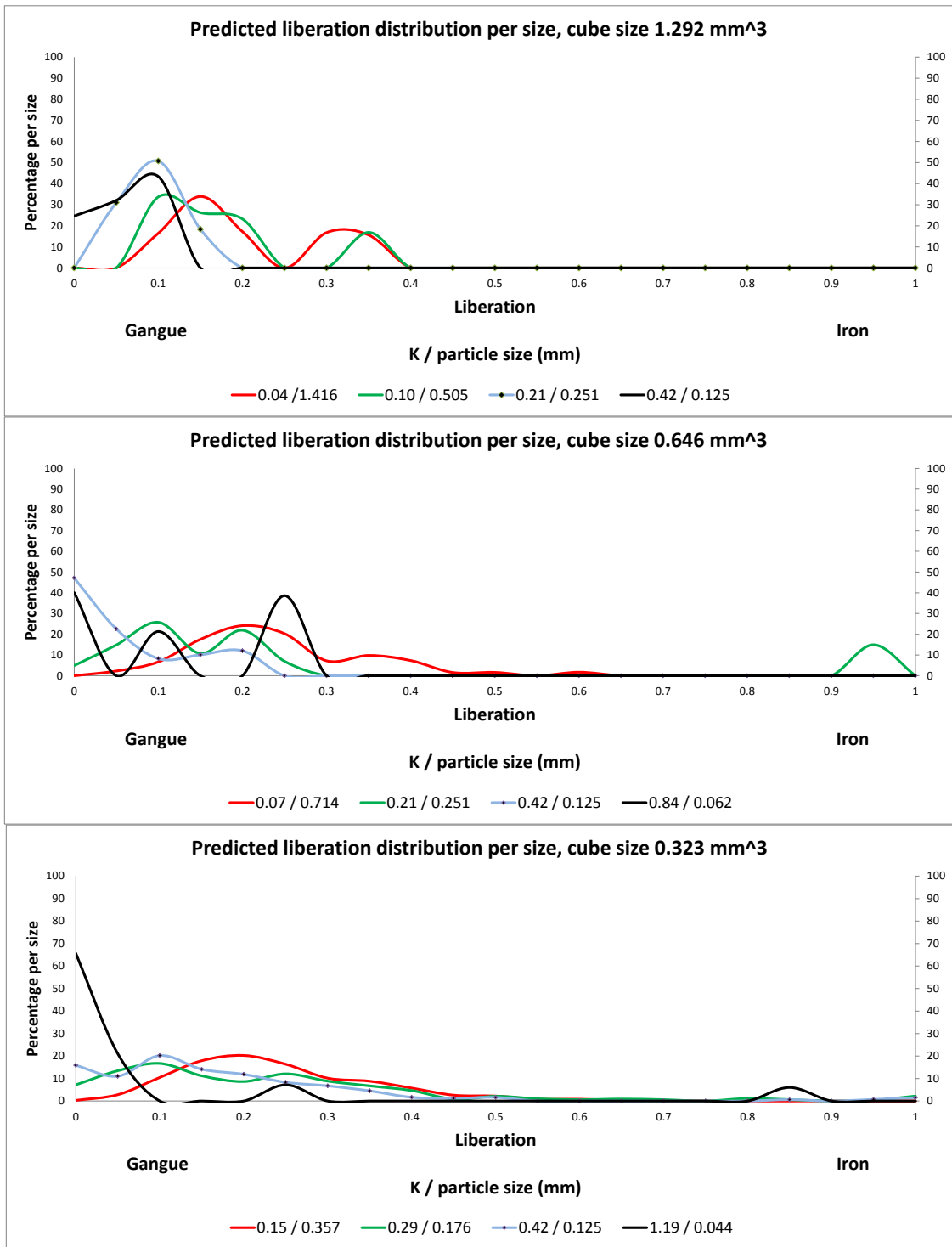
Figure 172: Family of lines of constant liberation, simulated for KE001
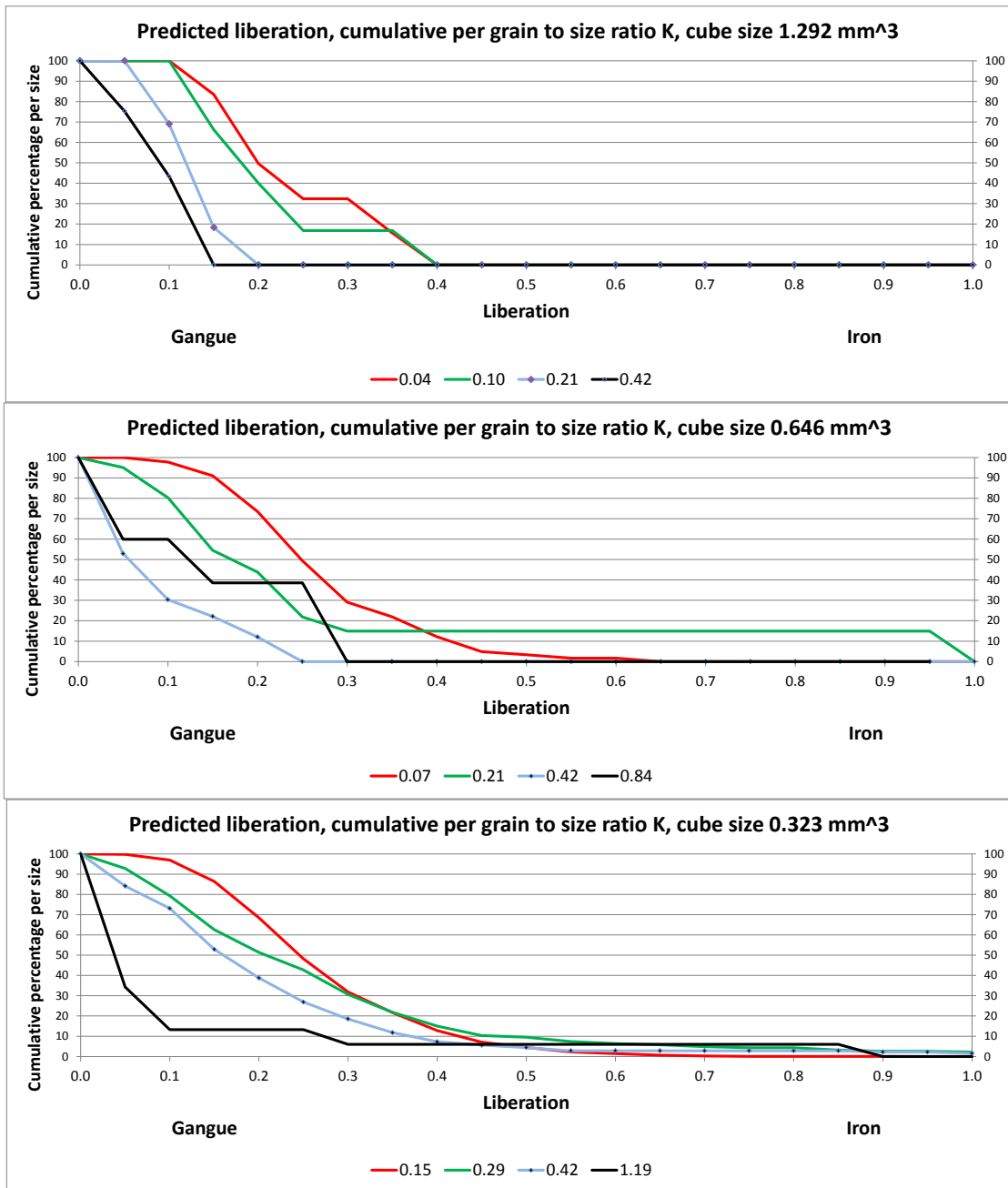
Figure 173 : Family of lines of constant liberation, cumulative per size, simulated for KE001

K	0.02	0.04	0.05	0.07	0.10	0.15	0.21	0.29	0.42	0.59	0.84	1.19	1.68	2.34
Size (mm)	2.89	1.42	1.00	0.71	0.50	0.36	0.25	0.18	0.125	0.09	0.06	0.04	0.03	0.02

Figure 173 demonstrates the possibility of using simulated cubes to predict liberation of similar ore type. It provides the cumulative percentage of volume per liberation size class

313

(Figure 172). With reduced progeny size (simulated cube size) more liberated gangue particles are accounted for.

The family lines of constant liberation show specific ore liberation distribution signature. As the simulated cube size is reduced, the percentage of finer liberated gangue or valuable phase increased (Figure 172 and Figure 173).

For coarse particles (red lines) there are two peaks (at 15% and 35% liberated gangue) shown in Figure 172 using coarse simulated cube size. As the progeny size is reduced, the liberation distribution of coarse particles concentrates around the parent liberation value. For fine particles, as the simulated cube size is reduced, the percentage of liberated gangue is increased from 25% liberated gangue to over 65% liberated gangue.
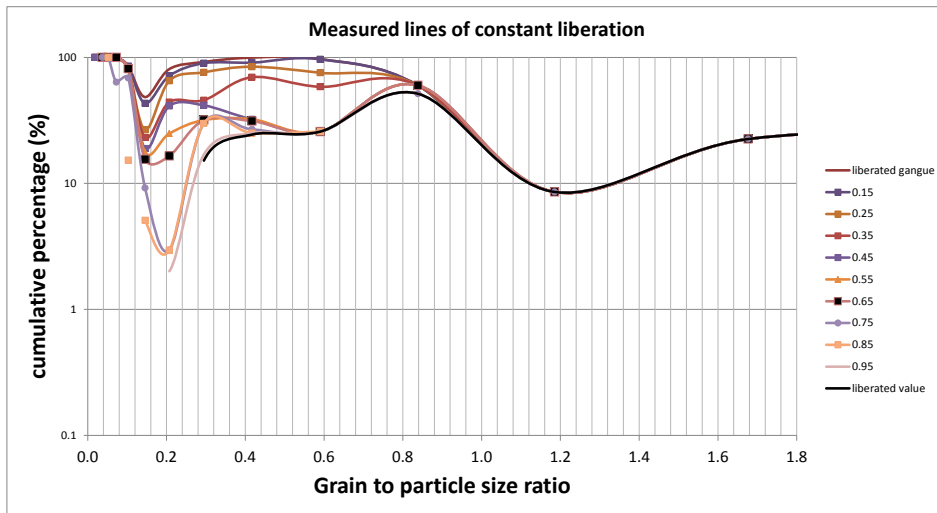
Figure 174: Measured lines of constant liberation, particle KE002
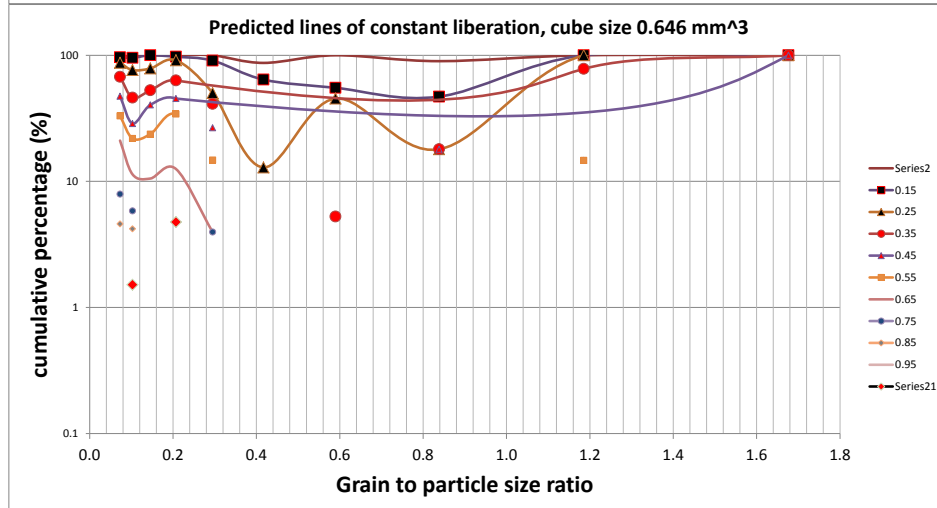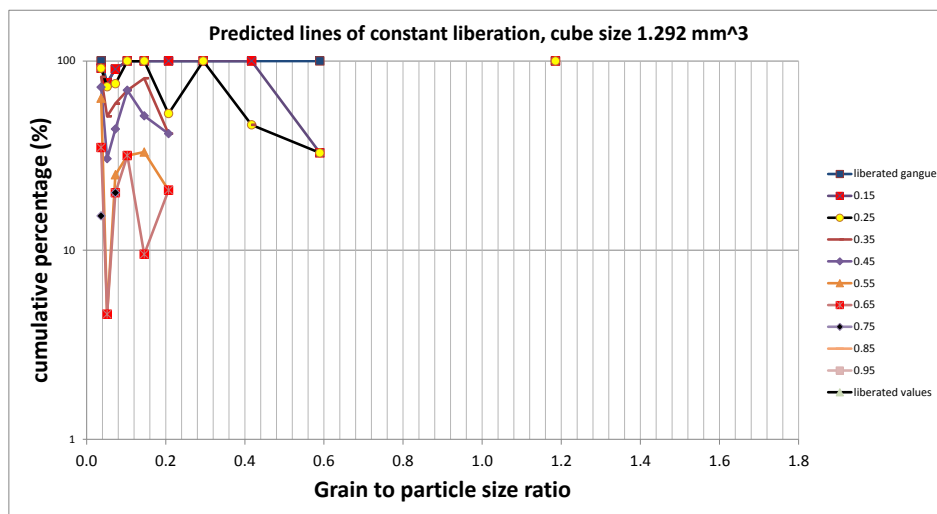
Figure 175: Predicted lines of constant liberation, KE002 particle, using 100 pixels^3 and 50 pixels^3 simulated cubes

Figure 174 represent a complete liberation distribution expressed as cumulative volume percentage passing which was measured for parent particle KE002. The random breakage model using simulated cubes is shown in Figure 175. If the figure is replotted in terms of particle composition per size fraction (Figure 176 and Figure 177) it will show that with increased simulated cube size, the value of liberated gangue and liberated valuable mineral phase is closer to the measured values.
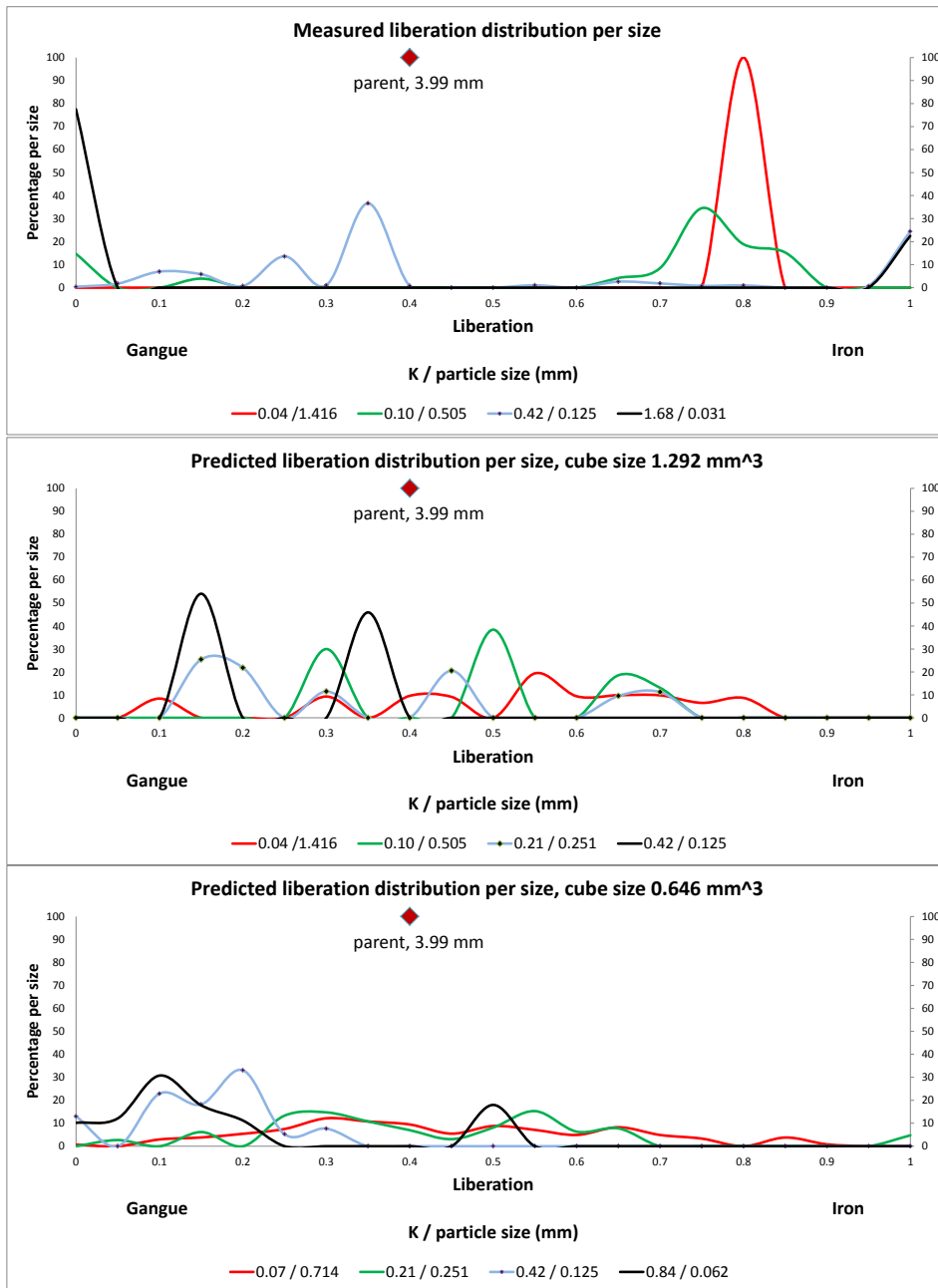
Figure 176: Family of lines of constant liberation, measured and simulated for KE002

317
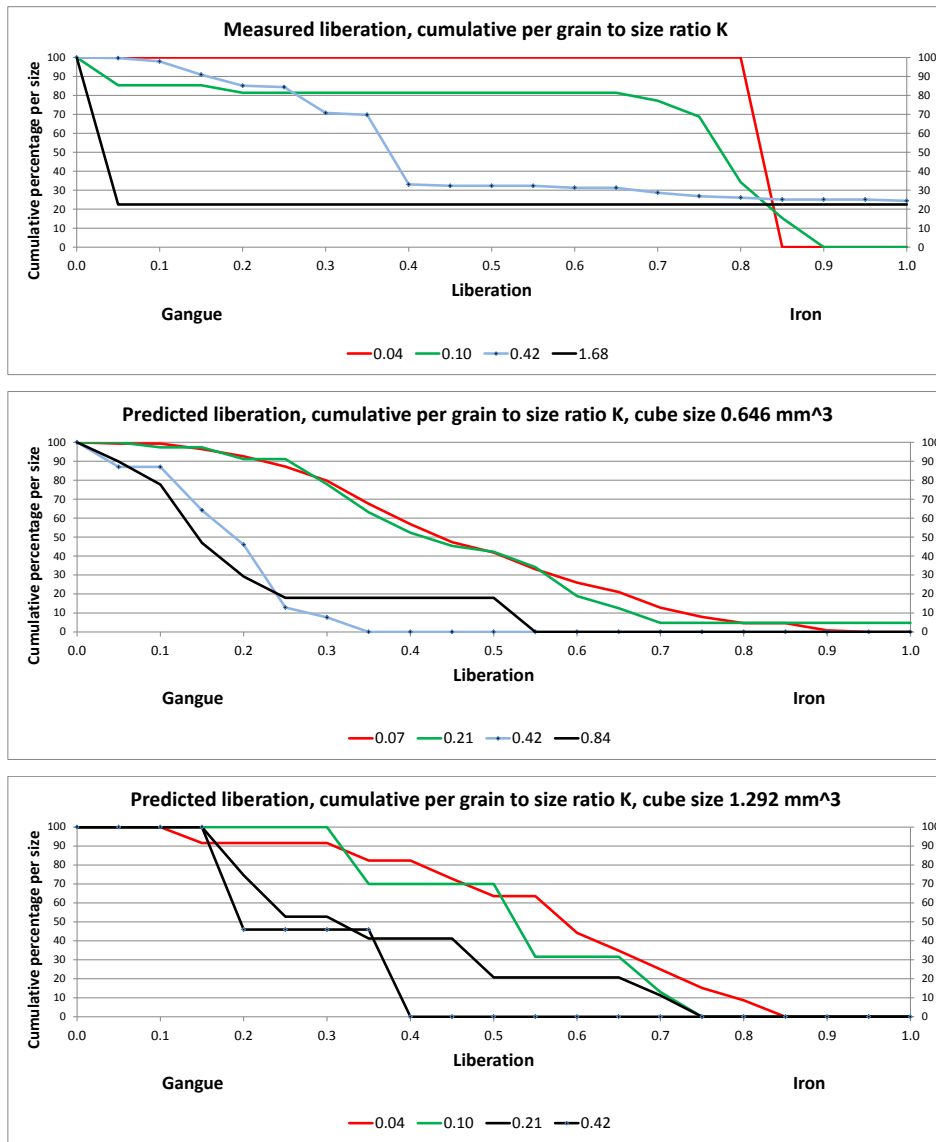
Figure 177: Family of lines of constant liberation, cumulative per size, measured and simulated for KE002

K	0.02	0.04	0.05	0.07	0.10	0.15	0.21	0.29	0.42	0.59	0.84	1.19	1.68	2.34
Size (mm)	2.89	1.42	1.00	0.71	0.50	0.36	0.25	0.18	0.125	0.09	0.06	0.04	0.03	0.02

The particle KE003 presented in appendix 9.26, had a coarser grain size distribution than particle KE001. It started to liberate around 185μm size compared with 125μm the starting liberation point of KE001.

The simulation was constrained by the lack of fully automated analysis that could analyse particles in a reasonable time. Due to the insufficient number of particles related to size limitation, reach in iron phase particles cannot be seen. A strong correlation between coarse particles liberation is noticed between measured and predicted data. The improvement in correlation in liberation distribution when the fracture pattern size is reduced is also apparent in coarser grain size distribution. (6.4.3.3.3)

There is good model correlation in highly liberated gangue, showing the gangue tendency to break into coarser liberated particles, unlike the valuable phase which has a tendency to break into finer liberated particles, based on the measured liberation. As already mentioned, the mineral grain size distribution indicated heterogeneous rock in terms of rock texture (page 268 and 289). This was visible in the coarser cube simulation, but not in the finer cube simulation due to the pre-set cube size.

Simulated random breakage particles showed that liberation by size reduction will happen. The data presented clearly shows that preferential breakage plays major role, especially as the particle size approaches the mineral grain size.

However, without random simulation of breakage of the measured texture of the parent particle, this statement would simply be speculation and not a proper observation.

The possibility of predicting liberation using 50 pixels cube size simulated random breakage pattern is noticed with coarser grain size distribution. The full data set is provided in appendix 9.27. As this particle broke into coarser liberated gangue and coarser particles with liberation similar to the parent liberation, the model predicted these values reasonably well.

Figure 178 to Figure 180 present the numbers of particles and measured volume of particles in terms of percentage of parent volume for KE001 and KE003, distributed into size and liberation fractions. Using higher energies in breaking the ore result in more size

reduction liberation in a coarser textured ore (KE003). The texture of KE001 was finer than KE003, but the energy applied to break them was different, lower for KE001 than others.

The additional information given below can be used to observe the probability of a grain reporting to each of the liberation classes. It is obvious from Figure 178 that the probability of progeny particle to reduce its size but keep the same liberation class as the particle it originates from was overestimated with simulated random liberation.

For industrial applications, reducing the number of liberation classes would be practical, for example particles with over 70-80% of valuable phase may be considered liberated depending on the process and flow sheet design.
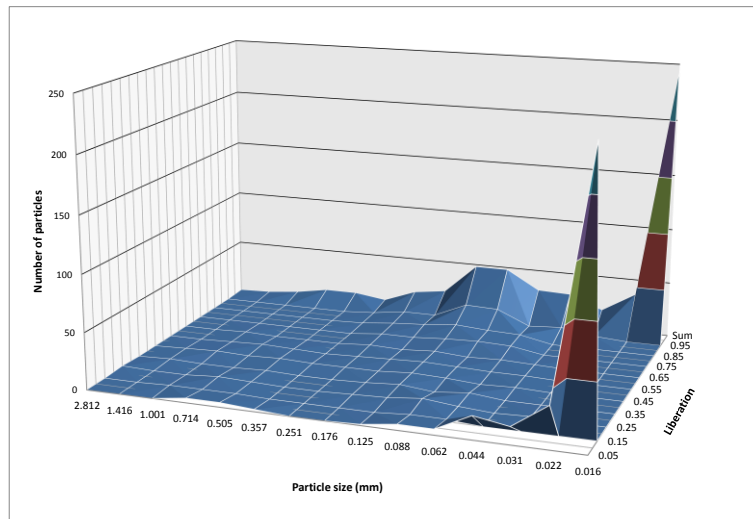
Figure 178: Three dimensional representation of measured liberation by volume in number of particles, measured progeny particles, KE001
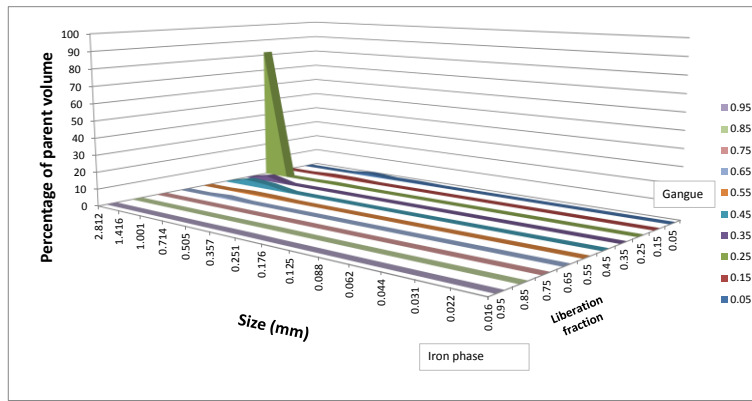
Figure 179 : Three dimensional representation of measured liberation by volume in percentage of parent volume, measured progeny particles, KE001
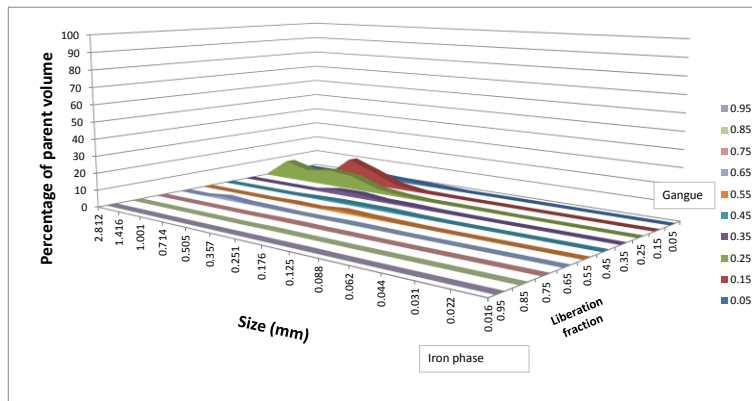
Figure 180: Three dimensional representation of measured liberation by volume, measured progeny particles, KE003
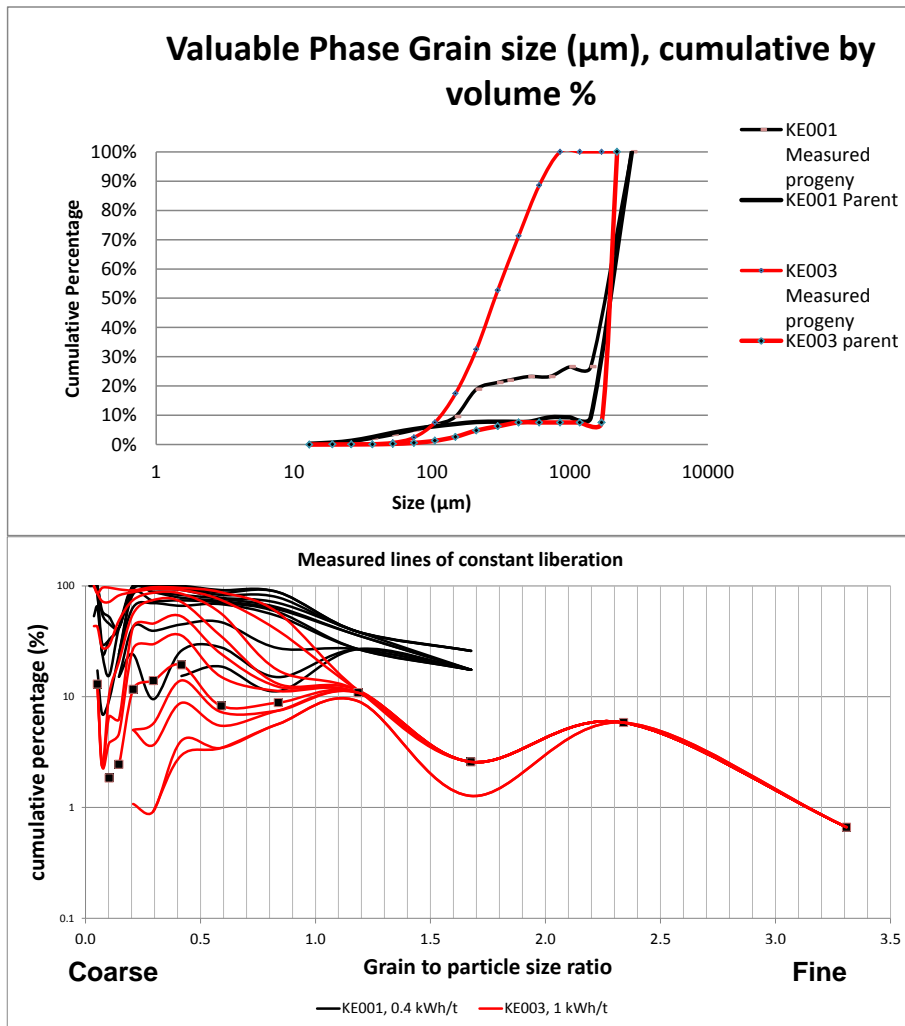
Figure 181: Valuable grain size distribution and measured lines of constant liberation for measured progeny and parent particles

Figure 181 demonstrates the impact of energy application in breakage. The results achieved here are when the parent particles were measured before and after a single breakage event. The progeny of repeated breakage should be measured in the same way. This will allow the assessment of micro and macro cracks which occurred as the result of the first breakage instance and their influence on the liberation kernel in secondary breakage.

This methodology may find its application in predicting the energy required to liberate particles sufficiently. To confirm this theory, more research needs to be done. Hence it is suggested for future work (section 7.3)

6.5 Conclusions

Liberation depends on both the texture of the parent particle and the severity of the breakage, as expected. But liberation becomes quite selective as the progeny size approaches the grain size.

From these studies it is observed that a random model would require a detachment factor as proposed by Hsih and Wen (1994) for a realistic simulation. The density difference between the iron phase and the gangue phase is considerable and cannot be underestimated when predicting liberation. From the data presented, it is obvious that the breakage mechanism was mixed and that there are both modes present, random and preferential.

These analyses demonstrate the perspective that a particle with a finer texture, randomly distributed in a grain matrix, as it is expected, would have high probability to break into a number of particles with similar liberation to their parent.

The analyses carried out showed that below a certain size, liberation becomes selective (Wiegel 1976).

Magnetite also has a tendency to break into finer particles (i.e. more severely), whereas the gangue phase (quartz) had a tendency to break into coarser particles (Figure 171 and Figure 173). The effect is not visible in simulated random breakage because of the model limitation where the cube size was set at 25 pixels (0.303mm). This tendency was also noted by Wiegel (1976b) and discussed in section 6.4.3.3.4.

As mentioned previously, there is a high variance due to small numbers of particles in some liberation classes with a single parent. However, it is believed that with several parent particles (of similar texture) the variance can be expected to decrease.

The results show that line and area liberation measurements on the same set of images are accurate but imprecise which implies uncertainty and reduced confidence in results. The standard deviation of volumetric high density component percentage was over 10%. For finer disseminated texture, as expected, t was not significant but for coarser texture it was significant with over 90% confidence.

The set of constant liberation curves which represent the first unknown in the kernel equation really only represent the parent texture that is the feed true particle volume distribution with three dimensional properties of the mineral of interest. However, this is only a single liberation per size box in the kernel matrix and more particles need to be measured for optimal kernel definition.

Also, two common cases could be estimated. When the valuable grain size and the grade increase, then the particle to grain size ratio should give a similar response noting that the grade will increase. The second case is where the valuable grain concentration decreases or increases, provided the volumetric concentration is reasonably low, the same curves should apply but less or more gangue will be liberated. This is much the same idea as the solitary grain model.

As mentioned earlier, the progeny results are the second unknown in the kernel equation, the true particle distribution or breakage function.

The aim of this work is to present a methodology which can be used to measure the grain size distribution of the parent particles and the progeny particles which resulted from a controlled breakage environment with well-defined energies. The lines of constant liberation which have been presented provide a full liberation matrix of the progeny particles, and the resulting family of liberation curves can be applied to predict liberation of measured parent particles at any degree of breakage. For a change in the valuable phase grain size, there is no need for complicated model modifications. If the test is repeated on industrial scale, the noise noticed in the lines of constant liberation is believed would be removed.

Therefore it is believed that the goal has been achieved and that future research work can successfully apply this methodology to characterise the liberation kernel and thus predict liberation by simulation based on measurement of ore texture.

7 Conclusions and Recommendations for Future Work

7.1 *Introduction*

Characterisation of the liberation of an ore within a breakage device during the comminution process has been a challenge for many years.

Previously it was difficult to adequately quantify the liberation status of the feed particles without size reduction in order to prepare adequate samples for various two dimensional analysis methods. This destructive preparation process would not only change the size of the parent particle, but also lead to destruction of texture and liberation information. The texture information of a feed material is defined as the internal arrangement of mineral grains, their size and distribution. This texture information is the first unknown in the kernel equation. The second unknown is the breakage function or the progeny particle distribution.

Although available techniques, such as automated SEM, provide excellent mineral recognition at high resolution, the two dimensional mineral data obtained needs to be adjusted to estimate three-dimensional liberation characteristics. This process is called stereological adjustment and the degree of adjustment depends on ore texture. There is a problem noticed with these measurement when two different sets of particles can produce similar sections (Cruz-Orive 1976; Moran 1972)

7.2   *Major findings*

This Thesis proposes a solution to these problems, by providing an improved optimised method for characterising the liberation kernel. The liberation kernel is defined as the mathematical transformation which relates the feed size and liberation distribution presented to the breakage device to the liberation distribution of the sized progeny particles.

The method presented here measures intact particle texture and allows for measurement of particles texture and liberation of the progeny with no destruction of the particles. The sample preparation process for Micro CBT does not involve any physical damage to the particles as particles are mounted in Styrofoam in order to stop any potential movement of the samples inside the sample chamber. The full composition of the parent and its progeny particles can be measured in three dimensions using this method.

A random breakage model prediction has been presented where the measured liberation of progeny created by breaking a parent particle was compared with the liberation simulated by cutting the parent particle Micro CBT reconstructed two dimensional images into different size cubes. Examination of the measured progeny particles indicated that the liberation pattern was very variable depending on the particle size. There was a reasonable agreement between simulated and measured liberation in the range of finer particles where the liberation tends towards fully liberated particles. The maps with a measured degree of liberation of the progeny particles are presented.

The data presented here show that both random and preferential breakage modes are present in breakage of the ore tested. The measured areas confirm that below a certain particle size, liberation becomes selective as previously observed by Wiegel (2006). The random simulation of breakage helped reveal liberation by size reduction. The selective breakage identified in this research plays a major role especially in the range where the particle to grain size ratio is 1. There was tendency for the gangue to break into coarser liberated particles, unlike the valuable phase which has a tendency to break into finer

liberated particles. The need for a detachment factor to be incorporated into random liberation model, as noted previously by Hsih and Wen (1994), was confirmed. In many cases, the predicted grind size required to liberate gangue sufficiently may be the most useful outcome of the measurement.

The set of lines of constant liberation which represent the kernel represent the parent texture and may be estimated for two common cases, when the valuable phase grain size increases and when the valuable phase volume concentration is low. The method has been optimised for magnetite-silicate ore and it is believed that further development is needed for other ore types. The method is optimised for binary particles which had one group of high density component minerals (in this case magnetite-iron oxide) and the second was the gangue mineral group. The development of a method for copper ores depends on flow sheet design and whether there is a need for selective separation of pyrite and other high density minerals during processing. However, application of this method to low grade copper ore is limited due to its detectability in low grade range.

Mineral identification using Micro CBT has been successfully validated with the MLA, where barite, chalcopyrite, pyrite, magnetite and gangue minerals have been identified. The quality of the acquired Micro CBT images was improved by assessing different parameters that influenced the image quality. These parameters can be optimised to suit the analysis and image reconstruction process.

The image analysis method developed in this Thesis enables the user to adequately characterise texture and liberation of the parent particle and progeny particles in three dimensions. A range of methods for quality assurance have also been established. The methods can be time consuming and possibly not practical for industrial application. However with improved computer capabilities further optimisation is achievable.

Therefore the results demonstrated that with the improved measurement techniques developed and presented in this Thesis, for a known ore type and a known energy, one can use the data to predict the liberation distribution which would occur at any reasonable

degree of liberation and thus characterise the liberation kernel. Hence, the major goal of this Thesis has been achieved.

7.3   Recommendations for Future work

The following work is recommended for future research:

General Mineral Processing

The influence of porosity, rock type and grain shape on liberation should be considered. Quantifying these factors can improve the understanding of the correlation between parent particles and the broken progeny particle and help to predict liberation.

An assessment of available stereological adjustment methods can be undertaken using this technique. The variable degree of preferential breakage will challenge most techniques for stereological adjustment.

Figure 5 in Chapter 2 shows the predicted particle composition (Gay 1995). The investigation can focus on separating coarse binary parent particles into different texture classes before breakage and assess the correlation between the predicted parent composition distribution and the measured composition distribution. This examination may provide a better insight into the direct relationship between two dimensional and three dimensional analyses for many ore types.

Application of the method presented here could be extended to different ore types and grades.

The method is suitable for investigating iron ore deposits and could be used in magnetite processing plants as the type of liberation directly influences flow sheet design.

An assessment of published liberation models can be made using this technique.

The level of impact of energy applied during the breakage can be considered. Only two energy levels have been presented, and the particles were broken one at the time. For a better understanding of the particle behaviour and liberation kernel, it is recommended that a larger number of particles with similar textural and liberation properties be assessed before and after breakage by breaking them together in an energy-controlled environment such as the JK-RBT.

The proposed technique can be used to investigate the liberation map of the ore and to design the comminution process in the most energy efficient mode, so that sufficiently liberated particles can be removed from the comminution circuit and treated before excess energy is spent on overgrinding. The methodology could be used for waste rejection in the processing plants earlier in the flow sheet design.

If the grain size distribution is the same, and the ore grade increased, it is believed that the proportion of coarse and fine liberated phase would increase. An investigation of this is proposed for future research.

Considering the shape of the particles and the degree of surface liberation, the impact on flotation can be assessed using this technique. Further development of the measurement of finer size fractions also should be done.

In this work, the main aim was to establish a technique to measure the ore texture and characterise the liberation kernel. The results were achieved by measuring the parent particles before and after breaking them at a controlled energy. The progeny of repeated breakage should be measured in the same way. This will allow the assessment of micro and macro cracks which occurred as the result of the first breakage instance and their influence on the liberation kernel in secondary breakage.

Considering different breakage modes and incorporating them into liberation models, as suggested by Stamboliadis (2008), is now possible using the measurement method developed in this Thesis.

To address the hypothesis in this Thesis, a mineral grain to particle size ratio of one eighth was used. Smaller ratios can be assessed as suggested by Wiegel (1976b) in future work.

Image acquisition

Process multiple scans applying different energies when scanning using the SkyScan or other Micro CBT system increase contrast between chalcopyrite and other minerals with higher density, such as pyrite, magnetite, and galena. Some work is already published (Ghorbani 2012; Ghorbani et al. 2013) but further developing of dual energy methods is needed to better distinguish between mineral phases with similar atomic numbers. This hypothesis may help in developing multi-mineral identification, multi-mineral liberation and multi-mineral liberation kernel characterisation in three dimensions. However, it will also require software to composite the images for analysis. The systems with dual energy are available (Xradia 2014).

This is a great opportunity for beam hardening effects to be removed with the use of a Gaussian filter. Further investigation of available filters during the acquisition and reconstruction process is also recommended.

Image analyses

Improving the programing rule set used in eCognition8 image analysis software or the development of new software is recommended to allow for automatic separation of touching particles and to provide particle by particle data with minimal operator intervention.

For this kind of analysis to become part of the daily operational plant protocols it would have to be operator friendly and less time consuming. Hence, the need for automation of image analyses process is very appealing here, as the capabilities and opportunities that lie in this kind of analysis are important for mineral processing. Further automation of the acquisition process would also be beneficial.

Programming a specialist software package to handle automated acquisition, reconstruction and image analysis with incorporating the ideas mentioned in this work would be a great step forward in liberation research.

The acquisition of a complete valuable mineral phase internal intact matrix provides an opportunity to optimise ore recovery by focusing on liberation of this phase to the point where it will be sufficiently liberated for recovery while minimising losses to fines.

"The only source of knowledge is experience."" Learn from yesterday, live for today, hope for tomorrow. The important thing is not to stop questioning." Albert Einstein

8 References:

Andres, U and Bialecki, R 1986, 'Liberation of mineral constituents by high-voltage pulses', *Powder Technology*, vol. 48, no. 3, pp. 269-77.

Andrews, JRG and Mika, TS 1975, 'Comminution of a heterogeneous material : development of a model for liberation phenomena', in *Proceedings of XI International Mineral Processing Congress*, Cagliari, pp. 59-79.

ASTM 2009, *Standard Test Method for Dry and Wet Bulk Density, Water Absorption, and Apparent Porosity of Thin Sections of Glass-Fiber Reinforced Concrete*, ASTM International, DOI 10.1520/C0948-81R09.

ASTM E1441-00 2005, *Standard Guide for Computed Tomography (CT) Imaging*, American Society for Testing and Materials.

Austin, LG and Luckie, PT 1988, 'Problems of quantifying mineral liberation: a review', *Particle and Particle Systems Characterization*, vol. 5, no. 3, pp. 122-9.

Avinash, K and Malcolm, S 1988, *Computerized Tomographic Imaging*, IEEE PRESS, New York.

B.L., D and Clark, CM 2013, *X-ray Powder Diffraction (XRD)*, Eastern Michigan University, Louisiana and Michigan.

Bajic, S 2010, *Quantitative analyses of minerals in multiphase particles using X-Ray microtomography procedures* The University of Queensland, Brisbane, Australia.

Barbery, G 1991, *Mineral liberation : measurement, simulation and practical use in mineral processing*, Editions GB, Quebec, Canada.

- 1992, 'Liberation 1, 2, 3: Theoretical analysis of the effect of space dimension on mineral liberation by size reduction', *Minerals Engineering*, vol. 5, no. 2, pp. 123-41.

Barbery, G and Leroux, D 1987, 'Prediction of particle composition distribution after fragmentation of heterogeneous materials', *International Journal of Mineral Processing*, vol. 22, no. 1-4, pp. 9-24.

Bazin, C and Ouellet, V 2009, 'Simulation of Ore Textures', paper presented to SME, Denver.

Bearman, RA, Briggs, CA and Kojovic, T 1997, 'The applications of rock mechanics parameters to the prediction of comminution behavior', *Minerals Engineering*, vol. 10, no. 3, pp. 255-64.

Berube, MA and Marchand, JC 1984, 'Evolution of the mineral liberation characteristics of an iron ore undergoing grinding', *International Journal of Mineral Processing*, vol. 13, pp. 223-37.

Beucher, S and Meyer, F 1993, 'The morphological approach to segmentation: the watershed transformation.', *E.R. Dougherty (Editor), Mathematical Morphology in Image Processing. Marcel Dekker, New York*, pp. 433-81.

Blatt, H and T., RJ 1996, *Petrology*, 2 edn, W.H.Freeman.

Bond, FC 1952, 'Third theory of comminution', *Min. Engineering*, vol. 4, no. 5, pp. 484-94.

Bond, FC 1954, 'Crushing and grinding calculations', *Canadian Mining and Metallurgical Bulletin*, vol. 47, no. 507, pp. 466-72.

- 1961, 'Crushing and grinding calculations', *British Chemical Engineering*, vol. 6, no. 6, 8.

Bourgeois, FS and Banini, GA 2002, 'A portable load cell for in-situ ore impact breakage testing', *International Journal of Mineral Processing*, vol. 65, no. 1, pp. 31-54.

Burrows, D and Gu, Y 2006a, 'JKMRC Mineral Liberation Analyser - A modern tool for ore characterisation and plant optimisation', in *Metallurgical Plant Design and Operating Strategies, September 2006*, Perth, Australia, pp. 125-39.

Burrows, D and Gu, Y 2006b, 'JKMRC Mineral Liberation Analyser, a modern tool for ore characterisation and plant optimisation ', paper presented to AUSIMM MetPlant Conference, Perth, Sep 2006.

Burrows, D and Louwrens, E 2007, *Process Mineralogy*, JKTech, The University of Queensland, Brisbane.

Bushberg, JT, Seibert, JA, Leidholdt, EMJ and Boone, JM (eds) 2002, *The Essential Physics of Medical Imaging*, Lippincott Williams & Wilkins, Philadelphia, PA 19106 USA.

Cakici, M 2009, 'Characterisation of Samples of Ore Particles using X-Ray MIcrotomography', Master of Philosophy thesis, The University of Queensland.

Carmichael, SR 1989, *Physical Properties of Rocks and Minerals- Practical Handbook*, CRC Press, INc., Iowa City.

Clarke, AJ and Wills, BA 1989, 'Enhancement of cassiterite liberation by high pressure roller comminution', *Mining Engineering*, vol. 2, no. 2, pp. 259-62.

Cochran, W 1976, 'A random sample', *Geotimes*, vol. 21, no. 11, pp. 20-2.

Cressie, NAC 1991, 'Statistics for Spatial Data', *John Wiley and Sons, INC; New York.*

Criddle, AJ 1998, 'Ore Microscopy and Photometry (1890-1998)', *Modern approaches to ore and environmental mineralogy*, vol. Short Course 27, pp. 1-74.

Cruz-Orive, LM 1976, 'Particle size-shape distributions: the general spheroid problem. I. Mathematical model. ', *J. Microscopy*, vol. 107, pp. 235–54.

Delesse, MA 1847, 'Procede mecanique pour determiner la composition des roches', *C. R. Acad. Sci.*, vol. 25, p. 544.

Department of Geological Sciences, UoTaA 2004, *BLOB3D User's Guide*, <ftp://ctlab.geo.utexas.edu/blob3d/Blob3D%20Documentation.doc>.

Dieter, GE 1989, *Mechanical Metallurgy, SI Metric Adaptation*, McGraw-Hill Education, Maidenhead, UK, 0-07-100406-8. .

Djordjevic, N, Shi, FN and Morrison, R 2004, 'Determination of lifter design, speed and filling effects in AG mills by 3D DEM', in vol. 17, pp. 1135-42.

Djordjevic, N, Shi, FN and Morrison, RD 2003, 'Applying discrete element modelling to vertical and horizontal shaft impact crushers', *Minerals Engineering*, vol. 16, no. 10, pp. 983-91.

Dobbe, R, Martin, CJ, Bajic, S, van der Wal, D and Thorpe, R 2013, 'Application of Daily Onsite Automated Mineralogical Analysis to Track Controls on Flotation Recovery', paper presented to Flotation 2013 Conference, Cape Town, South Africa.

DOE 2001, *Mining – Industry of the future*, Office of industrial technologies (OIT), Office of Energy Efficiency and Renewable Energy, USA, <www.oit.doe.gov/mining.>.

Dooryhee, E, Martinetto, P, Walter, P and Anne, M 2004, 'Synchrotron X-ray analyses in art and archaeology', *Radiation Physics and Chemistry*, vol. 71, no. 3-4, pp. 863-8.

Eberhardt, C and Clarke, A 2002, 'Automated reconstruction of curvilinear fibres from 3D datasets acquired by X-ray microtomography', *Journal of Microscopy*, vol. 206, pp. 41-53.

eCognition 2008, *ReferenceBook Definiens XD 1.1*, Trimble Geospatial Imaging, Munich, Germany.

EDUSPACE 2010, *LeoWorks*, <http://www.eduspace.esa.int/eduspace/subtopics/default.asp?document=6>.

Evans, C 2002, *Mineral Liberation research at the JKMRC - Past , Present and Future*, JKMRC, the University of Queensland in Collaboration with the University of Cape Town and McGill University, Brisbane.

Evans, CL, Andrusiewicz, MA, Wightman, EM, Brennan, M, Morrison, RD and Manlapig, EV 2013, 'Simulating concentrators from feed to final products using a multi-component methodology', paper presented to SME Annual Meeting Feb. 24 - 27, 2013, Denver, CO.

Evans, CL, Wightman, EM, Manlapig, EV and Coulter, BL 2011, 'Application of process mineralogy as a tool in sustainable processing', in Langford Lane, Kidlington, Oxford, OX5 1GB, United Kingdom, vol. 24, pp. 1242-8.

Evans, CL, Wightman, EM and Yuan, X 2012, 'Characterising ore micro-texture using x-ray micro-tomography ', in *44th Annual Meeting of the Canadian Mineral Processors*, Ottawa, Canada

Fandrich, R, Gu, Y, Burrows, D and Moeller, K 2006, 'Modern SEM Based Mineral Liberation Analysis', *IJMP*.

Fandrich, RG 1997, 'A mineral liberation model for confined particle bed breakage', paper presented to Fine Powder Processing 97, Pennsylvania, September 1997.

FEI 2014, *Mineral Liberation Analyser (MLA) and QEMSCAN, MineSite (MLA and QEMSCAN)*, viewed March 2014, <http://www.fei.com/products/sem/>.

Feldkamp, IA, Davis, LC and Kress, JW 1984, 'Practical cone-beam algorithm', *Journal of the Optical Society of America A: Optics and Image Science, and Vision*, vol. 1, no. 6, pp. 612-9.

Ferrara, G, Preti, U and Meloy, TP 1989, 'Inclusion shape, mineral texture and liberation', *International Journal of Mineral Processing*, vol. 27, no. 3-4, pp. 295-308.

Flatman, GT, E.J., E and Yfantis, AA 1988, 'Geostatistical Approaches to Design of Sampling Regimes', *In Principles of Environmental Sampling*, pp. 73-84.

Forssberg, E, Sundberg, S and Hongxin, Z 1988, 'Influence of different grinding methods on floatability', *International Journal of Mineral Processing*, vol. 22, no. 1–4, pp. 183-92.

Fuerstenau, DW, Kapur, PC, Schoenert, K and Marktscheffel, M 1990, 'Comparison of energy consumption in the breakage of single particles in a rigidly mounted roll mill with ball mill grinding', *International Journal of Mineral Processing*, vol. 28, no. 1-2, pp. 109-25.

Gaines, RV, Skinner, CH, Foord, EE, Mason, B, Rosenzweig, A, King, VT and Dowty, E 1997, *Dana's New Mineralogy*, 8th edn, Dana Classification, John Wiley & Sons, Inc. .

Gaudin, AM 1939, *Principles of Mineral Dressing*, McGraw-Hill, New York.

Gauss, JCF 1828, *Theorema Egregium*.

Gay, SL 1995, 'Stereological equations for phases within particles.', *J. Microscopy,*, vol. 179, pp. 297–305.

Gay, SL 2005, 'A simple texture-based liberation model', *Minerals Engineering*, vol. 17, no. 11-12, pp. 1209-16.

Gay, SL and Morrison, RD 2006, 'Using two dimensional sectional distributions to infer three dimensional volumetric distributions - Validation using tomography', *Particle & Particle Systems Characterization*, vol. 23, no. 3-4, pp. 246-53.

Ghorbani, Y 2012, 'On the progression of leaching from large particles in heaps', PhD thesis, The University of Cape Town.

Ghorbani, Y, Becker, M, Petersen, J, Mainza, AN and Franzidis, J 2013, 'Investigation of the effect of mineralogy as rate-limiting factors in large particle leaching', *Minerals Engineering*, vol. 52, pp. 38-51.

Goergen, E, Thorpe, R, Palko, A, Martin, T, Bajic, S, Jaime, P, Dobbe, R and van der Wal, D 2013, 'Application of Daily Onsite Automated Mineralogical Analysis to Track Controls on Plant Recovery Performance', paper presented to 10th International Mineral Processing Conference, Santiago, Chile.

Goertzen, A 2003a, *Development of a Combined microPET and microCT System for Mouse Imaging*, University of California.

Goertzen, AL 2003b, 'Development of a Combined microPET and microCT System for Mouse Imaging', University of California.

Gu, Y 2003, 'Automated Scanning Electron Microscope Based Mineral Liberation Analysis, An Introduction to JKMRC/FEI MLA', *Journal of Minerals & Materials Characterization & Engineering*, vol. 2, no. 1, pp. 33-41.

- 2004, 'Rapid Mineral Liberation Analysis with X-Ray and BSE Image Processing', paper presented to ICAM.

Gurnett, I 2009, 'Ore Characterisation of Dense Medium Separated Particles by Cone Beam Tomography and MLA Analysis', Undergraduate thesis, The University of Queensland.

Gy, P 1982, *Sampling of the Particulate Materials*, Elsevier, Amsterdam.

- 2003, 'Sampling of discrete materials—a new introduction to the theory of sampling; I Qualitative approach', *Science Direct*, vol. 74.

- 2004a, 'Part IV: 50 years of sampling theory—a personal history', *Chemometrics and intelligent laboratory systems*, pp. 49-60.

- 2004b, 'Part V: Annotated literature compilation of Pierre Gy', *Chemometrics and intelligent laboratory systems*, pp. 61-70.

- 2004c, 'Sampling of discrete materials II Quantitative approach—sampling of zero-dimensional objects', *Science Direct*, vol. 74.

- 2004d, 'Sampling of discrete materials; III. Quantitative approach—sampling of one-dimensional objects', *Chemometrics and intelligent laboratory systems*, pp. 39-47.

Haberlah, D 2011, 'Recent advances in the textural quantification of commercially important clay minerals in subsurface applications', in Antalya, Turkey.

Haddamard, J 1902, 'Sur les problèmes aux dérivées partielles et leur signification physique. ', in *Princeton University Bulletin*, pp. 49-52, <http://en.wikipedia.org/wiki/Well-posed_problem.>.

Hangartner, TN 2005, 'Thresholding technique for accurate analysis of density and geometry in QCT, pQCT and microCT images.', paper presented to 2nd International Conference on Osteoporosis and Bone Research, October 19-23, 2005.

Hartner, R 2012, 'Integration and analysis of optical and MLA-based microscopy for optimisation of geometallurgical modelling and ore deposit characterisation', Doctor of Philosophy thesis, The University of Queensland.

Hsieh, J 2009, *Computed Tomography, Principles, Design, Artifacts, and Recent Advantages*, second edn, Wiley Interscience, SPIE PRESS, Bellingham, Washington USA.

Hsih, CS and Wen, SB 1994, 'Extension of Gaudin's liberation model for quantitatively representing the effect of detachment in liberation', *International Journal of Mineral Processing*, vol. 42, no. 1-2, pp. 15-35.

Iovea, M, Oaie, G, Ricman, C, Mateiasi, G, Neagu, M, Szobotka, S and Duliu, OG 2009, 'Dual-energy X-ray computer axial tomography and digital radiography investigation of cores and other objects of geological interest', *Engineering Geology*, vol. 103, no. 3-4, pp. 119-26.

Jaime, P 2009, 'The applicability of Automated Mineralogy on process planning, process optimisation, quality control, audit studies and trouble shooting, with emphasis on processing plants. ', paper presented to Procemin Santiago, Chile.

Jaynes, ETJ 1968, 'Prior Probabilities', *IEEE Trans. Syst. Sci.Cyber*, vol. 4, pp. 227–41.

Jerram, D and Higgins, DM 2007, '3D Analysis of Rock Textures: Quantifying Ingeneous Microstructures', *Elements*, vol. 3, pp. 239-45.

JKMRC (ed.) 2003, *MLA System User Operating Manual Module 4*, 2.1 edn, Brisbane, Australia.

JKTech 2011, *JKTech Pty Ltd*, <www.jktech.com.au >.

Jones, MP 1987, *Applied Mineralogy- a quantitative approach* Graham and Trotman Ltd., UK and USA, London.

Keeney, L 2007, *High Resolution Cone Beam Tomography Study of Sulphide Ore Minerals Using the Skyscan-1072*, JKMRC, The University of Queensland, Brisbane, <http://physics.nist.gov/PhysRefData/Xcom/html/xcom1-t.html>.

Keith, JM 1997, 'A new method of stereological correction', paper presented to Sixth JKMRC Student Conference, pp. 75–86, Australia, JKMRC, The University Of Queensland.

- 2000, 'A stereological correction for multiphase particles', PhD thesis, The University of Queensland.

Kern, JW 1995, 'Spectra and Cross Spectra models for large scale frequency domain simulation of D-variate n-dimensional random functions: applications in groundwater modeling; and a statistical examination of Pierre Gy's sampling procedures', PhD thesis, The University of Wyoming.

Ketcham, R 2005, 'Computational methods for quantitative analysis of three-dimensional features in geological specimens', *Geosphere, University of Texas at Austin, USA* vol. 1 no. 1, pp. 32-41.

Ketcham, RA and Carlson, WD 2001, 'Acquisition, optimization and interpretation of X-ray computed tomographic imagery: applications to the geosciences', *Computers & Geosciences*, vol. 27, no. 4, pp. 381-400.

Ketcham, RA and Iturrino, GJ 2005, 'Nondestructive high-resolution visualization and measurement of anisotropic effective porosity in complex lithologies using high-resolution X-ray computed tomography', *Journal of Hydrology*, vol. 302, no. 1-4, pp. 92-106.

King, P 2001, *Modeling and Simulation of Mineral Processing Systems*, 1 edn, Butterworth Heinemann Oxford, USA.

King, RP 1979, 'A model for the quantitative estimation of mineral liberation by grinding', *International Journal of Mineral Processing*, vol. 6, pp. 207-20.

King, RP 1982, 'The Prediction of Mineral Liberation from Mineralogical Texture', in *Proc. 14th Int. Mineral Processing Congress*, Toronto, pp. VIII 1. - VIII .17.

- 1987, 'Overview of Methods to Predict Mineral Liberation', paper presented to 4th ICRA Workshop.

- 1990, 'Calculation of the liberation spectrum in products produced in continuous milling circuits ', in *Seventh European Symposium on Comminution*, Ljubljana, vol. 2, pp. 429-44.

- 1994a, 'Comminution and Liberation of MInerals', *Min. Engineering*, vol. 7, pp. 129-40.

- 1994b, 'Linear stochastic models for mineral liberation', *Powder Technology*, vol. 81, no. 3, pp. 217-34.

- 1994c, 'Linear stochastic models for mineral liberation.', *Powder Technology*, vol. 81, pp. 217-34.

King, RP and Schneider, CL 1993, 'Mineral LIberation in Continuous Milling Circuits', paper presented to XVIII International Mineral Processing Congress, Sydney, 1993.

King, RP and Schneider, CL 1998a, 'Mineral liberation and the batch comminution equation', *Minerals Engineering*, vol. 11, no. 12, pp. 1143-60.

King, RP and Schneider, CL 1998b, 'Stereological correction of linear grade distributions for mineral liberation', *Powder Technology*, vol. 98, no. 1, pp. 21-37.

Kojovic, T, Shi, F, Larbi-Bram, S and Manlapig, E 2008, 'Julius Kruttschnitt Rotary Breakage Tester (JKRBT) -Any Ore, Any Mine', in Perth, WA, Australia, pp. 91-103.

Laslett, GM, Sutherland, DN, Gottlieb, P and Allen, NR 1990, 'Graphical assessment of a random breakage model for mineral liberation', *Powder Technology*, vol. 60, no. 2, pp. 83-97.

Lastra, R, Petruk, W and Wilson, J 1998, 'Image Analysis Techniques and Applications to Mineral Processing', *Modern Approaches to Ore and Environmental Mineralogy*, vol. 27, no. Short Course, pp. 327-66.

Latti, D and Adair, B 2001, 'An assessment of stereological adjustment procedures', *Minerals Engineering*, vol. 14, pp. 1579–87.

Lawn, BR 2004, 'Fracture and deformation in brittle solids: a perspective on the issue of scale', *Journal of Materials Research*, vol. 19, no. 1, pp. 22-9.

Lawn, BR, Rice, JR and Wilshaw, TR 1977, 'Fracture of Brittle Solids (Cambridge Solid State Science Series)', *Journal of Applied Mechanics*, vol. 44, no. 3, pp. 517-.

Leica 2011, *Automated upright microscope for materials science and geoscience Leica DM6000 M.*, <http://www.leica-microsystems.com/>.

Lin, CL and Miller, JD 1996, 'Cone beam X-ray microtomography for three-dimensional liberation analysis in the 21st century', *International Journal of Mineral Processing*, vol. 47, no. 1-2, pp. 61-73.

Lin, CL and Miller, JD 2001, 'A new cone beam X-ray microtomography facility for 3D analysis of multiphase materials,pp. 98–109', paper presented to 2nd World Congress on Industrial Process Tomography, Hannover, Germany, 29–31 August,.

Lin, D, Gomez, CO and Finch, JA 1995, 'Comparison of stereological correction procedures for liberation measurements', *Transactions of the Institution of Mining & Metallurgy, Section C: Mineral Processing and Extractive Metallurgy*, vol. 104, pp. 155-61.

Lynch, AJ 1977, 'Mathematical model of mineral liberation', in *Mineral crushing and Grinding Circuits, Their Simulation, Optimisation, Design and Control*, Elsevier Scientific Publishing, New York, pp. 187-202.

Malzbender, J 2003, 'Comment on hardness definitions', *Journal of the European Ceramics Society 23*, vol. 1355.

Man, YT 1999, 'A model-based scale up procedure for wet overflow ball mills', PhD thesis, The Univeristy of Queensland (JKMRC).

Manlapig, EV, Drinkwater, DJ, Munro, PD, Johnson, NW and Watsford, R 1985, 'Optimisation of grinding circuits at the lead/zinc concentrator, Mount Isa Mines Ltd', in *Automation for mineral resource development (IFAC '85)*, Brisbane, pp. 265-74.

Markowicz, AA 1993, *X-ray physics*, Handbook of X-ray Spectrometry, Marcel Dekker, New York.

Marpu, PR, Lippold, J, Gloaguen, R, Niemeyer, I and Jonckheere, R 2006, 'Object-based Classification Algorithm for Automatic Identification of Fission Tracks', in *Int. Assoc. for Mathematical Geology*, Université de Liège - Belgium.

Martin, CJ, Thorpe, R, Palko, A, Dobbe, R, Bajic, S, Kalstrom, M, Haecker, R and Martin, T 2014, 'Mineral process plant monitoring at Greens Creek: by looking at the minerals themselves', paper presented to Canadian Mineral Processors, Ottawa.

Mazurkiewicz, M and Rakowski, Z 1995, 'Materials disintegration by high pressure water jet — review of recent development : M. Mazurkiewicz, in: Geomechanics 93. Proc. conference, Ostrava, 1993, ed Z. Rakowski, (Balkema), 1994, pp 261–264', *International Journal of Rock Mechanics and Mining Sciences & Geomechanics Abstracts*, vol. 32, no. 2, p. A81.

McCoy, TJ, Ketcham, RA, Wilson, L, Benedix, GK, Wadhwa, M and Davis, AM 2006, 'Formation of vesicles in asteroidal basaltic meteorites', *Earth and Planetary Science Letters*, vol. 246, no. 1-2, pp. 102-8.

McNab, B, Jankovic, A, David, D and Payne, P 2009, 'Processing of Magnetite Iron Ores – Comparing Grinding Options', paper presented to Iron Ore Conference, Perth.

Mehta, RK, Adel, GT and Yoon, RH 1990, 'Liberation modeling and parameter estimation for multicomponent mineral systems', *Minerals and Metallurgical Processing*, vol. 7, no. 3, pp. 156-63.

Meloy, TP 1984, 'Liberation theory -- Eight, modern, usable theorems', *International Journal of Mineral Processing*, vol. 13, no. 4, pp. 313-24.

Miles, R 1985, 'A comprehensive set of stereological formulae for embedded aggregates of non-necessarily-convex particles', *Microscopy*, vol. 138, pp. 115-25.

Miller, C, Zanetti, A, Thoni, M and Konzett, J 2007, 'Eclogitisation of gabbroic rocks: Redistribution of trace elements and Zr in rutile thermometry in an Eo-Alpine subduction zone (Eastern Alps)', *Chemical Geology*, vol. 239, no. 1-2, pp. 96-123.

Miller, J, Lin, CL, Garcia, C and Arias, H 2003, 'Ultimate recovery in heap leaching operations as established from mineral exposure analysis by X-ray microtomography', *International Journal of Mineral Processing*, vol. 72, no. 1-4, pp. 331-40.

Miller, JD and Lin, CL 1987, 'TREATMENT OF POLISHED SECTION DATA FOR DETAILED LIBERATION ANALYSIS', *International Journal of Mineral Processing*, vol. 22, no. 1-4, pp. 41-58.

Miller, PR, Reid, AF and Zuiderwyk, MA 1982, 'QEM*SEM image analysis in the determination of modal assays, mineral association and mineral liberation', in *Mineral Processing Congress*, Toronto, Canada, pp. 8-13.

Minnitt, RCA, Rice, PM and Spangenberg, C 2007, 'Understanding the components of the fundamental sampling error: a key to good sampling practice', *The Journal of The Southern African Institute of Mining and Metallurgy*, vol. 107.

Mitschke, M and Navab, N 2003, 'Recovering the X-ray projection geometry for three-dimensional tomographic reconstruction with additional sensors: Attached camera versus external navigation system', *Medical Image Analysis*, vol. 7, no. 1, pp. 65-78.

Moen, K, Malvik, T, Breivik, T and Hjelen, J 2006, 'Particle texture analysis in process mineralogy', in *23rd International Mineral Processing Congress, IMPC 2006, September 3, 2006 - September 8, 2006*, Istanbul, Turkey, pp. 242-6.

Moran, P 1972, 'The probabilistic basis of stereology', in *Probabilistic problems in Metallurgy*, Seattle.

Morrell, S 2006, 'AG/SAG mill circuit grinding energy requirement-how to predict it from small-diameter drill core samples using the SMC test', in *2006 SME Annual Conference, March 26, 2006 - March 29, 2006*, St. Louis, MO, United states, vol. 2006, pp. 115-28.

- 2007, 'The effect of aspect ratio on the grinding efficiency of open and closed circuit AG/SAG Mills', in *Australasian Institute of Mining and Metallurgy Publication Series*, Fremantle, WA, pp. 121-4.

- 2008, 'A method for predicting the specific energy requirement of comminution circuits and assessing their energy utilisation efficiency', *Minerals Engineering*, vol. 21, no. 3, pp. 224-33.

- 2009, 'Predicting the overall specific energy requirement of crushing, high pressure grinding roll and tumbling mill circuits', *Minerals Engineering*, vol. 22, no. 6, pp. 544-9.

- 2010, 'Predicting the specific energy required for size reduction of relatively coarse feeds in conventional crushers and high pressure grinding rolls', *Minerals Engineering*, vol. 23, no. 2, pp. 151-3.

Morrell, S 1996, *The Optimisation of Mineral Processes by Modelling and Simulation*.

Morrell, S, Dunne, R and Finch, W 1993, 'The Liberation Performance of a Grinding Circuit Treating Gold Bearing Ore', in *XVIII International Mineral Processing Congress*, Sydney, vol. 1, pp. 197-202.

Morrell, S, Finch, WM, Kojovic, T and Delboni, H 1996, 'Modelling and simulation of large diameter autogeneous and semi-autogeneous mills', *International Journal of Mineral Processing*, vol. 44-45, pp. 289-300.

Morrell, S and Morrison, DRD 1989, 'Ore charge, ball load and material flow effects on an energy based SAG mill model', in Ma Agar (ed.), *Advances in Autogenous and SAG Technology*, Vancouver, pp. 697-712.

Morrell, S, Sterns, UJ and Weller, KR 1993, 'The Application of Population Balance Models to Very Fine Grinding in Tower Mills', in *XVIII International Mineral Processing Congress*, vol. 1, pp. 61-6.

Morrison, A 2011, 'Quantifying respirable crystalline silica in the ambient air of the Hunter Valley, NSW - sorting the silica from the silicon. ', paper presented to 20th Clean Air Society of Australia and New Zealand Christchurch, New Zealand.

Morrison, RD 2000, 'Applying image analysis to process control - from blasting to flotation', paper presented to J. A. Herbst, ed. Control 2000 - Mineral and Metallurgical Processing, Colorado, USA: SME.

Mular, AL, Halbe, DN and Barratt, DJ 2002, *Mineral processing plant design, practice, and control proceedings*, vol. 1, USA.

Napier-Munn, TJ 1996, *Mineral Comminution Circuits, their operation and optimisation*, JKMRC monograph series in mining and mineral processing, No. 2, Hall & Jones Pty Ltd, Brisbane, Australia.

Napier-Munn, TJ, Morrell, S, Morrison, RD and Kojovic, T 1999, *Mineral Comminution Circuits- Their Operation and Optimisation*, Julius Kruttschnitt Mineral Research Centre, Australia, Brisbane.

Narayanan, SS 1985, 'Development of a laboratory single particle breakage technique and its application to ball mill scale-up', PhD thesis, The University of Queensland (JKMRC).

Narayanan, SS and Whiten, WJ 1983, 'Breakage characteristics of ores for ball mill modelling', in *Proceedings of AusIMM*, vol. 286, pp. 31-9.

- 1988, 'Determination of comminution characteristics from single particle breakage tests and its application to ball mill scale up', *Trans. Inst. Miner. Metall.*, vol. 97, pp. C115-C24.

Nickel, EH 1995, 'The definition of a mineral', in *The Canadian Mineralogist*, , vol. 33, pp. 689-90, via minsocam, <http://www.minsocam.org/msa/ima/ima98(04).pdf>.

NIST 2011, National Institute of Standards and Technology, <http://physics.nist.gov/PhysRefData/Xcom/html/xcom1.html>.

O'Brien, G, Firth, B and Adair, B 2010, 'The application of the coal grain analysis method to coal liberation studies', in *16th International Coal Preparation Congress, ICPC 2010, April 25, 2010 - April 30, 2010*, Lexington, KY, United states, pp. 922-30.

Peterson, RD and Herbst, JA 1985a, 'Estimation of kinetic parameters of a grinding liberation model', *International Journal of Minerals Processing*, vol. 14, pp. 111-26.

Peterson, RD and Herbst, JA 1985b, 'Estimation of kinetic parameters of a grindingliberation model', *International Journal of Minerals Processing*, vol. 14, pp. 111-26.

Petruk, W 2000, *Applied mineralogy in the mining industry*, Elsevier, Ottawa, Ontario, Canada.

Petruk, W and Schnarr, JR 1981, *An evaluation of the recovery of free and unliberated mineral grains, metals and trace elements in the concentrator of Brunswick Mining and Smelting Corp. Ltd. 33,* .

Pilny, V and Janacek, J 2006, *Anisotropic Diffusion 2D filter*, <http://imagej.nih.gov/ij/plugins/anisotropic-diffusion-2d.html>.

Plante, A, Peck, D and Von Bargen, D 2003, *The Mineral Identification Key*, Mineralogical Society of America, <http://www.minsocam.org/MSA/collectors_corner/id/mineral_id_keyi1.htm>.

Plas, Lvd and Tobi, AC 1965, 'A chart for judging the reliability of point counting results', *American Journal of Science*, vol. 263, no. 1, pp. 87-90.

Pokrajcic, Z 2010, 'A Methodology for the Design of Energy Efficient Comminution Circuits', PhD thesis, The University of Queensland.

Prince, JL and Links, JM 2006, *Medical Imaging, Signals and Systems*, Pearson Education , Inc, NJ 07458.

Prothero, DR and Schwab, F 2004, *Sedimentary geology : an introduction to sedimentary rocks and stratigraphy*, New York.

Rasband, W 2010, *Image J, Java Image Analyses*, 1.6.0_05 edn, National Institute of Health, USA, <http://rsb.info.nih.gov/ij/>.

- 2011, *ImageJ*, 1.40g edn, National Institute of Health, USA, Java 1.6.0_05, <http://rsb.info.nih.gov/ij/>.

Roberts, WL, Rapp, GR and Weber, J 1974, *Encyclopedia of Minerals*, Litton, 0-442-26820-3.

Rumpf, H 1973, 'Physical aspects of comminution and new formulation of a law of comminution', *Powder Technology*, vol. 7, no. 3, pp. 145-59.

Salmon, P 2005, *Getting the most of Your Micro-CT*, SkyScan NV, Bruker, Belgium.

Schena, G, Chiaruttini, C, Dreossi, D, Olivo, A and Pani, S 2002, 'Grade of fine composite mineral particles by dual-energy X-ray radiography', *International Journal of Mineral Processing*, vol. 67, no. 1–4, pp. 101-22.

Schneider, CL, Lin, CL and King, RP 1991, 'Improved Transformation Techniques for the Prediction of Liberation by a Random Fracture Model', *Powder Technology*, vol. 62, pp. 103-11.

Schonert, K, Vogel, L and Peukert, W 2002, 'Separation of the influences of material and machine in impact comminution - Modelling with population balances

Trennung der einflusse von material und maschine bei der prallzerkleinerung - Modellierung mit populationsbilanzen', *Aufbereitungs-Technik/Mineral Processing*, vol. 43, no. 8, pp. 19-30.

Serra, J 1980, 'The Boolean model and random sets', *Computer Graphics and Image Processing*, vol. 12, no. 2, pp. 99-126.

Shannon, CE 1948, 'A Mathematical Theory of Communication', *The Bell System Technical Journal*, vol. 27, pp. 379–423, 623–56.

Shi, F, Kojovic, T, Esterle, JS and David, D 2003, 'An energy-based model for swing hammer mills', *International Journal of Mineral Processing*, vol. 71, no. 1-4, pp. 147-66.

Shi, F, Kojovic, T, Larbi-Bram, S and Manlapig, E 2009, 'Development of a rapid particle breakage characterisation device - The JKRBT', *Minerals Engineering*, vol. 22, no. 7-8, pp. 602-12.

Shi, FN 2002, 'Development of a power-draw model for estimation of the dynamic recirculating load of swing hammer mills with internal classifiers', in vol. 111, pp. C111-C9.

SkyScan 2010a, *NRecon*.

- 2010b, *SkyScan 1172*, <http://www.skyscan.be/company/methods.htm>.

Stamboliadis, ET 2008, 'The evolution of a mineral liberation model by the repetition of a simple random breakage pattern', *Minerals Engineering*, vol. 21, no. 3, pp. 213-23.

Stanley, CJ 1998, 'Optical Microscopy in Studying Ores and Process Products', *Modern approaches to ore and environmental mineralogy*, vol. Short Course 27, pp. 123-37.

Strunz *Classification*, <http://www.mindat.org/strunz.php?a=9 >.

Takács, L 1967, *Combinatorial Methods in the Theory of Stochastic Processes* vol. XIV + 262 S., Preis s. 96, John Wiley & Sons, Inc., New York, London, Sydney

Thompson, SK 1987, 'Sample-size for estimating multinomial proportions', *American Statistician*, vol. 41, no. 1, pp. 42-6.

- 1991, 'Adaptive cluster sampling - designs with primary and secondary units', *Biometrics*, vol. 47, no. 3, pp. 1103-15.

- 1993, *MULTIVARIATE ASPECTS OF ADAPTIVE CLUSTER SAMPLING*, vol. 6, Multivariate Environmental Statistics.

Thompson, SK and Seber, GAF 1994, 'DETECTABILITY IN CONVENTIONAL AND ADAPTIVE SAMPLING', *Biometrics*, vol. 50, no. 3, pp. 712-24.

Tikhonov, AN 1963, 'Solution of incorrectly formulated problems and the regularization method', *Sov. Math. Dokl. 4*, pp. 1035-8.

Trimble 2008, *eCognition: Object-based image analysis*, Trimble Geospatial Imaging, Munich, Germany.

Van der Zanden, H, Van der Zanden, M and Van der Zanden, R 2002, 'The SynchroCrusher - Determinism versus chaos

Der SynchroCrusher - Exakte partikelsysteme statt ungenauer zufallsgemische', *Aufbereitungs-Technik/Mineral Processing*, vol. 43, no. 10, pp. 13-26.

van Latum, LA 1985, 'The evaluation, conceptualization and development of single particle breakage testing apparatus', Masters Thesis (unpublished) thesis, Technical University of Delft.

- 1995, *Comparison of devices for ore breakage characterisation. The optimisation of Mineral Processes by Modellind and Simulation, AMIRA Project P9K Final Report*, vol. 1.

Vogel, L and Peukert, W 2004, 'Determination of material properties relevant to grinding by practicable labscale milling tests', *International Journal of Mineral Processing*, vol. 74, Supplement, no. 0, pp. S329-S38.

Webb, A 2003, 'Introduction to Biomedical Imaging', review of Kagadis, George C., *Medical Physics*, vol. 30, no. 8, p. 2267.

Webb, A and Kagadis, GC 2003, 'Introduction to Biomedical Imaging', *Medical Physics*, vol. 30, no. 8, pp. 2267-.

Weedon, DM 2001, 'A perfect mixing matrix model for ball mills', *Minerals Engineering*, vol. 14, no. 10, pp. 1225-36.

Weedon, DM and Napier-Munn, TJ 1990, 'Sulphide deposits - their origin and processing', *Int. Mining Metallurgy*, pp. 137-54.

Weibull, W 1951, 'A statistical distribution function of wide applicability', *Journal of Applied Mechanics*, vol. 18, pp. 293-7.

Weller, KR, Morrell, S and Gottlieb, P 1996, 'Use of grinding and liberation models to simulate tower mill circuit performance in a lead/zinc concentrator to increase flotation recovery', *International Journal of Mineral Processing*, vol. 44-45, no. 0, pp. 683-702.

Whiten, WJ 1972, 'The use of periodic spline functions for regresion ans smoothing', *Aust Comp*, vol. 4, pp. 31-4.

Whiten, WJ 1974, 'A matrix theory of comminution machines', *Chemical Engineering Science*, vol. 29, pp. 588-99.

Wiegel, RL 1964, 'A mathematical model for mineral liberation by size reduction. ', Master thesis, carnegie Mellon University, Chemical Engineering Department.

- 1965, 'A quantitative approach to mineral liberation', in N Arbiter (ed.), *VII Internation Mineral Processing Congress*, New York, vol. I.

- 1975, 'Liberation in magnetite iron formations', *Transactions of the Society of Mining Engineers of AIME*, vol. 258, no. 3, pp. 247-56.

- 1976a, 'The Development and Use of Magnetical Models in the Computer Simulation of the Magnetic Taconite Concentration Process', PhD thesis, The University of Queensland.

- 1976b, 'Integrated size reduction – mineral liberation model', *Trans. Soc. Min. Eng. AIME,260*, pp. 147-52.

- 1976c, *Simulation of magnetic taconite concentration processes*, The University of Queensland, JKMRC, Brisbane, dec 1976.

- 1979, 'Application of process modeling to taconite'.

- 1999a, *Fitting of LIberation Model Parameters to Davis Tube Test Data*, CMRL/TR-99-13, Coleraine Minerals Research Laboratory, The University of Minnesota Duluth.

- 1999b, *Magnetite Taconite Concentration Modeling*, CMRL/TR-99-12, Coleraine Minerals Research Laboratory, The University of Minnesota Duluth.

- 2002, 'Size reduction/mineral liberation simulation for a magnetic taconite concentrator', *Minerals & Metallurgical Processing*, vol. 19, no. 3, pp. 113-22.

- 2006, 'The Rationale behind the Development of One Model Describing the Size Reduction/Liberation of Ores', paper presented to Advances in Comminution, Littleton, 2006.

- 2010, 'Comparison of volumetric and section area particle compositions using the Gaudin random mineral liberation model', *Minerals and Metallurgical Processing*, vol. 27, no. 1, pp. 24-33.

Wiegel, RL and Li, K 1967, 'A random model for mineral liberation by size reduction ', *AIME Transactions 238,* pp. 179-89.

Wightman, EM and Evans, CL 2014, 'Representing and interpreting the liberation spectrum in a processing context'.

Wills, BA and Atkinson, K 1993, 'Some observations on the fracture and liberation of mineral assemblies', *Minerals Engineering*, vol. 6, no. 7, pp. 697-706.

Xradia, Z 2014, *X-ray Microscope to Advance Pursuit of Discovery*, ZEISS Xradia, <http://www.zeiss.com/microscopy/en_de/products/x-ray-microscopy/zeiss-xradia-520-versa.html#highlights>.

Zbijewski, W, Gang, GJ, Xu, J, Wang, AS, Stayman, JW, Taguchi, K, Carrino, JA and Siewerdsen, JH 2014, 'Dual-energy cone-beam CT with a flat-panel detector: Effect of reconstruction algorithm on material classification', *Medical Physics*, vol. 41, no. 2, p. 021908 (15 pp.).

9 Appendices:

9.1   *Mineral properties*

In materials science, hardness is the characteristic of a solid material expressing its resistance to permanent deformation. Hardness can be measured on the Mohs scale or various other scales. This scale is relative and goes from 1 to 10. Minerals with a given Mohs hardness can scratch the surface of any mineral that has a lower hardness than itself. Some of the other scales used for indentation hardness in engineering - Rockwell, Vickers, and Brinell - can be compared using practical conversion tables (Dieter 1989; Malzbender 2003). Hardness should not be confused with a mineral's overall "toughness." Diamond is the hardest known mineral, but it has a perfect cleavage and breaks easily along that cleavage (Plante et al. 2003).

One of the very useful mineral properties (when it comes to mineral separation) is specific gravity, which relates the mineral mass to the mass of an equal volume of water, namely the relative density of the material. While most minerals, including all the common rock-forming minerals, have a specific gravity of 2.5 - 3.5, a few are noticeably more or less dense, e.g. several sulphide minerals have high specific gravity compared to the common rock-forming minerals (Gaines et al. 1997).

9.2   *Particle terminology*

Since the terminology used by various authors differs, the following definitions relevant to mineralogical analysis and liberation modelling are taken from Barbery (Barbery 1991) and Evans (Evans 2002, appendix 1):

"A particle is a 3-D fragment consisting of one or several mineral phases. It is a part of broken rock. A parent particle is the designation given to particles prior to breakage. A

progeny particle is the designation given to particles that result from breaking parent particles. Particle size is the result of a convenient method of measuring a linear characteristic of particles. It will be taken as a screen size that is the side of a square opening through which the particle will just pass, given all probabilities.

A grain is a 3-D entity consisting of only one mineral. This is the mineral in its original state before breakage. Composition is the proportion of a mineral in a particle. Composition can be by mass, volume, area, surface area, perimeter, etc.

The kernel is a mathematical term that generally denotes a relationship between one function and another. In regard to liberation, there are three kernels of interest. These are the comminution kernel, the liberation kernel and the stereological correction kernel. A comminution kernel represents a proportion of particles from one size-class that, when broken, go to another size class. This kernel is obtained from a comminution model.

A liberation kernel represents the proportion of particles from one size-class and one liberation class that go to another size class and liberation class. This kernel is generally normalised so that when summed over all progeny liberation-classes it equals 1. With this expression, the definition kernel is more specifically given as: the proportion of particles from one size-class and one liberation class that, given they go to another size-class, go to a liberation class. This kernel is four-dimensional. The liberation class is extended to multiphase by considering a liberation class as itself being multidimensional.

In a stereology a kernel represents the proportion of sections from parent particles of a particular composition that form progeny sections of a particular composition. This kernel is two-dimensional and can be volume-weighted, area-weighted and number-weighted. Like the liberation kernel it can also be extended to multiple phases.

The degree of liberation is the percentage of the mineral or particle occurring in liberated particles considering the total of that mineral or particle occurring in the rock. It can be by volume, mass, section, perimeter, surface area or any other self-consistent measurable property."

9.3   Key Geometric Probability Equations

The first equation is well known, commonly used and has its origins as early as 1847. (Delesse 1847)

Equation 52 (Delesse 1847):

$$\frac{E_v(V_m)}{E_v(V)} = \frac{E_a(A_m)}{E_a(A)}$$

The terms used in this equation are as follows:

E denotes statistical expectation, with the subscripts 'v' referring to particles, and 'a' referring to particle sections;

V is volume (of particle); A is area (of particle); the subscript 'm' refers to mineral-of-interest.

Therefore, this equation states that the mineral composition from particle sections is equal to the mineral composition in the particle, assuming that the sampling of the particle section from the particle will not introduce any errors. In practice, this mineral composition "means" the mean of many sections. The difference between and which was derived by Gay is consideration of the spatial grouping of minerals within each particle:

Equation 53(Gay 1995):

$$\frac{E_v(V_m V_n)}{E_v(V^2)} = \frac{E_a(A_m A_n d_{m,n})}{E_a(A^2 d)}$$

Here, m and n represent the m-th and n-th mineral. The new parameter included in this equation is 'd' that represents the average distance between particle points on the same planar section. Therefore $d_{m,n}$ here represents the average distance between pixels of the m-th mineral and the n-th mineral on the same particle section. When looking at mineral of interest, then m=n, the two derived equations from the previous one are:

Equation 54:

$$\frac{E_v(V_m V_m)}{E_v(V^2)} = \frac{E_a(A_m A_m d_{m,m})}{E_a(A^2 d)}$$

Equation 55:

$$\frac{E_v(V_m V)}{E_v(V^2)} = \frac{E_a(A_m A d_m)}{E_a(A^2 d)}$$

Here d_m (pixels) is the average distance between the mineral of interest and the particle pixels on the same planar section. By representing Gay's equation in terms of mineral composition with c_v being volume composition and c_a being aerial composition, it can be seen the volumetric variance given by:

Equation 56 (Gay and Morrison 2006):

$$Var(c_v) = \frac{E_v(c_v^2 V^2)}{E_v(V^2)} - \left[\frac{E_v(c_v V^2)}{E_v(V^2)} \right]^2$$

can be estimated from particle section information. In qualitative terms, the variance is related to the slope of each of the curves shown in Figure 182. Liberation depends on particle texture, and sectioning will influence the data. The problem is when the texture is mainly fine and finely dispersed grains in the particle. Then the lines or areas tested will present very similar texture data.
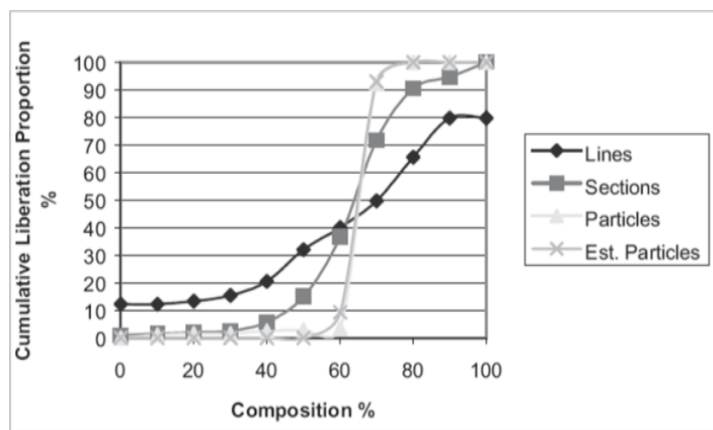

Figure 182: Cum. volumetric proportion of the composition distribution-lines sections and particles, the estimated particle composition distribution using particle section info.(Gay and Morrison 2006)

9.4 Stereological Adjustment Procedure (Gay and Morrison 2006)

Because of the information loss caused by sectioning, Gay and Morrison state that even with the use of stereology it is not possible to estimate precisely the volume composition distribution exactly but it is possible to provide a reasonable estimate.

That is the problem of estimating the volume composition from particle section information. It is an ill-posed problem that in many cases does not have a unique solution (Haddamard 1902). Two main approaches to finding reasonable solution of this ill-posed problems are the regularisation approach (Tikhonov 1963), and the probabilistic approach (Jaynes 1968; Shannon 1948). Gay also developed the 'allocation method' assuming that the geometric probability equations given in the previous section are true not only for the entire particle sections, but it is also true for all subgroups of particles. However, it is not true for all subgroups of particle sections(Gay 1995).

This approach was more formalised and made consistent with the general probabilistic approach of Jaynes (1968) by Keith (2000). A method developed by Keith (1997) was to use a kernel approach, but with the kernel for particles to particle sections approximated by the kernel for planar sections to linear intercepts.

A method of stereological correction was discussed in detail in the paper from which the majority of this topic is cited (Gay and Morrison 2006). A stereological correction based on the solution f of the inverse problem Kf, = F, is developed in the paper cited above.

The concept of using the kernel from planar intercepts to linear intercepts as a guide for the kernel from particles to planar intercepts was used in the Gay model (Gay and Morrison 2006). In some cases the result may have negative values caused by using an approximation and further adjustment is required to ensure a physically meaningful solution. The equations based on these assumptions are presented in Gay (2005).

9.5 Development of a model for liberation phenomena (Andrews and Mika 1975)

Liberation of the individual mineral phases is important for heterogeneous ores. Andrews and Mika (1975) investigated the liberation of mineral phase when batch grinding binary ore. Continuous variables in their model are particle size and mineral assay, where the most important assumption is that assays adequately describe the degree of liberation. Therefore Andrews and Mika (1975) have investigating the modifications that are required in order to apply the batch comminution equation to binary ores.

Equation 57 (Andrews and Mika 1975)

$$\frac{\partial P(D;t)}{\partial t} = \int_{D}^{\infty} S(y)B(D|y)p(y;t)dy$$

They proposed a different equation to describe the simultaneous liberation and size reduction behaviour of a two-phase material while in batch grinding and an internal relation given below, along with the constraints. This fundamental equation has been used by many researchers as the basis for their work (King and Schneider 1998a; Peterson and Herbst 1985a).

Equation 58 (Andrews and Mika 1975)

$$\frac{\partial f(m,a,t)}{\partial t} = -s(m,a,t,)f(m,a,t) + \int_{m}^{m_{max}} \int_{\frac{ma}{M}}^{\frac{-m(1-a)}{M}} b(m,a,M,A)s(M,A,t)f(M,A,t)dAdM$$

Where:
- $f(m,a,t)$ is a description of the mill contents at time t;
- m_{max} is the mass of maximum particle size in batch grinding;
- m is progeny particle mass and M is parent particle mass;
- a is progeny particle assay (grade) and A is parent particle assay (grade);
- $b(m,a,M,A)$ is breakage function of the two phase material;
- $s(m,a,t)$ is selection function of the two phase material.

The logical constraints shown in equation relate to conservation of mass, and provide theoretically possible values of particle and broken particle mass and their assays.

Equation 59 (Andrews and Mika 1975)

$M \geq m$; $MA \geq ma$; $M(1-A) \geq m(1-a)$

shows the previously mentioned set of possible theoretical values ($R_{M,A}$).
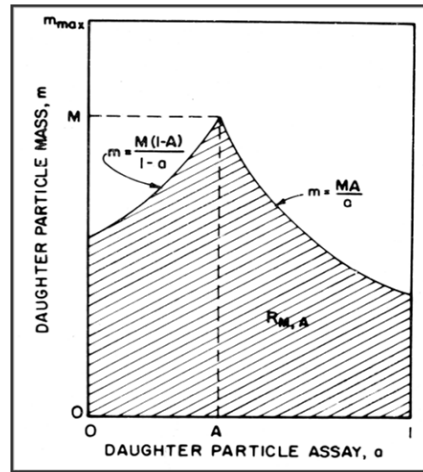
Figure 183: Diagram showing the possible progeny particles from breakage of a parent particle of mass M and assay A (Andrews and Mika 1975; King and Schneider 1998a)

Figure 183 and Figure 184 are known as Andrews-Mika diagrams, where the first one represents the possible values of progeny particles and the later one represents the set of possible values of the parent particle. The set values at a=0 and a=1 represent liberated particles, gangue and valuable. The curve is very important because it identifies the maximum values of the assays in the progeny particles for a given parent particle, whose mass cannot exceed the mass value of the heaviest particle coming from the batch grinding circuit. In this way, it is certain that the mineral mass is conserved.

"The mass or the largest possible liberated progeny particle is equal to the mass of the mineral phase contained in the parent particle" is the conservation from Andrews and Mika (1975). "The segments on the vertical axes are achievable from the point M because a particle of mass m and grade a can produce progeny consisting of pure gangue provided that the mass of the liberated gangue particle is less than the mass of the gangue phase in the parent particle." (e.g. King and Schneider 1993; 1998a)
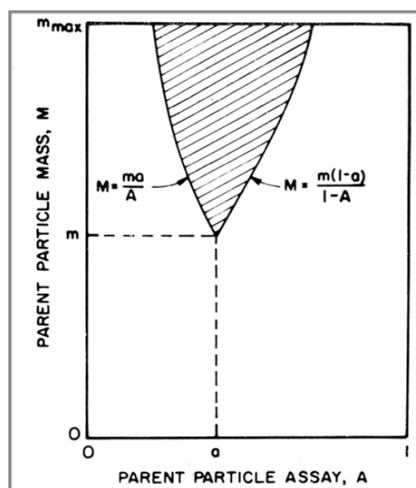
Figure 184: The possible parent particles which form a given progeny particle of mass m and assay a (Andrews and Mika 1975)

This model can be solved for some special cases. The solution can be obtained where size reduction does not produce any liberation or where breakage occurs around grain boundaries (just for special cases) but only by simplifying the equation. Andrews and Mika suggested treating continues variables, mass and assay, as discrete in their next stage of work, which they have never published. Hence, this phase was later published by other researchers, King and Schneider (King and Schneider 1993).

9.6   King and Schneider models (1993; 1998a; 1998b)

As mentioned before, King and Schneider (1998a) have modified Andrews and Mika's work (Andrews and Mika 1975) in order to use it in a population balance model of liberation in comminution. In 1979, King (King 1979) developed a theoretical model for predicting the fractional liberation of mineral at sieve size D. By using the distribution of linear intercept lengths of the minerals in the ore he developed a theory which required no assumptions about the shape of the particles. As mentioned in section 2.5.3.2, the linear intercept model did not show good correlation with measured reality. This verification immediately causes huge doubt about the reliability of Kings model. Selecting a single

surface for measuring linear intercepts distribution doesn't provide an adequate sample of the texture of the particle. Hence the resulting prediction is often not adequate as well.

The ore used in this model is binary, with randomly dispersed non-touching grains. There were different size grains. King used pyrite ore that was crushed in a roll crusher and separated by density and magnetic fractions. Based on King's data, Gaudin's, and Wiegel's model outcomes were also compared here. Due to the large error in estimating liberation with linear intercepts distribution method, the decision was to use area measurements instead. This type of error is incorporated in the method and published in King and Schneider (1998b). Observation from King and Schneider (1998a) indicate that it is much easier to classify particles by size than by individual mass, which leads to the King modification of the Andrews and Mika (1975) equation, written as:

Equation 60 (King and Schneider 1998a)

$$\frac{\partial P(g,D;t)}{\partial t} = \int_{R'} \int S(g',D')B(g,D\mid g'D')p(g',D';t)dg'\,dD'$$

Where :
- g is grade of progeny particle, g' is grade of parent particle;
- D is size of progeny particle, D' is size of parent particle;
- P(g,D;t) is cumulative distribution and p(g ,D ;t) is distribution density in g-D space;
- S(g,D) is the selection function for particles of grade g and size D;
- B(g,D|g D) is cumulative breakage function in two dimensional space.

The constraints are:

Equation 61 (King and Schneider 1998a):
$gD^3 \le g'D'^3$ **(for the mineral phase)**
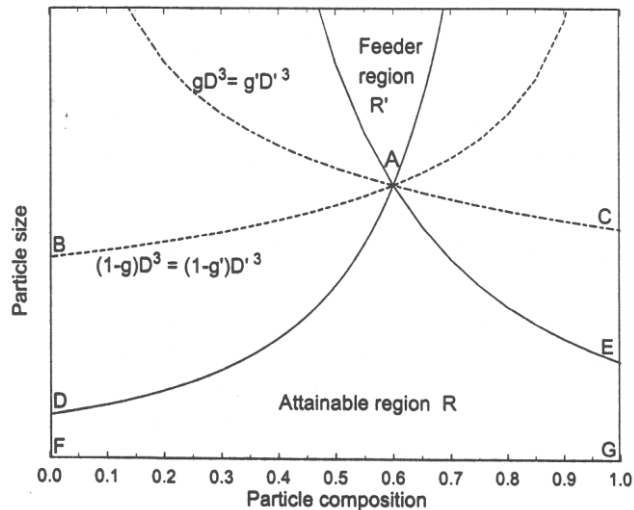$(1 - g)D^3 \le (1 - g') D'^3$ **(for the gangue phase)**

Figure 185: The Andrews-Mika diagram represented in terms of particle size (King and Schneider 1998a)

King and Schneider (1998a) combined the two graphs presented by Andrew and Mika into a single diagram (Figure 185). The double integral in is taken over a region R' in the particle composition space which contains all parent particles that can generate a progeny particle of mass D and composition g. The constrains given above keep the mass of the particles constant and provide concern about the mineralogy and texture. The boundaries defined here are indistinct unless they all have similar or same shape because particles can have similar mass and different shape with a distribution of sizes.(Evans 2002)

It is also obvious that the boundaries of the feeder region never touch values 0 and 1 for the reason that it is impossible for liberated particles to form an unliberated progeny during the breakage. Thereafter, boundaries for attainable regions in are controlled by the texture of the ore. It is of great importance that the shape of the particles is not considered to be irregular as in real ore, but regular defined shape. (King and Schneider 1998a) The additional constraints presented in the next equation ensure that the total amounts of each mineral over all sizes are conserved in the grinding process. (King and Schneider 1998a)

Equation 62:

$$\int_0^{D'}\int_0^1 gb(g,D|g',D')dgdD = g'$$

Equation 63:

$$\frac{\partial}{\partial t}\int_o^\infty\int_0^1 gp(g,D)dgdD = 0$$

can be written as:

$$\frac{\partial p(g,D;t)}{\partial t} = -S(g,D)p(g,D;t) + \int\int_{R'} b(g,D|g',D')S(g',D')p(g',D')dg'dD'$$

Multiplying this equation by g and integrating gives

Equation 64:

$$\frac{\partial}{\partial t}\int_0^\infty\int_0^1 gp(g,D)dgdD = -\int_0^\infty\int_0^1 gS(g,D)p(g,D)dgdD$$

Equation 65:

$$+\int_0^\infty\int_0^1 S(g',D')p(g',D')\int_{g^*}^{g^{**}}\int_0^{D'} gb(g,D|g',D')dDdgdg'dD'$$

A sufficient equation for to be satisfied is therefore:

Equation 66:

$$\int_{g^*}^{g^{**}}\int_0^{D'} gb(g,D|g',D')dDdg = g'$$
(**for all g' and D'**)

Values g* and g** represent the left and right hand boundaries respectively of the feeder region at each value of D. The another useful form of the is:

Equation 67:

$$\int_0^{D'} b(D|g',D')\int_0^1 gb(g|D,g',D')dgdD = g'$$

These equations show that the function b must be available in order that solutions for the batch comminution equation can be generated.(King and Schneider 1998a)

After the construction of Andrews Mika diagrams by decoupling the size reduction process from liberation process using the conditional breakage functions, the solutions to the batch comminution equation can be determined (King and Schneider 1998a). A general discrete solution to the equation for batch comminution was presented which provides the size and liberation distribution as a function of the grind time t.(Evans 2002) A suitable algorithm was developed in King(1990) and King and Schneider (1993).

Equation 68:

$$p_{ij} = \sum_{l=1}^{j} \sum_{k=1}^{12} \alpha_{ijkl} e^{-s_{kl}t}$$

The objective is that this model, as any other liberation model, may be simplified by considering breakage as random. Under this assumption, the fracture of the particle during comminution process is independent of the mineralogical composition and texture of the particle.

The following six conditions characterize random fracture (King and Schneider 1998a):

- "**No selective breakage**

The mineral phases are equally brittle and the specific rate of breakage S_{ij} is therefore not a function of the composition of the parent particle- $S_{ij}=S_{j.}$ it is only function of the size.

- **No differential breakage**

Differential breakage does not occur during comminution and the size breakage function $b_{j,kl}$ is independent of the composition of the parent particle- $b_{ijkl}=b_{j,l}b_{i,jkl}$

- **No preferential breakage**

The internal consistency condition () takes on the simple form $\sum_{i=1}^{12} g_i b_{i,jkl} = g_k$ for all j,k,l.

This is quite common form of breakage.(Fandrich 1997; King and Schneider 1998a)

- **No phase-boundary fraction**

This is the case where cracks tend to propagate along phase boundaries rather than across a mineral phase. King (King, 1994 #184) state that phase-boundary fracture does not influence liberation significantly unless it is severe enough to cause detachment and

therefore no special provision is made in the models of the attainable region to accommodate this effect.

- **No liberation by detachment**

Some minerals become easily detached from the ore during comminution leading to significant liberation of the original mineral grains which increases liberated class in the region of mineral 'grain-size' when attainable region is considered. If this effect occurs, it will greatly influence the liberation characteristics.(Gaudin 1939)

- **No boundary-region fracture**

If there is preferential breakage in the area of phase boundary where significant difference in material elastic module is present, fracture produces the interesting result that finer particles are less liberated than coarser particles." (King and Schneider 1998a)

9.7 Morrell's liberation model

Dr Steve Morrell has spent a huge effort during his career emphasising the importance of calculating the real energy consumption in the operational plants. Here it is very important to understand the liberation properties as well as the breakage properties of the particles.

During the P9K project (1992-1995) Morrell studied the behaviour of pyrite ore in comminution circuits at Newcrest Mining's Celebration gold operation (Morrell 1996; Morrell, Dunne, et al. 1993) and his approach was modified and implemented in tower milling of a zinc ore(Morrell, Sterns, et al. 1993).(Evans 2002)

The assumptions had to be made here since at the time of the research QEM*SEM(FEI 2014) analysis provided data in the size range -425 +10µm. Hence pyrite finer than 10µm was assumed to be liberated and all pyrite larger than 425µm assumed to be unliberated. QEM*SEM analysis confirmed that most of the pyrite was less than 80µm in size and gold was up to 170µm but mostly in the 40µm range, while the maximum gold grain size included in or associated with pyrite was 20µm. It has been revealed that the dependence of the gold recovery efficiency on size is related to the degree of the liberation of pyrite. (Morrell, Dunne, et al. 1993a) The implication of these results is that the breakage is sufficiently random, that the expected value of the liberation distribution at the finer size will be the same in feed to as product from the circuit.

"The New Celebration liberation data showed that in a given size fraction within a grinding circuit, the proportion of a mineral which is present in the "liberated" class (defined as particles of grade greater than 90%) is the same regardless of whether the size fraction is from the feed to or product of the grinding circuit. Any difference in the values of the liberated material is within the expected measurement error. This characteristic has been observed by other workers on other ores (e.g. Berube and Marchand 1984; Manlapig et al. 1985; Petruk and Schnarr 1981). Note that at the time of Morrell's work, no widely-accepted stereological correction was available to correct the measured areal liberation data to volumetric data. Therefore, all of the liberation data used by Morrell were sectional liberation values." (Evans 2002)

Liberated valuable, liberated gangue and unliberated valuable were the three streams considered in the Morrell's model, where liberated gangue and valuables can only be liberated gangue and valuables at the end of the size reduction process, where unliberated particles may become liberated during this size reduction process. (Figure 186) This approach has been used by other researchers (for example Peterson and Herbst 1985b)
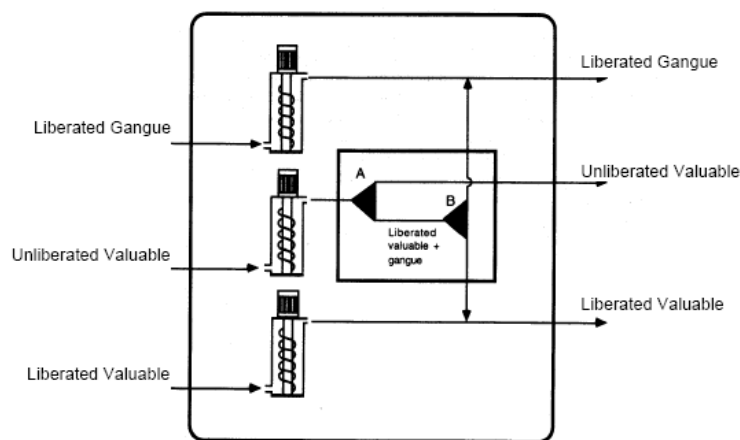

Figure 186: *Morrell's conceptual model for liberation in grinding (Napier-Munn et al. 1999)*

The difference between this model and others presented in this work is also in considering ore as two-phase system but each of the phases can consist of two or more minerals whose data have be grouped together. This model may be extended to cover multi component ore if needed.

Whiten's perfect mixing ball mill model was used to describe how each of the streams is ground in the mill where JKMRC's non-linear fitting routine 'NLF" was used for fitting the classification curve and ball mill model parameters. (Whiten 1974) In the case of the breakage distribution function or appearance function and breakage rate distribution, the same values were assumed for all streams. These values were obtained from pendulum breakage testing of the bulk ore (Narayanan and Whiten 1983).

The mean residence times used in the model were assumed to be different since more dense and hard particle will need more time to grind to the certain size, there will also be a difference in cut size in cyclones. Hence three cyclones were used for three streams (Figure 187).
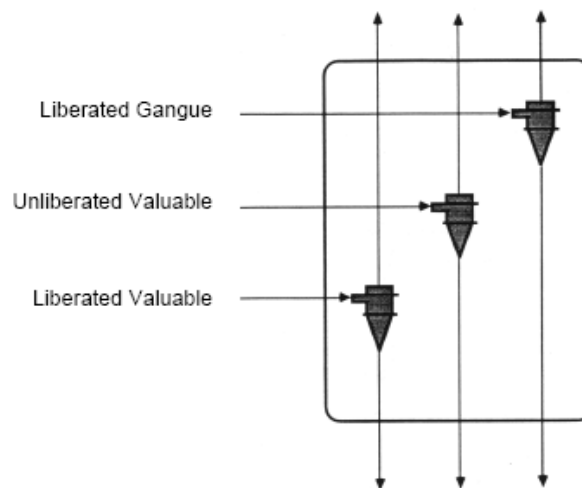

Figure 187: *Morrell's conceptual model for classifying liberated and unliberated particles in cyclone (Morrell 1996)*

The results for the size distribution for the unliberated pyrite in the +425µm size fraction were not very good as QEMSCAN System data were not available for that size range.

"The mass balance across the mill was maintained using two relationships A and B within the model. The relationships A and B described the breakage and liberation of the unliberated feed stream. They also assisted in meeting the liberated mineral mass conservation constraint. Relationship A describes the relationship between particle size and the proportion of unliberated mineral, which becomes liberated during the size

reduction while relationship B is effectively a size-by-size grade curve for the unliberated material. Figure 194 shows examples of these relationships for a zinc ore." (Evans 2002)
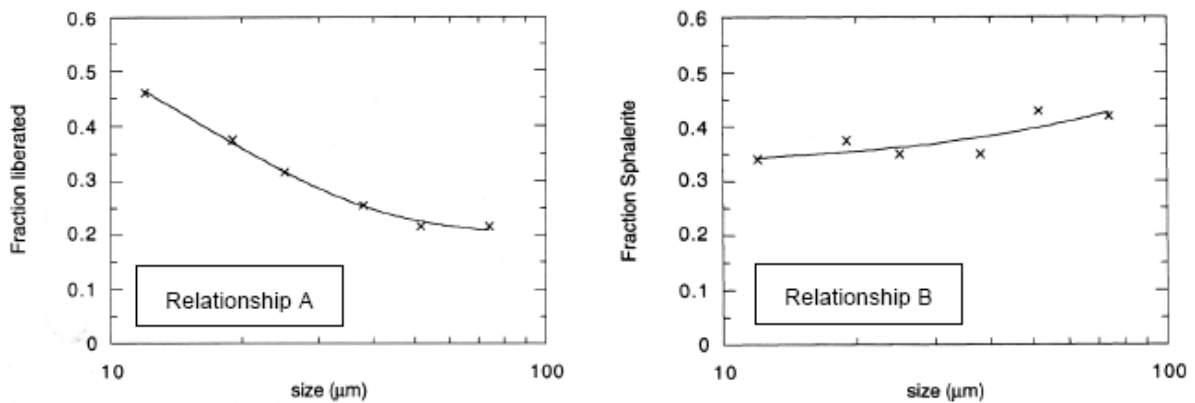

Figure 188: Measured liberation data which represent relationships A and B in the Morrell model (Napier-Munn et al. 1999)

Two surveys were used for testing the model of an industrial tower mill treating a zinc ore. The first survey outcome was defining the relationships A and B to fit the model and calculate the breakage rates for the liberated sphalerite, liberated gangue and unliberated sphalerite. The model was then used in the second survey. The tower mill performance was predicted under conditions of a finer size distribution and lower feed rate.

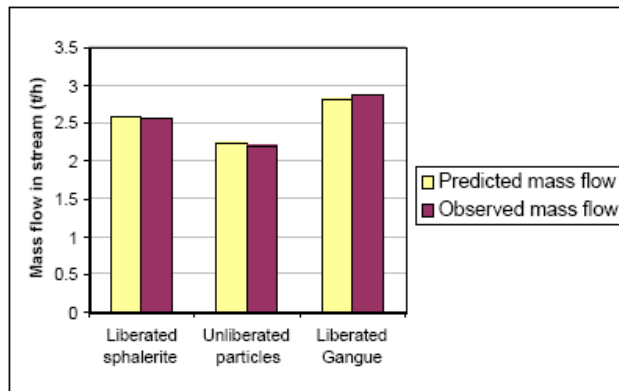**Figure 189: Comparison of the observed mass flow of liberated and unliberated particles with the values predicted by the Morrell approach (Evans 2002)**

As Figure 189 shows, the model prediction gave reasonable close results in the second survey. It was also provided a good prediction for the size distributions of the liberated sphalerite and gangue particles (Figure 190). But, there was more error in the case of the

size distribution of unliberated particles. The values for fine particles were well predicted. This cannot be said for coarser ones.
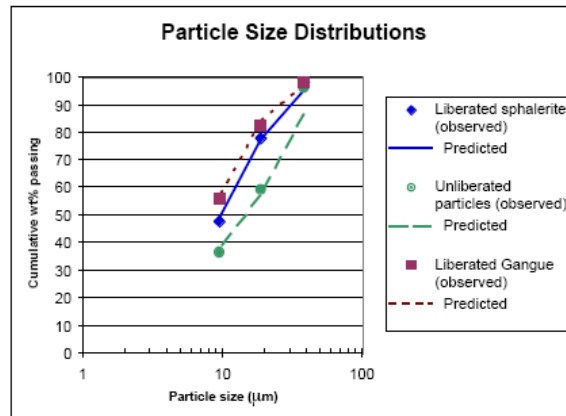

Figure 190: **Comparison of the observed size distributions by Morrell approach (Evans 2002)**

This model was successful in simulating the liberation behaviour of two different ores in two different comminution circuits, unfortunately without giving any information about the unliberated particles. The prediction of an increase in liberated gangue and valuables as well as gangue flow rate reduction was very good with the use of this model.

9.8 Simple random breakage model (Stamboliadis 2008)

A mineral liberation model described by Stamboliadis (2008) was applied to a binary system where mineral size and grade were treated as discrete variables. He believes that this model predicts the distribution of particles of the same size class into different grade classes.

A critical liberation size is defined here, after which liberation starts to occur. However, the disadvantage of this model is that it does not considering mineral properties, such as texture, and the possibility of non-random breakage. The Stamboliadis liberation model combines size reduction and liberation patterns at finer than the critical liberation size where model is relating the size class of progeny particles to the probability of falling into

368

any available grade classes. He extends previously mentioned models where the particle consists of two mineral phases and the minority valuable phase is distributed inside the gangue phase in equal grains. Grains here have different sizes which will influence the ore composition as well (Stamboliadis 2008). The shape of the grains and particles is spherical, the breakage is random and the parent particle breaks into two particles of equal volume.

The solution for size reduction pattern lies in a knowledge of selection and breakage functions. The selection function will determine whether a parent particle is broken and the breakage function will determine the size distribution of the progeny particles. However, the liberation pattern requires the information about the minerals and therefore liberation of the progeny particles which will depend on relationship between minerals and their position in the matrix. (Stamboliadis 2008)

To conclude, there are two important concepts of this model (Stamboliadis 2008). The classification of the particles based on particle size distribution and grain size distribution of the minority phase is the first concept. The second concept is the definition of a critical liberation size which is the size of the particle where liberation begins.

Stamboliadis presented a breakage pattern where he related the size of a progeny particle to its grade. The most important assumption made is that breakage is in a continuous system and that it is random. Up to the critical liberation size of the progeny particle, all progeny particles have the same grade and if equal to the parent grade. It is only when this critical liberation size is reached that mineral grains start to break. The great opportunity for testing is also the assumption that after the breakage of the progeny particle at this critical size, its progeny particle will contain only one or zero grain of the mineral considered a minority mineral in the initial parent particle. However, by extending the model to more grain sizes present in the parent particle, we can verify the model on a wider spectrum than previously.

The only difference is the volume between particles, however the sum of volume is considered to be the same before entering comminution devise and when exiting. The

same applies to the grade. Stamboliadis (2008) believes that these last two assumptions are correct for balanced continuous systems where the mineral volume units are constant, regardless of the position of the sampling (feed or discharge).

The simplified breakage pattern considered here is that progeny volume will be exactly half of the parent volume. Because of this, two progeny particles are considered complementary particles in order to constrain parents metal and volume units. Although it seems unrealistic, Stamboliadis is referring to the fact that his model is liberation model and not breakage. However, it is believed that there is a great opportunity for modifying this model by applying different breakage pattern that could be more realistic and therefore lead to more realistic liberation model.

The grade of the progeny particles will be the same as parent particle until there is only one grain of mineral "a" left in the parent particle. The size of this parent particle is named the critical liberation size since after breaking this particle, the grade of progeny particles may change and the boundaries of the mineral a have to be broken too. Previously used ratio K (particle to grain size ratio) is replaced by ratio r (critical liberation particle size to particle size).

The author is protecting his model by referring to the fact that his model has lower volume and size ratios than usually used in screening. He is accepting the limitations of existing models (Andrews and Mika 1975) in regards to the grade of the progeny particle but is also extending it considering the probability of the progeny to acquire a certain grade.

When considering selective breakage, Stamboliadis introduces a new value called "tendency of the progeny particle", where it is equal to 1 if progeny has a tendency to acquire its parent grade, if the breakage is random. It was found that this tendency was not so different to the random breakage pattern. In order to introduce selectivity, parameter S (grade acquisition coefficient) will take values greater than 0 if the breakage is faster than random and smaller than 0 if opposite. Whether these parameters have relations to mineral properties have yet to be verified.

9.9   Simulation of ore textures (Bazin and Ouellet 2009)

Bazin and Ouellet (2009) computer program was developed to simulate mineral liberation when the ore is broken in a comminution process. A three dimensional simulated grain is imported into the matrix of gangue and thereafter it is growing either randomly or in preferential directions. Here texture is defined as description of arrangements and size of the minerals grains in the ore. Grain sizes and association are determined by analysing 2D sections of an unbroken ore and then extending it to three dimensions by applying stereological corrections.

The grain here is a crystal of a mineral that forms a volume in the space. Texture is combined in terms of concentrations of the minerals, grain size and shape, and if analysis that were used to determine these properties are not in 3 dimensions (Lin and Miller (1996), this Thesis) then stereology needs to be used. For common mineral associations, preferential association between minerals has to be taken in the account. The assumption here is that the three dimensional texture is not available and simulation relies on two dimensional textural information.

The parameters needed from simulation are number of minerals, volume concentration of each mineral, average grain volume and their standard deviations, shape factor and the probability of association between minerals, that is set to zero for random growing or not equal to zero if mineral have tendency of neighbouring.

However, the situation where we have mineral grains that are mixture of unaccompanied grains in the matrix and grains touching mineral grains of preferential mineral is not covered in this breakage simulation. This type of association is most likely to happen in the ore.

9.10 Useful mineral properties

"The process mineralogist can use the following properties to aid in mineral identification of minerals :

- *Relief,* to detect minerals, which have the higher resistance to abrasion than the others, for example, garnet, has higher relief than the feldspar in the same sample after that particular sample is polished. The lighter colour of the feldspar is also able to be seen;
- *Shape* , some grain sections retain the shape of the mineral crystal;
- *Cleavage,* where the angle of cleavage for particular mineral is measured;
- *Pleochroism,* where the colour of the mineral changes and that change depends on orientation of grain relative to polarizer
- *Interference,* every mineral has specific interference colour,
- Quartz (in sandstone)has low *birefringence*
- Plagioclase has low (white to grey) *birefringence* and *polysynthetic twinning*
- Calcite and titanite /sphene have extremely high *birefringence*." (Burrows and Louwrens 2007)

9.11 SEM image production

High resolution image have been produced using this method with subsequently detailed and accurate particle images and data output. The first image processing stage is usually particulation which involves removing of epoxy and background noise from the image. It may also remove the undersize particles and particles touching the edge of the frame if correctly set up in a measurement template file. Since we have used the cross section of the whole particle in original size as a polished section, there were no undersize particles. The second stage of processing XBSE image is pre-segmentation. Here grain boundaries are determined based on BSE greyscale   differences. Each of the different grey levels is assigned an X-ray point which helps to determine exact mineral species.

The XBSE measurement generates two files from each measurement, where the first one is raw greyscale image file and the second is the coloured X-ray image file with grains identified from the pre-segmentation. The offline processing stage compares the measured

mineral spectra with known mineral standards to determine the mineral identity for each grain. (Burrows and Gu 2006b; Fandrich et al. 2006; Gu 2003, 2004)

Sample analysis could be carried out using the following techniques:

- BSE (Back Scattered Electron) - The intensity of the BSE signal varies with the average atomic number of the sample. The grey scale images are used to separate particles and identify the boundaries of different mineral phases.
- XBSE – extended BSE
- GXMAP – Grain X-ray Mapping
- SPL – Sparse Phase Liberation is commonly used for PGM (Platinum Group Minerals), Au and Ag characterisation, sulphide liberation in tailings and penalty elements in concentrates.
- Dual Zoom – Schouwstra method
- SXBSE – Latti method
- X-ray modal (XMOD) - this analysis could provide the information about elemental distribution and modal mineralogy but it does not provide any information about grain size, mineral liberation and locking.
- and Rare Phase Search (RPS).

X-ray trigger and BSE trigger can be set in order to reduce the measurement time if there are known distinguishable mineral properties.

9.12 Lead-Zink ore characterisation

The data was generated as part of another published work (Pokrajcic 2010). There was the issue with separation of mineral phases (sphalerite, pyrite and galena), details in Chapter 3. Observing of acquisition process and analysis were incorporated in optimisation process of this Thesis.

A number of particles were selected from heavy media dense separation plant and subjected to Micro CBT analysis. Figure 191 shows the accuracy of measured particle volume, which confirms reduced noise in the images generated.
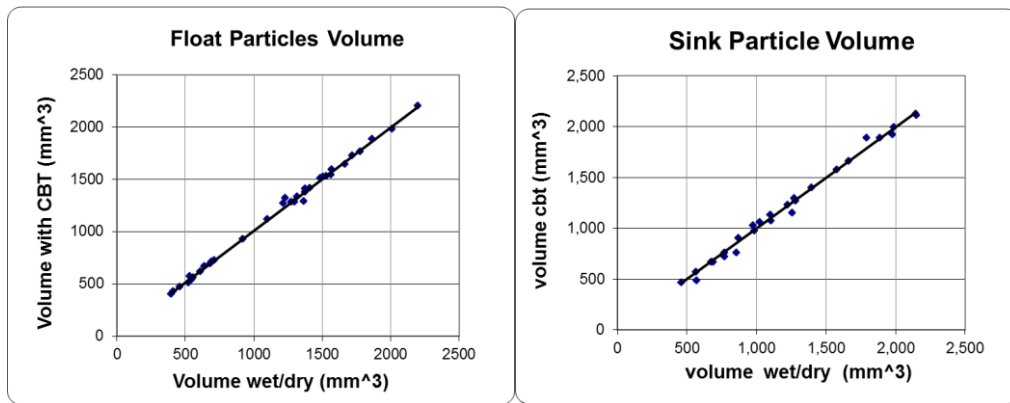
Figure 191: Volume of the particle, float and sink, generated by micro CBT and wet/dry measurement technique

Accuracy and precision

Some of the particles were sent for XRF analysis in order to confirm the accuracy of the data generated. Elemental information was used to back calculate mineral phase distribution and volumetric composition of the particles. Since the accurate definition of different mineral phase was not observed using Micro CBT due to insufficient instrument quality to obtain high quality radiographs to enable better reconstruction (especially of galena phase), the minerals were grouped in high density and low density mineral group. Using the historic data, the summary of Fe, Pb, S, and Zn was compared with the summary of the same elemental information obtained with XRF elemental analysis.

Table 39: Comparative analysis of lead zinc ore using Micro CBT and XRF, sink particle

	XRF	Micro CBT	
Sink Sample	combined assay	calculated assay	difference
Sample 1	14.34	18.37	-4.03
Sample 2	23.54	19.62	3.91
Sample 3	27.04	26.08	0.96
Sample 4	29.06	27.02	2.04
Sample 5	29.44	21.19	8.24
Sample 6	35.12	31.49	3.63
Sample 7	35.44	31.96	3.48
Sample 8	35.76	37.94	-2.18
Sample 9	46.76	48.46	-1.69
average	1.60		
stdev	3.79		
n	9		
t	1.27		
df	8		
confidence limits for 90% confidence		3.94	
		-0.75	

For sink particle (Table 39), statistical analysis of the difference between methods indicated that the difference is not significant. Confidence limits are +3.94 -0.75, hence the difference is at least 0.85% with 90% confidence, which is acceptable difference for this type of analysis. Statistical analysis of the difference between methods in float particle analysis (Table 40) indicated that the difference is also not significant. Confidence limits are +0.78 -0.2, hence the difference is at least 0.09% with 90% confidence. Graphical representation is given in Figure 192.

Table 40: Comparative analysis of lead zinc ore using Micro CBT and XRF, float particle

Float Sample	XRF combined assay	Micro CBT calculated assay	difference
Sample 1	1.04	1.84	-0.80
Sample 2	1.17	0.67	0.50
Sample 3	1.55	0.75	0.80
Sample 4	2.53	1.81	0.72
Sample 5	3.30	3.82	-0.52
Sample 6	4.84	4.32	0.52
Sample 7	5.32	4.49	0.84
average	0.29		
sd	0.67		
n	7		
t	1.16		
df	6		
confidence limits for 90% confidence	0.78		
	-0.20		
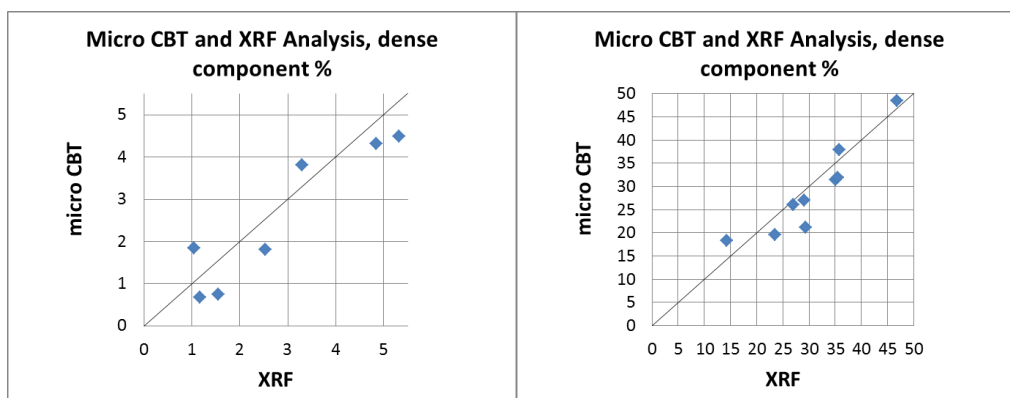
Figure 192: Combined Pb, Fe, Zn and S assay analysis of lead zinc ore using XRF and calculated Micro CBT assay, float particle and sink particle

9.13 Radiograph QAQC check

9.13.1   Radiograph grey scale level cumulative distribution
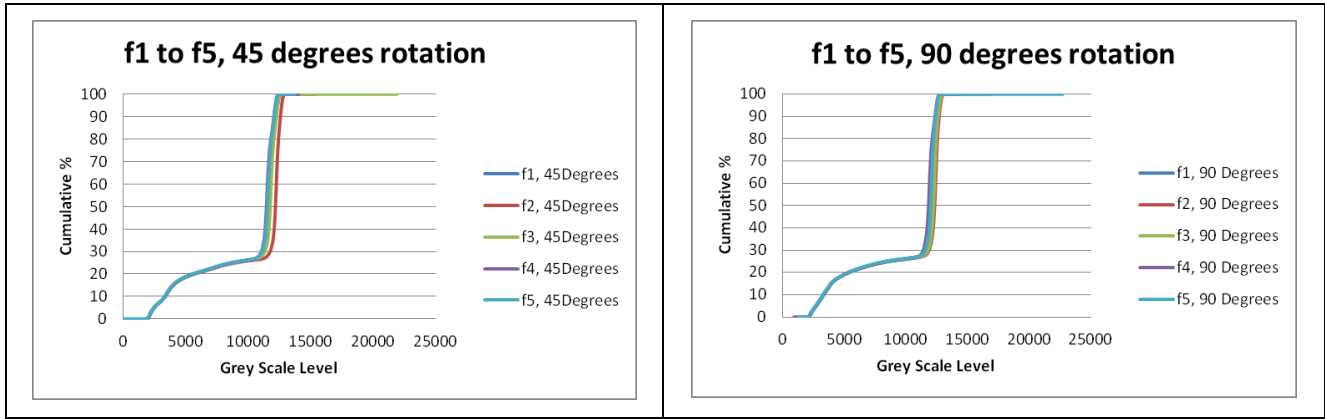
Figure 193: Grey Scale level cumulative distribution showed on radiographs from five acquisitions with equal settings, conducted on the same day, of the HMP float sample and using the SkyScan1072
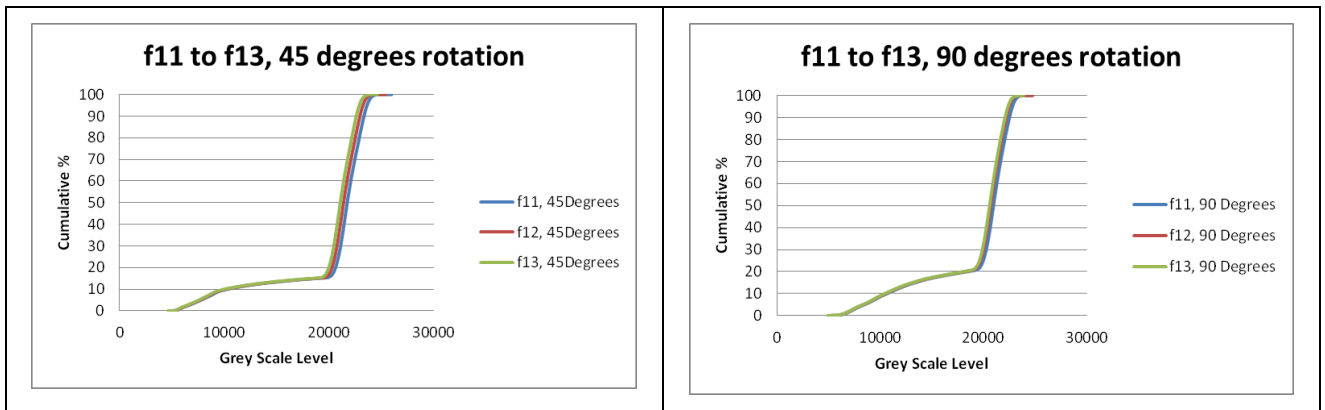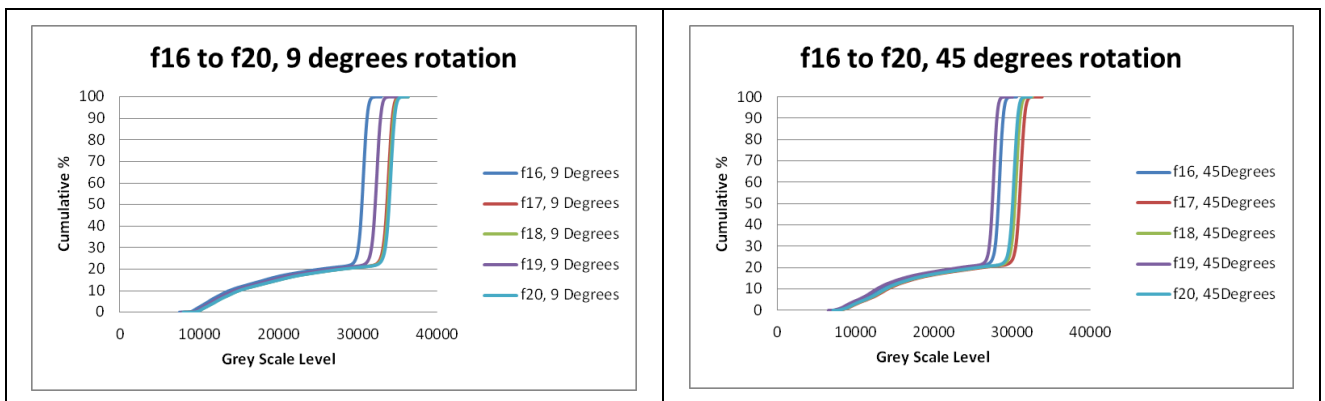

Figure 194: Grey Scale level cumulative distribution showed on radiographs from three acquisitions, conducted on the same day, of the HMP float sample and using the SkyScan1172
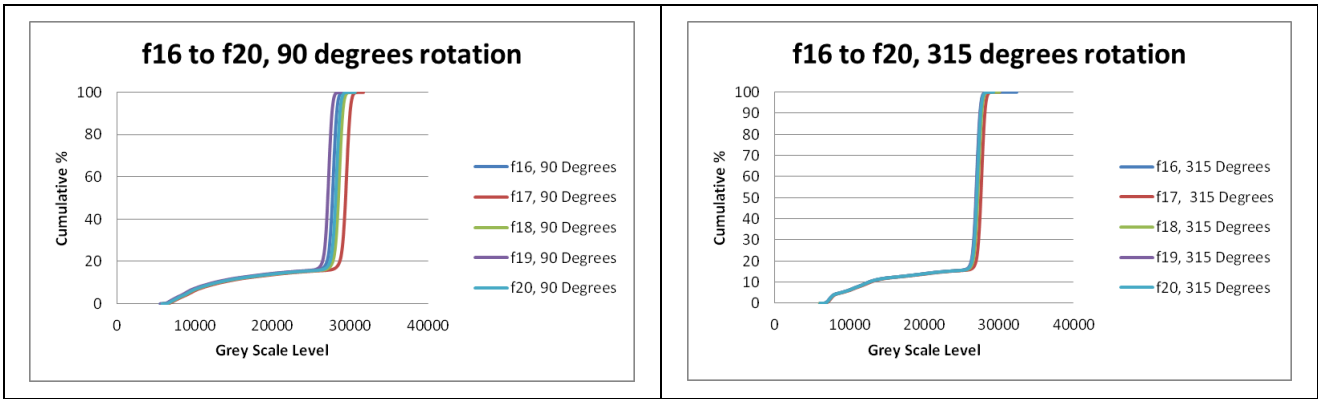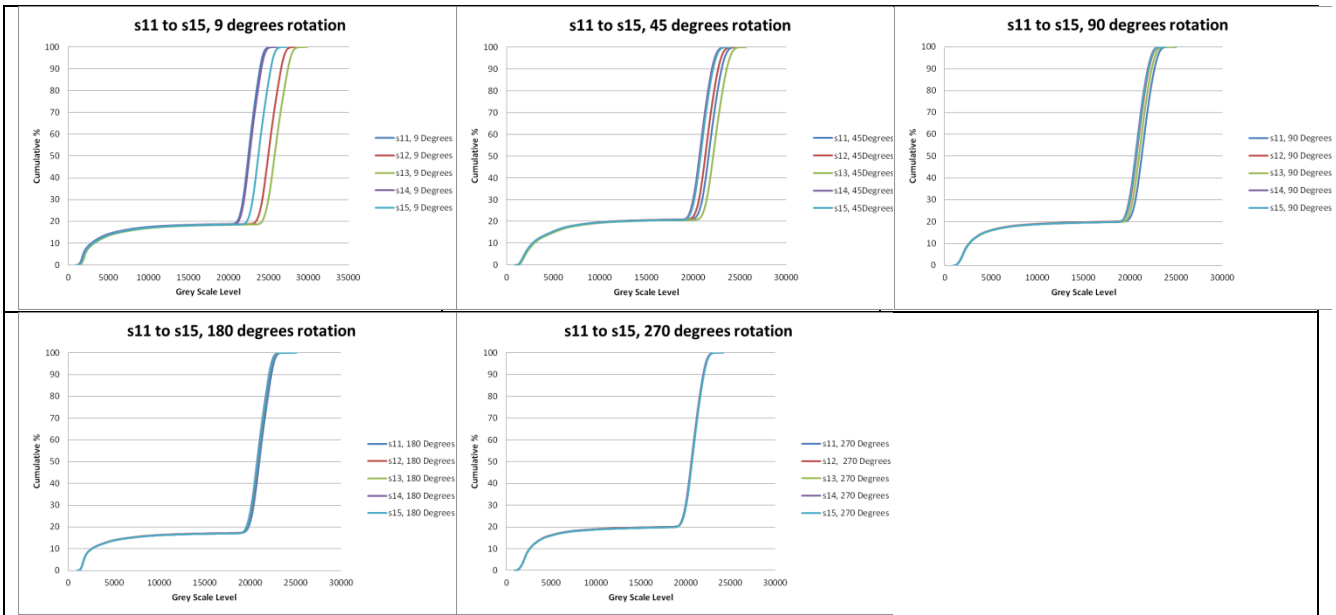
Figure 195: Grey Scale level cumulative distribution showed on radiographs from five acquisitions with equal settings, conducted on the same day, of the HMP float sample and using the SkyScan1172

Figure 196: Grey Scale level cumulative distribution showed on radiographs from five acquisitions with equal settings, conducted on the same day, of the HMP sink sample and using the SkyScan1172
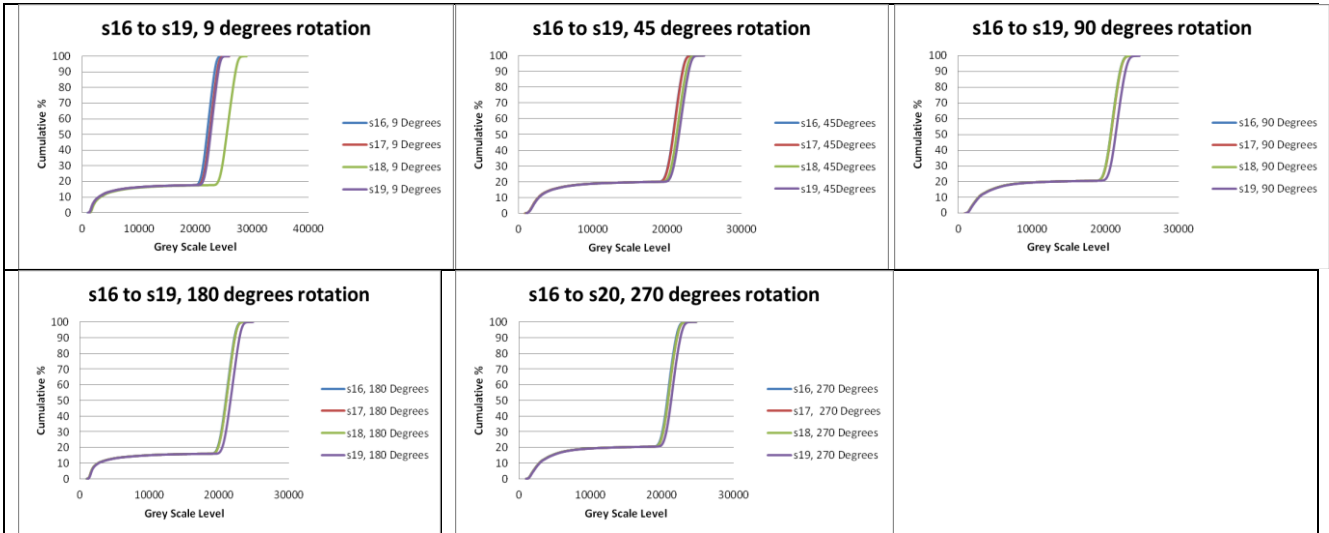
378

Figure 197: Grey Scale level cumulative distribution showed on radiographs from four acquisitions with equal settings, conducted on the same day, of the HMP sink sample and using the SkyScan1172

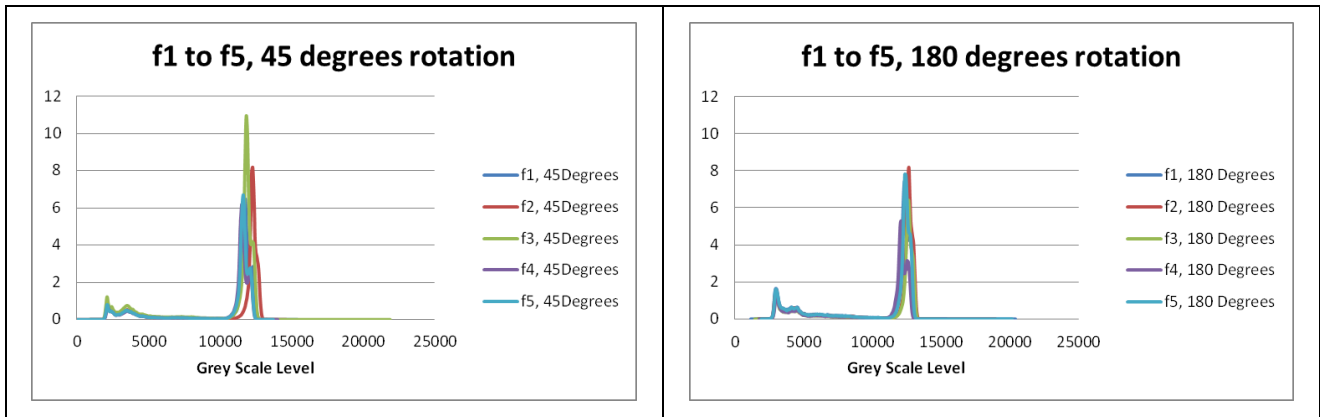379

9.13.2   Radiographs normalised distribution

Figure 198: Grey Scale level normalised distribution showed on radiographs from five acquisitions with equal settings, of the HMP float sample and using the SkyScan1172
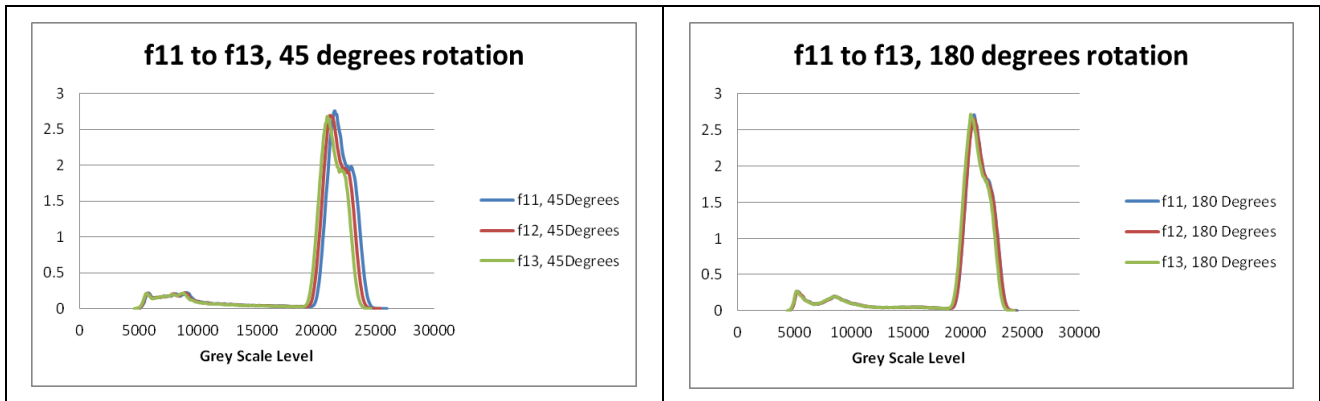

Figure 199: Grey Scale level normalised distribution showed on radiographs from three acquisitions with equal settings, of the HMP float sample and using the SkyScan1172
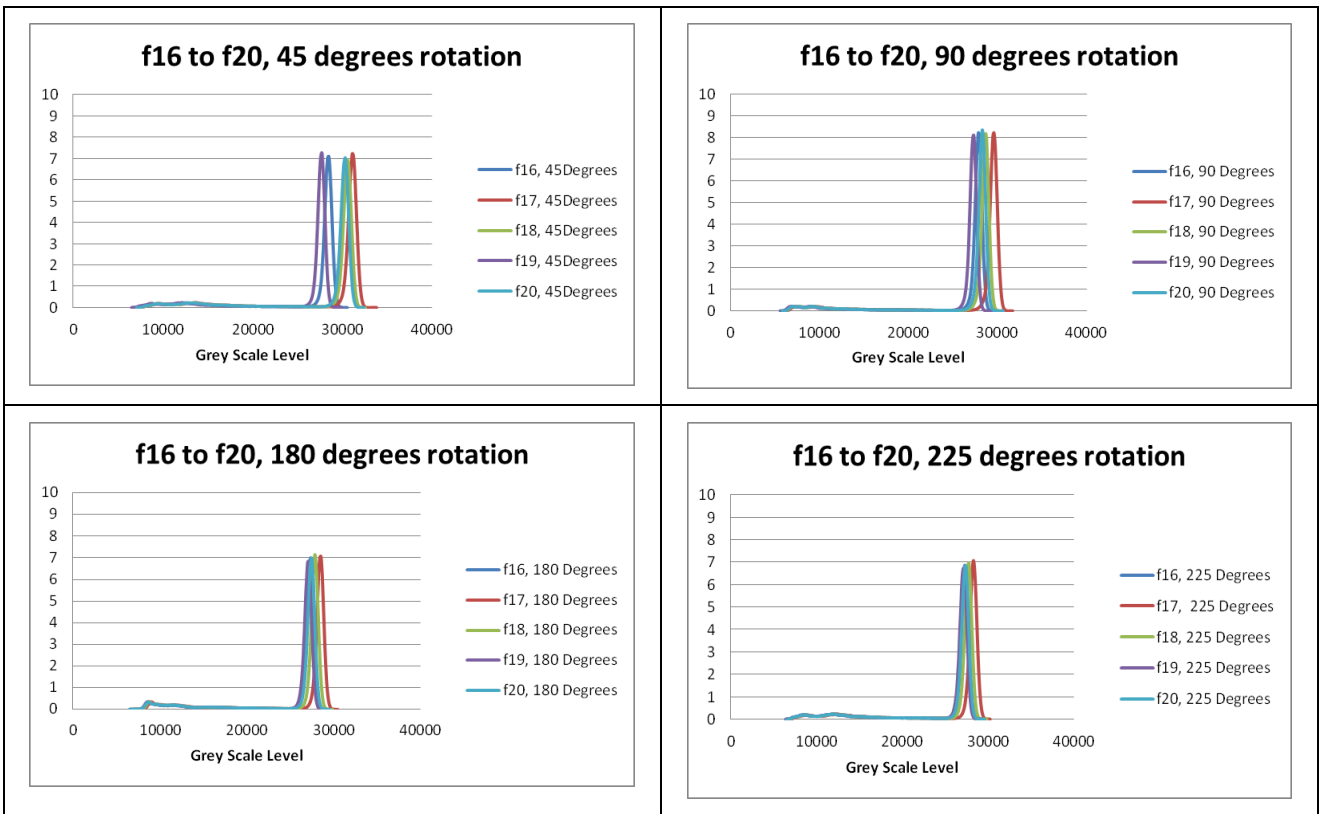
Figure 200: Grey Scale level normalised distribution showed on radiographs from five acquisitions with equal settings, of the HMP float sample and using the SkyScan1172

Figure 201: Grey Scale level normalised distribution showed on radiographs from five acquisitions with equal settings, of the HMP sink sample and using the SkyScan1172
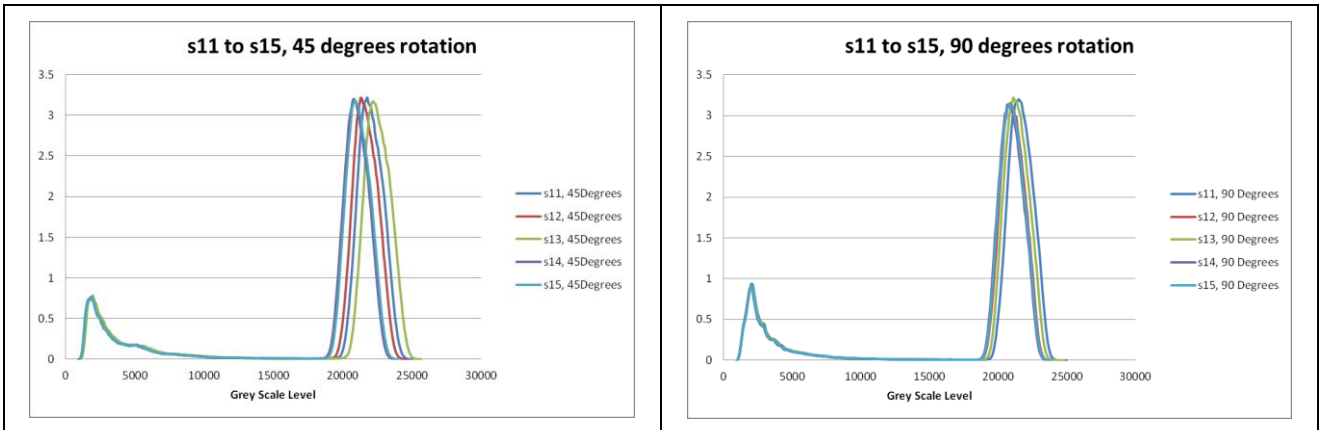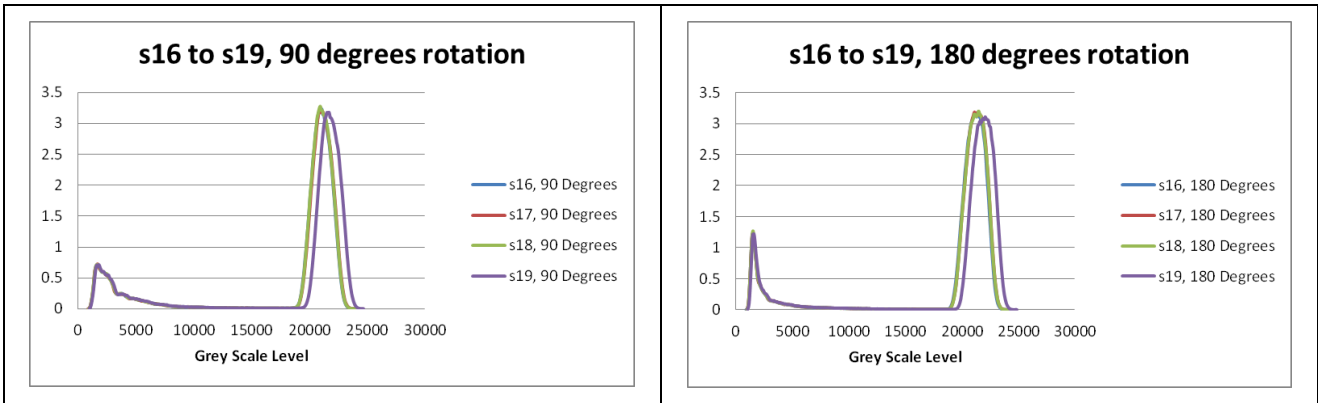
Figure 202: Grey Scale level normalised distribution showed on radiographs from five acquisitions with equal settings, of the HMP sink sample and using the SkyScan1172
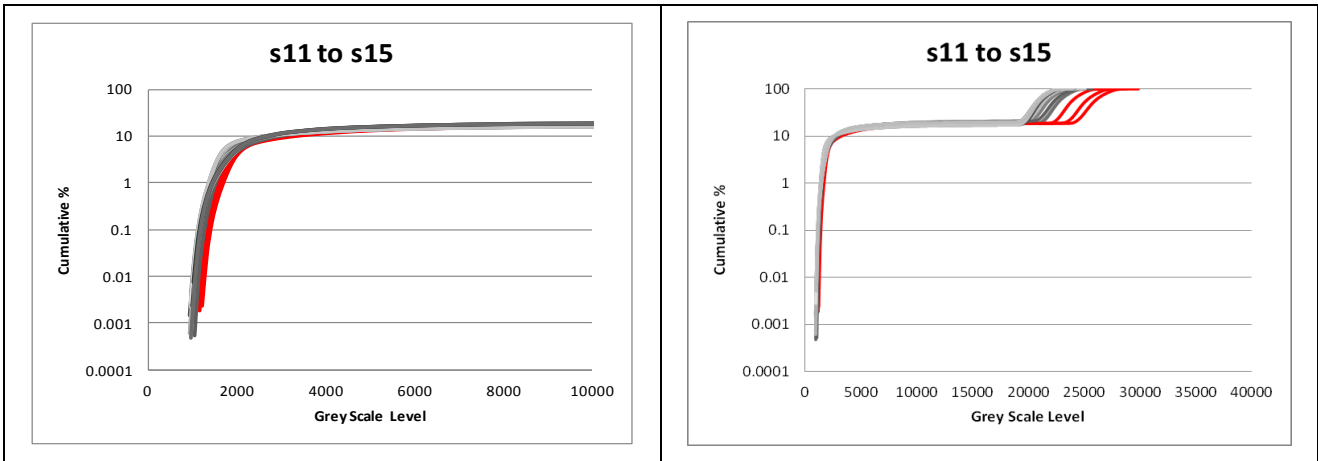

Figure 203: Summary of cumulative grey scale distribution of the radiographs, mineral section of grey scale, sink sample, SkyScan1172, the data in red from 9 degrees rotation

Float Sample SkyScan1072, test2

Figure 204: Radiograph grey scale level, normalised distribution, cumulative distribution and cumulative log distribution, 8 and 16 bit image, test2

383

Float Sample SkyScan1172, test16

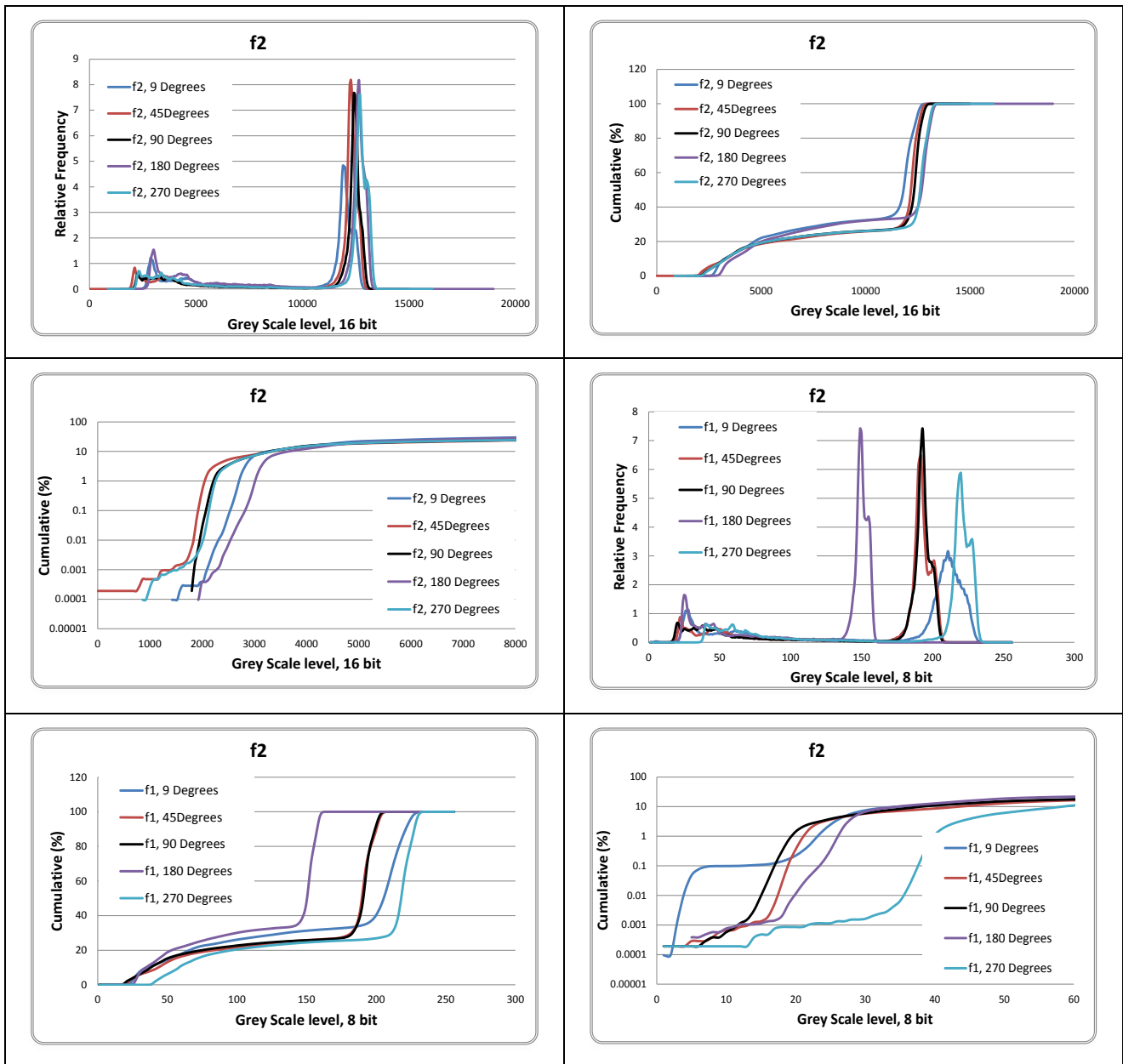**Figure 205: Radiograph grey scale level, normalised distribution, cumulative distribution, cumulative log distribution, 16 and 8 bit image, test16**

Sink Sample SkyScan1172, test19

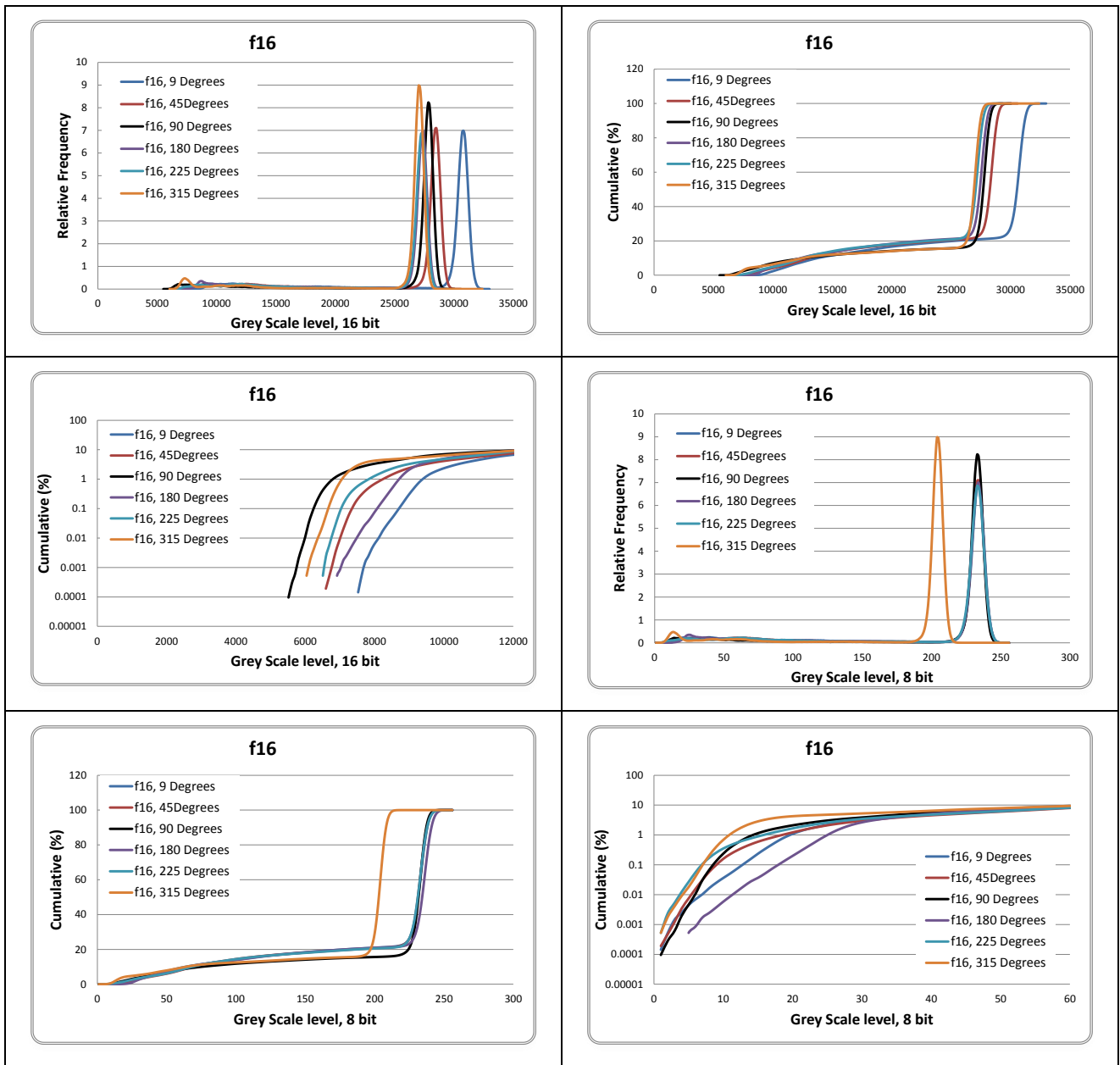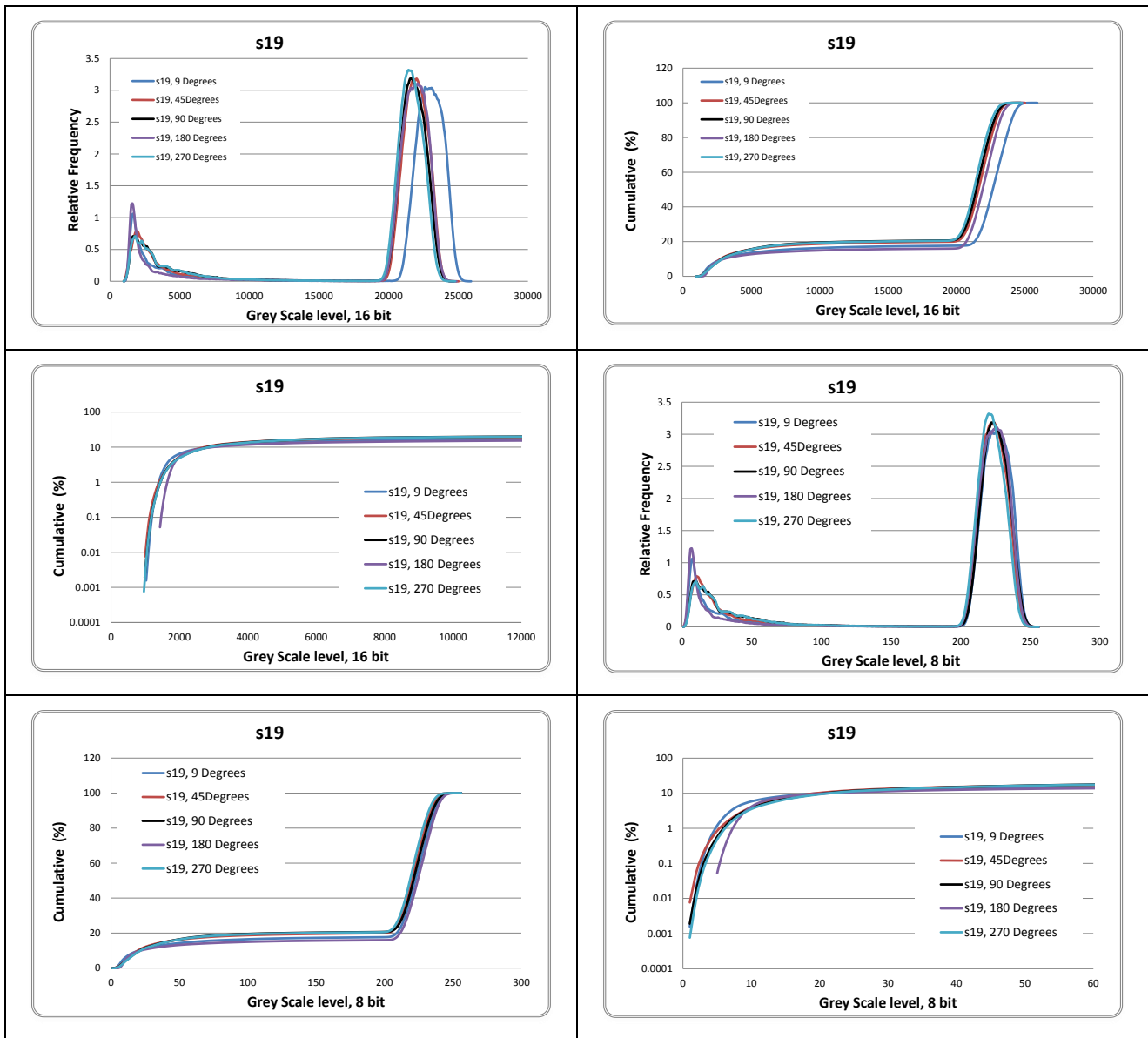**Figure 206: Radiograph grey scale level, normalised distribution, cumulative distribution, cumulative log distribution, 16 and 8 bit image, test19**

9.14 Grain size distribution, float sample
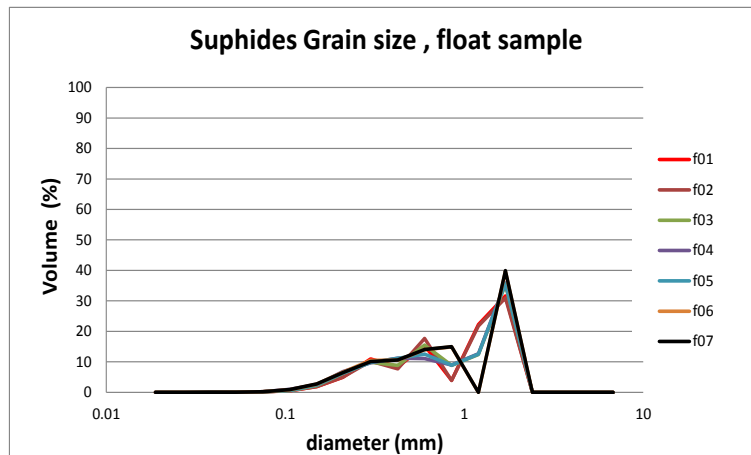
Figure 207: Sulphide grain size volume percentage, float sample scanned in SkyScan1072
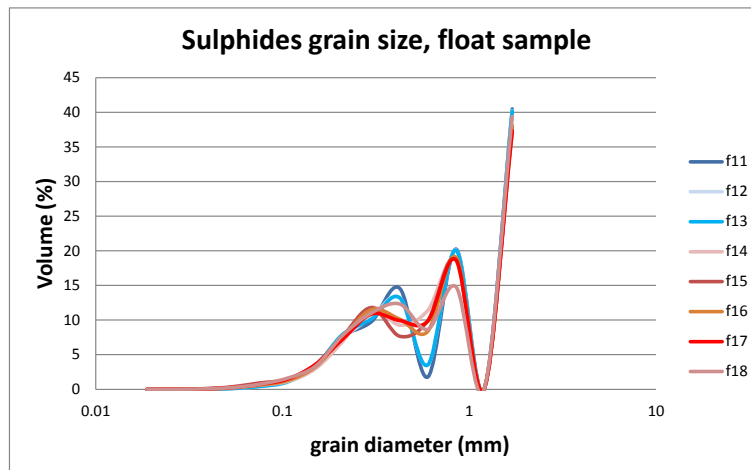
Figure 208: Sulphide grain size volume percentage, float sample scanned in SkyScan1172

9.15 Grain size distribution, sink sample

Figure 209: Galena grain size volume percentage, sink sample scanned in SkyScan1172

Figure 210: Sulphide grain size volume percentage, sink sample scanned in SkyScan1172

9.16 The example of grain size table, exported from eCognition

Table 41: Magnetite (valuable phase) grain size three dimensional results table

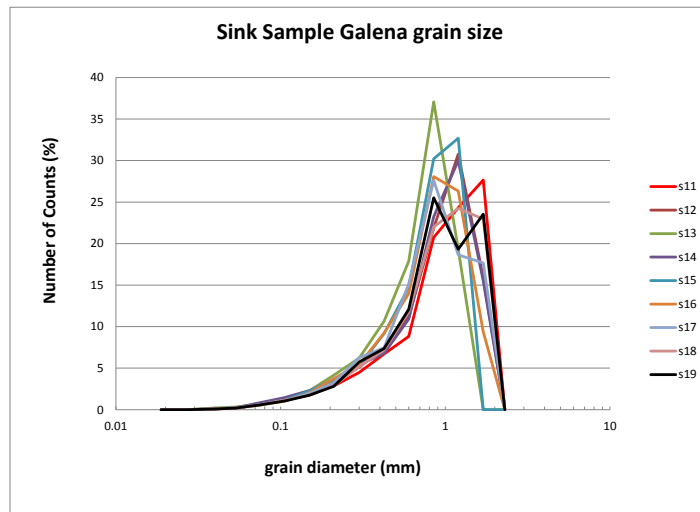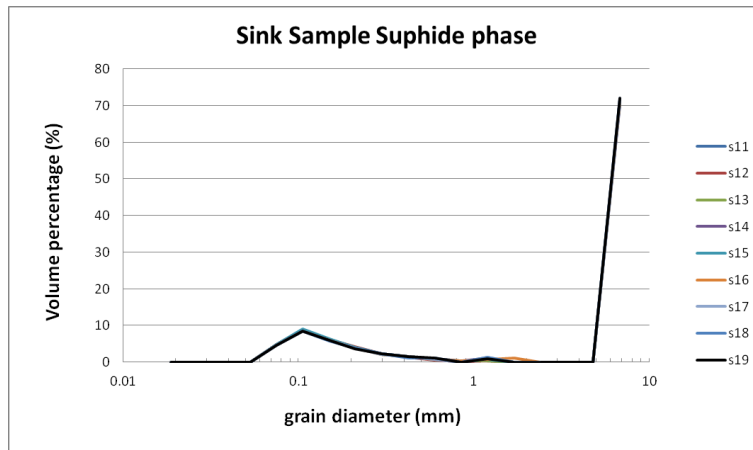| inner_x	inner_y	level_name	class_name	Area (µm²)	Length (µm)	Thickness (µm)	Width (µm)	Volume (mm³)
88	2897	New Level (map_copy)	Magnetite	2228339.92	615.16	252.54	354.11	0.02880444
92	9475	New Level (map_copy)	Magnetite	8521.70	116.73	35.29	51.06	0.00011015
67	5193	New Level (map_copy)	Magnetite	6015.31	129.76	25.50	44.87	0.00007776
89	9563	New Level (map_copy)	Magnetite	5346.95	84.31	27.27	57.41	0.00006912
71	6396	New Level (map_copy)	Magnetite	5346.95	72.63	26.95	67.43	0.00006912
74	3997	New Level (map_copy)	Magnetite	5346.95	78.32	38.06	44.29	0.00006912
66	4296	New Level (map_copy)	Magnetite	5179.85	141.50	22.22	40.66	0.00006696
95	3696	New Level (map_copy)	Magnetite	4344.39	74.70	22.77	63.05	0.00005616
87	2397	New Level (map_copy)	Magnetite	4344.39	65.63	28.13	58.09	0.00005616
75	7492	New Level (map_copy)	Magnetite	3676.03	73.36	27.00	45.82	0.00004752
87	3590	New Level (map_copy)	Magnetite	3341.84	100.77	23.24	35.23	0.00004320
79	8467	New Level (map_copy)	Magnetite	3174.75	66.54	26.24	44.88	0.00004104
91	4497	New Level (map_copy)	Magnetite	3174.75	62.38	29.07	43.22	0.00004104
98	4789	New Level (map_copy)	Magnetite	2673.47	87.62	17.95	41.96	0.00003456
88	4185	New Level (map_copy)	Magnetite	2673.47	76.12	26.52	32.70	0.00003456
95	2399	New Level (map_copy)	Magnetite	2673.47	81.42	18.84	43.02	0.00003456
73	8558	New Level (map_copy)	Magnetite	2506.38	54.12	24.20	47.25	0.00003240
71	9862	New Level (map_copy)	Magnetite	2339.29	109.73	13.95	37.72	0.00003024
86	1599	New Level (map_copy)	Magnetite	2339.29	73.57	22.15	35.44	0.00003024

Table 42: Gangue phase grain size three dimensional results table

inner_x	inner_y	level_name	class_name	Area (µm²)	Length (µm)	Thickness (µm)	Width (µm)	Volume (mm³)
64	594	New Level (map_copy)	gangue	167.09	12.93	12.93	12.93	2.16E-06
58	96	New Level (map_copy)	gangue	167.09	12.93	12.93	12.93	2.16E-06
72	94	New Level (map_copy)	gangue	1002.55	52.25	16.95	27.95	1.30E-05
88	97	New Level (map_copy)	gangue	167.09	12.93	12.93	12.93	2.16E-06
96	70	New Level (map_copy)	gangue	854007.60	477.49	143.56	307.56	0.011039252

9.17 Attenuation profile lines through minerals

pyrite			
min	max	sd	average
25	31	1.5	28.7
33	38	1.8	34.8
36	41	1.7	38.1
38	43	1.6	40.9
40	48	2.1	43.5
40	51	3.2	45.0
39	50	3.3	45.4
39	50	2.9	45.8

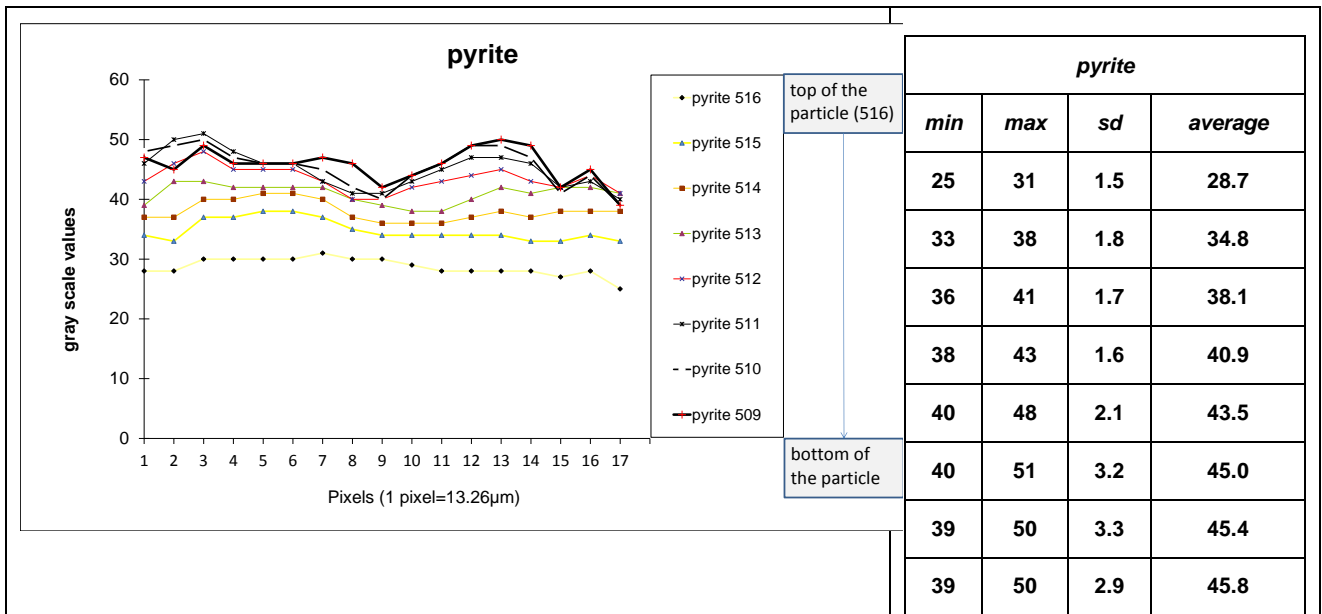**Figure 211: Attenuation profile line across pyrite grain in multiple consecutive 2D sections, grey scale values, pyrite**

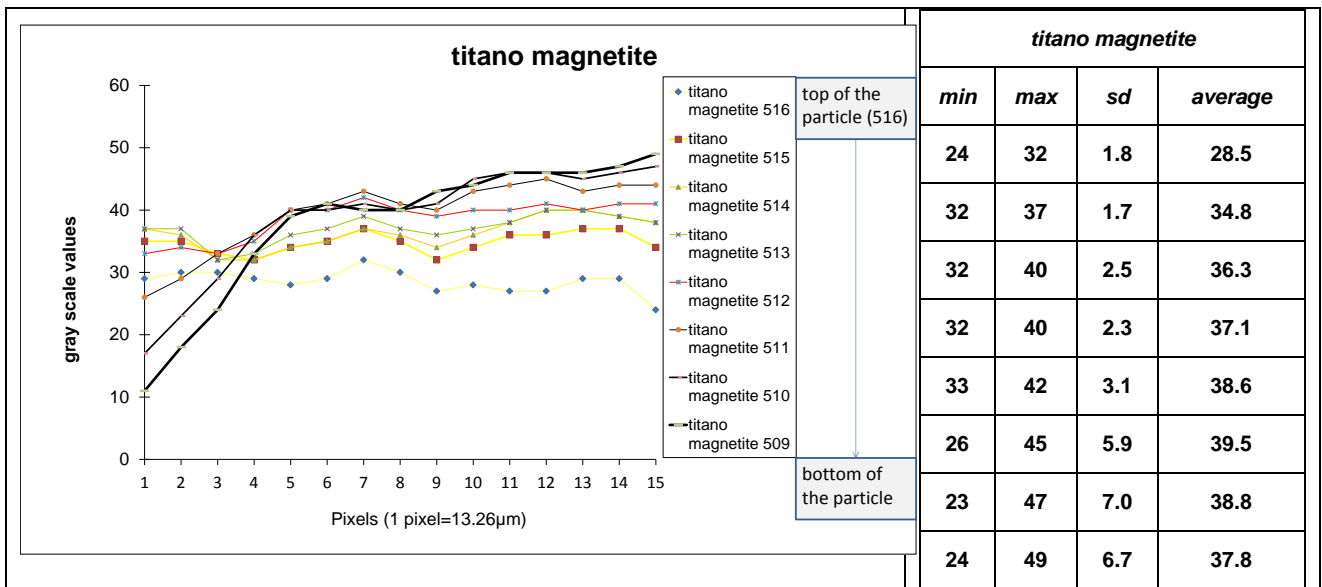| titano magnetite			
min	max	sd	average
24	32	1.8	28.5
32	37	1.7	34.8
32	40	2.5	36.3
32	40	2.3	37.1
33	42	3.1	38.6
26	45	5.9	39.5
23	47	7.0	38.8
24	49	6.7	37.8

Figure 212: Attenuation profile line across titano magnetite grain in multiple consecutive 2D sections, greyscale values, titano magnetite

389

9.18 Threshold definition in CTAn

The noise is visible and cannot be removed by analyses. The threshold value definition between different mineral phases has to be defined by the operator; the histogram is not providing the details or indication.
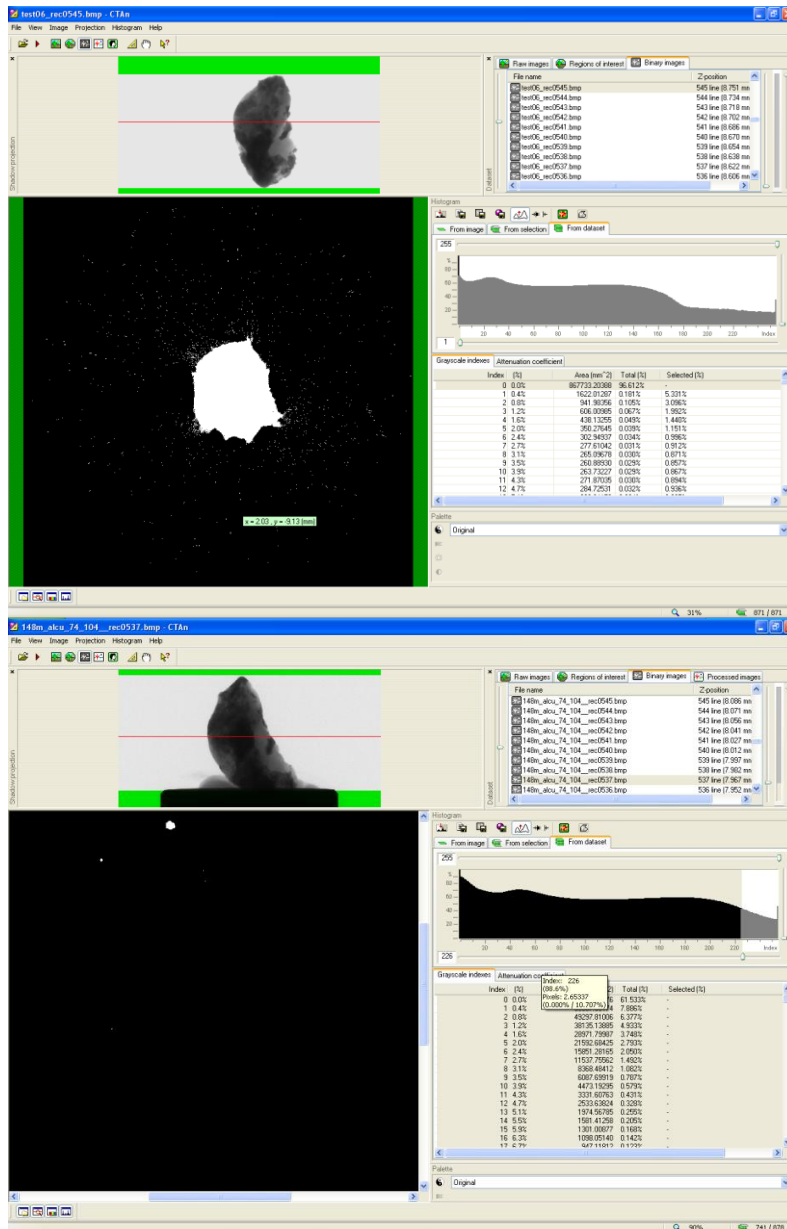

Figure 218: CTAn histogram of the profile line/cross section of the particle, threshold set up for the selected phase volume calculation

9.19 eCognition classification rule set

Classes:
   background
   gangue
   magnetite
   iron phase
set initial threshold for background and gangue
Customized Features:
   Area (μm2): ([p_pixelsize])^2*[Number of pixels]
Process: Main:
Copy map
      The images are copied on a separate working map
      The threshold value used to separate the background from the working particle pixels is operator defined threshold
background
        on smaller magnification create map
Merge background
Fine classification
      For fine background area inside the particle, it is classified into gangue
      The noise in background is classified as the background (area depends on the particle size)
Auto threshold of unclassified=auto threshold (for background definition)

Unclassified quadtree 5
Unclassified with brightness <auto threshold background
Unclassified with brightness >80 into high iron
Unclassified with brightness <30 into gangue
      The initial brightness set here is approximate
shape optimization (if needed)
        on smaller map
          measure rock and grow background into dark periphery
            automatic threshold: gangue at New Level: p_thresh=auto threshold on Layer 1
            update variable: p_thresh *= 0.4
            pixel-based object resizing: background at New Level: grow(3d)
              loop if needed
use neighbourhood function if needed for gangue and magnetite
merge high iron, gangue, unclassified
auto threshold on high iron=P_threshold_magnetite
auto threshold on unclassified=unclass_thr_3
Unclassified quadtree 4
High iron quadtree 4
Unclassified over initial set high threshold into high iron
Unclassified into magnetite based on threshold function (appendix 3)
Unclassified into gangue
High Iron into magnetite
Grow gangue into gangue with brightness < unclass_thr3
merge gangue
merge unclassified
merge magnetite
Connect mineral phases in three dimensions
export statistics (threshold values, object length, width, height and volume)

9.20 Mineral phase membership function used in eCognition

The membership function was used to identify the border between gangue and iron phase. The threshold values were assigned automatically by eCognition rule set.
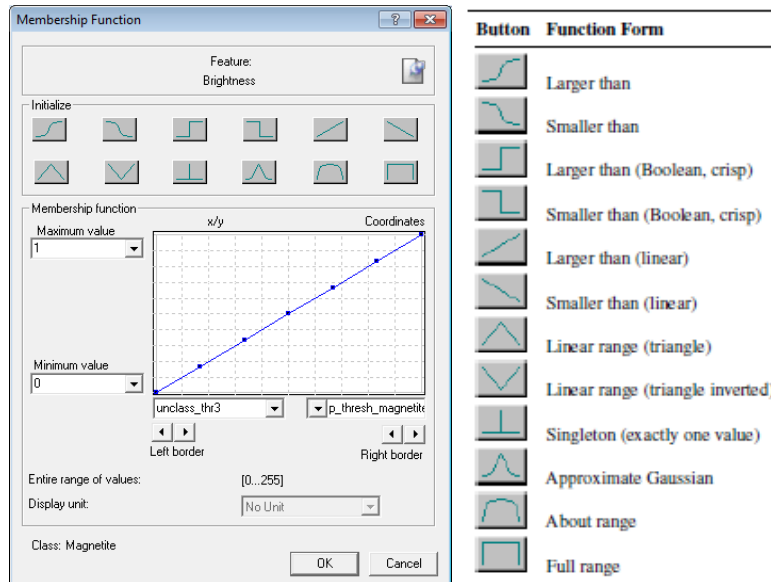

Figure 214: Used magnetite membership function (left), available types of function (right)

"Using Membership Functions for Classification:

Membership functions allow you to define the relationship between feature values and the degree of membership to a class using fuzzy logic. Double-clicking on a class in the Class Hierarchy window launches the Class Description dialog box. To open the Membership Function dialog, right-click on an expression the default expression in an empty box is 'and (min)' to insert a new one, select Insert New Expression. You can edit an existing one by right-clicking and selecting Edit Expression.

• The selected feature is displayed at the top of the box, alongside an icon that allows you to insert a comment

• The Initialize area contains predefined functions;

It is possible to drag points on the graph to edit the curve, although this is usually not necessary we recommend you use membership functions that are as broad as possible

• Maximum Value and Minimum Value allow you to set the upper and lower limits of the membership function. (It is also possible to use variables as limits.)

• Left Border and Right Border values allow you to set the upper and lower limits of a feature value. In this example, the fuzzy value is between 100 and 1,000, so anything below 100 has a membership value of zero and anything above 1,000 has a membership value of one

• Entire Range of Values displays the possible value range for the selected feature

• For certain features you can edit the Display Unit

• The name of the class you are currently editing is displayed at the bottom of the dialog box.

• To display the comparable graphical output, go to the View Settings window and select Mode > Classification Membership." (Trimble 2008)

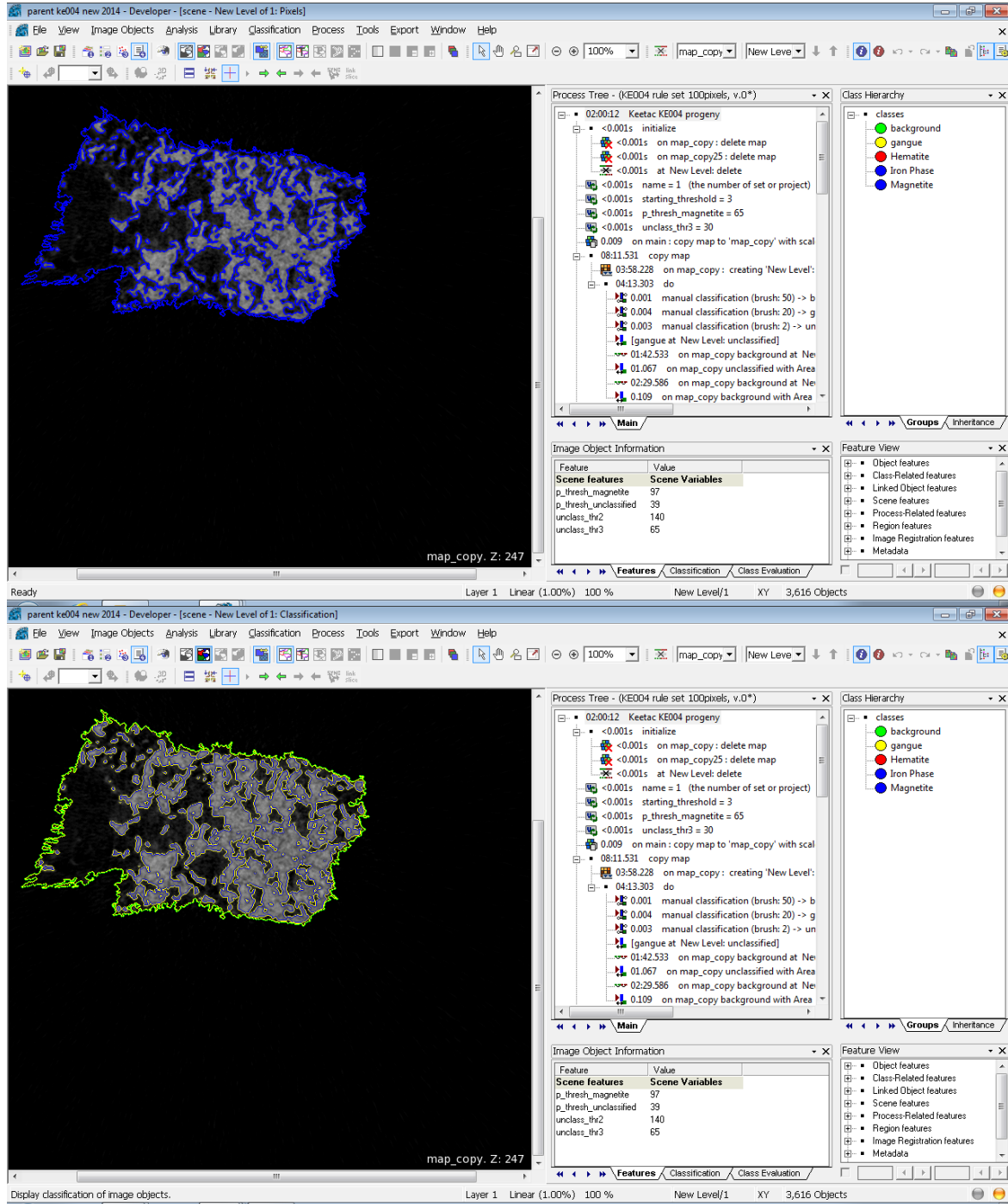# 9.21 Parent particle classification view in eCognition

Figure 215: KE004 parent particle classification view in eCognition8

9.22 Particle connection in 3D, section from Trimble eCognition Reference book

Connected 2D Convert all image objects in the domain to connected 2D objects. The conversion is performed only for image objects that are not of the type connected 2D.

Connected 3D Convert all image objects in the image object domain to connected 3D image objects. Internally, all image objects in the image object domain are converted to connected 2D objects. Connected 3D objects are then created based on the overlaps of connected 2D image objects over the slices. Connected 3D image objects are continuous with respect to slices. They may have several disconnected parts within a single slice.A special situation occurs if you have multiple image object levels and some parts of a connected 3D image object belong to different super objects. In that case, the super objects are merged automatically. If merging is not possible, then single disconnected super objects are generated.

Disconnected Convert all image objects in the image object domain to disconnected image objects. The algorithm tries to create a single image object per class. If some 3D image objects to be merged belong to different super objects, the conversion works according to the Fusion of Super objects settings; see below.
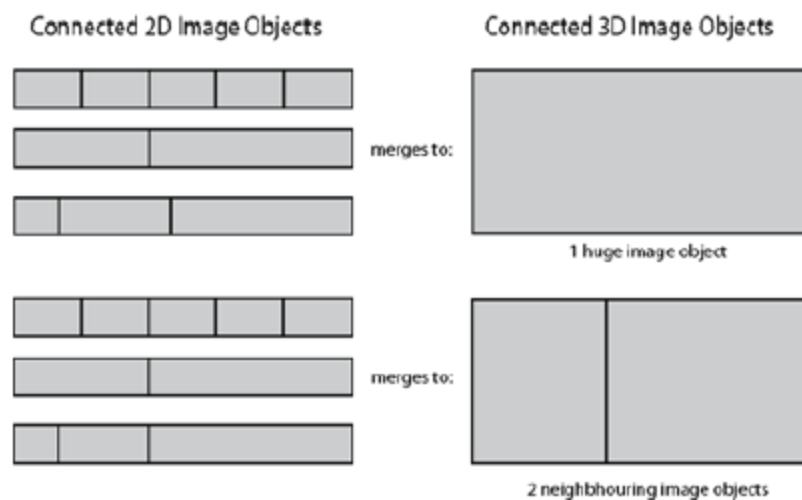

Figure 216: Merging scheme of overlapping image objects between slices (Trimble 2008)

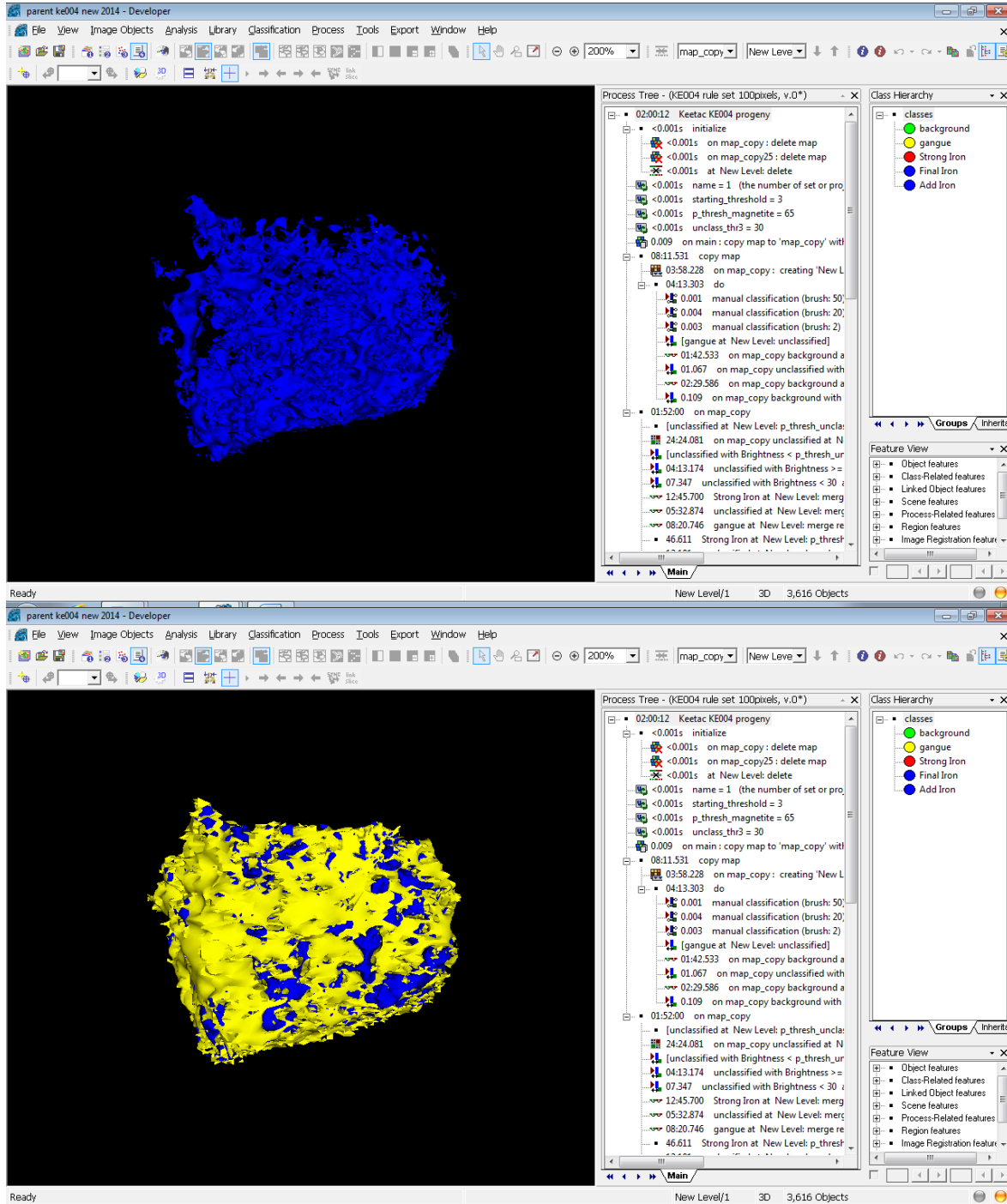# 9.23 Parent particle classification in three dimensions, view in eCognition

Figure 217: KE004 parent particle three-dimensional view in eCognition8

9.24 Grain frequency

Table 43: Measured and predicted grain size before and after breakage, frequency and volume percentage

Size (μm)	Frequency				Volume percentage			
	Predicted cube size		parent	Measured progeny	Predicted cube size		parent	Measured progeny
	646 (μm)	1292 (μm)			646 (μm)	1292 (μm)		
19	1553	952	226	864	0.09%	0.05%	0.01%	0.04%
26	574	346	97	622	0.09%	0.05%	0.01%	0.07%
37	652	398	107	489	0.29%	0.17%	0.05%	0.15%
52	633	360	117	498	0.79%	0.42%	0.14%	0.43%
74	594	314	96	689	2.14%	1.06%	0.34%	1.73%
105	414	245	72	714	4.26%	2.35%	0.72%	5.11%
148	280	147	48	492	8.07%	3.96%	1.35%	9.86%
210	186	77	27	264	15.31%	5.92%	2.17%	15.12%
300	131	48	6	121	31.43%	10.76%	1.41%	20.21%
425	55	19	2	39	37.52%	12.11%	1.33%	18.52%
600	0	21	0	13	0.00%	37.66%	0.00%	17.37%
850	0	5	0	3	0.00%	25.49%	0.00%	11.39%
1180	0	0	0	0	0.00%	0.00%	0.00%	0.00%
1700	0	0	0	0	0.00%	0.00%	0.00%	0.00%
2200	0	0	1	0	0.00%	0.00%	92.46%	0.00%

9.25 Liberation measurement in one, two and three dimension, comparison results
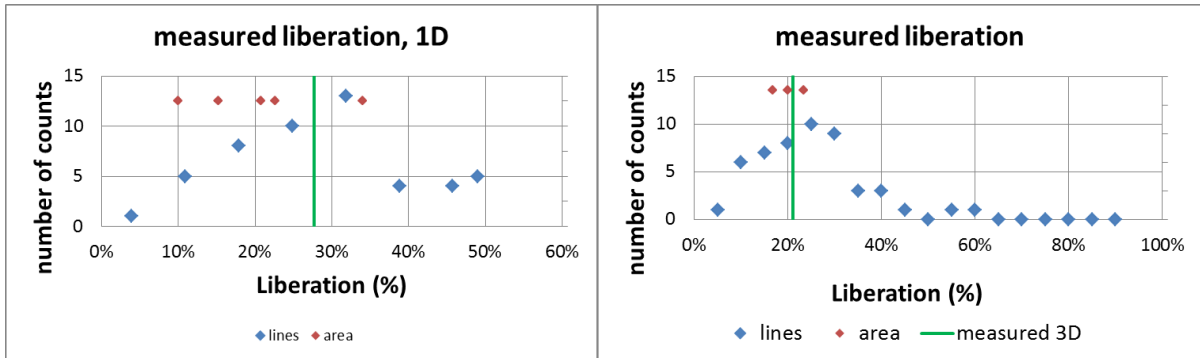

Figure 213: Number of counts of liberation range in line liberation and area liberation measurement (calculated to volume %) and three dimensional volumetric measurement, KE001 and KE003

Table 44: Liberation information in one, two and three dimensions, particle KE001

	Particle three dimensional volumetric liberation 27.7%										
	Volume liberation per area	**Line Liberation per profile line/per area**									
Area 1	15.3	26.7	13.1	20.7	21.3	10.8	20.4	17.1	13.7	24.7	24.7
Area 2	20.9	19.2	37.6	29.3	27.6	22.0	29.8	24.7	31.0	28.8	25.9
Area 3	22.7	46.5	27.7	49.3	37.8	30.8	33.7	28.1	30.1	25.4	40.3
Area 4	34.1	35.6	49.3	15.1	41.2	49.9	44.7	28.0	52.7	21.9	42.2
Area 5	10.1	4.9	11.3	9.9	14.9	13.0	3.9	24.5	10.0	15.5	8.0

Table 45: Liberation information in one, two and three dimensions, particle KE003

	Particle three dimensional volumetric liberation 21.31 %										
	Volume liberation per area	**Line Liberation per profile line/per area**									
Area 1	28.1	35.3	57.6	53.8	39.9	22.2	25.6	22.7	35.2	20.3	19.3
Area 2	20.2	9.5	14.5	21.9	26.5	20.7	14.5	20.8	21.0	32.3	18.9
Area 3	16.7	17.6	19.9	25.7	9.9	14.3	9.4	7.8	6.9	11.6	10.3
Area 4	20.0	13.3	31.5	11.9	24.6	17.9	43.0	29.6	28.7	24.1	7.1
Area 5	23.4	16.8	20.6	27.3	27.3	0.0	34.8	26.6	27.3	16.7	18.9

Table 46: Liberation information in one, two and three dimensions, particle KE004

	Volume liberation per area	Line Liberation per profile line/per area								
	Particle three dimensional volumetric liberation 40.02%									
Area 1	36.8	46.6	16.2	50.2	43.1	54.7	66.1	46.9	46.4	47.4	40.1
Area 2	34.1	54.5	30.7	19.5	63.1	30.0	40.1	47.5	71.9	43.1	38.8
Area 3	37.6	81.9	65.8	55.6	56.5	50.9	34.0	34.8	45.7	35.8	38.3
Area 4	45.7	35.2	48.4	5.3	56.0	52.9	42.7	71.9	80.5	47.1	64.6
Area 5	57.0	74.8	93.4	82.9	46.0	78.4	78.4	59.4	68.8	78.6	73.6

9.26 Liberation data, KE003
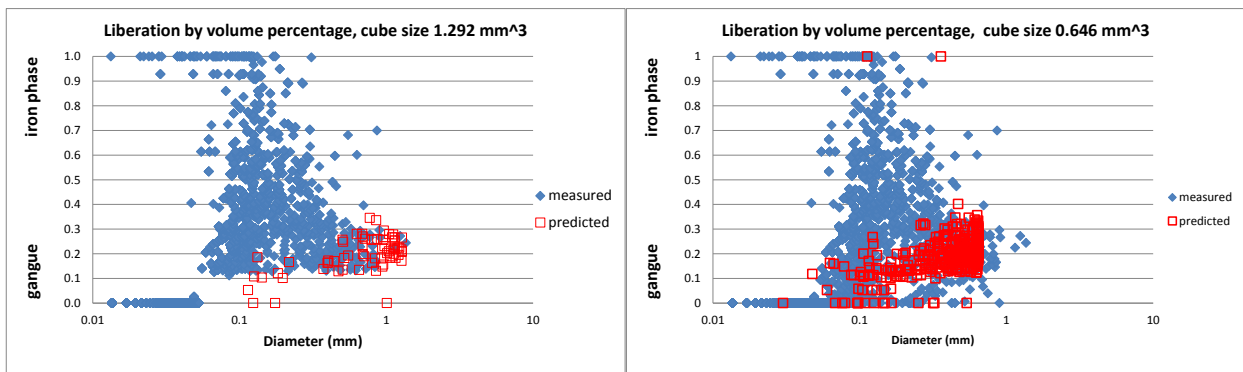
Figure 219: Measured progeny and simulated breakage of parent particle with 1292 and 646µm^3 cube size, particle KE003
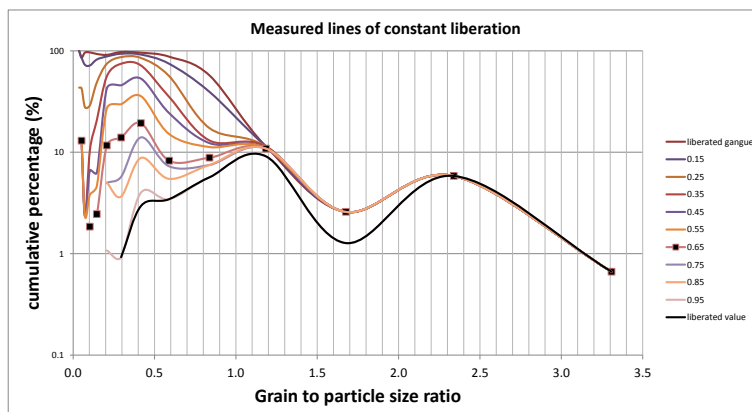

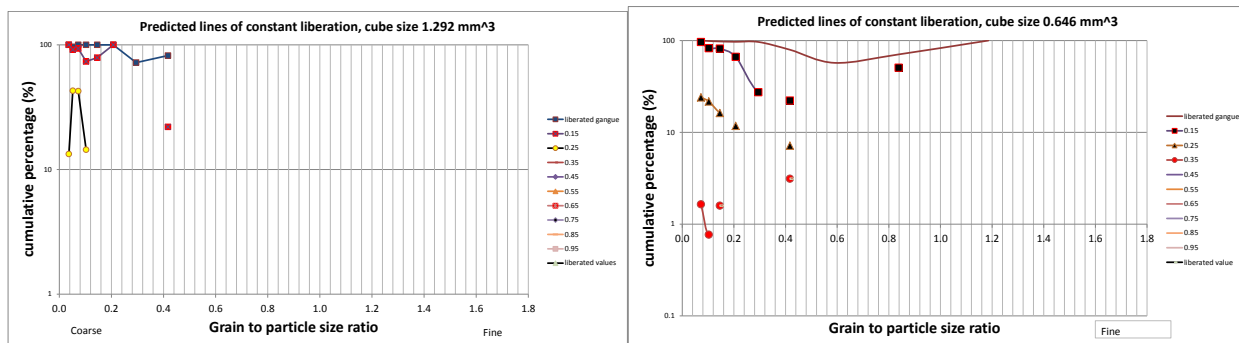**Figure 220: Measured lines of constant liberation, particle KE003**

Figure 221: Predicted lines of constant liberation, KE003 particle, using 100 pixels^3 and 50 pixels^3 simulated cubes
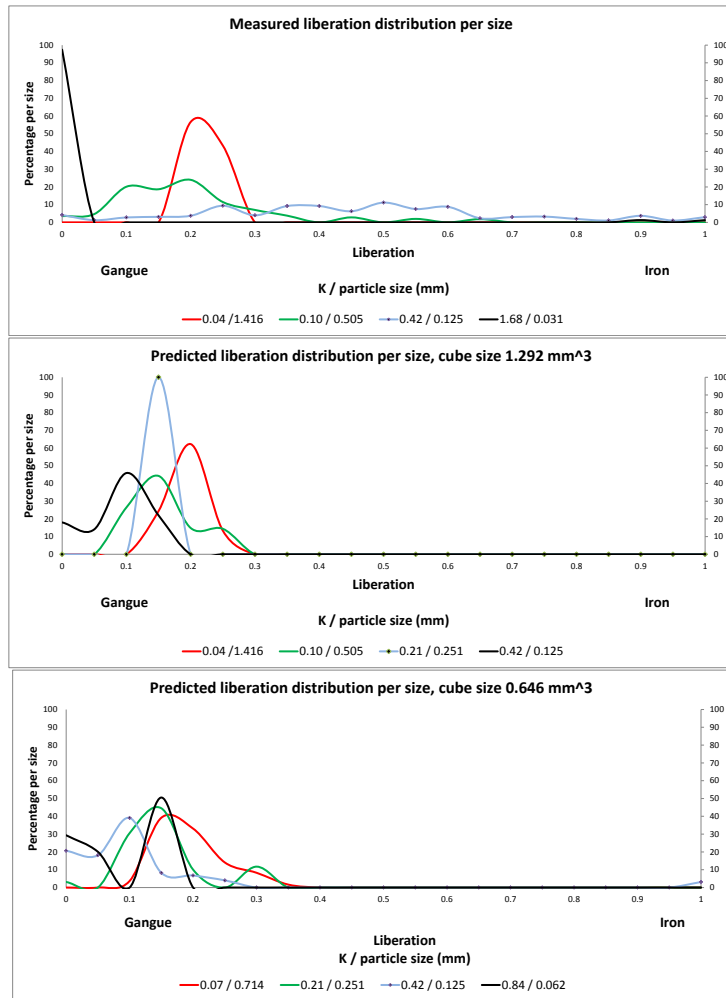
Figure 222: Family of lines of constant liberation, measured and predicted, KE003
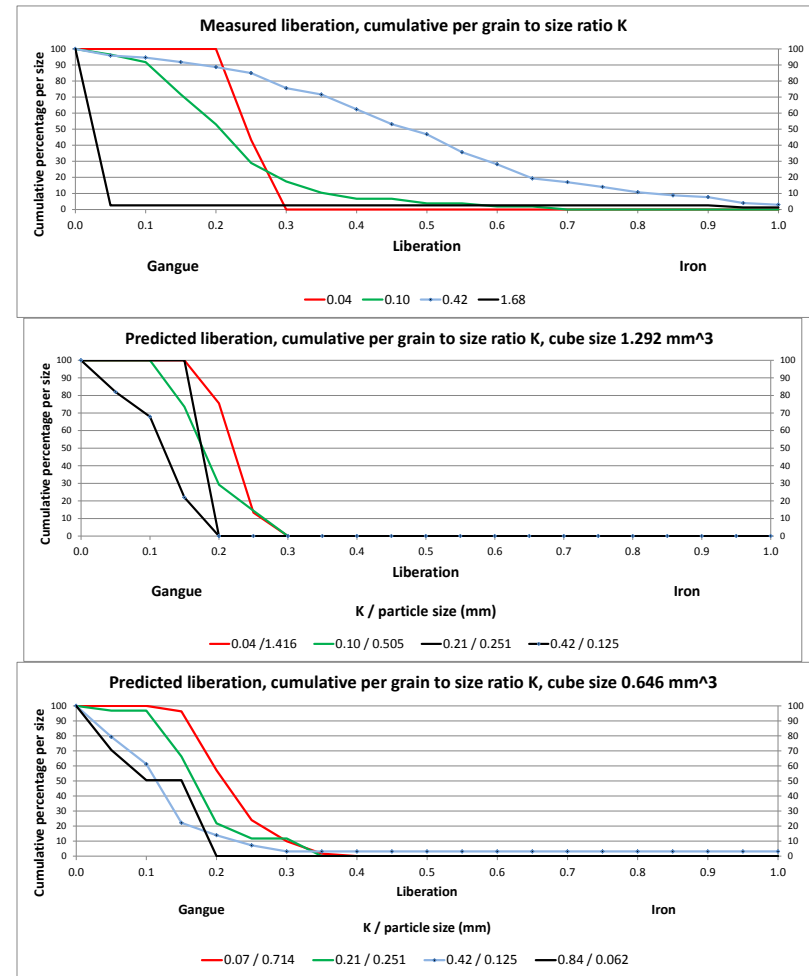

Figure 223: Family of lines of constant liberation, cumulative per size, measured and predicted for KE003
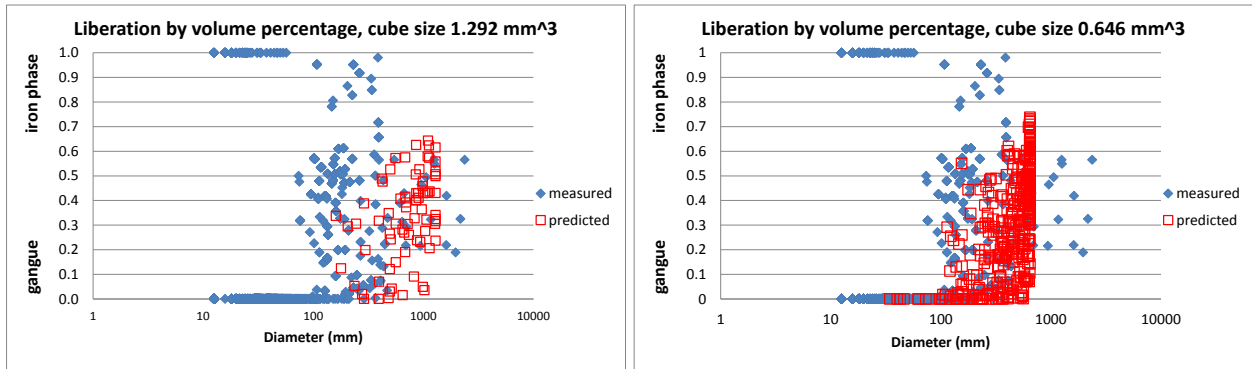
9.27 Liberation data, KE004

Figure 224: Measured progeny and simulated breakage of parent particle with 1292 and 646μm3 cube size, particle KE004
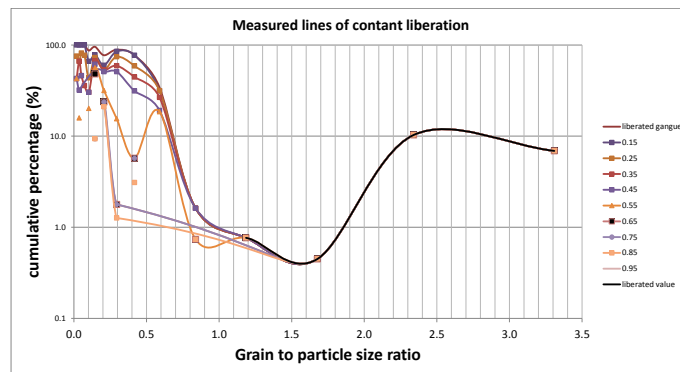

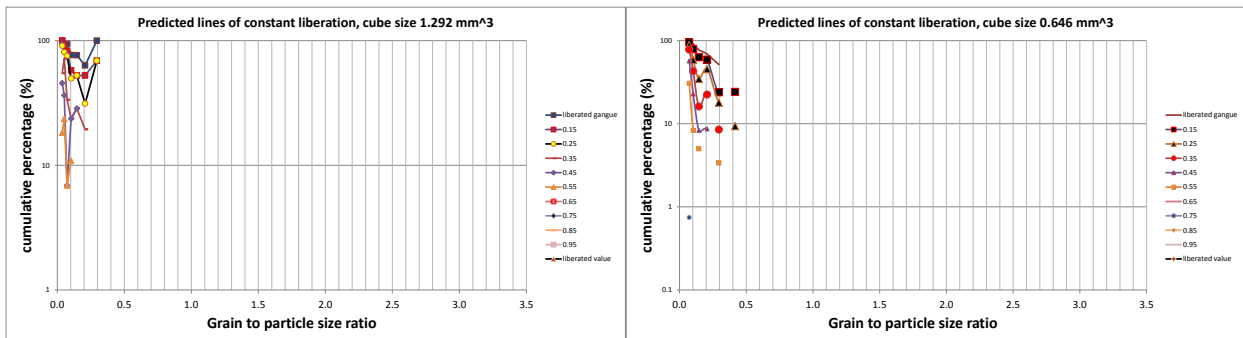**Figure 225: Measured lines of constant liberation, particle KE004**

Figure 226: Predicted lines of constant liberation, KE004 particle, using 100 pixels[3] and 50 pixels[3] simulated cubes

Figure 225 shows measured lines of constant liberation for parent particle KE004 and predicted lines are shown in Figure 226.
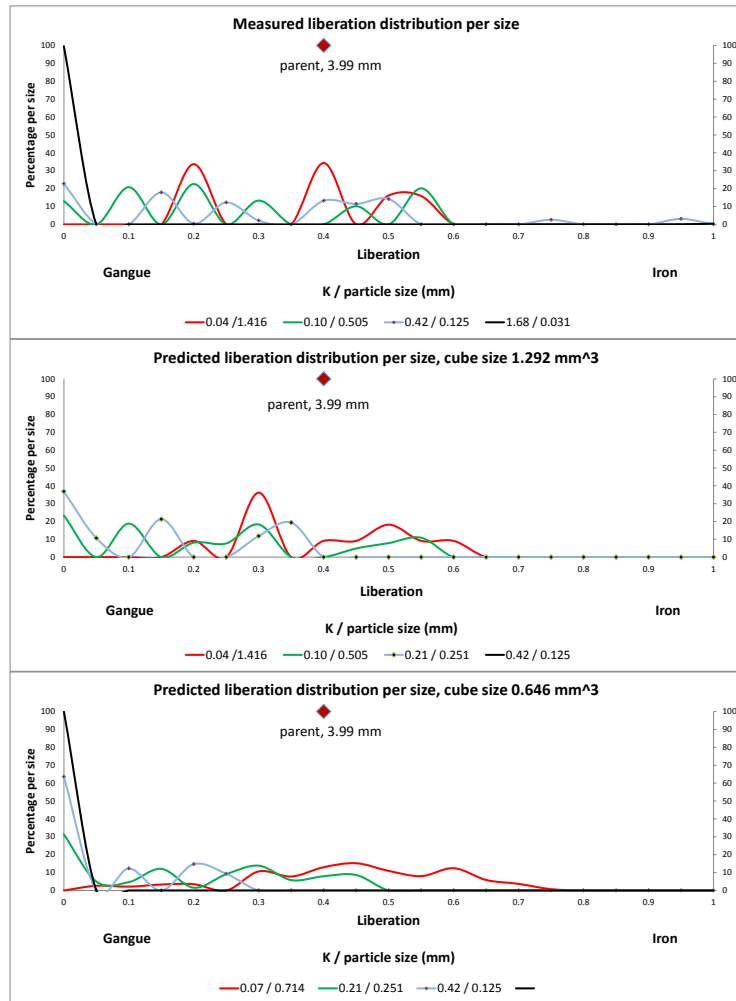
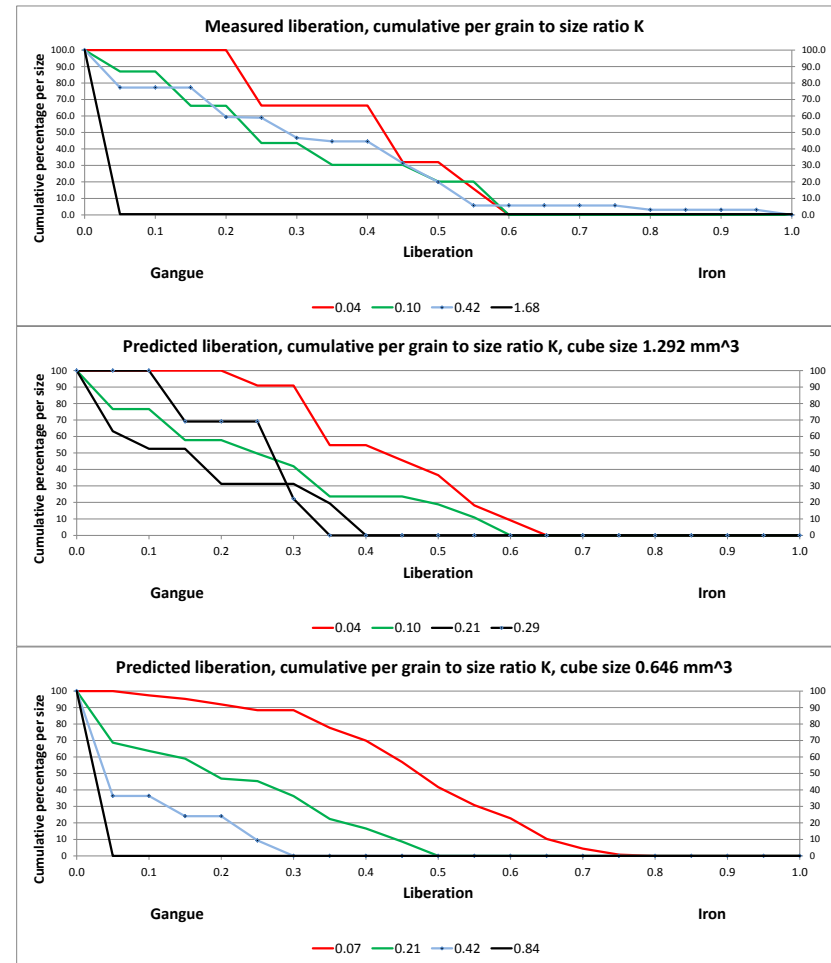**Figure 227: Family of lines of constant liberation, measured and simulated, KE004**

Figure 228: Family of lines of constant liberation, cumulative per size, measured and simulated for KE004

9.28 Iron Phase grain size distribution

Table 47: Cumulative Iron phase grain size distribution, KE001

Grain Size (μm)	Predicted Cube Size (μm)			Parent	Measured progeny
	323	646	1292		
13	0%	0%	0%	0%	0%
19	1%	1%	1%	1%	1%
26	2%	2%	2%	1%	1%
37	5%	4%	3%	3%	2%
52	9%	7%	5%	4%	3%
74	14%	10%	7%	5%	5%
105	20%	12%	8%	6%	7%
148	31%	16%	10%	7%	10%
210	71%	21%	11%	8%	19%
300	100%	34%	13%	8%	21%
357	100%	46%	15%	8%	22%
505	100%	97%	21%	8%	23%
714	100%	100%	54%	9%	23%
1001	100%	100%	100%	9%	27%
1416	100%	100%	100%	9%	27%
2812	100%	100%	100%	100%	100%

The header "Valuable Phase Grain size (μm), cumulative by volume %" spans the entire table.